UNIVERSITÀ DEGLI STUDI DI NAPOLI "FEDERICO II"

Scuola di Dottorato in Scienze della Terra
XXVII Ciclo
Tesi di Dottorato in Giacimenti Minerari

Ph.D. School in EARTH SCIENCES - _XXVII Cycle_
DOCTORAL THESIS in ECONOMIC GEOLOGY

The Jabali, Hakkari and Reef Ridge nonsulfide Zn(Pb) deposits: an evaluation by QEMSCAN® technology, and comparison to other analytical methods.

Ph.D. Student
Licia Santoro

Supervisor
Prof. Maria Boni

~ April, 2015 ~

TABLES OF CONTENTS

ABSTRACT

Supergene Zn(Pb)-nonsulfide deposits consist mainly of Zn/Pb-carbonates (smithsonite, hydrozincite, cerussite), Zn-(hydro)silicates (hemimorphite, sauconite), Fe-hydroxides, minor Fe-Pb-sulfates (i.e. anglesite, jarosite) and Zn-Pb-phosphates (i.e. tarbuttite, pyromorphite), commonly associated with remnants of primary sulfides (sphalerite and galena), which form from oxidation of sulfide-bearing concentrations by meteoric waters. The relative abundances of these mineral phases and the mineral species precipitating are strongly dependent on the type of host rock. Their variable mineralogy is complex to characterize, and it is crucial to define the processing method and foresee the metal recovery. Since most nonsulfide Zn-Pb deposits are amenable to be treated by hydrometallurgy, e.g. by leach/solvent extraction/electrowinning, AmmLeach®, etc., an incorrect evaluation of the modal distribution, or of the relations between ore and gangue minerals could lead to a severe increase of the production costs or drive the choice of the processing route in erroneous directions.

Objective of this thesis, hence, was to integrate the more traditional analytical technologies (OM, CL, SEM-EDS, WDS and CA) with the "Automated Mineralogy" analysis system (QEMSCAN®), in order to improve the accuracy of nonsulfide ores characterization. Part of this aim has been reached by the comparison of the quantitative evaluation of three nonsulfide deposits, carried out with two different methods: XRD-quantitative (i.e. Rietveld) and QEMSCAN®. As a conclusion, it was possible to discuss the advantages and limitations of both methods, for the choice of the best routine during feasibility study. Three supergene nonsulfide zinc deposit with different grades of mineralogical complexity have been considered for this purpose: Hakkari Zn(Pb) in Turkey; Jabali Zn-Pb(Ag) in Yemen; Reef Ridge Zn in Alaska. The general geology, mineralogy and geochemistry of each of these deposits have been evaluated separately, either from already known reference literature, or on the base of recently obtained scientific results. These data are considered preliminary to the QEMSCAN® analyses, and should be assimilated during the evaluation through Automated Mineralogy.

The Hakkari zinc deposit is located in the extreme southeastern region of Turkey, approximately 10 km west of the town of Hakkari, within a broad 20 km wide and 100 km long east-west belt. The orebodies, consisting of both sulfide and nonsulfide Zn≫Pb ores occur in Middle-Triassic to Early Cretaceous shallow water carbonate rocks within the northern margin of the Arabian Platform. The nonsulfide ore, which represent the

most economic portion of the deposit, consists of overall estimated compliant resources of at least 10 Mt @ 15% Zn.

Traditional techniques were used to carry out a complete geochemical, petrographic and mineralogic characterization of the Hakkari economic ore. This mineral association typically comprises smithsonite and hemimorphite, which apparently replace both sulfide minerals and carbonate host rock. Two generations of smithsonite occur: the first is relatively massive, the second occurs as concretions in cavities. Some zinc is also hosted within Fe–Mn-(hydr)oxides. Lead is present in cerussite, but also in Mn-(hydr)oxides. In the whole mineralized area a diffuse As-Sb-Tl geochemical enrichment also occurs. Silver is also present locally. The features of the supergene mineralization suggest that the Hakkari deposit belongs both to the "*direct replacement*" and "*wall rock replacement*" after the Hitzman et al. (2003) classification.

Carbon-oxygen stable isotopes geochemistry has been carried out on the nonsulfide minerals (smithsonite), in order to define the nature of the mineralizing fluids and the genesis of the mineralization. The $\delta^{13}C$ values range from -3.3‰ to -6.0 ‰ VPDB. These values are comprised in the characteristic $\delta^{13}C$ interval of supergene smithsonites, and are interpreted as a result of mixing between carbonate carbon from the host rock and soil/atmospheric CO_2. The $\delta^{18}O$ values of smithsonite lie between 24.2 ‰ and 25.3 ‰ VSMOW: these values can be associated with a smithsonite deposition from supergene weathering fluids of possible Upper Tertiary age.

The Hakkari samples were also analyzed quantitatively both by the XRD-Rietveld and QEMSCAN® methods. QEMSCAN® analysis also allowed a more detailed mineralogical characterization of several Hakkari drill cores. The study with the "Automated Mineralogy" technique confirmed the main mineral phases (smithsonite and hemimorphite) recorded with traditional methods, but identified other phases not previously detected (e.g. minerals in trace amounts such as sauconite), being also able to distinguish and quantify impure phases (e.g. Zn-dolomite, Cd-calcite), and identify amorphous phases [pyrite/Fe-(hydr)oxides/jarosite mix] that XRD had found challenging.

In particular, the modal mineralogy of the ore and gangue minerals, the mineral association and the spatial distribution data of the economic minerals at Hakkari provided information for the advanced exploration phase of the deposit.

Jabali is a Zn-Pb-(Ag) nonsulfide deposit, located 110 km northeast of Sana'a, the capital of Yemen along the western border of the Marib-Al-Jawf/Sab'atayn basin. The deposit covers an area of about 2 km^2. The orebody is hosted in the Jurassic carbonate rocks of the Shuqra Fm. (Amran Gp.). It is is almost completely oxidized with only a small portion unaltered thanks to an impermeable sediment cover. Ore characterization by the use of traditional analytical techniques revealed that smithsonite is the main zinc mineral, while hemimorphite and hydrozincite are less common. Cerussite and anglesite also occur as main lead minerals. Goethite, hematite, and Mn-(hydr)oxides are common throughout the mining area. Ag-sulfide and native silver are also present locally. Zn-enriched dolomite was detected by the use of SEM-EDS analyses in many samples from

several zones of deposit, even if not quantified by XRD-Rietveld analyses. The $\delta^{13}C$ values of smithsonite vary from -2.9‰ and 5.7‰ VPDB. The $\delta^{18}O$ values range from 19.0‰ to 21.4‰ VSMOW. The $\delta^{13}C$ values are in the range of supergene smithsonites worldwide and point to a mixed source of carbon (organic matter in the soil, atmospheric CO_2, and host rocks). The $\delta^{18}O$ values, instead, indicate the effects of temperature-related fractionation along the cores. This is probably due to variable precipitation temperatures of the Zn-carbonate; a hydrothermal component cannot be excluded. Several hypotheses have been formulated on the age and genesis of the supergene mineralization. Some authors propose a long period of oxidation, subdivided in several phases, extended from Cretaceous to Present, whereas others believe that there has been a single oxidation stage, which started in Miocene and continues until Present.

A renewed mineralogical characterization and quantitative evaluation of the Jabali deposit was carried out by the use of QEMSCAN® automated technology and proposed as one of the main subject of this thesis. The main aim was the improvement of the knowledge of mineral association and element deportment for the Jabali supergene ore.

The results confirmed the main findings of the previous studies and added new and more detailed information: smithsonite is mostly associated and intergrown with Fe-(hydr)oxides and remnants of primary sulfides; the host dolomite is locally replaced by broad bands of Zn-rich dolomite (which has been quantified by QEMSCAN®), where Zn has substituted for Mg. Hemimorphite, cerussite and anglesite occur in minor amounts (in agreement with previous studies). The Ag-sulfides are mainly associated with anglesite. Gypsum, Fe-(hydr)oxides (goethite>hematite), Zn-Mn-(hydr)oxides and Pb-Mn-(hydr)oxides have been detected locally. The QEMSCAN® technique, hence, combined with data previously obtained from other analytical techniques (XRD, SEM-EDS, optical petrography), has provided detailed mineralogical and textural information on the Jabali mineralization. A key outcome from this QEMSCAN® study is the textural data and quantification of the Zn-dolomite, and this was an important result, because the occurrence of abundant Zn-dolomite in the host rock caused issues in the recovery steps during the choice of the best processing route. The combination of techniques used to examine the Jabali supergene ore provides high quality information that not only characterizes the deposit in detail, but also offers a better understanding for the design of ore processing options and a more realistic predicted recovery of economic minerals.

The Reef Ridge prospect is a typical supergene nonsulfide zinc mineralization, located in the Yukon-Koyukuk region of west central Alaska (USA). It is hosted in sedimentary rocks of the Farewell Terrane, a continental fragment sandwiched between the Siberian and Laurentian cratons during the early Paleozoic. The mineralization occurs in Lower-Middle Devonian dolomites belonging to a Paleozoic carbonate platform succession. The mineralization consists of oxidized minerals, associated with minor sulfide remnants. The results of a complete petrographic and mineralogical study (XRD, chemical analysis, SEM-EDS and QEMSCAN®) show that Reef Ridge has a simple mineralogy compared to the Hakkari and Jabali deposits. The most abundant mineral in the nonsulfide ore is smithsonite. Similar to other nonsulfide zinc deposits worldwide, a first generation of smithsonite, has replaced both primary sphalerite and the

host carbonates. A second smithsonite generation precipitated as cement in vugs and
fractures. Minor zinc amounts also occur in the Fe-(hydr)oxides and zinc traces have
been identified in clay minerals.

Geochemical isotope analyses have been carried out on the carbonate minerals, in order
to define the genesis of the supergene ore. Carbon and oxygen isotope values of
smithsonite at Reef Ridge range from -0.7 to 2.1‰ VPDB and 19.1 to 21.9‰VSMOW,
respectively. The $\delta^{13}C$ values suggest that the predominant carbon source for smithsonite
were the host carbonates, with a limited contribution from organic carbon. The oxygen
isotope ratios are much more depleted in ^{18}O compared to supergene nonsulfides from
other parts of the world, formed under warm-humid, temperate or semi-arid climates.
The depletion in ^{18}O of precipitating waters, indicate that the formation of the Reef
Ridge nonsulfide deposit is probably related to cold/humid weathering episodes during
late Tertiary to Recent. These findings have subverted the "traditional" theory that the
supergene Zn nonsulfide deposits only form in warm-humid, temperate or semi-arid
conditions. As the other two analyzed deposits, also Reef Ridge shows the features of
both *"direct replacement"* and *"wall rock replacement"* supergene ores.

Although the considered deposits represent three typical examples of supergene
nonsulfide Zn-(Pb) ore concentrations, their study has revealed several important
mineralogical and petrographic differences: Jabali resulted to be the most
mineralogically complex of the three, due to the number of occurring mineral phases
(smithsonite, Fe-(hydr)oxides, cerussite, anglesite, remnants of sphalerite and galena,
and several other minor phases, i.e. Ag-minerals, sauconite, kaolinite, gypsum, calcite)
and because of the local occurrence of high amounts of Zn-(Pb) in several mineral
phases (i.e. Zn-dolomite). The mineralogy of the Hakkari deposit is also not quite
straightforward, with zinc occurring mainly as smithsonite and hemimorphite, lead as
cerussite and anglesite, associated with Fe- and Mn-(hydr)oxides. The mineralogy of the
Alaskan deposit, instead, is quite simple, because it consists of smithsonite, with some
Fe-(hydr)oxides and rare sphalerite.

The study of these three deposits was carried out with the use of several traditional
techniques, and a more recent analytical technique (QEMSCAN®) to better comprehend
the feature of the deposits mineralization. During the analyses we faced with several
issues that sometimes resulted in unaccurate information and misleading data: e.g. the
occurrence of unidentified amorphous phases, the absence of phases wrongly determined
earlier (i.e. ankerite and Zn-ankerite), the occurrence of not quantificable mixed phases,
and the difficulty to characterize a few mixed mineral compounds. To overcome this
problem, was necessary the support of several analytical techniques, and the comparison
of the results obtained with each of them.

The main conclusion of this study is that the characterization of nonsulfide Zn-
deposit, and especially their quantitative evaluation (QPA) may be quite tricky, because
of their complex mineralogy. The lack of accurate mineralogical results can cause

several problems in the processing and metallurgical stages (recovery issues, penalties at the smelter, poor metal quality, and environmental damage).

QEMSCAN® is an useful tool for ore characterization during exploration and potential processing steps, as it can provide detailed information on the texture, add significant information on the major and trace mineral distribution, and produce a good quantitative evaluation of the isomorphic phases that typically characterize the minerals occurring in nonsulfide deposits. However, even though there are many positive aspects in applying this technique, it is important to remark that the QEMSCAN® data **cannot be** used alone, because of some ambiguity in minerals identification.

RIASSUNTO

I depositi supergenici a nonsolfuri di zinco e piombo consistono principalmente di Zn/Pb- carbonati (smithsonite, idrozincite, cerussite), Zn-(idro)silicati (emimorphite, sauconite), Fe-(idr)ossidi, Fe-Pb-solfati (es. anglesite, jarosite) e Zn-Pb-fosfati (es. tarbuttite, piromorfite), generalmente associati a solfuri primari residui (blenda e galena). Tali concentrazioni si formano generalmente per l'ossidazione di depositi a solfuri primari ad opera di acque meteoriche. L'abbondanza relativa e la tipologia dei minerali secondari sono in stretta relazione con il tipo di roccia incassante. La caratterizzazione di questo genere di depositi è generalmente complicata dalla loro mineralogia variabile e complessa. Considerando che la maggior parte dei depositi supergenici a nonsolfuri di Zn-Pb può essere trattata tramite idrometallurgia (es. estrazione con solventi/electrowinning, AmmLeach®, ecc.) un'errata valutazione della distribuzione modale, o delle relazioni tra i minerali economici e quelli di ganga potrebbe portare a un aumento dei costi di produzione o causare una scelta sbagliata del metodo di arricchimento.

L'obiettivo di questa tesi è stato quello di integrare i metodi di analisi più tradizionali (OM, CL, SEM-EDS, WDS e CA) con i sistemi di "analisi mineralogica automatizzata" (QEMSCAN®), al fine di migliorare l'accuratezza della caratterizzazione dei giacimenti supergenici a nonsolfuri. Gran parte dei risultati sono stati ottenuti con il confronto delle analisi mineralogiche quantitative su tre depositi a nonsolfuri, portate avanti con metodi differenti (XRD-Rietveld e QEMSCAN®). Alla fine sono stati discussi vantaggi e i limiti di entrambi i metodi per poter quindi scegliere la migliore opzione analitica da impiegare durante gli studi di fattibilità.

Sono stati condotti studi accurati su tre depositi supergenici a nonsolfuri con differente grado di complessità mineralogica: Hakkari Zn(Pb) in Turchia; Jabali Zn-Pb(Ag) in Yemen; Reef Ridge Zn in Alaska. La geologia, mineralogia e geochimica di ognuno di questi depositi è stata valutata separatamente, prendendo in considerazione sia la letteratura di riferimento oltre che risultati più recenti ottenuti da studi portati avanti nel corso di questa ricerca, Tali informazioni sono da considerarsi preliminari all'effettuazione delle analisi con il QEMSCAN®, e devono essere integrate durante la fase di valutazione con tecnologie di "analisi mineralogica automatizzata".

Il deposito di Hakkari è situato nell'estremo sud-est della Turchia, a circa 10 km ad ovest dalla città di Hakkari, in un'ampia catena montuosa che misura circa 20 km di ampiezza e 100 km di lunghezza. Le mineralizzazioni sono costituite da solfuri e nonsolfuri di Zn>>Pb in rocce carbonatiche di mare basso di età Triassica-Cretacica inferiore, all'interno del margine settentrionale della Piattaforma Araba. La parte economica del giacimento è costituita da mineralizzazioni a nonsolfuri con risorse totali stimate di circa 10 Mt @ 15% Zn.

La caratterizzazione geochimica, petrografica e mineralogica del deposito di Hakkari è stata eseguita con l'utilizzo di tecniche analitiche tradizionali. I risultati indicano che l'associazione mineralogica tipica della zona di ossidazione supergenica comprende smithsonite ed emimorfite, che sostituiscono sia i solfuri primari che le rocce carbonatiche incassanti. Sono presenti due generazioni di smithsonite: la prima relativamente massiva, la seconda, invece, è presente come concrezioni in cavità e in vene. Lo zinco è presente inoltre anche in (idr)ossidi di ferro e manganese. Il piombo si rinviene sottoforma di cerussite, in (idr)ossidi di manganese (fino ad un valore massimo di 30 wt.% PbO). Nell'intera area mineralizzata sono inoltre presenti elementi quali As-Sb-Tl. Localmente si rinvengono basse percentuali di argento.

Le caratteristiche sopra descritte indicano che il depositi di Hakkari può essere considerato sia come un deposito di "*sostituzione diretta*", che di "*sostituzione della roccia incassante*" secondo la classificazione di Hitzman et al. (2003).

Sono inoltre state effettuate analisi geochimiche sugli isotopi stabili del carbonio e dell'ossigeno nella smithsonite, al fine di definire la natura dei fluidi mineralizzanti e la genesi della mineralizzazione supergenica. I valori di $\delta^{13}C$ vanno da -3.3‰ a -6.0‰ VPDB. Tali valori sono compresi nell'intervallo di $\delta^{13}C$ caratteristico delle smithsoniti supergeniche e sono interpretatti come risultato della commistione tra il carbonio proveniente dalla roccia incassante carbonatica e quello atmosferico o della sostanza organica presente nei suoli. I valori ^{18}O della smithsonite sono compresi tra 24.2‰ and 25.3‰ VSMOW e possono essere associati a precipitazione di smithsonite da fluidi di alterazione supergenica di probabile età Terziario superiore.

I campioni di Hakkari sono stati sottoposti anche ad analisi quantitativa con entrambi i metodi XRD-Rietveld e QEMSCAN®. Le analisi al QEMSCAN® hanno inoltre fornito una caratterizzazione mineralogica più dettagliata rispetto a quella ottenuta con altri metodi. Lo studio con una tecnologia di analisi mineralogica automatizzata ha confermato la presenza delle fasi mineralogiche principali (smithsonite ed emimorfite), precedentemente già rinvenute con tecniche analitiche tradizionali. Sono state identificate anche nuove fasi mineralogiche non rilevate precedentemente (es. minerali in traccia come la sauconite). Sono state inoltre distinte e quantificate fasi mineralogiche "impure" (es. Zn-dolomite, Cd-calcite), e fasi amorfe [pirite/Fe-(hydr)oxides/jarosite miste].

In particolare, la mineralogia modale dei minerali economici e di quelli di ganga, l'associazione mineralogica e i dati sulla distribuzione spaziale dei minerali economici ad Hakkari hanno fornito informazioni significative per la fase avanzata dell'esplorazione.

Jabali è un deposito a nonsolfuri di Zn-Pb-(Ag), sito a 110 km nord-est della città di Sana'a, la capitale dello Yemen. Esso si trova lungo il margine occidentale del bacino di Marib-Al-Jawf/Sab'atayn e copre un'area di circa 2 km^2. Le mineralizzazioni sono ospitate in rocce carbonatiche Giurassiche della formazione di Shuqra (Amran Gp). La mineralizzazione primaria è quasi totalmente ossidata; solo una minima porzione è rimasta inalterata grazie ad una copertura sedimentaria impermeabile che l'ha protetta dall'alterazione meteorica.

La caratterizzazione mineralogica del deposito con l'utilizzo di tecniche tradizionali ha rivelato che il principale minerale economico di zinco è la smithsonite, mentre emimorfite ed idrozincite sono meno frequenti. Il piombo è presente come cerussite e anglesite. Goethite, ematite e (idr)ossidi di manganese sono comuni in tutto il distretto, mentre l'argento nativo è presente solo localmente.

Grazie all'utilizzo di analisi SEM-EDS è stata rilevata la presenza di dolomite arricchita in zinco in molti campioni provenienti da diverse aree del distretto minerario. Tuttavia, le analisi XRD-Rietveld non sono risultate idonee a quantificare le percentuali di Zn-dolomite presenti nei campioni del deposito.

I valori isotopici del carbonio e dell'ossigeno per la smithsonite variano a seconda della profondità dei campioni. I valori di δ^{13}C vanno da -2.9‰ a 5.7‰ VPDB, e quelli di δ^{18}O da 19.0‰ a 21.4‰VSMOW. I valori di δ^{13}C rientrano nel campo delle smithsoniti supergeniche, che derivano da sorgenti di carbonio variabili tra la materia organica del suolo, la CO_2 atmosferica e i carbonati incassanti. I valori di δ^{18}O, invece, sono indicativi della variazione di temperatura delle acque nella zona mineralizzata. Ciò potrebbe essere dovuto a precipitazione dei carbonati di zinco a temperature variabili; non è da escludersi una componente idrotermale. Si ritiene comunque che il deposito supergenico di Jabali si sia formato durante il Miocene inferiore (~17 Ma), grazie a condizioni climatiche e tettoniche favorevoli. Vi sono varie ipotesi sulla genesi delle mineralizzazioni supergeniche di Jabali: alcuni autori ritengono che il deposito si sia formato in seguito ad un lungo periodo di ossidazione comprendente più fasi di alterazione, dal Cretaceo fino ad oggi. Da altre fonti di letteratura la formazione del deposito di Jabali viene considerata ascrivibile ad una sola fase di ossidazione che inizia nel Miocene e prosegue sino all'Attuale.

In questa tesi viene proposta una rinnovata caratterizzazione accompagnata da un'analisi quantitativa del deposito supergenico di Jabali tramite l'utilizzo del QEMSCAN®, al fine di migliorare le informazioni sull'associazione mineralogica e sulla distribuzione degli elementi nella zona mineralizzata. I risultati hanno confermato essenzialmente i dati ottenuti dagli studi precedenti, aggiungendo nuove e più dettagliate informazioni: la smithsonite è principalmente associata agli (idr)ossidi di ferro e a solfuri primari residui; la dolomite della roccia incassante viene localmente sostituita da ampie bande di dolomite arricchita in zinco, là dove lo zinco sostituisce il magnesio (la Zn-dolomite è stata anche analizzata quantitativamente). Emimorfite, cerussite e anglesite sono presenti in minori quantità, come già rilevato da studi precedenti. Il solfuro di Ag è associato principalmente con l'anglesite. Localmente sono stati individuati gesso, (idr)ossidi di

ferro (goethite ed ematite), (idr)ossidi di zinco e piombo e (idr)ossidi di piombo e manganese. Le analisi al QEMSCAN®, quindi, insieme ai dati ottenuti precedentemente con altre tecniche analitiche (XRD, SEM-EDS, OM), hanno fornito informazioni mineralogiche e tessiturali più dettagliate del deposito di Jabali. Informazioni chiave ottenute tramite l'uso di questa tecnologia sono i dati tessiturali, oltre che l'analisi quantitativa della Zn-dolomite. Quest'ultimo dato è di vitale importanza, poichè la presenza di alte concentrazioni di Zn-dolomite nella roccia incassante può causare numerosi problemi durante le fasi di recupero del metallo, e può influenzare la scelta del metodo di arricchimento.

L'uso combinato di più tecniche analitiche ha fornito quindi accurate informazioni sul deposito di Jabali. L'insieme di tali tecniche ha permesso di caratterizzare in dettaglio la mineralogia, al fine di scegliere le migliori opzioni in fase di *processing*, così da ottenere una previsione più realistica del recupero effettivo dei minerali economici.

Il prospetto di Reef Ridge rappresenta una tipica mineralizzazione supergenica a nonsolfuri di zinco. Esso è situato nella regione dello Yukon-Koyukuk, in Alaska centro-occidentale (USA). La mineralizzazione si trova in rocce sedimentarie appartenenti al Farewell Terrane, un frammento continentale che, dalle ricostruzioni paleogeografiche del Paleozoico, era situato tra il cratone Siberiano e la Laurentia. I livelli mineralizzati si trovano all'interno di rocce appartenenti ad una successione di piattaforma carbonatica Paleozoica, più precisamente dolomie del Devoniano Inferiore-Medio. La mineralizzazione è costituita da minerali ossidati, associati a rari residui di solfuri primari.

I risultati ottenuti da un completo studio petrografico e mineralogico (XRD, analisi chimiche, SEM-EDS and QEMSCAN®) mostrano che Reef Ridge presenta una mineralogia molto più semplice rispetto ai depositi di Hakkari e Jabali. Il minerale economico più abbondante è la smithsonite. Similmente ad altri depositi a nonsolfuri, una prima generazione di smithsonite sostituisce sia la blenda che le rocce carbonatiche incassanti, mentre una seconda generazione si ritrova sottoforma di concrezioni in vene e come cemento in cavità e fratture. Una quantità inferiore di zinco si rinviene negli (idr)ossidi di ferro. Zinco in tracce è stato inoltre rilevato anche in alcune argille.

Le analisi degli isotopi stabili sono state condotte sui carbonati di zinco, al fine di definire la genesi del deposito supergenico. I valori degli isotopi di carbonio e di ossigeno della smithsonite di Reef Ridge vanno da -0.7 to 2.1‰ VPDB e 19.1 to 21.9‰ VSMOW, rispettivamente. I valori di $\delta^{13}C$ suggeriscono che la sorgente predominante del carbonio nella smithsonite sono i carbonati della roccia incassante, con un limitato contributo della sostanza organica. Il rapporto isotopico dell'ossigeno è molto impoverito in ^{18}O rispetto ai nonsolfuri supergenici di altri depositi formatisi in condizioni climatiche caldo-umide, temperate o semi-aride. L'impoverimento in ^{18}O delle acque di precipitazione indica che la formazione dei minerali a nonsolfuri di Reef Ridge è avvenuta con un clima freddo/umido, probabilmente durante episodi di alterazione meteorica tardo Terziario/Recente. Tale risultato sovverte la teoria tradizionale, secondo la quale i depositi supergenici a nonsolfuri di zinco si formano

soltanto in zone a clima caldo-umido, temperato o semi-arido. Come i depositi considerati in precedenza, Reef Ridge risulta appartenere alle categorie di depositi supergenici di "*sostituzione diretta*" e "*sostituzione della roccia incassante*".

Nonostante i depositi sopra citati rappresentano tre tipici esempi di nonsolfuri supergenici a zinco-(piombo), il loro studio ha rivelato importanti differenze mineralogiche e petrografiche: Jabali è risultato essere il deposito più complesso dal punto di vista mineralogico a causa della varietà di fasi presenti (smithsonite, idrossidi e ossidi di ferro, cerussite, anglesite, blenda e galena residue ed altre fasi minori come sauconite, kaolinite, gesso, calcite, solfuri di Ag) e a causa della presenza di alte concentrazioni di Zn-(Pb) come elementi accessori in altri minerali (es. Zn-dolomite). Neanche la mineralogia del deposito di Hakkari è da considerare semplice. Qui lo zinco è presente principalmente come smithsonite ed emimorfite; il piombo come cerussite e anglesite oltre che contenuto in (idr)ossidi di ferro e manganese. La mineralogia del deposito di Reef Ridge, invece, è abbastanza semplice e consiste principalmente di smithsonite, (idr)ossidi di ferro e rara blenda.

Lo studio di questi tre depositi è stato condotto con l'uso di tecniche analitiche tradizionali e con tecnologie più moderne (QEMSCAN®), al fine di comprendere meglio le loro caratteristiche mineralogiche. Durante le analisi abbiamo riscontrato molteplici problemi che hanno portato, in alcuni casi, ad informazioni inaccurate o dati erronei: ad es. la presenza di fasi amorfe, l'assenza di fasi che erano state erroneamente identificate (ankerite e Zn-ankerite), la presenza di fasi miste non quantificabili, e la difficoltà nel discernere e caratterizzare tali fasi miste. Per superare questi problemi si è reso necessario il supporto di differenti tecniche analitiche, e il confronto dei dati ottenuti da ognuna di queste.

In conclusione, la caratterizzazione dei depositi supergenici a nonsolfuri di zinco e l'analisi quantitativa delle fasi presenti può essere difficile ed ingannevole a causa della complessità mineralogica che generalmente li caratterizza. La mancanza di dati mineralogici accurati può causare gravi problemi durante le fasi di *processing* e di metallurgia (scarso *recovery*, penalizzazioni dei prodotti di fonderia, bassa qualità del metallo, danni ambientali).

La tecnologia QEMSCAN® può essere di grande aiuto in fase di esplorazione e di *processing* poichè fornisce informazioni dettagliate sulla tessitura e sulla distribuzione dei minerali maggiori ed in traccia, producendo analisi quantitative accurate delle fasi isomorfe che spesso caratterizzano i minerali presenti nei depositi a nonsolfuri. Nonostante i numerosi vantaggi che si ottengono mediante l'utilizzo del QEMSCAN®, è importante ricordare che tale tecnica **non può essere mai utilizzata da sola,** a causa dell'ambiguità di una parte dati prodotti durante l'identificazione dei minerali.

INTRODUCTION

Supergene nonsulfide Zn-Pb(Ag) deposits are a peculiar category of ores, which typically consist of a mixture of oxidized ore minerals derived from the weathering of primary sulfide concentrations (Hitzman et al., 2003). Their mineralogical association mainly comprehends: Zn-Pb carbonate minerals (smithsonite, hydrozincite, cerussite), Zn-silicates (hemimorphite, Zn-clays, seldom willemite), sulfates (anglesite, jarosite), Fe/Mn-(hydr)oxides (hematite, goethite/ lepidocrocite, coronadite), and minor sulfide remnants (pyrite/marcasite, sphalerite, galena). Nonsulfide deposits significantly differ from the primary sulfide concentrations, not only in term of genesis, but for texture, petrography, mineralogy and geochemistry (Large, 2001; Hitzman et al., 2003; Boni and Mondillo, 2015).

Due to the complexity of their mineralogy, and considering the processing methods used for their recovery, accurate and reliable information is needed to avoid misleading data that can contribute to increase the expenses during processing and successive metallurgy. The economic value of nonsulfide zinc ores is therefore strictly dependent not only on the geological knowledge of each deposit, but also on the specific characteristics of its mineralogical association, and on the interaction between zinc- and gangue minerals during chemical and physical treatment (Boni, 2005; Woollett, 2005; de Wet and Singleton, 2008; Boni and Mondillo, 2015). For this reason, the mineralogical and petrographic characterization of this kind of deposits, the definition of the mineral association, their textural parameters, and the element deportment, are all very important issues to predict the metal (Zn-Pb) recovery, and hence the sustainability of an orebody.

Since the nonsulfide Zn-Pb(Ag) deposit are amenable to be treated by hydrometallurgy (Bodas, 1996; Abdel-Aal, 2000; Loan et al., 2006; Souza et al., 2007; de Wet and Singleton, 2008) e.g. leach/solvent extraction/electrowinning, AmmLeach® (Cole and Sole, 2002; MetaLeach Ltd: http://www.metaleach.com, ZincOx Annual Report 2007; de Wet and Singleton, 2008), and, less commonly, by pyrometallurgy (Clay and Schoonraad, 1976; Habashi, 2002), an incorrect evaluation of the modal distribution, or of the relations between ore and gangue minerals, could lead to a severe increase of the production costs or drive the choice of the processing route in erroneous directions. As an example, here are presented two typical cases of nonsulfide ores hosted in distinct lithologies:

1) In the case of a smithsonite-rich carbonate-hosted deposit (the most common type among others), a treatment with acid leaching (H_2SO_4), and an underestimation of the

17

gangue amount can lead to high acid consumption and hence to high production costs, since both calcite and dolomite are highly reactive to acid leaching (Frenay, 1985). A similar problem can occur in a smithsonite-rich deposit, where a wrong estimation of the relationships between the amount of the carbonate gangue and that of the economically valuable phases was obtained. For example, if a relatively low amount of carbonate gangue occurs in the nonsulfide-rich intervals, the best processing way is to use an acid-leach method. In this case, an overestimation of the carbonate gangue in the ore zone can drive the processing plan to other routes, thus reducing the effectiveness of the chosen method and increasing both expenses and time consumption.

2) In the case of silicate-rich nonsulfide deposits (containing mainly hemimorphite, sauconite), the main problem may reside in the precipitation of silica gels during the leaching stages (Dufresne, 1976; Matthew and Elsner, 1977, Frenay, 1985).

For certain nonsulfide minerals (such as smithsonite and other nonsilicates), a conventional production circuit, allowing a 90% Zn recovery would be the sequence roasting→leaching (±SX=solvent extraction) →electrowinning. However, this sequence should be adjusted to accommodate the different mineralogy and geochemistry of each deposit type and the importance of some of its steps may be either enhanced or downplayed (Woollett, 2005). The carbonate minerals smithsonite and hydrozincite, highly basic, can be quickly treated with LTC (leach-to-chemical), while the silicates with low basicity as hemimorphite, Zn-smectite (and more rarely willemite) may require an additional step to purify the leach solution using solvent extraction (SX) (Woollett, 2005). Direct leaching, can be applied in several cases where only limited calcite is mixed in with the mined ore, as in the Skorpion mine (Namibia), before SX (Cole and Sole, 2002). However, when nonsulfide Zn minerals are strictly intergrown with calcium carbonate, as in Accha, Peru (Boni et al, 2011) or Jabali, Yemen (Mondillo et al., 2011, 2014), there is a real problem of excess acid consuming during the leaching process, with a consequent raise in the processing costs. A possible alternative to this problem might be the ammonium leach extraction process (Alexander Mining Plc: http://www.alexandermining.com), which is a variant of the standard SX/ EW processing route, where ammonia-based chemistry is used to selectively extract metals from ores, using alkaline ammonium rather than acid to leach the metals (Boni et al., 2011). The difference from acid leaching is that the leaching process is conducted in moderately alkaline solution with ammonia present as a complexant.

From the previous assumptions it follows that, because even small differences in dissolution rates and in H_2SO_4 consumption, as well as the precipitation of unwanted phases such as silica gel, may have strong implications for the production strategies and metallurgical requirements, a thorough understanding of the mineralogy, but also of the petrographic associations is a "must" in exploration targeting and feasibility studies of each deposit type.

Mineralogy and petrography of nonsulfide Zn-Pb deposits are generally investigated using several methods: OM (Optical Microscopy), CL (Cathodoluminescence), SEM-

EDS (Scanning Elecron Microscopy by Energy Dispersive Spectroscopy), WDS (Wavelenght Dispersive Spectroscopy), XRD (X-ray diffraction), CA (Chemical Analyses). These methods can be time consuming, costly and generally produce semi-quantitative results from data sets that are too small to be effectively and statistically valid. Thus, the results cannot be always used effectively in digital mine planning.

The best method known so far to characterize an orebody, also from the quantitative point of view, consists in using technologies as QEMSCAN® (Quantitative Evaluation of Minerals by Electron Microscopy) or MLA (Mineral Liberation Analysis). Thank to these analytical systems, it is possible to obtain accurate information about several parameters of an ore: modal mineralogy of the samples from the mineralized areas, element deportment, particle images, mineral association, theoretical grade recovery, curve grain and particle size from whom depends the mineral liberation. Despite the high number of information that these technologies furnish, they have been mostly used for sulfide ores characterization because of their ability to output detailed information especially on mineral liberation and theoretical grade recovery curve (Goodall et al., 2005; Pascoe et al., 2007; Lotter et al., 2011; Anderson et al., 2014), which are particularly useful to plan the flotation process. The MLA and QEMSCAN® methods have been used only sporadically for the analysis of nonsulfide Zn-Pb ores, because their processing route does not make use of grain and particle size estimation, and of the mineral liberation grade for planning the size grinding for physical separation. However, these methods can be also useful to gain reliable information on the mineralogy and petrography of this kind of ores, in order to apply the best recovery process. QEMSCAN® has been used successfully for semi-quantitative mineralogical evaluation of Ni-laterite (Andersen et al., 2009) and bauxite deposits (Boni et al., 2013). A first attempt to characterize nonsulfide ores with QEMSCAN® was carried out on the Accha deposit (Peru) at the Camborne School of Mines, UK (Rollinson et al., 2011). A follow up was the application of this technology to the Hakkari deposit in Turkey (Santoro et al., 2013).

In the light of the above said, this thesis is regarded as an effort to integrate more traditional analytical technologies (OM, CL, SEM-EDS, WDS and CA) with the "Automated Mineralogy" analysis system, and apply them to the study of a number of nonsulfide Zn(Pb) ores. A second, but not less important aim of this work is a comparison between the quantitative evaluation of nonsulfide deposits carried out with QEMSCAN®, and one of the most common XRD-quantitative methods (i.e. Rietveld). The advantages and the limitations of both methods for the characterization of this type of concentrations will be thoroughly discussed. Three nonsulfide deposits have been used for this study: Hakkari Zn(Pb) in Turkey (Santoro et al., 2013, 2014); Jabali Zn-Pb(Ag) in Yemen (Mondillo et al., 2011, 2014; Santoro et al., in press); Reef Ridge Zn, in Alaska (Santoro et al. in press). The reason for choosing the above-mentioned mineralizations resides in the fact that, although genetically quite similar, they have distinct mineral associations. This is an advantage, because during this thesis there has

been the opportunity to come across several different mineralogical issues that had to be analyzed and resolved.

In the following chapters, will be firstly summarized the most important characteristics of supergene nonsulfide ores (chapter 1), followed by an accurate explanation of the QEMSCAN® technology and its applications (chapter 2). In the chapters 3, 4 and 5 there will be a general introduction on the geology and Zn(Pb) ore deposits (primary and secondary) of the chosen region, followed by an accurate description of the ore deposit itself, its geology, mineralogy and geochemistry (including isotope geochemistry). The results of X-ray and QEMSCAN® analyses will be then listed, compared and discussed.

Chapter 1

The supergene nonsulfide Zn-Pb deposits

1.1. Introduction.

With the word "nonsulfide ores" is intended a wide range of minerals, which form by the oxidization of primary sulfide-bearing deposits. The oxidization process is due to the chemical alteration (weathering) of the sulfide minerals (e.g. pyrite/marcasite, sphalerite, galena), which react with meteoric or hydrothermal waters commonly mixed with ground waters.

The nonsulfide ore deposits (also known as "zinc oxide deposits") were known since the antiquity. In fact, during the Roman and Medieval times it was common to use mixtures of ground metal-enriched carbonates and silicates (known as *"lapis calaminarius"* in Latin, *"calamine"*, in French, *"galmei"* or *"galman"* respectively in German and Polish languages) as zinc source for the production of brass (Boni and Large, 2003), even if was not possible to recover pure zinc metal from these kinds of ores, due to the high temperature to reduce zinc oxide with charcoal. The ability to recover zinc oxide from nonsulfide ores was discovered later in the nineteenth century, by the use of different kinds of kilns.

Nevertheless, after the development in the early twentieth century of the flotation process, and the increased ability to smelt and refine sphalerite concentrates, the attention in the economic geology world focused entirely on sulfide ores, with the subsequent reduction of interest in *"calamine"*. For several decades, hence, the nonsulfide materials were ignored because of the difficulties in metallurgical beneficiation of smithsonite ($ZnCO_3$) ores containing less than 20% Zn, and due to the general complex mineralogy of "nonsulfides", consisting of zinc carbonates, oxides, silicates, and clay minerals. Nevertheless, the development of new exploitation technologies such as solvent-extraction (SX), electrowinning (EW), and leach to chemical (LTC) at the beginning of the twenty-first century, resulted in a revival of commercial interest addressed to this style of mineralization throughout the world (Hitzman et al., 2003), and in a corresponding renewed scientific interest. Several papers, which had the aim to describe these ore deposits and better define their origin were

published at the beginning of 2000, starting with the first modern classification (Large, 2001), which modified the previous one of Heyl and Bozion (1962). Large (2001) subdivided the nonsulfide zinc deposits in three main categories: 1) *"Calamine"*-dominant deposits; 2) Willemite - dominant deposits; 3) Hydrated zinc silicate deposits, preserved in the supergene zone.

Hitzman et al., (2003) presented a more detailed classification, in which the attention was mainly on the genesis of the mineralization. Based on the genetic conditions, the authors proposed two main nonsulfide categories (Figure 1.1): *Supergene* and *Hypogene deposits*, further subdivided into other minor categories.
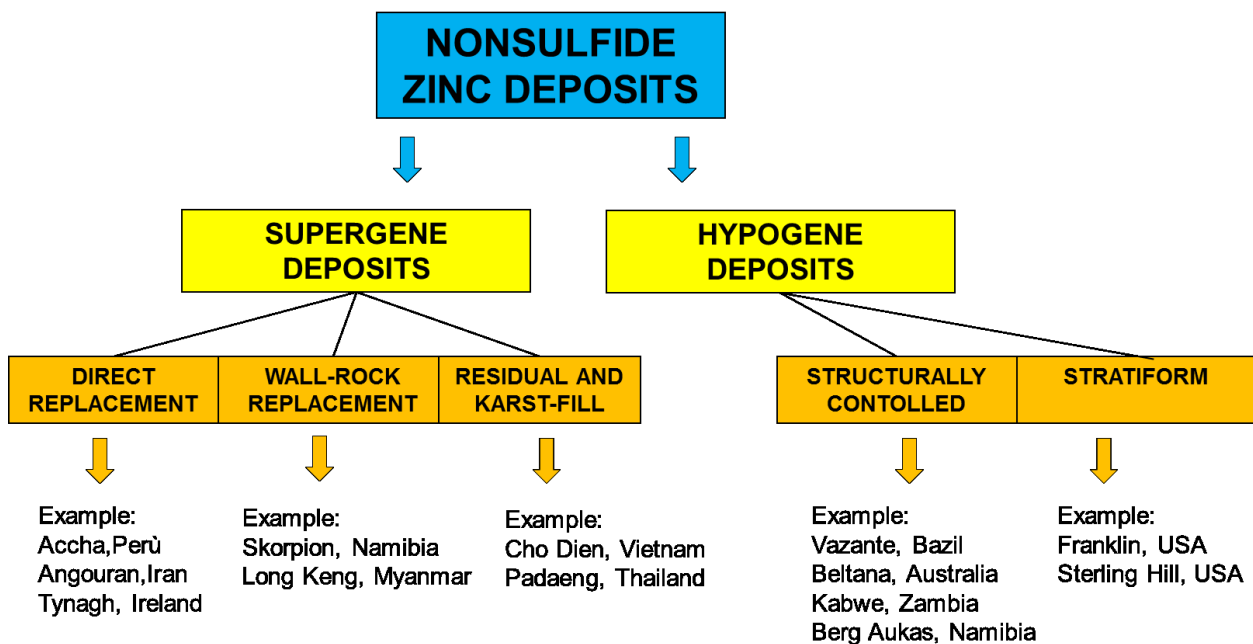
Figure 1.1: Classification of nonsulfide zinc deposits (Hitzman et al., 2003).

As mentioned, the supergene deposits form from the oxidation of sulfide-bearing ores in a weathering regime, and consist principally of smithsonite and/or hemimorphite. They are subdivided into:

➢ *Direct-replacement deposits*;
➢ *Wall-rock replacement deposits;*
➢ *Residual and karst-fill deposits.*

The hypogene deposits, instead, derive from the alteration of sulfide minerals in a hypogene environment; the mineralization mainly consists of zinc silicates (willemite), and oxides (zincite, hematite). They may contain also sulfides (sphalerite) and other high-temperature minerals (gahnite, franklinite). They are subdivided into:

➢ *Structurally controlled deposit;*
➢ *Stratiform nonsulfide deposits.*

1.2. Supergene nonsulfide Zn-Pb deposit classification.

The supergene nonsulfide zinc deposits have a worldwide distribution (Figure 1.2). They are generated via oxidation of both sulfide and hypogene nonsulfide deposits, and

are generally hosted in carbonate host rocks. This because of the high reactivity of carbonate minerals with acidic, oxidized, zinc-rich fluids derived from the breakdown of sphalerite-rich bodies. In rare cases the nonsulfide zinc deposits occur in sandstone-volcanoclastic-dominated host rocks (e.g. Skorpion, Namibia).

The precursor deposits generally consist of Mississippi Valley-type (MVT), Sedimentary exhalative (SEDEX) or Volcanic Massive Sulfide (VMS) ores. Also a Carbonate Replacement Deposit (CRD) or a sphalerite-Skarn orebody can be the precursor of a nonsulfide Zn-(Pb) deposit.
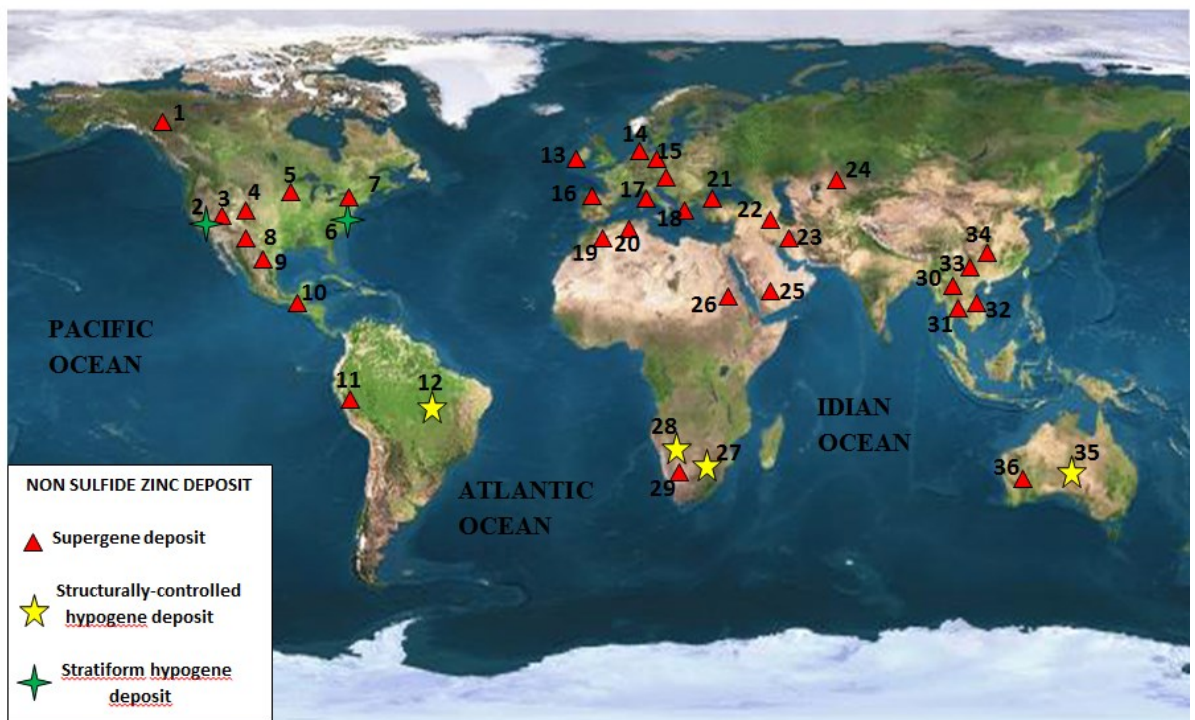
Figure 1.2: Location of nonsulfide zinc deposits. Deposits: 1 = Howards Pass, Canada; 2 = Desert View, United States; 3 = Tintic, United States; 4 = Leadville, United States; 5 = Upper Mississippi Valley district, United States; 6 = Franklin and Sterling Hill, United States; 7 = Balmat, United States; 8 = Sierra Mojada, Mexico; 9 = Santa Eulalia, Mexico; 10 = Torlon, Guatemala; 11 = Accha, Peru; 12 = Vazante, Brazil; 13 = Tynagh and Silvermines, Ireland; 14 = La Calamine, Belgium; 15 = Upper Silesian Mississippi Valley-type district, Poland; 16 = Reocin, Spain; 17 = Sardinian Zn-Pb district; Italy; 18 = Larium and Thassos, Greece; 19 = Touissit, Morocco; 20 = Hamman N'Baïls, Algeria; 21 = Zamanti Zn-Pb district, central Turkey; 22 = Angouran, Iran; 23 = Mehdiabad, Iran; 24 = Shaimerden, Kazakhstan; 25 = Jabali, Yemen; 26 = Abu Samar, Sudan; 27 = Kabwe and Star Zn, Zambia; 28 = Skorpion, Namibia; 29 = Berg Aukas and Abendab, Namibia; 30 = Padaeng (Mae Sot), Thailand; 31 = Long Keng, Myanmar; 32 = Cho Dien, Vietnam; 33 = Jinding (Lanping), China; 34 = Qiandong Shen, China; 35 = Beltana and Aroona, Australia; and 36 = Magellan Pb, Australia (Hitzman et al., 2003).

Most supergene nonsulfide concentrations have a Tertiary/Quaternary age, and their size depends on the original size of the weathered sulfide bodies. The formation of economically significant deposits (Hitzman et al., 2003) depends on:

(1) a preexisting zinc(lead) deposit,

(2) efficient oxidation promoted by tectonic uplift and/or prolonged, seasonal deep weathering,

(3) permeable wall rocks to allow for ground-water movement,

(4) effective trap sites,

(5) hydrogeologic environment that does not promote dispersion and loss of supergene Zn-bearing fluids.

As previously reported, nonsulfide Zn-deposits contain mostly smithsonite, hydrozincite, hemimorphite and sauconite as economic minerals; however, their mineralogical association can comprise also other, uncommon Zn and/or Pb minerals. In table 1 is listed the typical association of the supergene nonsulfide Zn-Pb deposits.

Here follows a brief description of the three subclasses of supergene nonsulfide deposits according to the Hitzman (2003) classification. For clarity, it is important to remark that they are not discrete types, but it is common to find more than one of the above components in a single deposit.

Table 1: Mineral association of supergene Zn-Pb nonsulfide deposit

Category	Mineral	Formula	Comments
Carbonates	Smithsonite	$ZnCO_3$	Common weathering product of sphalerite in carbonate hosted supergene nonsulfide deposits.
	Hydrozincite	$Zn_5(OH)_6(CO_3)_2$	Weathering product of sphalerite/smithsonite/hemimorphite. Highly soluble.
	Cerussite	$PbCO_3$	Common weathering product of galena in carbonate hosted supergene nonsulfide deposits.
Silicates	Hemimorphite	$Zn_4Si_2O_7(OH)_2 \cdot 2H_2O$	Common weathering product of sphalerite in silicate hosted supergene nonsulfide deposits or in impure carbonates.
	Fraipontite	$(Zn, Al)_3(Si,Al)_2O_5(OH)_4$	Zinc clay similar to kaolinite. Generally rare.
	Sauconite	$Na0,3Zn_3(Si,Al)_4O_{10}(OH)_2 \cdot 4(H_2O)$	Common weathering product in silicate hosted supergene nonsulfide deposits.
Oxides and and Hydroxides	Hematite	Fe_2O_3	Common in the gossan of oxidized deposits. It is well recognisable for its rust-red streak.
	Litharge	PbO	Rare secondary mineral which forms from the oxidation of galena ores.
	Coronadite	$Pb(Mn)_8O_{16}$	Weathering product of Manganese-bearing minerals in bedded sedimentary deposits.
	Hetaerolite	$ZnMn_2O_4$	Secondary mineral associated with other manganese minerals. Commonly associated with chaclophanite.
	Goethite/lepidocrocite	$FeO(OH)$	Common weathering product in deposit where pyrite, magnetite and other Fe-bearing minerals occur.
	Hydrohetaerolite	$Zn_2Mn_4O_8 \cdot H_2O$	Secondary mineral common in oxidized manganese-bearing zinc deposits.
	Chalcophanite	$(Zn,Mn,Fe)Mn_2O_5 \cdot 2H_2O$	Common component of the weathered zone above Zn-Mn base metal deposits. Generally associated with hetaerolite.
	Pyromorphite	$Pb_5(PO_4ASO4)_3Cl$	A secondary lead mineral typically found in the oxidised zones of lead deposits.
	Tarbuttite	$Zn_2(PO_4)(OH)$	A rare secondary zinc phosphate.
Phosphates	Mimetite	$Pb_5(AsO_4, PO_4)_3Cl$	A secondary mineral found in the oxidized zones of lead deposits.
	Scholzite	$CaZn_2(PO_4)_2 \cdot 2H_2O$	Rare wethering product found in the oxidized zone of a Zn base metal deposits hosted in carbonate rocks.
	Anglesite	$PbSO_4$	Common weathering product of galena. Commonly associated with cerussite.
Sulfates	Jarosite	$kFe_3(SO_4)_2(OH)_6$	Derived from the oxidation of pyrite, with gangue minerals and wall rock in the deposits. Generally formin conditions of weathering in arid climates.
	Plumbojarosite	$PbFe_6(SO_4)_4(OH)_{12}$	Common mineral in the oxidized zone of lead-bearing ore deposits.particularly in arid regions.
	Goslarite???	$ZnSO_4 \cdot 7H_2O$	Formed from the oxidation of sphalerite, soluble in water. Generally rare.

Direct-replacement

The name of this subclass of supergene nonsulfide deposits refers to the fact that the secondary minerals (such as smithonite, hemimorphite, hydrozincite and cerussite) tend to replace directly the primary sulfides (sphalerite and galena).

Direct-replacement deposits (Figure 1.3a) mainly form from the oxidation of both Mississippi Valley-type and Carbonate Replacement-type deposits (Hitzman et al., 2003).

Deposits derived from MVT mineralizations tend to be mineralogically simple and are dominated by smithsonite, hemimorphite, and hydrozincite. Deposits formed from high-temperature, Carbonate Replacement- type deposits are commonly more mineralogically complex, owing to the presence of other metals (Megaw et al., 1988).

Direct-replacement deposits often contain manganese-rich zinc minerals (i.e. hetaerolite and hydrohetaerolite), as well as smithsonite, hemimorphite, hydrozincite, copper carbonates (if the primary deposit hosts Cu-bearing sulfides), and complex arsenic minerals.

Iron sulfide-rich zinc deposits (which contained high amounts of pyrite and marcasite) produce enough acid to completely leach zinc from the near-surface environment. Such complete leaching results in the formation of a vuggy "jasperoid gossan" with Fe-(hydr)oxides, litharge, cerussite and lesser plumbojarosite, hemimorphite, and copper carbonates (Hitzman et al., 2003).

Some examples of supergene deposits, formed primarily by direct replacement are the Tynagh and Silvermines deposits in Ireland (Clifford et al., 1986; Boland et al., 1992; Boni and Large, 2003; Balassone et al., 2008), the Accha deposit in Peru (Boni et al. 2009), and the deposits in the Upper Silesian Mississippi Valley-type district of Poland (Sass-Gustkiewicz et al., 1982; Boni and Large, 2003; Coppola et al., 2009).

Wall-rock replacement

Supergene wall-rock replacement zinc deposits (Figure 1.3b) form adjacent to, and down the groundwater flow gradient from the original sulfide body. They are commonly associated with direct-replacement deposits.

As sulfide bodies are progressively oxidized, acidic ground waters containing zinc migrate out into the calcareous wall rock, where they react and precipitate zinc carbonates. The reaction is possible because of the buffering power of carbonate host rock; in fact, the acid waters enriched in sulfuric acid generated by the oxidation of pyrite or marcasite will be neutralized, thereby ensuring a buffered, nearly neutral pH environment. Under these conditions, smithsonite, hemimorphite, and hydrozincite are the normal products of oxidation of sphalerite deposits through contact with meteoric waters.

In many cases, the original sulfide body has been completely depleted of zinc (thanks to the high iron sulfide content that generates large quantities of H_2SO_4) and/or completely removed by erosion. The formation of a wall-rock replacement deposit is also favored by

tectonic uplift of the deposit and/or by the lowering of the phreatic zone, which enhances the transport of zinc-bearing fluids out of the original sulfide deposit.

Because of different metal solubility, the process of dissolution, transport, and re-precipitation separates zinc from lead, copper, silver, and iron (Sangameshwar and Barnes, 1983). As a result, wall-rock replacement deposits typically have a much simpler mineralogy than direct-replacement deposits. In addition, the high reactivity of adjacent wall rocks may also result in zinc concentrations of much higher grades than in most direct-replacement deposits.

Wall-rock replacement deposits derived from MVT ores were said to contain smithsonite and minrecordite (Garavelli et al., 1982), which is a kind of Zn-dolomite, whereas those derived from high-temperature sulfide bodies, with manganese-rich carbonates generally contain ferrous smithsonite with manganosiderite. As we will see later in text, the deposition of Zn-dolomite is a more complicated process, and minrecordite has hardly been found after its first description.

The deposits derived from high temperature primary orebodies are generally subjected to multicyclic oxidation and leaching that generate a large and complex mineralogical assemblage.

The amount of silicates and iron oxides present in these bodies depends largely on the composition of the host rocks, on the abundance of iron sulfides in the primary ores, and on the ratio of total FeS_x to $(Zn + Pb + Cu)S_x$ in the protolith.

MVT deposits are the zinc source for many wall-rock replacement deposits. Examples of dominantly wall-rock replacement deposits include the supergene Sardinian nonsulfide zinc ores (Moore, 1972; Boni et al., 1996; Boni et al., 2003), many of the nonsulfide zinc deposits in central Turkey (Ceyhan, 2003; Yilmaz et al., 1992; Yigit, 2009; Sağıroğlu, 1988), the ore deposits of Laurium in Greece (Skarpelis and Argyraki, 2009), the Jabali deposit in Yemen (Al Ganad et al., 1994; Mondillo et al., 2011, 2014), and the Skorpion deposit in Namibia (Corrans et al., 1993; Borg et al., 2003).

Residual and karst-fill

Residual and karst-fill nonsulfide zinc deposits (Figure 1.3c) are formed as accumulations of mechanically and/or chemically transported (from a first-cycle supergene enrichment event) zinc minerals in karstic depressions or in cave systems, which formed where a land surface was reduced by weathering (Hitzman et al., 2003). Such deposits are found in uplifted areas in wet tropical climates, where oxidation of sulfide bodies results in the formation of acidic, oxidized solutions that help promote karst development (Thornber and Taylor, 1992).

In regions of high rainfall, zinc is relatively quickly separated from other metals (Rose et al., 1979) and may form high-grade smithsonite accumulations within karst cavities. Repeated leaching of smithsonite, and concomitant formation of hydrozincite may result in downward migration of successive supergene zinc profiles into sinkholes and cavern systems. Sinkhole collapse can also lead to mechanical concentration of smithsonite, often with a hydrozincite matrix. Colluvial deposits may also occur with downslope transport of residual surface material. Deposits where residual accumulation and karst fill are the dominant process tend to be small in size (Table 1) and highly irregular in their

geometry. However, metal grades can be very high. An example of residual and karst fill deposit is The Cho Dien district in northern Vietnam (Hitzman et al., 2003).
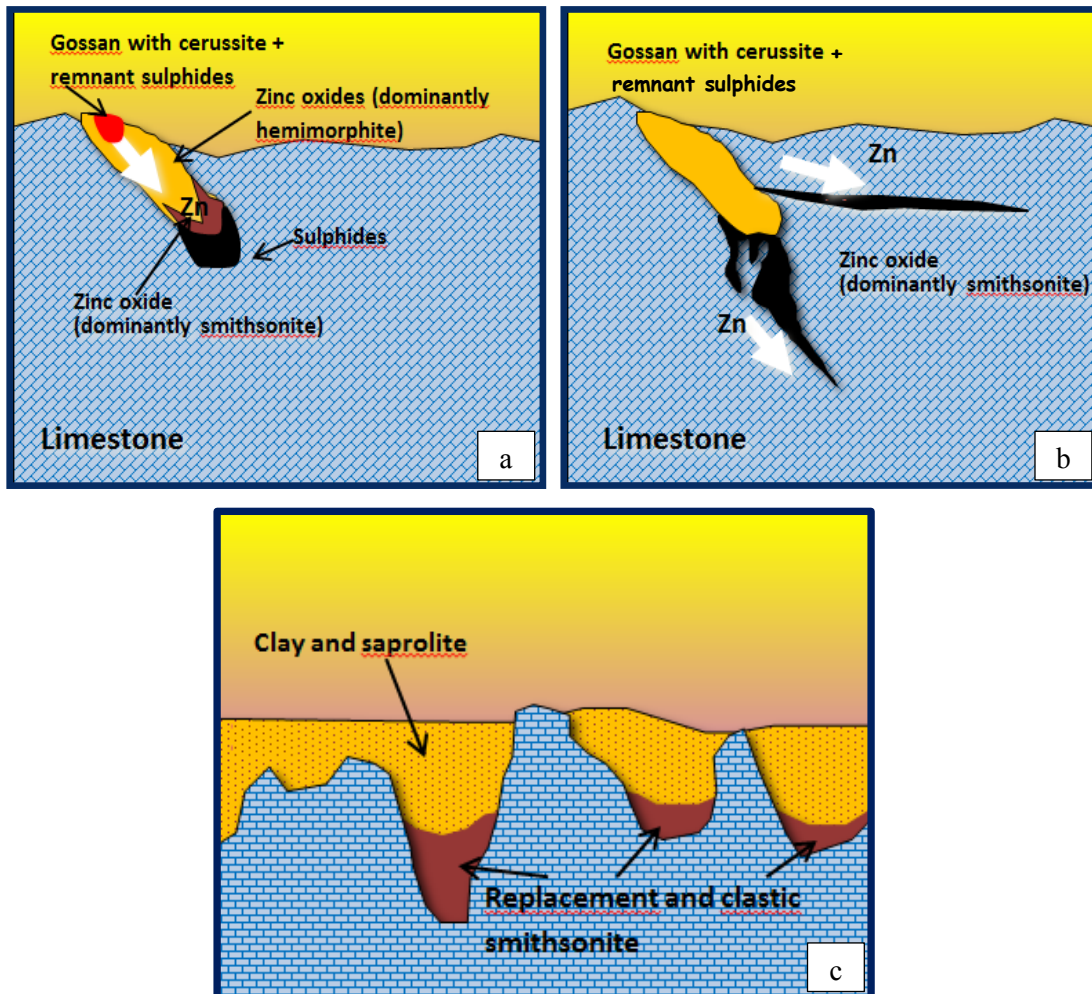
Figure 1.3: a) Direct replacement deposit: zinc moves down through the gossan, carried by low pH groundwater, changing the mineralogy of oxide minerals downward; b) Wall-rock replacement deposits: lead remains in the gossan, while zinc moves down and outward to form high-grade nonsulfide bodies; c) Residual and karst-fill deposits: Highly irregular zinc oxide distribution in karst features; zinc oxide bodies may be far removed (Hitzman et al. 2003).

1.3. Genesis of supergene nonsulfide zinc deposits

Nonsulfide ores form by oxidization of primary sulfide deposit, as result of reactions between meteoric waters, metal sulfides, and reactive host rocks (Sangameshwar and Barnes, 1983). Although sphalerite and in minor extent galena are very susceptible to oxidate (Bladh, 1982; Boyle, 1994), they produce relatively small quantities of acid sulfate-bearing solutions necessary for the further leaching of sulfide minerals (Williams, 1990), whereas a conspicuous iron sulfide content in the primary Zn-Pb sulfide ore is one of the main factors for the genesis of these kind of deposits. In fact, pyrite/marcasite (FeS_2) oxidation and subsequent hydrolization of Fe^{3+} allow the

production of high quantity of sulfuric acid (H_2SO_4) providing low pH, which is necessary to leach out the metallic elements from sulfide minerals.

The following reactions describe the oxidation of pyrite/marcasite (R1), the formation of ferric iron (Fe^{3+}) (R2) and the oxidization of pyrite by reaction of ferric iron (R3) (Herbert, 1999):

$$2FeS_{2(s)} + 7O_{2(g)} + 2H_2O_{(l)} \rightarrow 2Fe^{2+}_{(aq)} + 4SO_4^{2-}_{(aq)} + 4H^+_{(aq)} \qquad (R1)$$
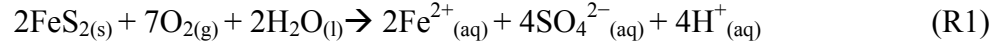
The oxidation of sulfide to sulfate solubilizes the ferrous iron ($\underline{Fe^{2+}}$), which is subsequently oxidized to ferric iron ($\underline{Fe^{3+}}$):

$$4Fe^{2+}_{(aq)} + O_{2(g)} + 4H^+_{(aq)} \rightarrow 4Fe^{3+}_{(aq)} + 2H_2O_{(l)} \qquad (R2)$$
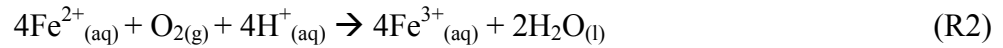
The reaction (R2) is very slow at pH<4.0 and has been described as the rate-determining step in pyrite oxidation; nevertheless, Fe-oxidizing bacteria (e.g. *Thiobacillus ferrooxidans, Thiobacillus thiooxidans*), commonly present in the oxidation zone, tend to increase the oxidation rate of Fe^{2+} (Singer and Stumm, 1970; Schippers, 2003) and thus, the oxidation rates for pyrite are 10- to 20-times higher than those resulting from purely chemical oxidation (Battaglia et al., 1998; Boon and Heijnen, 1998).

Nevertheless, if from one hand the process to form $\underline{Fe^{3+}}$ in acidic environments (pH<4.0) is very slow, on the other hand, under very low pH conditions (pH<3.0), $\underline{Fe^{3+}}$ can remain in solution, react with pyrite and oxidize into ferrous ions (R3):

$$FeS_{2(s)} + 14Fe^{3+}_{(aq)} + 8H_2O_{(l)} \rightarrow 15Fe^{2+}_{(aq)} + 2SO_4^{2-}_{(aq)} + 16H^+_{(aq)} \qquad (R3)$$
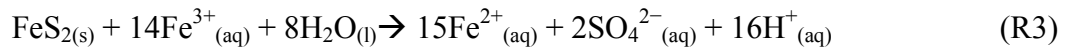
Ferric iron also leads to the precipitation of Fe-(hydr)oxides by hydrolysis (R4, Stumm and Morgan, 1996), which always occur in association with nonsulfide zinc minerals (smithsonite, hemimorphite), or in the altered soils above the mineralization (*gossan*):

$$Fe^{3+}_{(aq)} + 3H_2O \rightarrow FeO(OH)_3 + 3H^+_{(aq)} \qquad (R4)$$
$$\text{(goethite)}$$
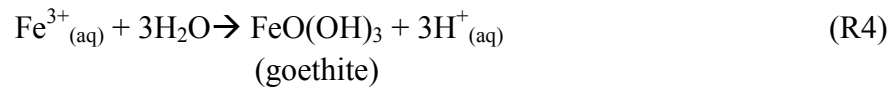
The sulfuric acid resulting from the oxidization of pyrite form according the following equation:

$$2FeS_2 + 7O_2 + 2H_2O \rightarrow 2FeSO_4 + 2H_2SO_4 \qquad (R5)$$
$$\text{(sulfuric acid)}$$
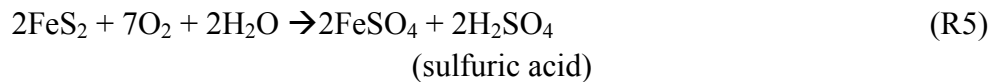
Hitzman et al. (2003) report that the quantity of iron sulfides in a deposit drives the size of the resulting nonsulfide Zn deposits, as it is strictly related to the amount of sulfuric acid produced: as above reported, sphalerite is generally the first mineral to go under oxidation (prior to pyrrhotite, pyrite, galena and chalcopyrite, Rose et al. 1979) in acidic condition (low pH) and at temperatures ranging from ~25° to 60°C with Zn^{2+} remaining

in solution (Fig. 1.4) (Sangameshwar and Barnes, 1983). However, the production of H_2SO_4 from sphalerite is very low.
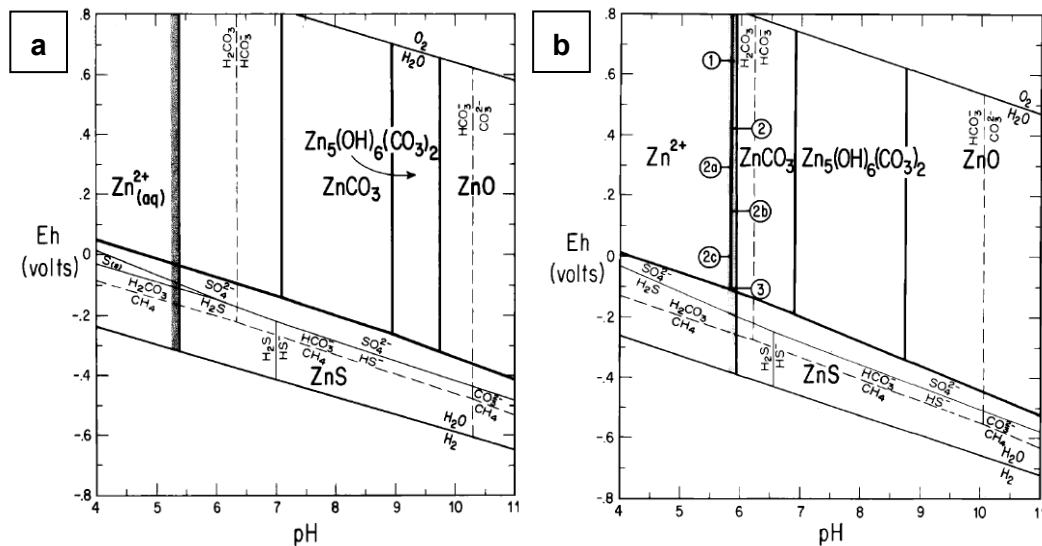
Figure 1.4: a) Eh-pH stability relations at 25° and 1 atm of zinc compounds. The activity of Zn^{2+} is $10^{-5.17}$. b) Eh-pH stability relations at 60° and 1 atm of zinc compounds. The activity of Zn^{2+} is $10^{-3.70}$ (Sangameshwar and Barnes, 1983).

Hence, the oxidation of sphalerite and galena low pyrite-bearing deposits, generate poor amounts of sulfuric acid and the resulting deposits (*direct-replacement* or *wall-rock replacement* deposits) form in the immediately adjacent rocks.

The presence of high amounts of Fe-bearing sulfides (pyrite/marcasite) is necessary to generate abundant sulfuric acid so that zinc can be maintained in solution longer and, consequently, migrate farther from the system (Sangameshwar and Barnes, 1983) and generate wide and distal supergene wall-rock replacement deposits. Moreover, the resulting type of supergene deposit is strictly dependent from the ratio between the amount of gangue and the total sulfides occurring in the area. High gangue and low total sulfide content favor the formation of a *direct replacement* nonsulfide zinc deposit *in situ*. Instead, the absence of carbonate gangue and a high sulfide content favor the removal of zinc from the sulfide body and the formation of a *wall rock-replacement* zinc deposit (Hitzman et al., 2003).

The presence of *gangue* buffering host rocks (carbonates, silicates) neutralizes the acidity of the solutions, and allows zinc to precipitate as smithsonite, hemimorphite, and hydrozincite (Hitzman et al., 2003). Smithsonite ($ZnCO_3$) is the dominant mineral, because at 25°C and neutral pH this is the least soluble of the zinc-oxidation minerals (Takahashi, 1960). The genesis of smithsonite is strongly linked to a series of reactions, starting with that between sphalerite (ZnS), and ferric sulfate [$Fe_2(SO_4)_3$]:

$$ZnS + Fe_2(SO_4)_3 + 4H_2O \rightarrow ZnSO_4 + 8FeSO_4 \qquad (R6)$$

The newly produced Zn-sulfate ($ZnSO_4$) is strongly soluble at room temperature and pressure; it can precipitate only if it gets in contact with *"reactive gangue"* (limestone, dolostone), according to the following reaction:

$$ZnSO_4 + CaCO_3 + H_2O + CO_2 \rightarrow ZnCO_3 + CaSO_4 \cdot 2H_2O \qquad \text{(R7)}$$
$$\text{(smithsonite) (gypsum)}$$

Takahashi (1960) determined that the pH and the activity of CO_2 of ambient ground waters are the controlling factors in the paragenesis and distribution of zinc minerals. In particular, the conversion of smithsonite to hydrozincite, according the following equation (R8)

$$5ZnCO_3 + 6H^+ + 3CO_3^{2-} \rightarrow Zn_5(CO_3)_2(OH)6 + 6CO_2(gas), \qquad \text{(R8)}$$
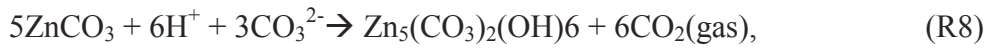
is mainly controlled by the pH and the partial pressure of CO_2 (P_{CO2}). In arid enviroments hydrozincite is much more common than smithsonite at the surface, whereas in the deeper portions of weathering profiles the amount of smithsonite rises (with consequent decrease of hydrozincite content).

This is due to the fact that, above the water table, the carbon dioxide escapes to the atmosphere, thereby lowering the activity of CO_2 and stabilizing hydrozincite. Below the water table, instead, carbon dioxide is soluble and, owing to its slow rate of diffusion, results in an elevated activity of CO_2 and consequently in the stability of smithsonite (Takahashi, 1960).

More recent studies (Brugger et al., 2003; McPhail et al., 2003; Reichert and Borg, 2008) came to the same results of Takahashi (1960): it was calculated that the precipitation of smithsonite is restricted to relatively high $P_{CO2(g)}$ values (Fig. 1.5) (log $P_{CO2(g)}$ >0.4 kPa at 298.2 K). This means that, in arid environments it is impossible to precipitate smithsonite from an aqueous solution, which is in equilibrium with the atmosphere as the atmospheric and soils $P_{CO2(g)}$ are much lower than the minimum conditions required for smithsonite precipitation ($P_{CO2(g)}$ <0.4 kPa), this resulting in the precipitation of hydrozincite according the (R8). These conditions are common for aqueous solutions on the surface or near-surface solutions in unsaturated zones. On the contrary, deeper aqueous solution or water-saturated zones are in disequilibrium with the atmospheric $CO_{2(g)}$ and reach values that are favorable for the precipitation of smithsonite (Reichert and Borg, 2008). In a more humid environment, instead, the ambient conditions are favorable to the precipitation of smithsonite, as the ground water in deeper zones or near the surface tends to be in equilibrium with atmospheric $P_{CO2(g)}$, which in humid condition is higher (log $P_{CO2(g)}$ >0.4 kPa) (Takahashi, 1960) (Fig. 1.5).

The CO_2 source of smithsonite is generally mixed. Literature states that it can come from biological processes related to the oxidation of organic matter (generally resulting in the light carbon component of smithsonites), or from the host rocks, by reaction of the carbonate rocks with acidic aqueous solutions (Boni et al., 2003; Gilg et al., 2008).
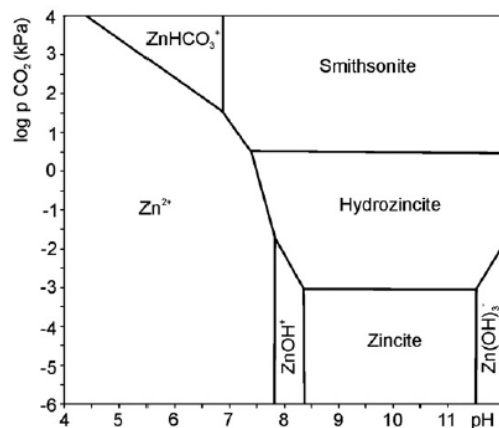
Figure 1.5: Stability of zinc carbonates in the chemical system Zn–O–H–C in relation to $P_{CO2(g)}$ and pH. The activity of zinc is a(Zn)= $10-5$ mol·l$-$1 (McPhail et al., 2003).

Hemimorphite [$Zn_4Si_2O_7(OH)_2 \bullet H_2O$] is another typical product of the weathering of sulfide ores. It derives from the following reaction between Zn-sulfate ($ZnSO_4$) and silicate host rock:

$$4ZnSO_4 + SiO_2 + 3H_2O \rightarrow 4H_2SO_4 + Zn_4SiO_2O_7(OH)_2 \bullet H_2O \qquad (R8)$$
$$(hemimorphite)$$
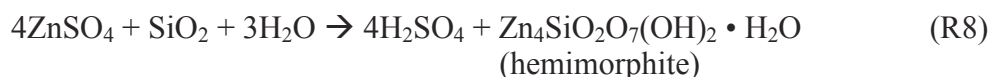
The amount of precipitation of hemimorphite and of other zinc silicates, anyway, depends on the availability of silica (SiO_4), which is highly soluble in water (Dove and Rimstidt, 1994). The amount of silica dissolved is generally low in carbonate-buffered solutions, hence, only small amounts of Zn-silicates form and consequently, zinc precipitates in the supergene oxidation stage predominantly as zinc carbonates (Reichert and Borg, 2008).

As regards the stability fields of hemimorphite, Takahashi (1960) calculated that hemimorphite is the most stable Zn-mineral at pH condition <7 and atmospheric $P_{CO2(g)}$ (compared to smithsonite and hydrozincite), hence it might not be expected to form under normal, nearly neutral weathering conditions.

Characteristically, hemimorphite forms where sufficient acid is generated to achieve and maintain low pH conditions, and where low total carbonate activity occur (Takahashi, 1960). It precipitates in acid-to-low basic condition in the earlier phases of oxidization.

Further leaching results in the conversion of hemimorphite to hydrozincite (with a variation of $P_{CO2(g)}$, Reichert and Borg, 2008) and progressive migration of zinc out of the original orebody if there are no residual carbonate minerals in the original sulfide body to buffer the pH.

Sauconite [$Na_{0.3} Zn_3(Si,Al)_4O_{10}(OH)_2 \bullet 4H_2O$] (Zn-smectite) is a supergene zinc product commonly found in areas where silicatic host rock occur (i.e. Skorpion, Namibia, Borg et al., 2003; Yanque, Peru, Mondillo et al., 2014). The formation of sauconite is related to several conditions and lithologies: it can occur where Zn-bearing waters circulate in clay-enriched lithologies, more specifically saponite (Ross, 1946; Faust, 1951).

32

However, high amounts of sauconite can form also as replacement product of mica, plagioclase and feldspar in relative alkaline environments. An example is Skorpion, Namibia (Borchardt, 1989; Borg et al., 2003), and another is Yanque, Peru (Mondillo et al., 2014b).

Other typical weathering products of a Zn-Pb sulfide deposit that can occur in association with supergene nonsulfide ores are anglesite ($PbSO_4$) and cerussite ($PbCO_3$). Anglesite can form by direct oxidation of galena (PbS), due to oxidant bacteria *Thiobacillus ferroxidans, Thiobacillus thiooxidans* (Silver and Toma 1974; Ballester et al., 1989) according to the following reaction:

$$PbS + 2O_2 \rightarrow Pb^{2+} + SO_4^{2-} \leftrightarrow PbSO_4 \qquad (R9)$$
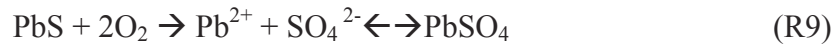
Tomizuka and Yagisawa (1978) suggested that the oxidation of galena could also happen via H_2SO_4, according the following equations (R10 and R11):

$$PbS + H_2SO_4 + 0.5O_2 \rightarrow PbSO_4 + H_2O + S \qquad (R10)$$

$$PbS + Fe_2(SO_4)_3 \rightarrow PbSO_4 + 2FeSO_4 + S \qquad (R11)$$
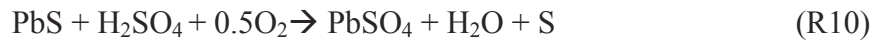
The conversion from anglesite to cerussite is driven by the equation R12 (Reichert and Borg, 2008):

$$PbSO_4 + H_2CO_3 \leftrightarrow PbCO_3 + SO_4^{2-} + 2H^+ \qquad (R12)$$

The reaction R11 shows that the precipitation and hence the stability of anglesite and cerussite is strictly dependent on pH, $H_2CO_{3\ (aq)}$ and SO_4.

The oxidation processes are associated with high activities of both SO_4^{2-} and H^+, which shift the reaction to the left. Generally, anglesite is highly soluble in pure water, and its solubility depends from the activity of both Pb^{2+} and SO_4^{2-}.

Additional SO_4^{2-} ions will decrease the solubility of anglesite and therefore the activity of lead within the aqueous solution. The additional source of SO_4^{2-} is given from sulfuric acid during the oxidation process and/or the presence of gypsum and other SO_4^{2-} bearing minerals.

Reichert and Borg (2008) report that the presence of gypsum (and other sulfates) can force anglesite to precipitate at even lower concentrations of Pb^{2+} compared to anglesite precipitation in pure water. The equilibrium in R13 is shifted to the right side, and the resulting concentrations of Pb^{2+} decrease.

$$Pb^{2+} + SO_4^{2-} \leftrightarrow PbSO_4 \qquad (R13)$$

Hence, after oxidation of the sulfide ore, the pH value tends to change to neutral and basic conditions, due to the absence of oxidation-related acid. The SO_4^{2-} concentration decreases and pH increases. Cerussite becomes more stable than anglesite and anglesite

is replaced by cerussite according to the equation R12 (Sangameshwar and Barnes, 1983).

Reichert and Borg (2008) observed that in a weathered sulfide deposit containing a pyrite–sphalerite–galena paragenesis, there is a different reactivity of these minerals during the oxidation stage. Although a theoretical geochemical calculation suggests that galena should be five times more reactive compared to sphalerite (Zeman, 1985), in the reality pyrite and sphalerite tend to corrode easier, while galena can persist in the weathered supergene deposit as armored minerals specks remnants (Reichert and Borg, 2008). In fact, in the supergene systems galena is commonly rimmed by anglesite that contains abundant sub-mm-size galena inclusions. The thickness of the anglesite coatings is commonly up to 150 μm. Anglesite precipitates in the presence of sulfate ions and low-pH conditions (Fig 1.6); it has a low solubility, especially in SO_4^{2-} ion-bearing aqueous solutions (Faure, 1998). The anglesite rims, hence, protect galena from the direct contact with oxidizing reagents.
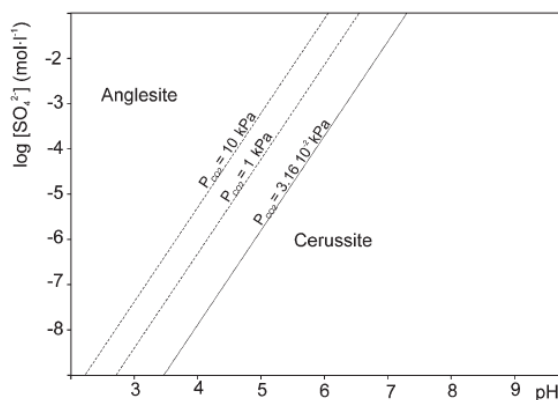
Figure 1.6: Stability fields of anglesite and cerussite (25 °C, 100 kPa, calculated with PHREEQC). The lines show the phase boundary for different $CO_{2(g)}$ partial pressures (atmospheric $P_{CO2(g)}$ =3.16·10− 2 kPa) (Reichert and Borg, 2008).

Reichert and Borg (2008) describe that the formation of such an insoluble "armor" starts with the precipitation of anglesite at low pH values, followed by insoluble lead carbonates, such as cerussite or hydrocerussite, which is $P_{CO2(g)}$ -controlled. Thus, the apparent resistivity of galena during the oxidation process can be explained by this "armouring" effect.

It is also important to notice that pH strongly drives the migration of metals during weathering (Jurjovec et al., 2002). In a Zn-Pb deposit, zinc is more mobile than lead. Zinc generally tends to migrate toward the lower portions of the original sulfide body; while lead is relatively immobile and remains in the original sulfide body as galena, protected by a mantle of cerussite and anglesite (Sangameshar and Barnes, 1983; Reichert and Borg, 2008). In figure 1.7 is shown a schematic weathering profile, with the distribution of metals encountered in different portions of the system, according to their mobility.

It is important to remark that wall-rock composition significantly influences the mineralogy of nonsulfide zinc deposits. Deposits in "clean" carbonate rocks tend to be

dominated by smithsonite and hydrozincite; whereas deposits in siliciclastic or impure calcareous rocks, or in areas where siliceous soils are present, tend to form hemimorphite- and sauconite-bearing assemblages owing to the availability of Al and Si (Hitzman et al., 2003).

One of the most important aspects in the genesis of a nonsulfide deposit regards the climatic and tectonic/topographic conditions. Although supergene zinc deposits are found both in arid and tropical environments, most of them are considered to have formed in semi-arid environments (Reichert and Borg, 2008). In humid environments, instead, the zinc-bearing fluids are lost if an effective trap site is not encountered (Hitzman et al., 2003). The occurrence of a trap site is another critical factor in the formation of a nonsulfide zinc deposit. The best trap sites are carbonate-rich host rocks, usually limestone or dolostone. Calcareous or dolomitic sandstones may also be effective traps. There are also other, very different cases of trap sites, as in the Torlon deposit in Guatemala (Kesler and Ascarrunz-K., 1973).

Also important for the formation of a supergene deposit is the permeability of the host rock: sulfide deposits in carbonate rocks are characterized by a low permeability and by lack of significant fractures.

In this situation, supergene zinc deposits form relatively close to the original sulfide body (through gravity-driven vertical solution movement). In mixed carbonate-clastic sequences, fluid flow may be instead dominated by the permeability of the clastic units, and horizontal stratal-fluid movement is hence possible. This may result in a lateral migration of fluids hundreds of meters away from the primary sulfide body (Silvermines, Ireland: Boland et al., 1992).

By the above-described situation, it follows that although uncommon, "exotic" supergene nonsulfide zinc deposit (similar to those around porphyry copper deposits) can exist (Long Keng, Myanmar, Griffith, 1956; Yanque, Peru, Mondillo et al., 2014b).

Supergene nonsulfide zinc deposits can also develop by oxidation of hypogene nonsulfide assemblages. Vazante (Brasil) (Monteiro et al., 2006; Slezak et al., 2014), Beltana (Australia) (Groves and Carman, 2003), Kabwe (Skerl, 1934), Sterling Hill (Johnson, 2001), all have in their weathering profile smithsonite-hemimorphite and secondary supergene sphalerite-rich assemblages (the latter ones precipitated in reducing condition) (Hitzman et al., 2003).
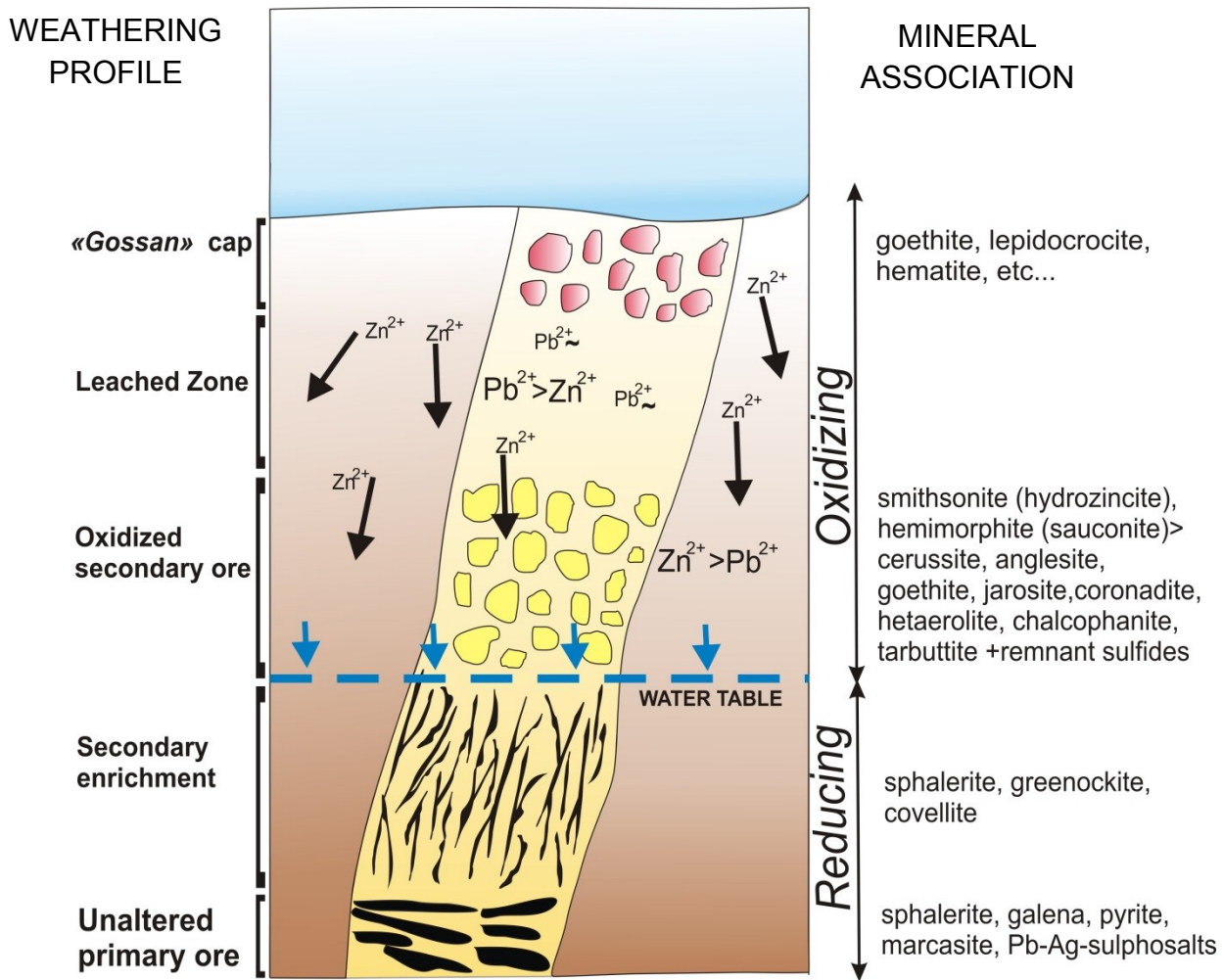
Figure 1.7: Weathering profile of a Zn-Pb protore, with secondary minerals precipitation.

Chapter 2

QEMSCAN®: *General outlines and sample preparation*

2.1. Introduction

Quantitative analyses on 12 samples of the Hakkari (Turkey) deposit, 25 samples of the Jabali (Yemen) deposit, and 10 samples of the Reef Ridge deposit (Alaska) were conducted by the use of QEMSCAN® technology, in order to define the strengths and the weakness of this methodology for the characterization of the supergene Zn(Pb) nonsulfide deposits.

The Hakkari and Jabali samples were selected from drill-core sections of different lengths (±1 m in the Jabali deposit and ~5 m at Hakkari). The study of the Reef Ridge deposit has been carried out both on cores (~50 cm in length) and on surface hand samples.

Here follows a full description of the QEMSCAN® methodology.

General outlines

QEMSCAN® is the acronym for Quantitative Evaluation of Minerals by Scanning Electron Microscopy, a system which differs from image analysis systems in that it is configured to measure mineralogical variability based on chemistry at the micrometer-scale.

The QEMSCAN® technology was developed in the late 1970's by CSIRO (*Commonwealth Scientific and Industrial Research Organisation*) in Australia (the earliest model was called QEM*SEM), mostly applied to complement bulk chemical assay data, exploration, mining, mineral processing and metal refining (e.g. Miller et al., 1982; Reid et al., 1984). In more recent times refinement and modification of the technology has broadened its application to other sectors, including oil and gas (e.g. Edwards and Butcher, 1999; Butcher and Botha, 2010), forensics (Pirrie et al., 2004), planetary geology (e.g. Botha et al., 2008); general geosciences (e.g. Liu et al., 2005;

Grauch et al., 2008), and geothermic studies (Hardardottir et al., 2010; Ayling et al., 2012).

The QEMSCAN® (Figure 2.1) utilizes both the back-scattered electron (BSE) signal intensity, as well as an Energy Dispersive Spectra Signal (EDS) at each measurement point. EDS signals are used to assign mineral identities to each measurement point by comparing the BSE signal and EDS spectrum against a mineral species identification protocol (SIP) or database. The use of SEM-EDS combined with a sophisticated software for image processing and automation, provides a fully-integrated mineral and rock analysis system that is rapid, accurate, repeatable and statistically valid (it has been used in the mining industry for over 30 years).
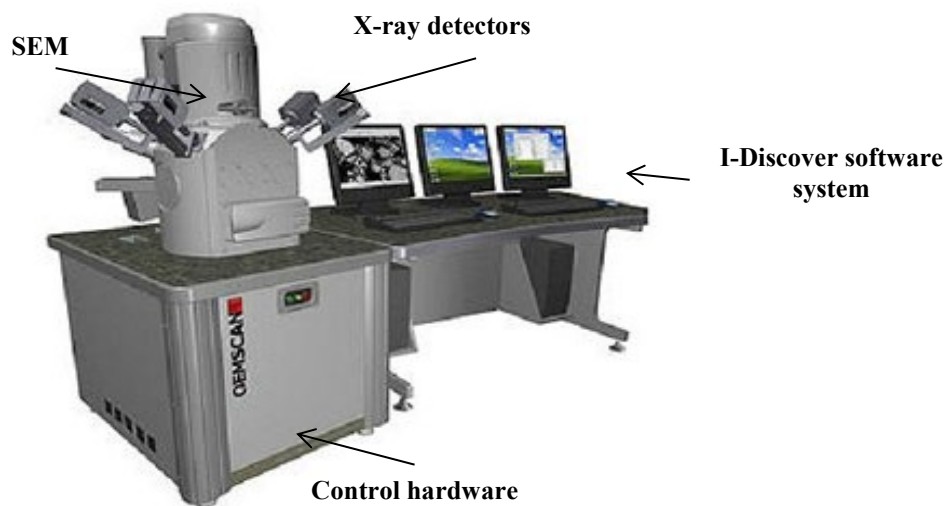
Figure 2.1: QEMSCAN® 4300 operative base.

2.2. Working system.

The system design consists of a hardware module and a software module that controls a scanning electron microscope to collect raw data, construct digital images, and process the data. In detail, the automation software scans or rasters a focused beam of electrons over the sample surface, measuring a variety of signals generated by electron-sample interactions (secondary electrons, back scattered electrons, X-rays, cathodoluminescence and transmitted electrons) and mapping the data into a high-resolution image. For automated mineralogy, the two most important signals are backscattered electrons (BSE) and characteristic X-rays for each analyzed point so that the species are automatically identified as individual minerals or groups of minerals with similar chemical compositions (Butcher and Botha, 2010).

A database, using "*a priori*" knowledge of the mineral system, identifies minerals from low count EDS spectra and constrains the possible identifications when there is a lack of

uniqueness. Real-time processing of the signals generates digital images that classify pixels as mineral species.

The EDS spectrum, obtained using 1000 counts per spectra, is analyzed by windowing (versions 4.3 and earlier only, version 5 onwards use peak intensity method, see Haberlah et al. 2010, 2011), background subtraction, overlap correction, thresholding, and the calculation of peak ratios to resolve individual element spectral lines. The data obtained for each point analysis are compared with a database of mineral species known as SIP file (Species Identification Protocol), which has been built by the user before the analysis and that can be modified after the first results.

The database lists elements that must be present, and elements that may be present. Species with similar X-ray spectra and BSE, such as chalcopyrite and cubanite, are differentiated by element ratios. Species with similar spectra but distinct BSE, such as magnetite and hematite, are differentiated by BSE. Some simple ore types can be analyzed by BSE alone using a subset of the system capabilities. Finally, off-line processing extracts mineral and particle statistics and condenses the identified species into mineral groupings suitable for interpretation (Gottlieb et al., 2000). The system combines these data points to generate digital false color mineral maps, from which it then extracts quantitative mineral and textural information for downstream applications. A schematic example of the analytical system is represented in Figure 2.2.
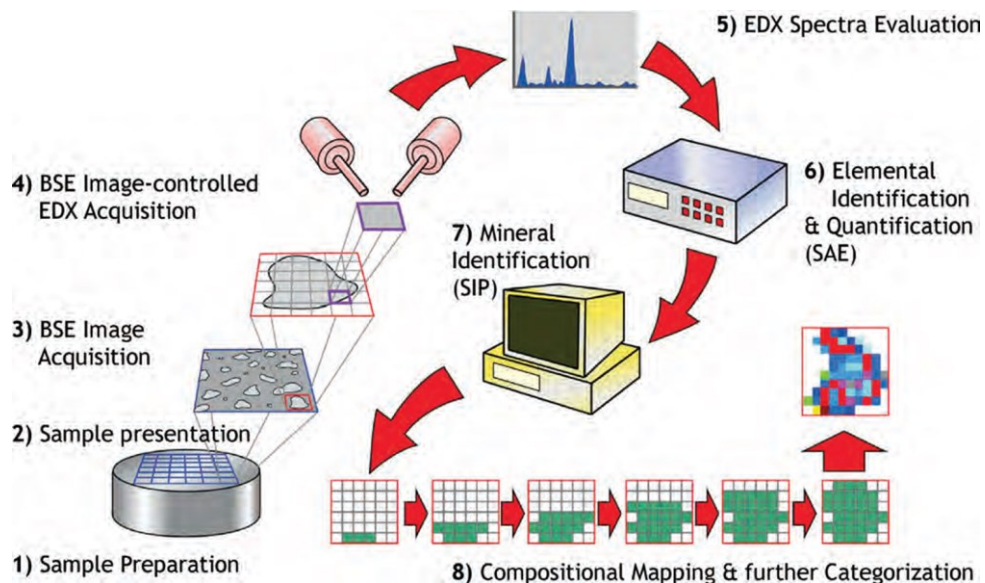
Figure 2.2: Starting at the bottom left, the sample is mounted in epoxy and sectioned, creating a smooth, flat surface. The electron beam scans across the sample surface and identifies particles based on the contrast between minerals and the mounting media. The system then scans each particle on a grid basis, and collects and interprets an X-ray spectrum for each pixel in the grid to determine its mineral phase. The results for all pixels are combined in a digital image that represents the mineralogy in the scanned particle. Digital mineral maps provide visual representation of the mineralogy and how minerals relate to each other (Haberlah et al., 2010)

Moreover, during the analyses a detailed database of the statistically representative mineralogical information is automatically built, which can be later interrogated by the user.

The automated mineralogy analysis platform is optimized for resolution, beam stability, stage precision, vacuum conditions and chamber size. In addition to the analysis and automation software, a key technological development is using multiple, high-speed energy dispersive X-ray spectrometry detectors in combination with carefully designed data acquisition algorithms, which permit much faster data acquisition than conventional SEM configurations.

It is possible to conduct analyses on a wide range of sample types, including drill cuttings, polished thin-sections and drilling cores. Automatic analysis of hundreds of thousands of data points per sample generates large and statistically- valid data sets (Butcher and Botha, 2010).

2.3. QEMSCAN® mineral identification and quantification: Spectral Analysis Engine (SAE) and Species Identification Protocol (SIP)

As reported above, QEMSCAN® mineral identification is performed during sample measurement and is totally automatic: but how does it work? The mineral identification is performed by iDiscover software in two main steps after that X-ray raw data are saved:

1) Elemental identification and quantification by the Spectral Analysis Engine (SAE);
2) Matching of elemental concentration ranges with phase (mineral) definitions in the Species Identification Protocol (SIP)

Spectral Analysis Engine (SAE)
The SAE is fitting up to 72 pure elemental spectra, measured on a given SEM platform-EDS detector configuration, into a measured low-count energy-dispersive X-ray (EDX) spectrum. The SAE *'element concentration'* approach calculates the best match, by recording the presence of elemental spectra, and also by quantifying the relative contribution of each element in the measured spectrum. The quality of the spectral match, as well as the measured X-ray count rate and backscatter brightness (BSE), is also recorded. The *'elemental concentration'*, or more specifically the relative contribution of elemental spectra in a measured mineral EDX spectrum, is different to the elemental mass percentage of the mineral. For example in the dolomite, the elemental weight percentages are Ca 21.7, Mg 13.2, C 13.0, and O 52.1, while *'elemental concentrations'* are given as Ca 12.8, Mg 21.2, C 12.8, and O 23.1. If spectra elements overlap, the result is the noise. For this reason, overlapping element and element substitution rule sets are in place to limit element mismatches. If the elements present in a measured spectrum have been disabled, the result would be a poor spectral match. Best results are achieved if the list of enabled elements coincides with those present in the measured sample.

Bulding a SIP file
The elemental *'concentrations'* reported by the SAE for each individual measurement point (EDX spectrum) are compared online to the Species Identification Protocol (SIP), which is a library of phase definitions commonly referred to as *'SIP list'*. A measured spectrum is assigned to a single phase, if it matches all the criteria of the phase definition. Mineral phase definitions include *'must have'* and optional *'may have'* elemental ranges. Elemental ranges reflect the fact that multiple iterations of low-count

spectra (typically 1000 X-rays) of a single high-count spectrum necessarily result in statistical variation. Elemental ranges can also be used to account for natural chemical variation in a mineral. However, significant chemical variations are best approached by defining multiple end member SIP entries for a given phase. In addition to elemental ranges, elemental ratios and more complex formulas can be set as rules in SIP definitions. Furthermore, optional thresholds for BSE brightness, X-ray count rate, and spectral match quality can be defined.

In contrast to the best-match elemental fitting approach in the SAE, phase identification in the SIP is performed on a first-match basis. Phase definitions are therefore position dependent in the SIP list. The measured elemental concentration, BSE brightness, count rate and spectral match data of a measured spectrum are sequentially compared to all phase definitions, and mapped to the first in the SIP list that provides a match (hierarchical). If a measured data point does not match any predefined entry, it remains unclassified, and will be reported as "Others". For the best results, the most important point is the building of a suitable and reliable classification protocol. Depending on the desired outcome, a user may use an existing Species Identification Protocol (SIP), modify an existing SIP, or create a new SIP. Expertise in SIP development is exercised by establishing elemental ranges that reliably capture all the variability inherent in low-count spectra, while preventing phase definitions to become too broad and potentially capturing spectra of non-identical phases. A number of software tools are available in iDiscover, the QEMSCAN® expert analysis and reporting software component, to facilitate this task. A layered approach to SIP development (Haberlah et al., 2011) is the best way to build the library.

Once all phases have been defined on a pixel-by-pixel basis, individual phases need to be grouped into real minerals or phases of interest, in order to be reported as volume or weight percentage contributions. Both are performed by grouping similar SIP phases in the 'Primary Mineral List', and by assigning them a single density and chemical composition. For analysis and reporting purposes, multiple Primary Mineral List entries can further be grouped into Secondary Mineral List entries or "*Final list*". For example, a Fe-rich version of dolomite will require a separate SIP entry for identification, and a Primary Mineral List entry for adequate chemical and density characterization.

However, both dolomite entries can be grouped in the final list for modal mineralogy. In Figure 2.3 is reported an example of the difference between SIP file, Primary and Final Mineral list built during the processing step by the use of iDiscover.

To conclude, the task of assigning relevant compositional data to identified phases requires a good understanding of the chemical variability inherent in some of the minerals occurring in the sample.

It is also important to underline the impact of sample preparation and measurement setup on the results and data interpretation.
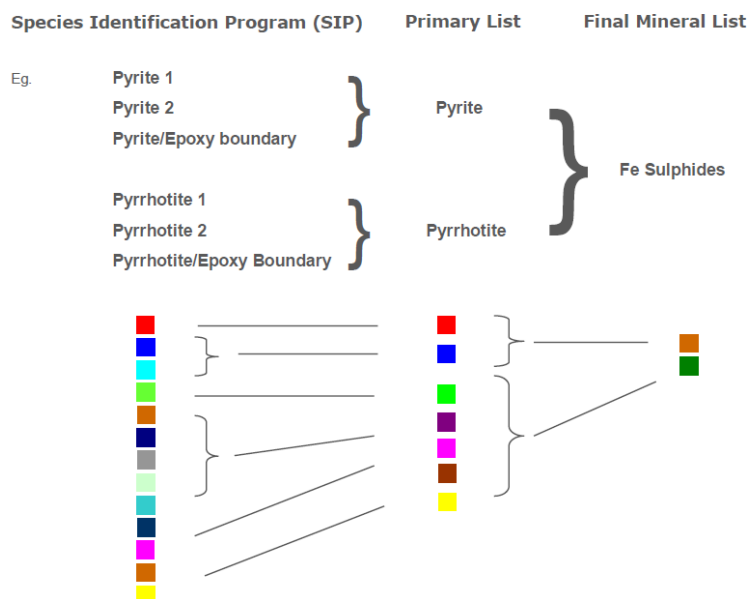
Figure 2.3: Example of SIP file, Primary and Final Mineral List for the classification of Fe-sulfides: in the SIP file is reported a list of all the different pyrite that could exist according to the elements substitutions and ratio, the same is for pyrrhotite; in the Primary Mineral list, all the pyrite and pyrrhotite are grouped together in two categories; in the Final Mineral list pyrite and pyrrhotite are grouped in one big general category, that is Fe-sulfides. It is important to note that in case of more precision in the species identification, it is possible to keep the Primary Mineral list.

2.4. Analytical modes.

One of the advantages of the instrument is the possibility to set several types of analyses according to the user interest. In detail, it is possible to undertake four different types of measurements (Gottlieb et al., 2000; Pirrie et al., 2004):

➢ Bulk Mineralogical Analysis (BMA);
➢ Particle Mineralogical Analysis (PMA);
➢ Trace Mineral Search (TMS);
➢ Field Scan (FS).

Bulk Mineralogical Analysis (BMA)
The BMA is performed by a linear intercept method, in which the electron beam is rastered at a pre-defined point spacing (variable with particle size), along several lines per field. The entire polished section is analyzed, in order to provide a robust data set for determination of the bulk mineralogy with statistical information on modal abundance, element deportment, texture, particle and mineral surface areas, mineral associations, mineral grain and particle sizes, degree of liberation. During the analysis no image of the sample is obtained. This analysis generally takes 10/45 minutes per sample. An example of a BMA measurement image is shown in Figure 2.4.
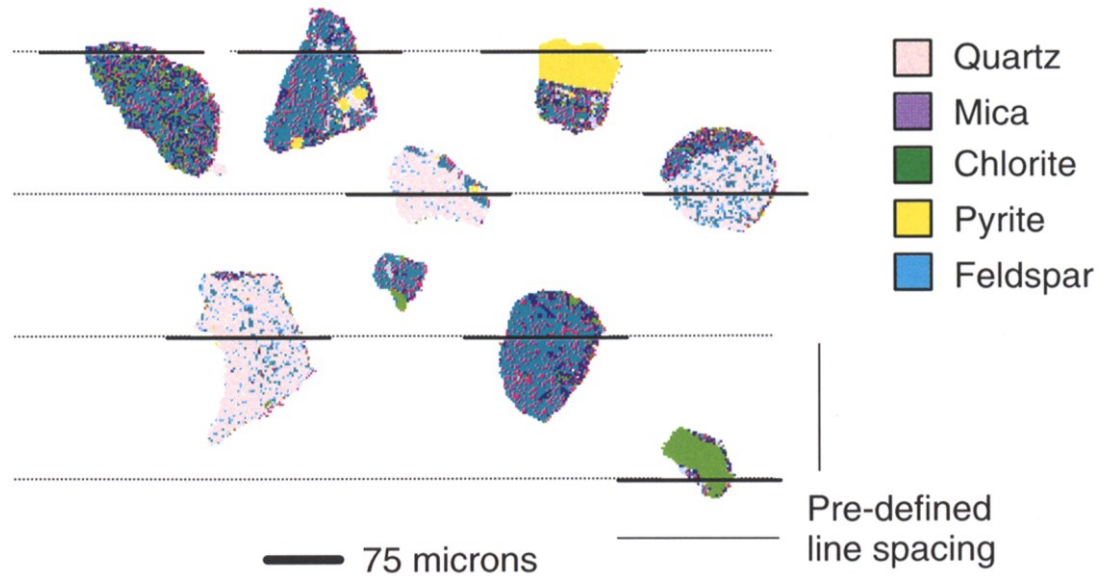
Figure 2.4: Example of operating system of a Bulk Mineralogical Analysis (Pirrie et al., 2004).

Particle Mineralogical Analysis (PMA)

Particle Mineral Analysis (PMA) is a two-dimensional mapping analysis aimed at resolving liberation and locking characteristics of a set of particles (Butcher and Botha, 2010). It is used for detailed mineralogical characterization of particles up to 1 mm. The operator chooses the size range of particles of interest, and the electron beam stepping interval (it can be as small as 0.2 μm). The beam stepping interval is decided upon based on the likely size of the target minerals of interest and also the degree of resolution required in the data set. Finally the operator may select the number of particles to be measured, which is dependent upon the nature of the work being carried out, but will commonly be in the order of 4000–5000 (Pirrie et Rollinson, 2011).

After the measurement is set up, a pre-defined number of particles are examined and mapped to provide particle-by-particle false colour images (Pirrie et Rollinson, 2011). The particles are examined in pre-defined fields dependant upon the particle size range (Figure 2.5a).

The particles are distinguished on the basis of the BSE. The BSE image obtained for each field-of-view (Figure 2.5b) helps to determine each particle-section perimeter, area, and location within a guard-frame. Filters are also applied to determine the particles that will be measured. Generally the filters reject particle sections that touch the frame boundaries, touch each other, or are smaller or larger than expected are. On each particle a grid is built (Figure 2.5c) and for each point of this grid X-ray analyses are acquired to define the mineralogy and the chemistry. At the end a false colour map of the particle is built (Figure 2.5d). Each colour represents a mineral or a mineral category (Pirrie 2004, Pirrie and Rollinson 2011). This analytical method is used to obtain data on modal mineralogy, elements deportment, grains and particles size, mineral association, and mineral liberation analyses. The analytical time goes from 30 minutes to 2 hours per sample. However, for a similar measurement time, the PMA modal abundance is usually

less accurate than the BMA results, since fewer particles are analyzed (Gottlieb et al., 2000). Figure 2.5 shows an example of the PMA analysis.
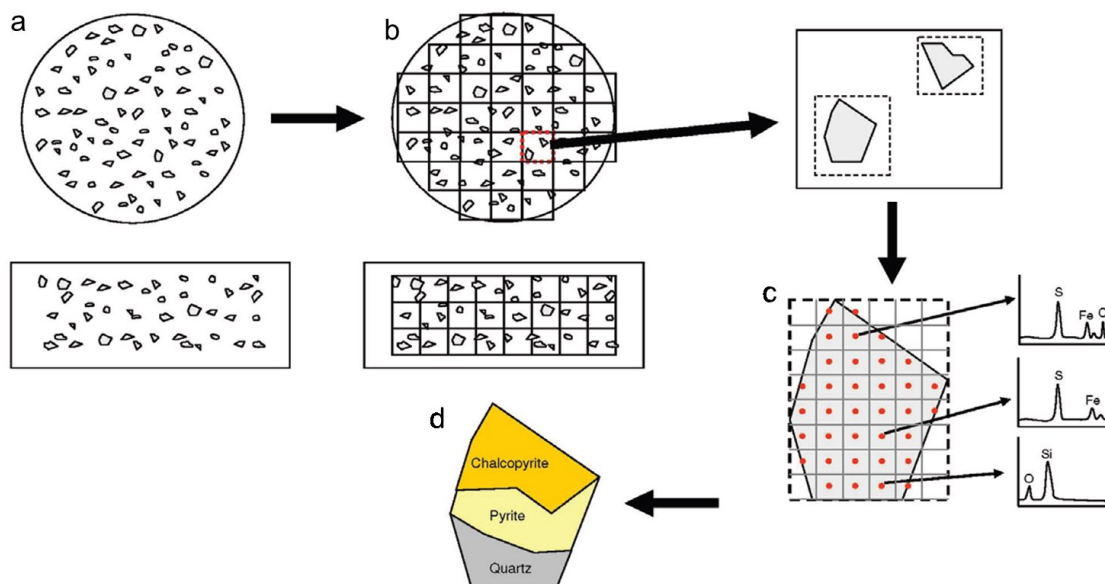
Figure 2.5: Example of operating system of a Particle Mineralogic Analysis (Pirrie and Rollinson, 2011).

Trace Mineral Search (TMS)

Trace Mineral Search (TMS) is an additional mapping routine, where a phase constituent can be located by thresholding of the back-scattered electron intensity only particles 'brighter' than the defined threshold will be measured (Pirrie and Rollinson, 2011). The objective of this routine is to reject barren fields and increase analysis efficiency. Again the operator create pre-defined field (Figure 2.6a) and decides the BSE thresold: only fields with pixels that exceede the thresold will be measured (Figure 2.6b). Each measured field is split into a predefined rid of pixels, each pixel with an X-ray analysis point; the acquired X-rays are compared to a database to define mineralogy and chemistry (Figure 2.6c). A false colour map is created for each field (Figure 2.6d) with each colour representing a mineral or a mineral category (Pirrie and Rollinson, 2011).

This mode of measurement is generally used for advanced studies of gold and PGE ores, or trace minerals of interest such as molybdenite. Although not all phases can be uniquely identified by their BSE, this mode greatly reduces the number of particles that are needed to be mapped by X-rays, in order to obtain information on a specific phase. This mode is used for samples where minerals are present at about 0.5 vol.% or less (Gottlieb et al., 2000). It is important to note that TMS results pertain only to the target minerals. That is, the analysis modes are designed to analyze only the target-bearing sub-population, and the results therefore do not reflect the bulk mineralogy of the overall sample BMA, or PMA must be selected if quantitative gangue characterization is required (Gottlieb et al., 2000).
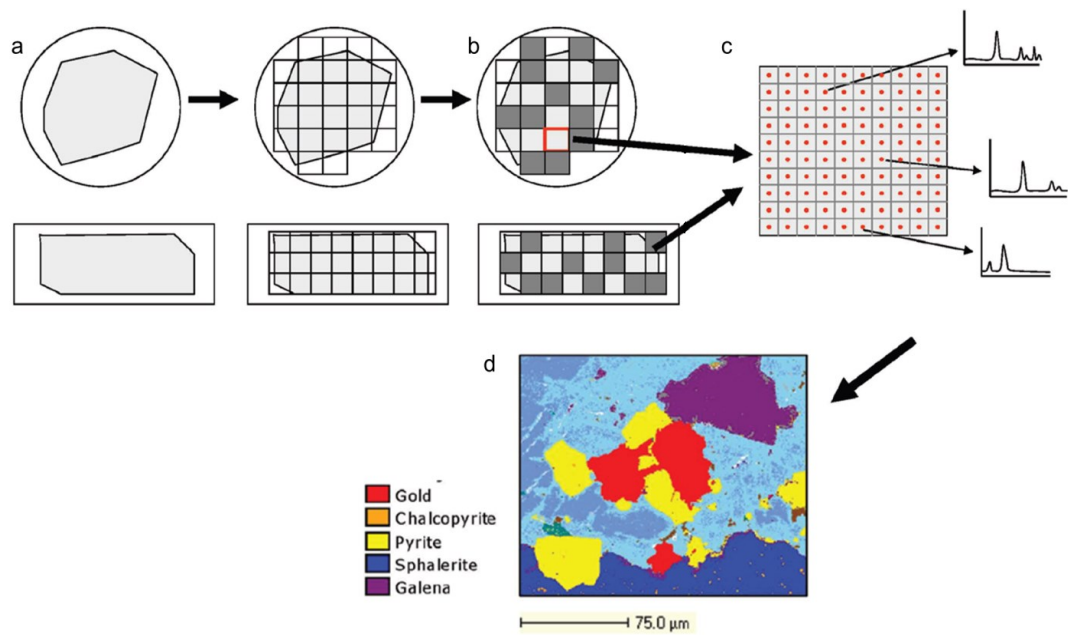
Figure 2.6: Example of operating system of Trace Mineral Search (Pirrie and Rollinson, 2011).

Field Scan (FS)

The Field Scan (FS) mode captures a full petrographic image of each field on a sample (Figure 2.7). It can be used for mapping rock chips or core samples mounted in the polished sections or also for stubs of granulated material. It collects a chemical spectrum at a set interval within the field of view. Each field of view is then processed offline to generate a single integrated image, and a false-colour image of the core sample is produced. It can take from 30 minutes (mapping only one frame at routine condition of 10 micron) to 3 hours (mapping all the sample at a routine condition of 10 micron). The informations that can be obtained are: modal proportion of phases, element deportment, estimated grain size, full textural parameters and fabrics. From the fieldscan image of a thin section it is also possible to quantify the porosity or microporosity, because any area in the image, which are not minerals are pores (Pirrie and Rollinson, 2011).

It is important to note that the thin sections are the best samples if we want to obtain textural information in FS, while the use of granulated stubs is better to obtain quantitative analyses. Careful sample preparation and the correct selection of the measurement mode are critical to obtain the best quality data set. In Figure 2.8 there is an example of thin sections analyzed in field scan mode.
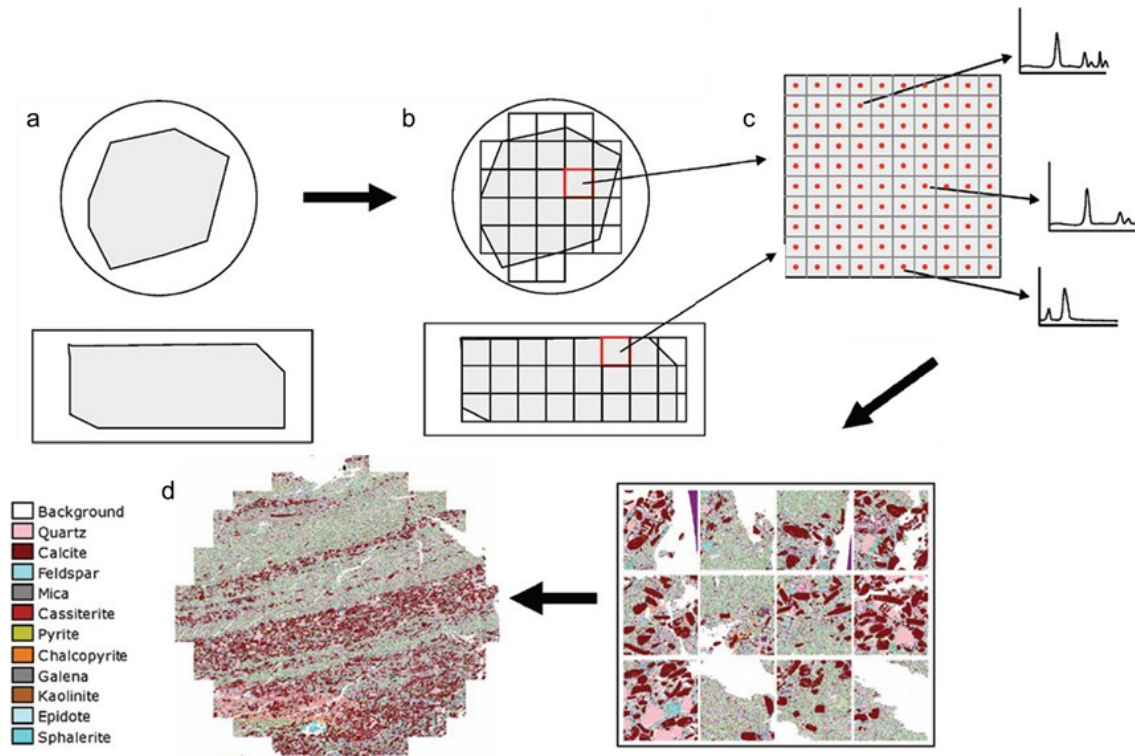
Figure 2.7: Example of operating system of Field Scan (Pirrie and Rollinson, 2011).
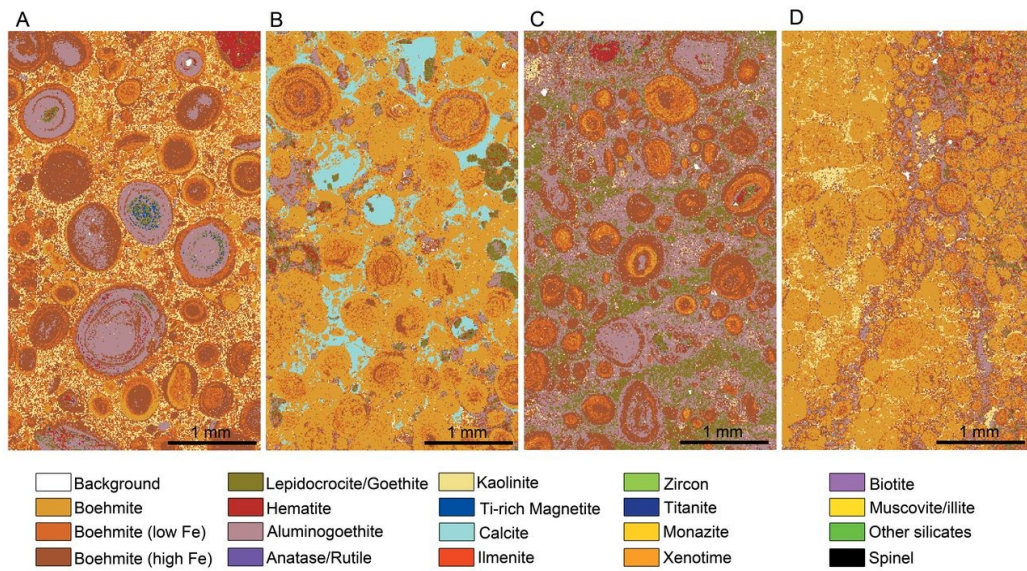
Figure 2.8: QEMSCAN® analysis in field scan mode on thin sections of bauxite from Southern Italy (Boni et al., 2013).

2.5. Applications of the QEMSCAN®

The applications of the automated mineralogy by the use of QEMSCAN® are extended to several fields of scientific research, as well as to practical aspects of life.

Nowadays, QEMSCAN® is used for several purposes in many fields of geology i.e. mineralogy, sedimentology (sediment diagenesis), environmental geology (for the analyses of soils, dusts, mine waste tailings, identification of sources of contamination), geology of the industrial minerals, igneous and metamorphic petrology, archeology (provenance of natural and man made materials such as pottery, archeometallurgy, e.g. Roman metallurgy), forensic studies (soil provenance, trace evidences analyses, filler in drugs).

However, the largest use of QEMSCAN® is in economic geology and metallurgy (for the characterization of ore deposit, studies on recovery and mineral liberation), and in oil and gas systems analysis (porosity and analyses on the cuttings). For this reason, here follows a brief description of the uses of QEMSCAN® in these two main fields, and on the information that can be acquired by the analyses.

Ore deposits and metallurgy studies with QEMSCAN®

As above mentioned, QEMSCAN® is extremely useful in ore deposits evaluation, because it allows to obtain accurate and statistically valid data, and can perform a quantitative characterization of mineral assemblages, associations, and textures of ores and other mineralogical compounds. Thanks to its several analytical modes, it can be a useful tool for the characterization of several types of ores such as sulfides (see references below), rare earth element deportment (Smythe et al., 2013 and references therein; Grammatikopoulos et al., 2013 and references therein), gold deposits (Goodall et al., 2005; Goodall and Scales, 2007 and reference therein), etc. Moreover, the option of having also accurate information on particle sizes and on the degree of liberation makes the QEMSCAN® a powerful tool for mineral beneficiation, including ore characterization, pilot-plant studies, process circuit surveys, routine plant period sampling. More precisely, the ability to output detailed information on mineral liberation, theoretical grade recovery curve, particularly useful for planning the flotation process, has made the QEMSCAN® one of the most evaluable methods for sulfide ores characterization (Goodall et al., 2005; Pascoe et al., 2007; Lotter et al., 2003; Anderson et al., 2014).

In the paper *"Modern SEM-based mineral liberation analysis"*, Fandrich et al. (2006) underlie the importance of Automated Mineralogy for the mineral liberation analysis and hence for plant operations and optimization during the feasibility studies. Gunning et al. (2009) also studied and reported how the Automated Mineralogy can be of benefit to the metallurgical processes data interpretation in mineral exploration.

In fact, plant and test samples can be measured for composition and liberation, so that more reliable design and optimization decisions can be reached. In addition, plant performance can be audited by mineralogy with confidence (Gottlieb, 2000).

An example of application of QEMSCAN® to the study of Process Mineralogy for metallurgical aims is well described by Charland et al., (2006). Considering that ore textures combined with modal mineralogy (Fandrich et al., 2006) would be a major

factor dictating the metallurgical performance and, hence, recovery by the degree of liberation achieved for a given grind (Montcalm Project Feasibility Study, 2003), automated mineralogy to the Montcalm Ni/Cu Ore (Falconbridge Ltd.) was introduced to better understand the processed ore, and assist in improving the flowsheet design or optimization at every level of the processing operations. A similar study has been undertaken also by Lotter et al. (2003), where QEMSCAN® is used to test the flotation process to the Sudbury Igneous Complex Ni–Cu ore (Falconbridge Ltd.), located 400 km north of Toronto (Ontario, Canada).

Another example of automated mineralogy applied to the mineral processing study is reported by Díaz et al., (2009), where QEMSCAN® has been used as main analytical technique for the characterization of the Radomiro Tomic Copper Mine. In the above study the QEMSCAN® has been used both to evaluate the copper sulfides resources located below the oxides, and also to assess the explotation by the use of flotation or bioleaching processes.

In the porphyry copper-molybdenum ore of Cerro Verde Mining Complex (Arequipa, Peru), QEMSCAN® was used with the double function of characterizing and optimizing the primary-sulfide reserves and support of the ongoing secondary sulfide leaching operation: The primary-sulfide ore feed material was characterized, in order to optimize flotation recovery by identifying the key mineralogical features such as sulfide deportment, grain size, locking/liberation characteristics, and the presence of hydrophobic gangue minerals. The information generated by the QEMSCAN® for the secondary-sulfide leaching process is being used to profile and refine the current leach ore types, in order to improve the overall copper recovery by characterizing and quantifying the copper losses in the final residue (Fennel et al., 2013).

Oil and Gas systems with QEMSCAN®
One of the big uses of QEMSCAN® is in the Oil and Gas field, for the modelling of the reservoir lithological and mineralogical proprieties. The Automated Mineralogy, in fact, can be useful to develop highly refined geologic and reservoir models for oil and gas exploration and production, in order to reduce the uncertainty in operational decisions and ultimately result in more successful exploration and be more efficient during production.

In these cases, QEMSCAN® is used for the analysis of the drill cuttings, which represent the material obtained directly from the drilled geological succession, and are generally utilized in the industry as a source of information.

The detailed study of the cuttings, hence, as well as the ability to describe and quantify their composition, texture, and lithology represents a very useful approach, which can assist in reducing reservoir uncertainties associated with stratigraphical subdivision, flow unit identification and reservoir property description (Moscariello et al., 2010).

Cuttings analysis has traditionally been regarded as simply too cumbersome, and questions have also been raised about the statistical validity of cuttings samples. For this reason, Automated Mineralogy provides a method by which thousands of cuttings can be analyzed in a fraction of the time required by conventional methods, providing results that are statistically robust and representative. Moreover, the digital mineral maps

provide visual representation of the mineralogy and how minerals relate to each other, providing contextual information, which is often critical in understanding depositional environments, diagenetic processes and petrophysical properties. Other information that can be obtained is the shape and the size of the grains and the textural parameters in sandstone and other sedimentary rocks, where they have great impact on the interpretation of depositional environments. Furthermore, it is possible to calibrate wireline logs and to understand why certain geophysical signatures exist in certain geologic formations by the study of the grain density (Butcher and Botha, 2010)

QEMSCAN® automated analyses are also used to classify cuttings in different categories by a process known as "lithotyping", so that each category represents a certain rock type, defined by basic classification rules that include composition and texture (Moscariello et al., 2010; Butcher and Botha, 2010). This step is useful for distinguishing between different rock types in each cuttings samples, adding this information to the mineralogy of the cuttings: thanks to this function it is possible also to correlate the mineral species to the lithotype in which they occur (Figure 2.9).

In this way, mineralogical, lithological and textural variations can be traced and quantified down-hole. Similarly, drilling contaminants/additives can be classified and selectively removed from the dataset. The data obtained from the analyses on the cuttings can be combined with data from core and used in correlation.

Automated Mineralogy can also identify and measure pore spaces (porosity) in the surface of the sample. In addition to providing a basic quantification of pore spaces, analysis software has the ability to separate and treat each area of discretely connected pore spaces individually (Butcher and Botha, 2010). The iDiscover software can classify pore spaces into digital size ranges (better referred to as "sectional area" ranges), so that the proportion of material in each category can be quantified. In addition, a density value (e.g. that of fresh water, saline water, hydrocarbons etc.) can also be assigned to porosity and bulk rock density, including porosity can be extracted from the dataset. Thus the values for both cutting-derived density and porosity can be derived from each sample and plotted against depth, to highlight the vertical trends and compare with other reservoir characteristics such as composition and response to wireline logs. Macro- to meso-porosity estimation is also possible for core samples. During measurement, resin-filled pores are marked as "internal background" or porosity and an area % value can be extracted. Porosity maps can also be built to allow visualization of the pore network (Moscariello et al., 2010).
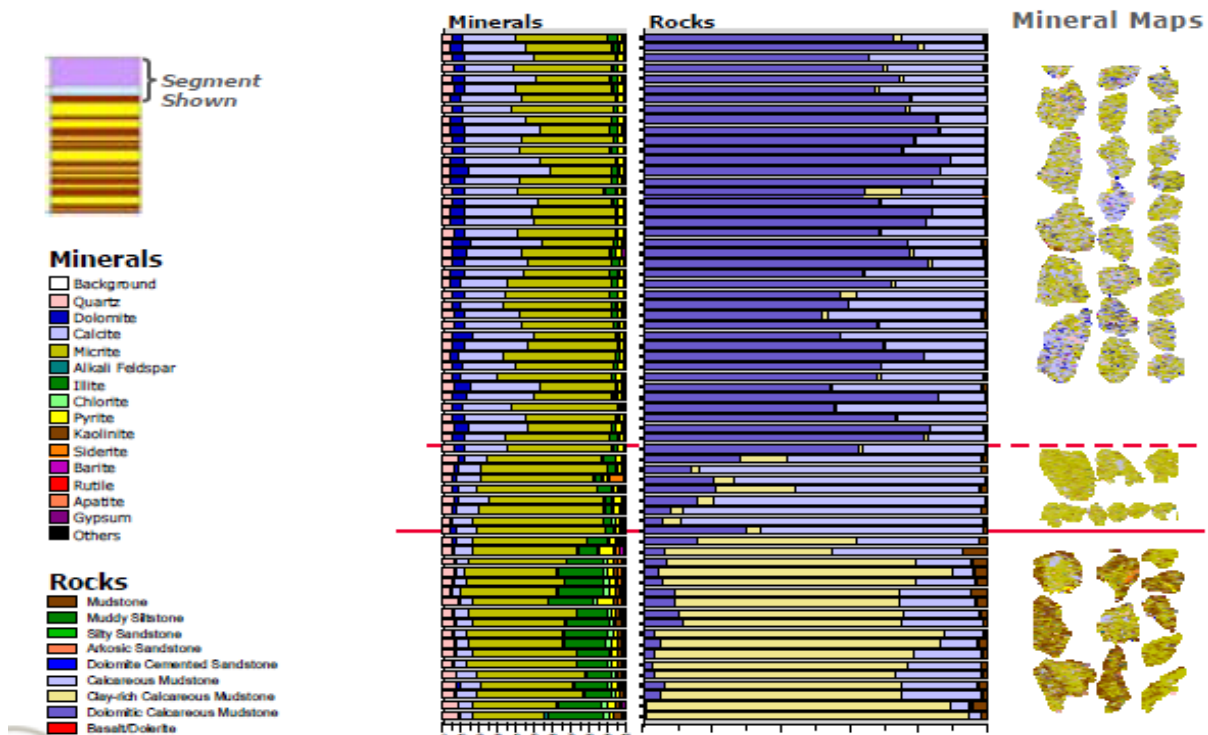
Figure 2.9: Comparison between minerals and lithotype logs (Butcher and Botha, 2010).

2.6. Sample preparation and QEMSCAN® analytical protocols

In this thesis, the QEMSCAN® analyses were carried out on 10 core samples from the Hakkari deposit, 20 core samples from the Jabali deposit and 8 core samples from Reef Ridge deposit, in order to carry out an accurate quantitative evaluation of the mineral species. The material used was taken from the same core interval used for chemical analyses even if was not exactly the same.

The samples have been selected on the basis of their higher zinc content, each one corresponding to 1 m-long core interval. The initial sample preparation was carried out at the University of Naples (Italy) and then finished at the Camborne School of Mines, University of Exeter (UK). The samples have been crushed to 3 mm, fully homogenized, granulated, and sieved to a size between 0.5 and 0.5 and 1 mm (Figure 2.10 a, b, c, d, e, f).

Thirty grams of the most Zn-rich samples for each deposit were further sieved (between 0.5 and 0.7 mm) and chemically concentrated by heavy-liquid separation, using Na-polytungstate. The heavy liquid separation method was used to evaluate if it was possible to separate the Zn-phases from carbonate host rock, and hence if the ore minerals can be liberated from the gangue. Each sample was taken under suspension for about 1 hour, in order to give sufficient time for particles to settle into the appropriate fraction. The heaviest fraction obtained was then dried in an oven and prepared into polished blocks to be analyzed by QEMSCAN®.

For all three deposits, representative quantities of material from each of selected samples from the crushed cores was split in two halves: an aliquot (50 grams/sample) was used

for QEMSCAN® analysis, whereas from the other 50 grams bulk chemical analyses of major and minor elements were carried out. Both aliquots were again quartered to obtain the amounts necessary for the two types of analysis: 1 gram/sample for QEMSCAN® analysis, 10 grams/sample for whole rock chemical analysis.

About 1–2 g of sieved material from each sample was prepared into resin (a mixture of Epofix resin and Epofix hardener) and left one night in a pressure vessel (minimize bubbles) to obtain ~3 cm2 diameter blocks (Figure 2.11 a, b, c).

Samples were labeled and Araldite resin used to encase the label and produce a thickness of approximately 15 mm (Figure 2.11 d, e, f).
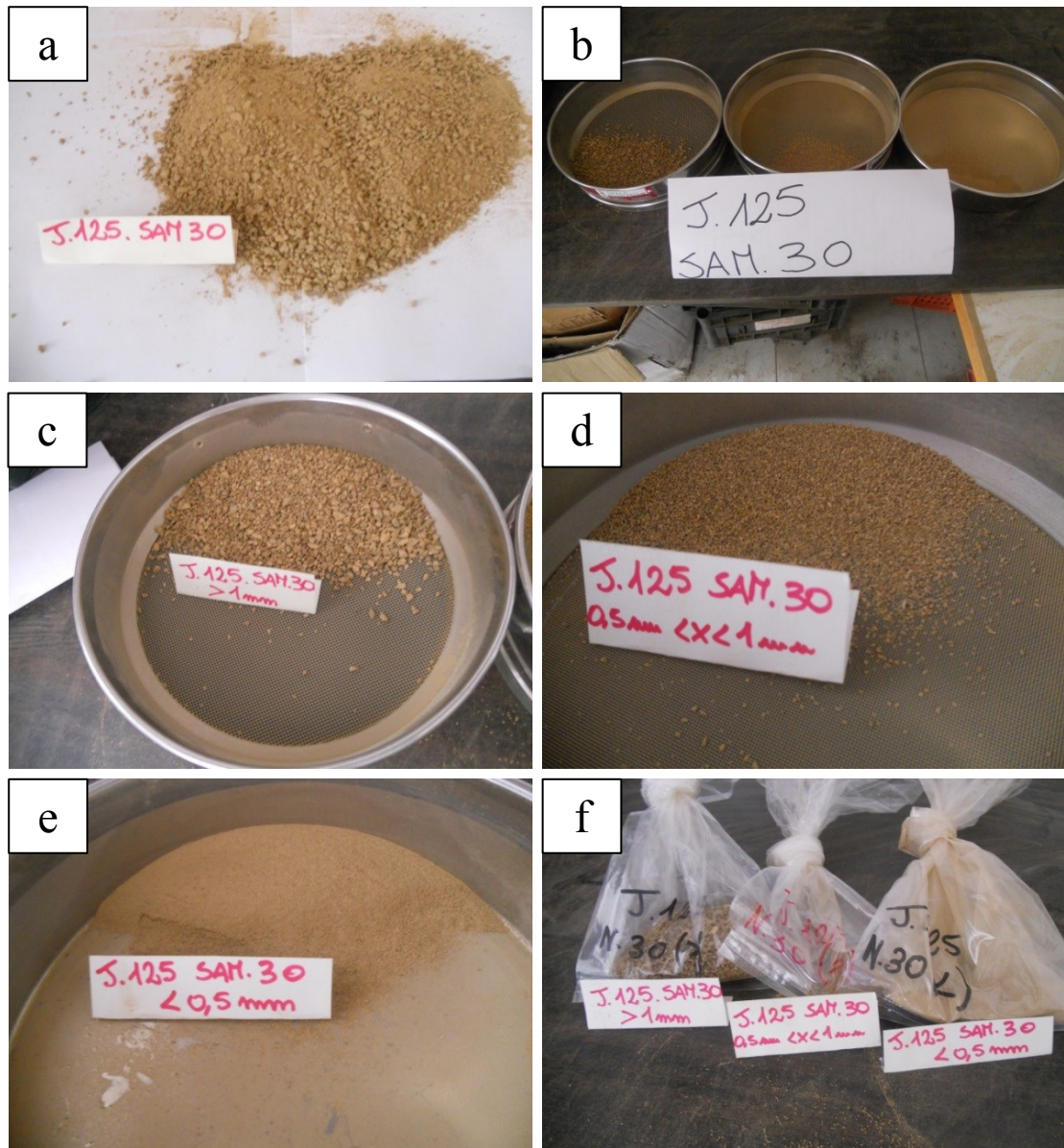
Figure 2.10: Sieving stage for sample preparation (Università Federico II, Naples): a) granulated material; b) Sieves used for the sample preparation (Mesh n° 18 and Mesh n°35); c) granulated material > 1mm; d) granulated material comprised between 0.5 mm and 1mm used for the analyses; e) powder material <0.5 mm; f) bags of the sampled material.

The latter were polished to 1 µm (Figure 2.11 g, h) and carbon-coated (Figure 2.11 i). In Figure 2.12 are shown the grain stubbs before carbon coating. QEMSCAN® analysis was carried out using the fieldscan analytical mode (Gottlieb et al., 2000; Pirrie et al., 2004; Goodall and Scales, 2007), which produces distribution maps of the mineral phases, and allows the development of a customized database. This in turn allows statistical information on the particles, grain sizes, mineralogical association and quantitative analyses for each sample. For clarity, in the following text we refer to ''*particles*'', as the pieces of material (generally consisting of a mixture of different materials/minerals) incorporated in the resin, while the word ''*grains*'', refers to the mineral phases. In addition, the term ''*mineralogical association*'' refers to the adjacency of a mineral/phase with other mineral compounds/phases: two minerals are ''associated'' if a pixel of one of them occurs adjacent to the pixel of another. When considering a specific mineral, the ''iExplorer'' software scans the measured particles horizontally, from left to right, counting the associations that may occur on either side of a mineral/ phase, and then calculates the amounts (%).

The sample preparation aimed to maximize the number of particles at the sample face to increase the chance of finding minerals with a very low abundance, with a mono-layer of sample used during the preparation to minimize settling bias.

Two uncrushed mineralized samples in polished thin section from the Jabali deposit (J109-5 and JS-Mon-2) were also analyzed with QEMSCAN®, in order to visualize the texture of the ore, to serve as a guide for the interpretation of the granulated material.

The analyses were carried out at the Camborne School of Mines, University of Exeter, UK, using a QEMSCAN® 4300. The instrument system is fully automated (electron beam, stage
control, spectrum acquisition and classification), and enables the measurement of EDX spectra along a grid. The data acquisition and the data processing were conducted by iMeasure v. 4.2 and iDiscover v. 4.2 software packages, respectively.

The image resolution used for each sample was 10 µm, which was adequate to estimate the quantities and the spatial distribution of the mineral phases. QEMSCAN® analyses were carried out at the conventional 1000 total X-ray counts per spectrum acquired, with an analytical time of about 3 h per sample. This analytical setting has sufficient precision to discriminate the mineral phases that contain chemical elements over ~3 wt.% (Andersen et al., 2009; Rollinson et al., 2011). The analyses were operated using an accelerating voltage of 25 kV and a current of 5 nA. Prior to each analysis, a standard instrument calibration was performed: beam focusing, beam alignment, calibration of the backscatter range (quartz 42 and gold 232 were used) and the X-ray detectors.

The QEMSCAN® modal mineralogy was output in both volume and weight % (wt.%) using the iDiscover software. For pure mineral phases, with known densities (International Mineralogical Association database), the mass data used the average chemistry and density data for each mineral.

For the impure phases (see paragraph on the Species Identification Protocol development in chapters 3, 4 and 5), whose composition was not well constrained, the density data were evaluated considering the backscattered electron intensity of these compounds,

relative to pure phases with known density, and the concentration of the elements they contained. For this research, major minerals refer to those that occur >1 wt.%, minor minerals between 0.1 wt.% and 1 wt.%, whilst trace minerals are those <0.1 wt.%. Quality control validation measurements were performed at the Camborne School of Mines, on a Zeiss EVO 50 SEM with Bruker 4010 EDS SDD detectors, and with Bruker Esprit 1.8 software (standard- less EDS analysis approx. ±1%).
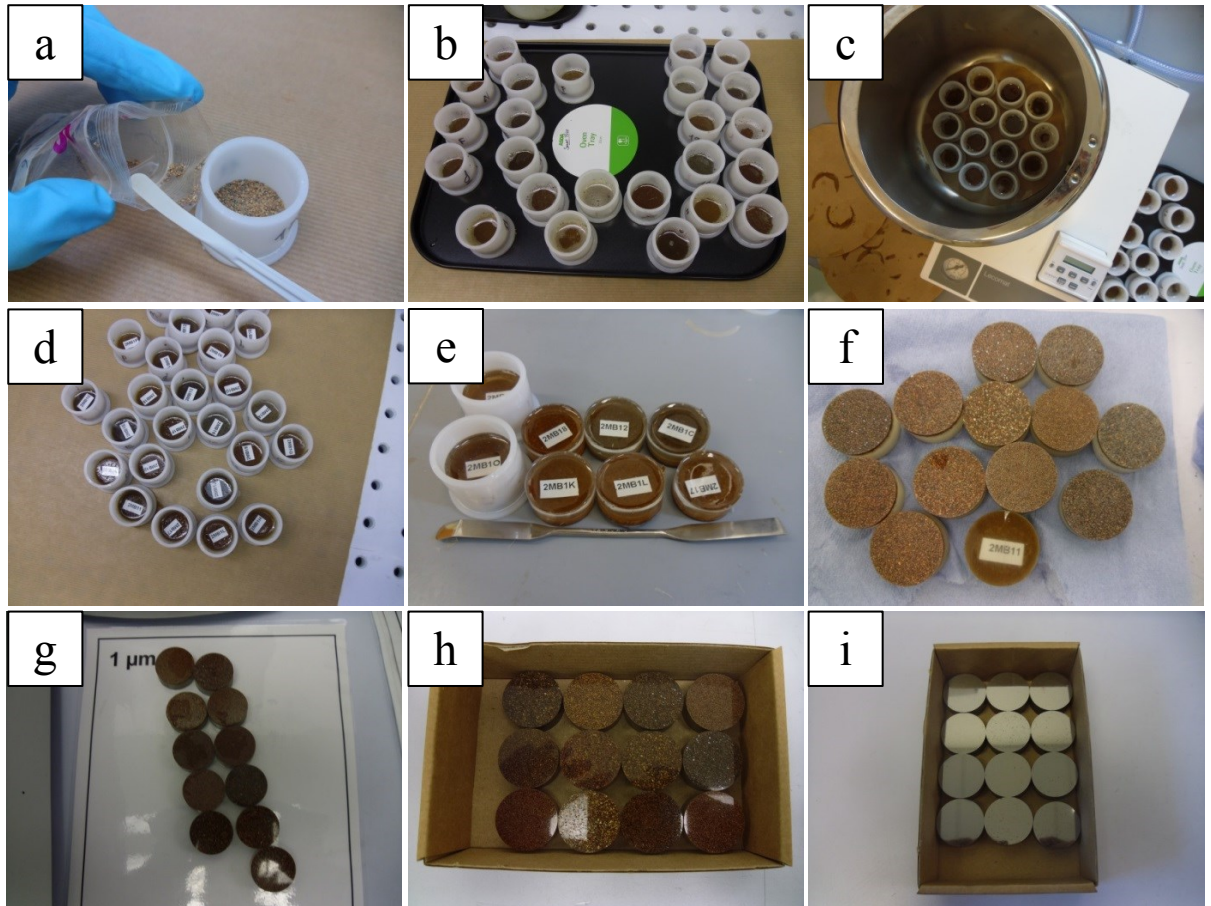
Figure 2.11: Stubbs preparation stage (Camborne School of Mines): a) 2 grams of granulated material (size comprised between 0.5 to 1mm) were put in the holder; b) the material was covered by a mixture of epofix resin and hardner; c) The material was left under pressure during the night to avoid formation of bubbles; d) The stubbs were labeled and covered with more resin to enhance their thickness; e) the stubbs were taken off; f) stubbs samples before polishing; g) the samples were polished to 1 μm; h) polished stubbs; i) carbon coated stubbs.
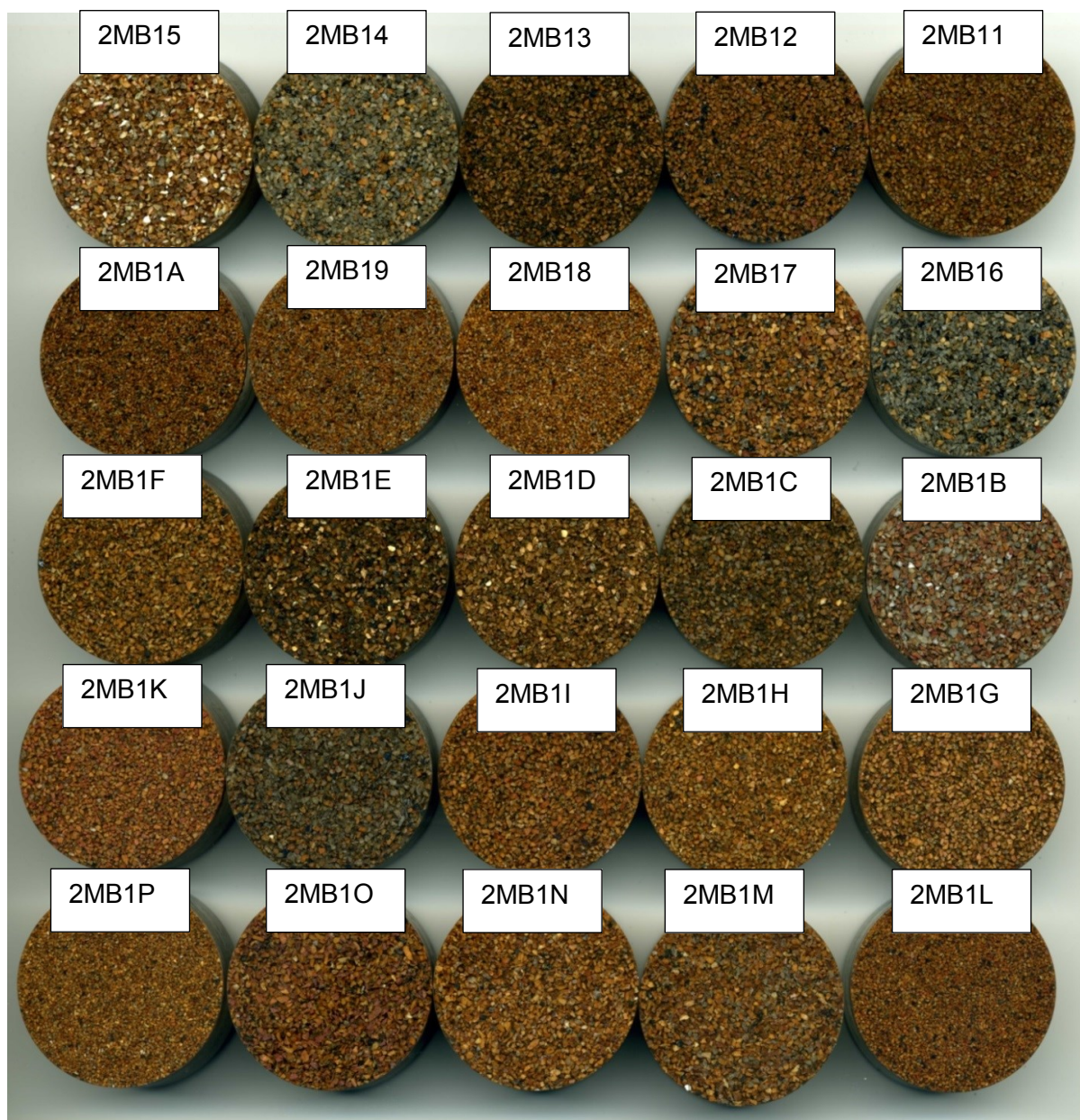
Figure 2.12: Jabali stubbs before carbon coat.

Chapter 3

The supergene nonsulfide Zn-Pb deposit of Hakkari, Turkey

3.1. Introduction

The Hakkari Zinc Project (HZP) is located in the southeastern region of Turkey, approximately 10 km west of the town of Hakkari, within a broad 20 km wide and 100 km long east-west belt extending from 60 km east of Hakkari and Şirnak Provincial boundary. Currently, the HZP comprises three Operation Licenses (License 5, License 26 and the Pentagon License) and one Exploration License covering a cumulative area of 5065.4 hectares. The deposit, once belonging to Red Crescent Resource Limited (RCR), (Canada), is currently owned by Ebullio Mining Limited ("Ebullio", UK). The Hakkari mineralization, mainly consisting of supergene Zn>>Pb nonsulfides, consists of a series of small deposits (approximately 2.5 Mt each), located along a narrow belt of Mesozoic, structurally deformed sedimentary rocks belonging to the Arabian Platform (AP). The ore is mainly hosted in locally dolomitized and brecciated limestone, interbedded with minor clastic layers (Grodner, 2010).

Hakkari was already known by the Romans, who exploited there a few galena-rich veins; in fact, it is still possible to observe many remnants of Roman underground mining in the upper lead-rich portion of the mineralized zone (Figure 3.1). Even if probably no zinc was mined in Roman time, it is highly likely that zinc had been sporadically mined in the Hakkari area for at least 2000 years.

Figure 3.1: Examples of Roman tunnels in recently excavated open pit.

Informal small-scale mining activities have been locally undertaken on mineralized zones located between License 5 and the Pentagon License. In excess of 600,000 tonnes of zinc-lead material have been officially recorded as sold under contracts through traders with typical grades (certified by SGS and Alfred Knight laboratories) ranging from 25% to 40% Zn and 4% to 8% Pb. A significant proportion of this material has

been mined from areas adjacent to and between the license areas. Apart from the above, and from other similar small-scale operations within the Hakkari area, no record of any previous systematic mineral exploration carried out in the last decades exists before 2010. A systematic exploration activity with modern methods started in the area in 2010 (RCR), with a program comprising mapping, grab and trench (channel) sampling and diamond core drilling aimed to mineral resource estimation. The nonsulfide ore, with an overall estimated compliant resources of at least 10 Mt @ 15% Zn (RCR), consists of variable amounts of smithsonite and hemimorphite (Santoro et al., 2013). However, its full potential is believed to be several hundreds of millions of tonnes across the > 100 km available strike length of the mineralized belt. Based on the 2010 exploration activities, a maiden Inferred Mineral Resource of 2.41 Mt at 1.92% Zn, 0.54% Pb and 1.67 g/t Ag, at a cut-off grade of 0.5% was declared for License 5. Metal grades for the Pentagon License are encouraging, but no mineral resources have been declared for this license so far. Additionally, also License 26 has been historically mined, and a fast-tracked exploration program will be implemented in order to define a maiden mineral resource on this License too.

Preliminary metallurgical test-work on several stockpiles samples first indicated that the Hakkari nonsulfide concentrations were amenable to direct acid leaching. Further test-works proved that it was possible to upgrade the 7.5% Zn feed to 22 % Zn by gravitational concentration (MSA report, 2013). However, test-work indicates that AmmLeach® has at Pilot Plant scale extracted zinc economically from the Hakkari carbonate ores, where physical separation is largely ineffective (Clegg et al., 2014). A proprietary solvent extraction step has been used to avoid ammonia carry-over into the electrolytic metals recovery. There is potential for significant cost savings, because not using acid is a great advantage for carbonate-hosted deposits. For this reason, the current owner is planning to use ammonia leaching to process the nonsulfide ores.

Scientific literature on the Hakkari deposit is extremely scarce, with brief descriptions in Yigit (2009) and a mention in the paper of Reynolds and Large (2010). In a paper that focuses on the Pb-isotope geochemistry of a series of Turkish deposits, Ceyhan (2003) reported that the zinc-lead primary ores occurring in the Hakkari area were stratabound, carbonate-hosted and Mesozoic in age. He also suggested that they were originally MVT deposits, related to a widespread circulation of hydrothermal fluids mobilized by Alpine-Himalayan compressive events. In contrast, Reynolds and Large (2010) considered the Hakkari ores to belong to a syngenetic/diagenetic SEDEX- or Irish-type class of deposit, related to the Triassic – Jurassic initial break-up of Pangea.

The origin of the nonsulfide deposit has been ascribed to Upper Tertiary oxidization events by Santoro et al. (2013). These authors hypothesize a possible sub-aerial exposure of the sulfide ores during the last uplift stages, following the collision between Eurasian and Arabian plates. Evidence of a Late Eocene deformation, sub-aerial uplift and erosion of the northeastern edge of the Arabian Platform are recorded in many sedimentary succession of northern Iraq (Jassim and Goff, 2006), and confirmed by faunal data. In this part of Turkey, it is highly probable that the main weathering happened in a period possibly spanning between Upper Miocene and Lower Pliocene, following the

emergence of the Turkish portion of the Arabian Platform (the AP remained submerged until Middle Miocene, Rigo de Righi and Cortesini, 1964; Tolun and Pamir, 1975; Karig and Kozlu, 1990). The Neogene would be the ideal period for the main weathering phase at Hakkari, because it represents a transitional stage between the greenhouse world of Cretaceous/Paleogene and the Quaternary icehouse situation (Bruch and Zhilin, 2006; Flower and Kennett, 1993; Jacobs et al., 1996; Woodruff and Savin, 1989, 1991; Yilmaz, 1993).

The closure of the Tethys Ocean has been considered the main cause of the cooling trend as it was followed by:

1) waning volcanic activity across southwest Asia: it was subsequent to the end of the magmatism related to the subduction of Tethys, brought to a reduction of the amounts of CO_2 degassing into the atmosphere with a consecutive cooling of global temperatures (Allen and Armstrong, 2008);

2) increased weathering: the continental collision and increased sub-aerial erosion in newly elevated areas would have enhanced the weathering of silicates at low latitudes (Raymo and Ruddiman, 1992), a process promoting the CO_2 drawdown from atmosphere. This also caused a climatic cooling;

3) new ocean circulation: the Tethys closure provided substantial changes in the currents circulation in both Indian and Atlantic Oceans, which became closer to a modern pattern of ocean circulation and upwelling. While during Cretaceous and Eocene the warmer surface currents at low latitude were dominated by the circum-global westwards flow from the Indian Ocean to the Atlantic via the Tethys gateways (Bush, 1997; Hallam, 1969; Huber and Sloan, 2001), after late Eocene the circum-equatorial surface waters were directed southwards in the Indian Ocean, because of the constriction of the Tethys gateways (Diekmann et al., 2004). As a result, the low latitude water temperature decreased because of the circulation of cold water (originated from northern Atlantic). Many basins registered this cooling: within the western Tethys region there was an increased intensity of abyssal circulation associated with the initial entry of the northern Atlantic water (Barbieri et al., 2003). The cooling in the ocean water caused a general cooling in the climate in the affected areas.

One of the aims of this chapter is to carry on, through different analytical techniques, a characterization of the Hakkari nonsulfide deposit that could be of use for choosing the processing routes. For completeness, a geological, tectonic, and metallogenic frame has been also provided in order to better comprehend the nature of the Hakkari deposit.
In conformity to the declared aims, in the following paragraphs are reported:
1) the geological setting of Turkey and its Zn-Pb ores, in the metallogenic context of the Tethys;
1) the Hakkari supergene deposit framed in the geological evolution of the district;
2) a complete mineralogical (qualitative and quantitative), petrographic and geochemical, characterization (including stable isotopes geochemistry) of the nonsulfide ore association in the deposit, to define the mechanisms leading to the secondary mineral

enrichments. The quantitative analyses should provide information for eventually planning the processing strategies during the feasibility stage.

3. 2. Geology of Turkey

The geological setting of Turkey is quite complex, due to the strong tectonics that affected this area. Presently lying within the Alpine-Himalayan mountain belt, at the junction of Eurasia, Africa and Arabia, the lithologic units which currently correspond to Turkey were once situated at the collisional boundary between two megacontinents separated from the Thetyan Ocean: Gondwana in the south and Laurasia in the north.

During its long evolution the Thetys Ocean was not a single continuous oceanic domain (Şengör et al., 1987; Ricou et al., 1994; Stampfli et al., 1996), but consisted of several isolated lithospheric plates with oceanic crust. Throughout this geological history, small fragments of both the continents and of the Thetyan Ocean migrated through the oceanic domains and collided with the opposite continental margins. Therefore, many regions that were part of the Gondwana or Laurasia border show a complex tectonic setting with several sutures. This is obvious especially in Turkey, whose geological framework consists of many lithospheric fragments that were amalgamated in Late Cretaceous-Tertiary when the Thetyan Ocean closed (during the Alpine orogeny), and the Arabian Plate collided with the Anatolian Plate.

Ketin (1966,) subdivided what is presently Anatolia into the Pontides (Laurasia realm), the Anatolides, the Taurides, and the Border folds (Gondwana realm) (Figure 3.2).

A more detailed tectonic setting was given by Okay and Tüysüz (1999), who subdivided the whole Turkey in six lithospheric blocks separated by four tectonic lineaments (sutures): i) *the Strandja Zone (SZ), ii) the İnstanbul Zone (IZ), iii) the Sakarya Zone (SZ), iv) the Anatolide-Tauride Block (ATB), v) the Kirşehir Block (KB), vi) the Arabian Platform (AP)*. A tectonic map showing the major lineaments and the continental blocks is shown in Figure 3.3.

The first three zones have a Laurasia affinity and are called "*Pontides*" (Ketin, 1966). They are separated from the Kirşeir Massif and the Anatolide-Tauride Block by the İzmir-Ankara-Erzincan suture. The latter is in contact with the Arabian Platform along the Assyrian-Zagros suture, which was already formed during the Pan-African orogeny (Altiner et al., 1989). Although separated by a suture, the Anatolide-Tauride Block shows affinity with the Arabian Platform and hence with the Gondwana continent. The Inner Tauride suture separates the Anatolide-Tauride Block from the Kirşehir Massif (a Cretaceous metamorphic and granitic massif), and the Intra-Pontide suture is set between the Sakarya Zone and the İnstanbul Zone.

The Pontides (Strandja Zone, İstanbul Zone, Sakarya Zone) are characterized by Hercynian metamorphism and magmatism (Carboniferous), by the occurrence of Permo-Triassic Tethyan accretion-subduction complexes, by traces of the Cimmeride orogeny (Triassic) and by clastic sediments related to the Liassic transgression. There are no records of such events in the Anatolides and Taurides regions. The Anatolides-Taurides
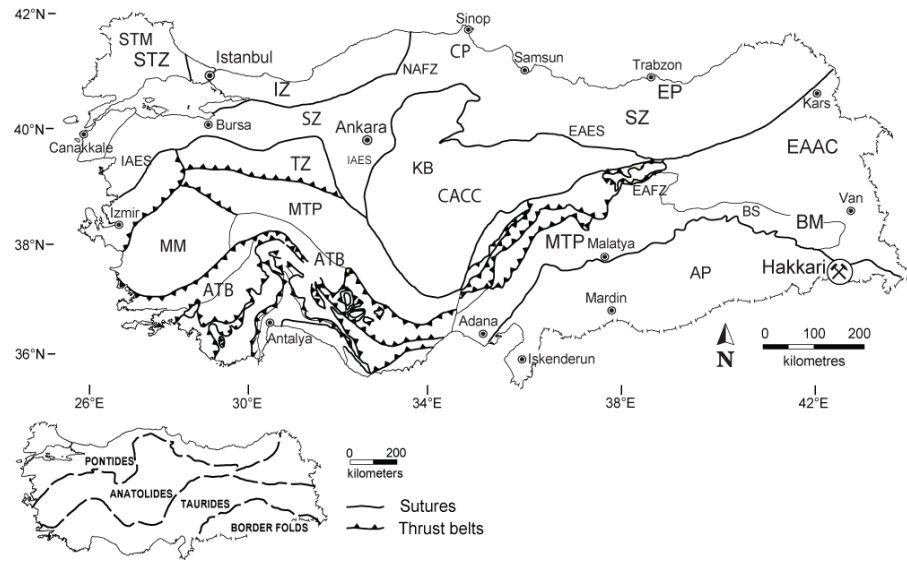
Figure 3.2: Geological–structural map of Turkey according to Ketin, 1966 (small, bottomleft) and Okay and Tüysüz (1999). AP=Arabian Platform, ATB=Anatolian Tautide Block; BS=Bitlis Suture, CACC=Central Anatolian Crystalline Complex, CP=Central Pontides, EAFZ=East Anatolian Fault, EAAC=East Anatolian Complex, EP=Eastern Pontides, IAES=Izmir–Ankara–Erzincan Suture, IZ=Istanbul zone, KB=Kirsehir Block, MM=MenderesMassif, MTP=Menderes–Tauride Platform, NAFZ=North Anatolian fault zone, STM=StrandajaMassif, STZ=Strandaja zone, SZ=Sakarya zone, TZ=Tansvali zone. In the circle the position of the Hakkari zinc district (Santoro et al., 2013).
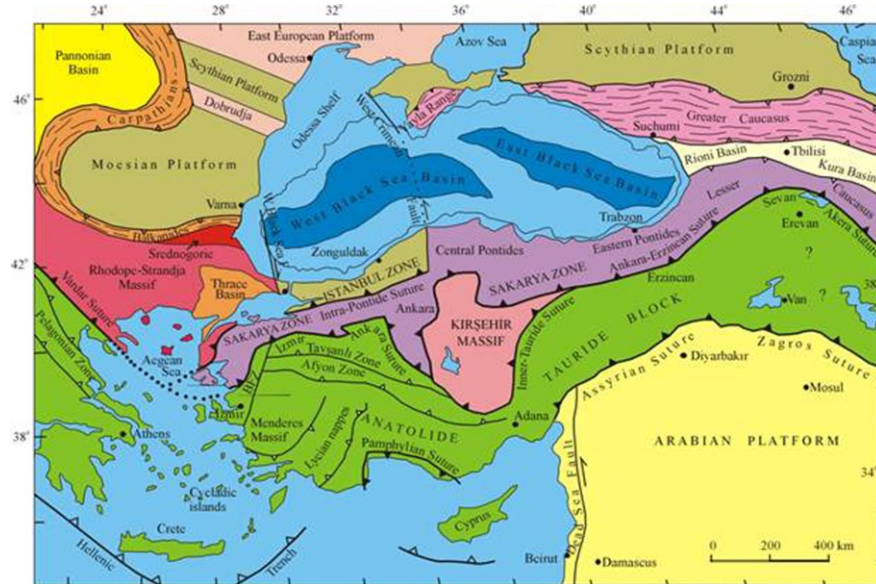
Figure 3.3: Tectonic map of northeastern Mediterranean region showing the major sutures and continental blocks. The sutures are indicated by heavy lines, with the polarity of former subduction zones shown by filled triangles. Heavy lines with open triangles represent active subduction zones. The Late Cretaceous oceanic crust in the Black Sea is shown by grey tones. Small open triangles indicate the vergence of the major fold and thrust belts. BFZ denotes the Bornova Flysch Zone (Okay and Tüysüz 1999).

platform is characterized by relatively autochthonous Paleozoic sedimentary rocks, and by complex nappe structures. Alpine regional metamorphism is widely diffused in the Anatolides, but rare in the Taurides. The Anatolides were buried beneath the southward-moving slices of ophiolitic and accretionary-complex material; their northern margin was deeply subducted and underwent HP-LT metamorphism at depth of 50 km (during Cretaceous).

Consequently, the northern part of the Anatolides was strongly deformed and metamorphosed, whereas the Taurides consisted of allochtonous nappes (Okay et al., 2001). The Pontides are devoid of nappe structures of the Alpine orogeny, while possessing a major Late Cretaceous magmatic-arc complex, characterized by granitoid intrusives and by widespread volcanoclastic flows intercalated with sediments (Tüysüz et al., 1995; Çamur et al., 1996; Okay and Sahintürk, 1997; Ylmaz et al., 1997; Bektas et al., 1999; Tüysüz et al., 1999). The present configuration of the Pontides and Anatolides-Taurides Blocks has been acquired since Late-Pliocene intra-continental convergence and consequent N-S shortening. The N-S shortening has been concluded in western Turkey, whereas it is still ongoing in its eastern part.

Southeastern Anatolia forms the northernmost extension of the Arabian Platform. During Mesozoic and Tertiary, the Arabian Platform was separated from the Anatolide-Taurides by the southern branch of the Tethys Ocean, today represented by the Assyrian suture (Şengör and Yılmaz, 1981). From middle- to late-Miocene (Langhian-Serravalian), the Arabian and Eurasian plates collided along the Bitlis–Zagros Suture zone, which is a complex continent and continent-ocean collisional boundary lying in the north of the fold-and-thrust belt of the Arabian platform, extending from southeastern Turkey to the Zagros mountains in Iran. Upper Cretaceous–Middle Eocene volcano–sedimentary lithologies and an ophiolitic mèlange mark the suture zone. The southeastern Anatolian orogenic belt is considered as an assemblage of several east-west trending tectonic units separated by major thrusts (Ylmaz, 1990). These are: *1) the Arabian Platform* (known as "Border Folds" by Ketin, 1966); 2*) the Zone of imbrication* (known as the "Orogenic zone" by Rigo de Righi and Cortesini, 1964); *3) the Nappe region* ("Orogenic zone", Rigo de Righi and Cortesini, 1964). The Zone of imbrication and the Nappe region represent the suture domain and the orogenic zones after the complete Tetyan closure and the continental collision between the Arabian Platform and Laurasia during the Alpine-Hymalayan orogeny (Late Cretaceous, Eocene-Miocene).

Since the Hakkari deposit is hosted in the Northern border of the Arabian Platform, here follows a more detailed description of its stratigraphy.

The Arabian Platform (AP)

The Hakkari deposit is located on the leading edge of the Arabian Platform (AP), which consists of an autocthonous and a parautocthonuous sedimentary succession, accumulated since Early Paleozoic on a cratonic area stabilized during the pan-African orogenic events Altiner, 1989; Yilmaz, 1993). The Upper Cretaceous ophiolite nappes, and their late Cretaceous to Miocene sedimentary cover occur here as well. The AP can be divided in four units, which are from bottom to top (Figure 3.4): *1) Lower*

autochtonous succession (where the Hakkari deposit is hosted), 2) Lower allochtonous units, 3) Upper autochtonous succession, 4) Upper allocthonous succession.

1) The Lower authocthonous succession consists of a series of nappes composed of two groups of lithologies. At the top there is an ophiolitic suite. Below the ophiolite there are two distinct and internally chaotic assemblages separated by thrusts: at the top the Koçali complex (Rigo de Righi and Cortesini, 1964), which is a *"mèlange"*; at the bottom the Karadut complex (Sungurlu, 1974; Pernçek, 1979) which is a flysch. The Kardut complex (Upper Triassic-Upper Cretaceous) is a chaotic assemblage of sedimentary rocks and igneous ophiolitic fragments. The lower part of this succession consists of hemipelagic limestones and of a calcareous turbiditic succession, aged from late Triassic upward. This succession, commonly interpreted as having been deposited in the outer-shelf and continental slope (Şengör and Ylmaz, 1981), is followed by a flysch succession.

Figure 3.4: Generalized (composited) stratigraphic section of Arabian plate in southern Anatolia, from the suture mountains (in the north) to the north of the Arabian Platform (in the south) (Yalçin, 1976).
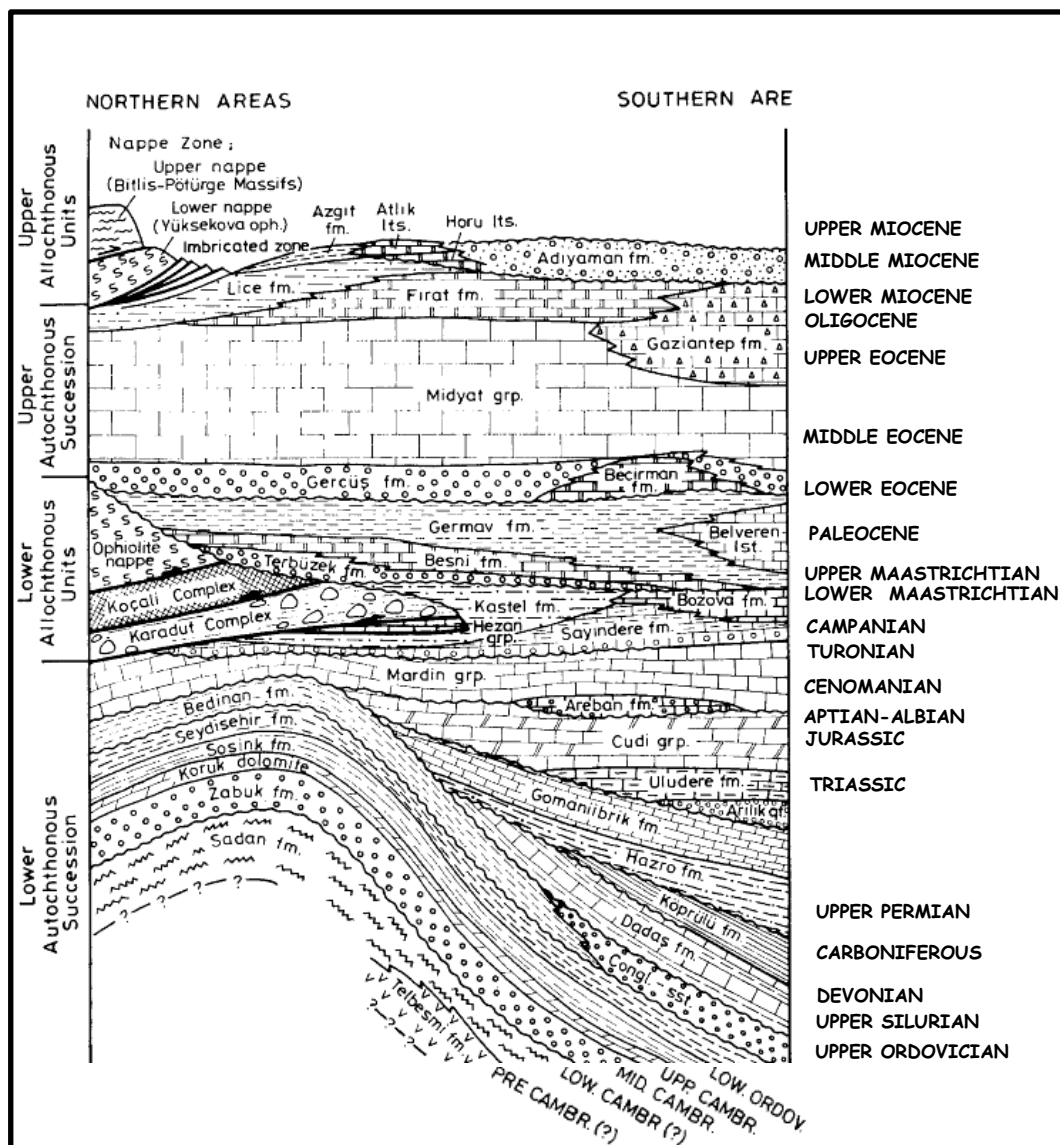
3.3. Zinc–lead deposits in Turkey/Primary Sulfides and Supergene Nonsulfides

The numerous mineral deposits occurring in Turkey are related to the evolution of the Tethys Ocean (Tethyan Metallogenic Belt). Although Turkey is best known for its porphyry and epithermal copper and gold deposits (Lips, 2007), it hosts a range of significant zinc–lead concentrations (Reynolds and Large, 2010). In Figure 3.5 is shown the distribution of the carbonate-hosted Zn–Pb deposits in Turkey, which include both primary sulfide and secondary nonsulfide concentrations.
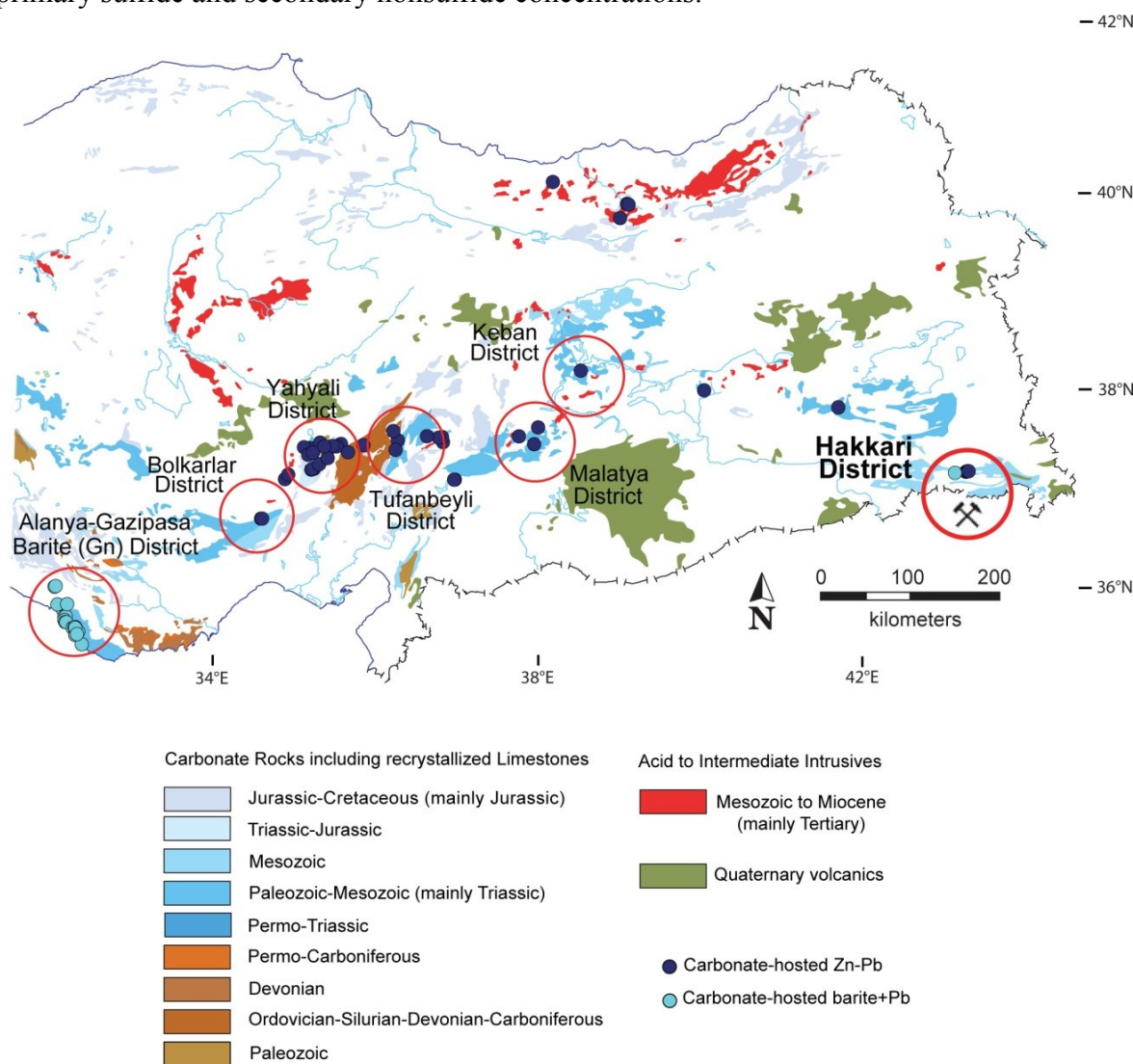
Figure 3.5: Distribution of the carbonate-hosted Pb–Zn districts of Turkey (red circles) with emphasis on host-rock lithology (modified from Yigit, 2009). The carbonate lithologies in the legend are locally repeated, due to their different position in the tectonic (Santoro et al., 2013).

Volcanic hosted massive sulfides (VHMS or VMS) deposits
Several polymetallic, felsic volcanic-associated traditionally classified as "*Kuroko-type*" deposits mainly occur in the Pontide belt (north-eastern Turkey), which relate to the subduction of Paleotethys beneath Eurasia (Robertson and Grasso, 1995; Yilmaz et al., 2000). The deposits are associated with Late Cretaceous bimodal volcanics (Yigit, 2009). The largest known VHMS deposit is Murgul, which contains chalcopyrite and pyrite, but

also minor galena and sphalerite. The Cayeli, Lahnos, Koprubasi and Cerrattepe deposits (northern Turkey) also contain Cu–Zn–Pb ores (Yigit, 2009). Copper-dominated mafic volcanic-hosted 'Cyprus type' deposits are of lesser economic importance and typically occur in southeastern Turkey, associated with the Anatolian orogenic belt (Late Cretaceous to Middle Miocene) (Yigit, 2009). The Ergani deposit is the largest of this type, and comprises mostly chalcopyrite with minor amounts of sphalerite and galena.

Sediment-hosted massive sulfide (SHMS or SEDEX) deposits
SHMS sulfide deposits, directly related to the Neo-Tethyan stage of rifting, are mainly located in the South and in South-East of Turkey, hosted in Middle Cambrian to Jurassic shelf carbonates. The Yahyali (Zamanti) district includes several small deposits, hosted by Devonian–Early Cretaceous carbonates (Ceyhan, 2003; Vache, 1964, 1966). The mineral associations consist almost entirely of sphalerite, galena and pyrite/marcasite The Hakkari Zn–Pb mineralization has been interpreted by several authors (Yigit, 2009; Reynolds and Large, 2010) to represent a carbonate-hosted Jurassic–Cretaceous system of SHMS affinity.

Mississipi Valley Type (MVT) deposits
These deposits have been related (Ceyhan, 2003) to the closure of Neothetys Ocean during Late Cretaceous and Tertiary and to the subsequent orogenic events, which mobilized a large-scale fluid flow producing widespread Zn-Pb concentrations in Late Paleozoic and Mesozoic carbonates. This kind of deposits is widespread in the Taurides district (e.g. Delikkaya, Koptagel et al., 2005 in the Tufanbeyli area). The ore concentrations in the Zamanti as well as in the Hakkari districts are still open to discussion in regard to their primary genesis, since they have been considered as belonging either to a SHMS or to MVT-style of mineralization (Venter and Robertson, 2009).

Skarn-Carbonate Replacement Deposits (CRD)
Several Zn-Pb-Cu skarn deposits occur in the Tauride block, as the Çadirkkaya mineralization, related to Late Cretaceous to Paleogene calc-alkaline magmatic events (Boztuğ et al., 2003). Other Zn–Pb skarn ores are known in the Akdağ and Malatya districts, where the mineralization occurs within fault zones in Permo-Carboniferous metamorphic rocks (Önal et al., 1990; Sağıroğlu, 1988). The most important mineralizations of this type is Keban (Ceyhan, 2003; Yilmaz et al., 1992), hosted by Paleozoic marbles of the eastern Taurides. Other skarn-CRD deposits are related to the Oligocene and Miocene post-collisional extension, which was also accompanied by calc-alkaline and alkaline intrusions. Among these deposits, the most significant is Balya in northwestern Turkey (Yigit, 2009), hosted by Permian and Triassic limestones (Reynolds and Large, 2010).

Supergene NSZ-lead deposits
This kind of deposits is known from the Tauride block (southern and central Turkey) to the Arabian Platform in the southeast. They are interpreted to have been formed by the weathering of primary sulfide ores through the action of meteoric waters, eventually

followed by reprecipitation of the metallic elements in new mineralogical phases (Boni and Large, 2003; Hitzman et al., 2003).

In the Zamanti district the primary sulfide mineralization has been almost entirely replaced by a supergene mineral association, mainly consisting of smithsonite, hemimorphite, hydrozincite, Zn–Al-silicates and high amounts of Fe-(hydr)oxides (Ceyhan, 2003 and reference therein). Also the Keban Zn–Pb primary deposit, hosted in Paleozoic marbles has been oxidized by meteoric waters, resulting in thick horizons of supergene nonsulfide ores containing smithsonite, cerussite and Fe-(hydr)oxides (Yilmaz *et al.*, 1992). The primary sulfide deposits in the Tufanbeyli district have been strongly oxidized, producing a widespread high-grade smithsonite-rich mineralization (Yigit, 2009). In the Malatya district, nonsulfide zinc ores, also dominated by smithsonite have been recognized in Carboniferous limestones (Sağıroğlu, 1988). Hakkari is another example of a Turkish NSZ deposit, to which has been dedicated part of this thesis.

3. 4. Geology and stratigraphy of Hakkari

The project area is situated within the northern margins of the AP, which is characterized here by north-vergent fold-and-thrust tectonics with the overriding Taurides separated by the Bitlis suture from the weakly deformed Arabian Platform (Yigit, 2009) (Figure 3.6). The lithotypes of the southeastern AP beneath the Bitlis Thrust can be generally described as a package of autochthonous, north-facing, folded and thrusted marine platform carbonate-dominated rocks and interbedded subordinate clastic units. The oldest unit is represented by Lower Cambrian clastic rocks, followed by Middle Cambrian carbonates (Koruk Fm.), and by clastic units of the Habur Group (Cambrian to Ordovician) (Perinçek, 1990). The Upper Devonian strata overlie directly the Ordovician rocks. They consist of alternating sandstone and limestone (Yığınlı Fm.), followed by shale and limestone (Köprülü Fm.). The Carboniferous limestones (Belek Fm.) and Upper Permian sandstones and limestones (Tanin Group, Figure 3.7) complete the Paleozoic succession. The Lower Triassic beds (Çığlı Group) are subdivided into three different successions consisting of limestones, marls and reddish mudstones. A thick sequence of alternating limestone and dolomite sediments (Cudi Group) follows, whose age ranges from Middle–Late Triassic to Early Cretaceous. At Hakkari this Group comprises the Çanaklı (Middle–Late Triassic to Early Jurassic) and the Latdağı Fms. (Late Jurassic–Early Cretaceous) (Figure 3.7). After a regional unconformity, the Mardin Group (Aptian–Turonian) follows with the clastic sediments of the Areban Fm. and the shallow marine carbonates of the Derdere Fm., unconformably overlain by shales, argillaceous limestones (Ortabağ Fm.) and/or clayey limestones of the Sayındere Fm. (Campanian). The overlying Maastrichtian–Paleocene Bozova and Germav Fms. are of limited thickness. The Germav Fm. is then followed by clastic rocks grading to a carbonate sequence (Midyat and Silvan Groups), deposited during Eocene–Oligocene, and then by marine and terrestrial sediments deposited up to Late Miocene (Perinçek, 1990). The whole region was affected by compressional tectonics between Late Cretaceous and Late Miocene (Perinçek, 1990). The above-described succession is tectonically overlain by the allochtonous Hakkari and Yüksekova Complexes. Quaternary volcanism has locally affected part of the Hakkari Complex.

The northward younging sedimentary succession has been duplicated by a major east–west striking, south directed thrust structure; most mineralized sites at Hakkari are situated in the upper thrust package. Along the thrust some limited outcrops of gabbroic rocks with high chromium grades have been detected in Licenses 18 and 19 (M. Grodner, oral communication), which may be part of an ophiolitic fragment. The Maden Complex is the age-equivalent of the Hakkari Complex in the regions west of Hakkari. It differs from the Hakkari Complex by the presence of abundant Tertiary volcanic rocks.
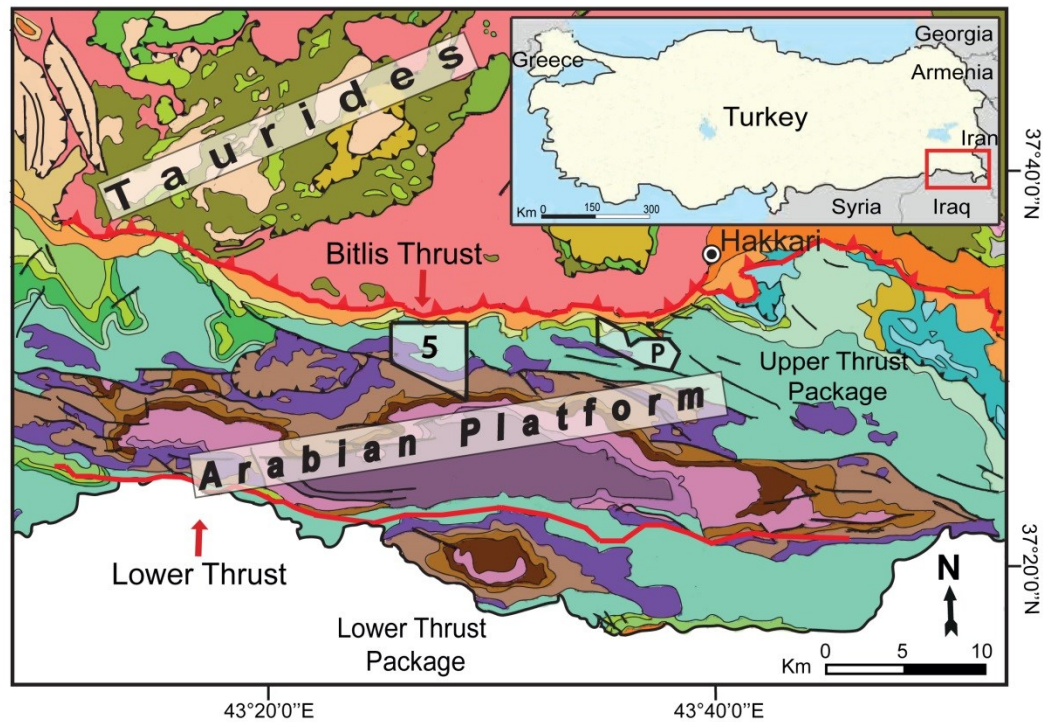
(from the Geological Map of Turkey 1:500.000 - Cizre)

⬠ Sampled areas at Hakkari: 5=License 5; P= Pentagon

Lithotypes occuring in the sampled areas:

Clastic and carbonate rocks (Upper Senonian)

Carbonate and clastic rocks (Lower Triassic)

Neritic limestone (Jurassic-Cretaceous)

Neritic carbonate and clastic rocks (Upper Permian)

Figure 3.6: Geological sketch map of the Hakkari area with the location of License 5 and Pentagon, where the sampling has been carried out (Santoro et al., 2013).
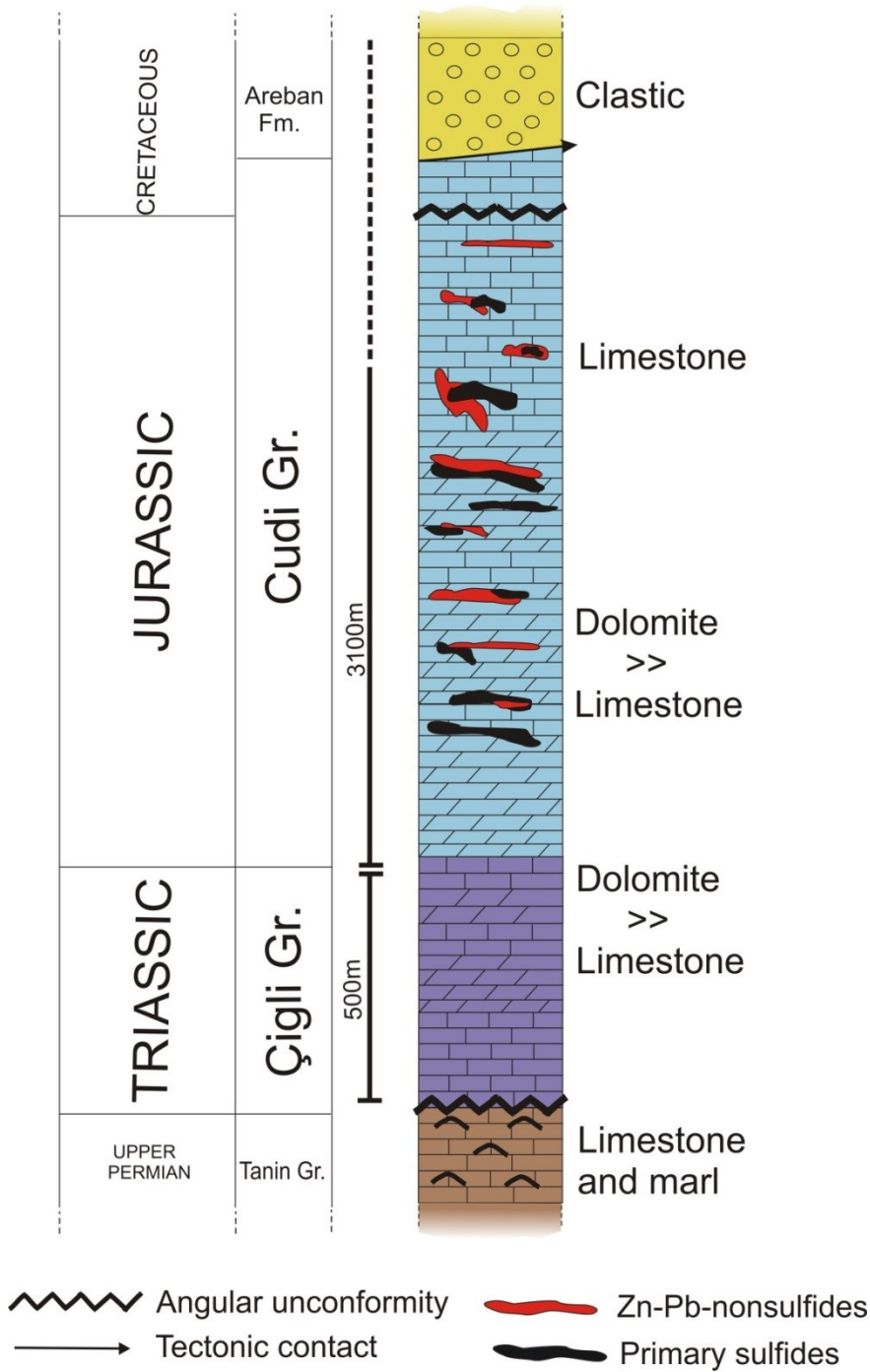
Figure 3.7: Stratigraphic column of Hakkari zone, with the position of the most important orebodies. Primary sulfides and nonsulfides ore lenses have been associated together in several horizons, due to their random occurrence in the deformed and thrusted lithotypes (modified from Perincek, 1990).

3. 5. Hakkari mineralization

Small-scale near-surface exploitation of the zinc (>lead) ores has been active for an estimated 2000 years in the Hakkari area. However, no official estimates of historical zinc production from the area exist. Information from local operators suggests that hundreds of thousands of tons have been extracted at an average grade of 25% Zn (MSA Group, 2011).

The Hakkari orebodies occur in shallow water limestone belonging to the Cudi Gr. (Middle-Triassic to Early Cretaceous), with interbedded clastic layers (MSA Group Ltd., 2011; Venter and Robertson, 2009). The zinc mineralization is generally hosted in a porous or brecciated limestone, flanked by cryptocrystalline and/or cherty dolomite. The limestone host is usually folded, while the more competent dolomite typically exhibits a brittle deformation resulting in extensive breccias cut by calcite veins (Figure 3.8a). The limestone is also strongly karstified, due to the enhanced solubility of the carbonate associated with sulfide oxidation. The ore concentrations have been remobilized along joints and fractures of the host rock (Figure 3.8b). The potentially economic deposit at Hakkari consists of nonsulfide Zn>Pb concentrations (Figure 3.8c), associated with abundant Fe-(hydr)oxides (Figure 3.8d,e), all derived from the weathering of primary sulfides. The mineralized district can be traced over at least 60 km of strike. The features of the supergene mineralization suggest that the Hakkari concentrations belong both to the "direct replacement" and the "wall-rock replacement" types of nonsulfide ores, according to the Hitzman et al. (2003) classification. The mineralization varies in style from tabular bodies of variable thickness (0.5 to 13 m) to cross-cutting breccia zones and disseminated ore minerals in pore spaces and fracture planes. A description of the different styles of mineralization, made by the geologists of the MSA Group Ltd. (2011), is as follows:

· Tabular replacement zones of variable thickness, width and strike extent, conformable with respect to the host strata,

· Pods parallel to bedding,

· Cross-cutting breccia zones, locally interconnected, with open space filling,

· Solution collapse zones and breccias, particularly in areas of enhanced dissolution.

These may result in mineralized bodies with irregular geometry as: disseminated mineralization occupying original pore spaces, and remobilized concentrations along fractures, breccias and joint planes. The ore bodies occur within a series of thrust sheets with a general east–west trend. Since Hakkari is situated in a fold-and-thrust belt region, adjacent to two suture zones (the Bitlis and Zagros sutures), the compressive tectonism of the area has produced a repetition (and hence thickening) of most mineralized levels (Figure 3.8f).

The primary orebody is likely to have been deformed and oxidized during Tertiary (Venter and Robertson, 2009).

In this thesis we have concentrated on License area 5 and on the Pentagon (Figure 3.6). Drilling on License 5 has revealed the presence of two discrete mineralized zones (upper and main), each one comprising a number of mineralized horizons interstratified with calcareous host rocks. Drilling on the Pentagon was severely limited by the morphology

of the area and failed to definitively identify a discrete upper and main mineralized zone. However, both zinc and silver grades in the Pentagon License are significantly higher than in License 5, whereas the lead grades are similar.
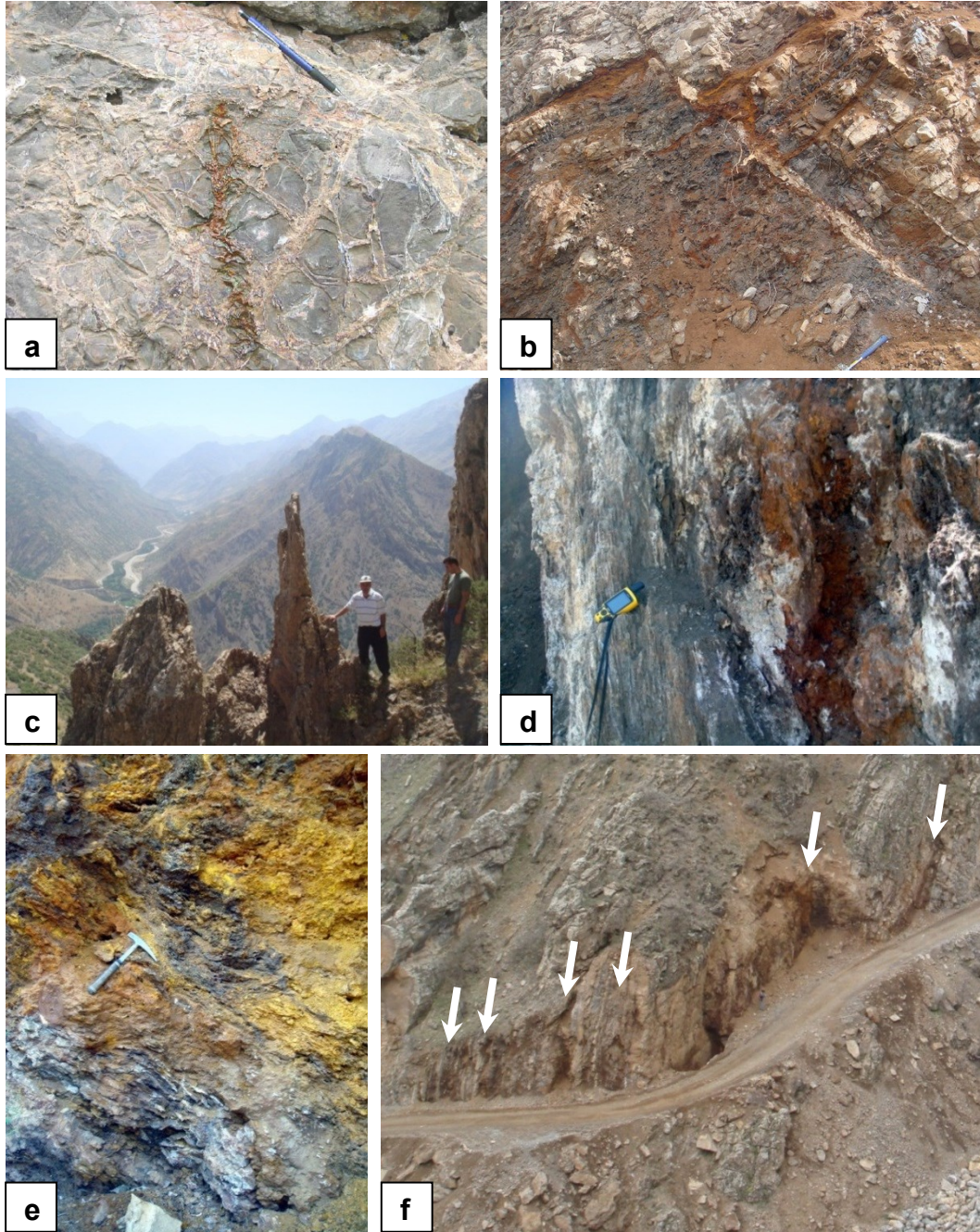
Figure 3.8: a) Hydrothermal breccia with calcite veins; b) Remobilization of mineralization along joints and fractures; c) Pinnacle of massive smithsonite mineralization; d) Massiv3 smithsonite+hemimorphite mineralization (with surficial white hydrozincite coatings) and adjacent iron oxide leached zone; e) High grade smithsonite ore overlain by partly leached iron oxide mineralization; f) Multiple mineralized layers/zones of oxidized zinc–lead mineralization (Santoro et al., 2013).

Preliminary mineralogical studies, undertaken by Red Crescent Resources have revealed that the main sulfide phases are sphalerite, pyrite and galena, accompanied by calcite, barite and quartz. Company reports identified that the main nonsulfide minerals at Hakkari consist of smithsonite and hemimorphite, with subordinate hydrozincite and cerussite (MSA Group Ltd., 2011). There is clear evidence for several supergene mineralization stages. For example, the early deposited massive smithsonite concentrations are partially leached in places, resulting in brittle red-brown ores with a spongy structure, which contain late-precipitated smithsonite and hemimorphite concentrations. Further leaching resulted in a porous network of hematite-goethite dominated ores.

The formation of the supergene ore at Hakkari is likely Upper Tertiary in age as, during this period, there have been tectonic and climatic conditions favorable for this type of ore (Santoro et al., 2013). In fact, the sub-aerial exposure of the sulfide ores probably happened in a period spanning between Upper Miocene and Lower Pliocene (Rigo de Righi and Cortesini, 1964; Tolun and Pamir, 1975; Karig and Kozlu, 1990). Favorable climatic conditions developed in Turkey during Neogene, which represents a transitional stage between the greenhouse world of Cretaceous/Paleogene and the Quaternary icehouse situation (Santoro et al., 2013).

3. 6. Analytical methods

Mineralogical, petrographic, and geochemical characterization has been performed on 31 drill core samples (1 m in length) from the Hakkari project area (Figure 3.9).

Figure 3.9: Core photograph of typical oxidized mineralized material intersected on License 5 from boreholes 5DD002 and 5DD003 (Santoro et al., 2013).

The analyses have been carried out on the best-mineralized nonsulfide cores, as well as on a few host rock samples from License 5 and the Pentagon areas (Figure 3.6).

Initially, handpicked samples were examined using hand lens. A summary of the observations, location and depth for each sample from both License 5 and Pentagon areas is shown in table 1.

Polished thin sections (~30 μm of thickness) were prepared for optical microscopy in a commercial laboratory specialized in soft sediments (OMT, Aosta, Italy). Due to the nature of the nonsulfide ores (generally soft and crumbly), the big part of the material

71

was impregnated with Araldite D and Raku Hardener EH 2950. Observations in OM were carried out using a Nicon Eclipse E200 microscope at the university of Naples.

Observation under cathodoluminescence (CL) microscopy were also carried out using a CITL8200 Mk3 Cold Cathodoluminescence instrument mounted on a petrographic microscope at the Geologisch-Paläntologisches Institut of the Heidelberg University (Germany). The thin sections were placed in a vacuum chamber and operated by X-Y manipulators. It was used a beam with a 23-25 kV voltage and a current of 400-450 µÅ beam current was used for this work.

Secondary electron imagining by scanning electron microscopy (SEM) were carried out on the same thin sections used for the OM and CL observations. The thin sections were coated with a 15µm carbon film in order to make them conductive. The analyses were performed with a Jeol JSM 5310 (CISAG, Università di Napoli, Italy) and with a Jeol JSM 5900LV (Natural History Museum, London, UK). The operating conditions were: 20 mm objective lens to specimen working distance, with 15 kV acceleration voltage (for Jeol JSM5310) and 20 kV acceleration voltage (for Jeol JEOL 9500LV).

Qualitative energy-dispersive (EDS) spectra and quantitative analyses were obtained with the INCA X-stream pulse processor and the 4.08 version Inca software (Oxford Instruments detector), interfaced with the Jeol JSM 5310. The following reference standards were used: albite (Si, Al, Na), orthoclase (K), wollastonite (Ca), diopside (Mg), almandine (Fe), rutile (Ti), barite (Ba), strontianite (Sr), Cr_2O_3 (Cr), rhodonite (Mn), sulfur (pyrite), sphalerite (Zn), galena (Pb), fluorite (F), apatite (P), chlorine (sylvite), smithsonian phosphates (La, Ce, Nd, Sm, Y), pure vanadium (V) and Cornig glass (Th and U). Analytical errors are 1% rel. for major elements and 3% rel. for minor elements.

Quantitative data sets of selected samples were obtained by wavelength dispersion spectrometry (full WDS), using a Cameca SX100 electron microprobe operating at 15 Kv, 20 nÅ, and 20 µm spot size for carbonates and 5 µm beam size for oxides and silicates (Natural History Museum, London, UK). Detection limits are in the order of 0.01 wt.% for almost all elements. The following reference standards were used: forsterite (Mg), wollastonite (Ca), zinc sulfide (Zn, S), vanadinite (Pb), silver (Ag), manganese (Mn), fayerlite (Fe, Si), gallium arsenide (As) barite (Ba), greenockite (Cd). Detection limits for WDS are in the order of 0.01 wt%. The CO_2 contents in carbonates and water content in hydrated carbonates and silicates were calculated by stoichiometry.

XRPD analyses were carried out on Hakkari specimens at the Natural History Museum of London, (UK): the core samples were previously ground in an agate mortar in order to obtain granulometrically homogeneous powders (fraction <200µm). The analyses were performed with two different detectors and two diffractometer types to enhance the accuracy of the results: 1) Nonius PDS120 Powder Diffraction System, with an INEL curved position sensitive detector (PSD), with Cu Kα1 with a germanium 111 single-crystal monochromator. Measurements were made in reflection geometry with the powder sample surface at an angle of 5° to the incident beam. Data were collected for 15 minutes and 6 hours and the angular range recorded was from 5° to 120° 2θ. NIST silicon powder SRM640 and silver behenate were used as external 2θ calibration standards and the 2θ linearization of the detector was performed using a least-squares

cubic spline function. Powder X-ray Diffraction was used to identify mineral phases by search-match procedures using STOE WinXPOW software containing the Powder Diffraction File PDF-2 supplied by the International Centre for Diffraction Data (ICDD); 2) Panalytical ExPert Pro MPD and preparation of the samples: X-ray powder patterns for phase quantification (QPA) were collected on a PANalytical X'Pert Pro MPD scanning diffractometer prior to Rietveld mineralogical phase analysis. Measurements were made in reflection geometry with the pressed powder mount spinning at 1 rotation per second. Some of the samples were spiked with 10% Silicon standard. Cu (or Co) Kα1 radiation was selected using a germanium 111 single-crystal monochromator (45kV, 40mA). Data were collected between 3 and 120° 2θ in continuous scanning mode (0.02° step size), on an X'Celerator RTMS detector. The instrument was controlled using X'Pert-Pro software (version 1.9E), accompanied by X'Pert Data Collector (version 2.2 h) application software. For the Fe-rich samples data was additionally collected using Co Kα1 radiation and a Fe filter (0.016 mm thickness) was placed in front of the detector. Some of the samples were spiked with a 10% Silicon standard. Detection limit is 2%. The spectra were interpreted by the use of RayfleX software package (GE Inspection Technologies) XDATA program (part of the XDAL 3000 software package from Rich. Seifert & Co.) has been used to evaluate the obtained profiles and to permit the comparison with JCPDS-ICDD database. Regarding the analyses carried out with Co radiation, we have used for interpretation the XPowder software package.

Whole rock chemical analyses of major and minor elements for the same core samples were carried out on identical powder splits to those used for XRD analysis. These analyses were carried out at OMAC Laboratories Ltd (Co. Galway, Ireland). 30 g of pulp was used in each case for chemical analysis. After *aqua regia* digestion, the samples have been analyzed by multi-element inductively coupled plasma mass spectrometry (ICP-MS) for 46 element analysis in total (Al, Ca, Fe, K, Mg, Mn, Na, P, Pb, S, Zn, Ag, As, B, Ba, Be, Bi, Cd, Ce, Co, Cr, Cu, Ga, Ge, Hg, La, Li, Mo, Nb, ni, Rb, Re, Sb, Sc, Se, Sn, Sr,Ta, Te, Th, Ti, Tl, U, V,W, Y, Zr).

Stable isotope (C and O) analyses were conducted at the University of Erlangen-Nuremberg (Germany). Five concretionary smithsonite and six calcite specimens (2 calcites from the host rock and 2 sparry calcite crystals from hydrothermal veins, plus 2 sparry calcites associated to the supergene ore) sampled by hand picking, were analyzed. The powdered samples were allowed to react at least for 36 hours with 103% phosphoric acid at 70°C using a Gasbench II connected to a Thermo Finnigan Five Plus Isotope Ratio Mass Spectrometer. Carbon and oxygen isotope values are reported in per mil (‰) relative to V-PDB and V-SMOW, respectively, by assigning a $\delta^{13}C$ value of +1.95‰ and a $\delta^{18}O$ value of -2.20‰ to standard NBS19. Reproducibility was checked by replicate analysis of laboratory standards and was better than ± 0.07 ‰ (1σ) for both carbon and oxygen isotope analyses. Oxygen isotope values of dolomite and smithsonite were corrected using the phosphoric acid fractionation factors given by Kim et al. (2007), Rosenbaum and Sheppard (1986) and Gilg et al. (2008) respectively.

A first quantitative phase analysis (QPA wt%) was performed on the XRD patterns using the Rietveld method (Rietveld, 1969; Bish and Howard, 1988; Bish and Post, 1993; Hill,

1991): X-ray powder diffraction data were analyzed using the GSAS package (General Structure Analysis System, Larson and Von Dreele, 1994, 2000) and its graphical interface EXPGUI (Toby, 2001). The XRD patterns were converted to ASCII format using ConvX software.

Table 1: Location, depth and description of the core samples for License 5 and Penttagon area.

Sample no	Hole no	From (m)	To (m)	Total width mineralization intersected (m)	Descriptions
Hole from license area 5					
H2050	5DD002	6,54	10,51	7,67	crumbly, high oxidized (ligth brown)
H2051					crumbly, high oxidized (ligth brown)
H2052		25,1	31,35		crumbly, high oxidized (ligth brown)
H2053					crumbly, high oxidized (ligth red-brown)
H2054	5DD003	13,91	24,24	12,09	crumbly, high oxidized (ligth brown)
H2055		31,59	34,01		crumbly high oxidized (light brown)
H2056		48,5	49,6		muddy grey (smell of S if crushed)
H2071	5DD008	51,18	53,25	5,12	crumbly high oxidized (light-yellow /brown)
H2072					crumbly high oxidized (light brown)
H2073					crumbly high oxidized (light brown)
H2074	5DD009	50,3	56,38	11,88	crumbly high oxidized (light brown)
H2075					crumbly high oxidized
H2076		60,6	70,3		massive highly brecciated (pale grey) smell of S if crushed
H2077					massive highly brecciated (pale grey) smell of S if crushed
H2078	5DD013	186,3	190,2	5,01	massive highly brecciated (pale grey) smell of S if crushed
H2079					massive highly brecciated (pale grey) smell of S if crushed
H2080					crumbly high oxidized (light brown)
Hole from Pentagon license area					
H2057	PENDD004	1,17	3,9	2,41	crumbly (darker brown)
H2058					crumbly (brown)
H2059		9,8	11,9		crumbly (light brown)
H2060					crumbly (pale brown)
H2061	PENDD006	11,4	14,1	1,55	crumbly/ dry rock (pale brown)
H2062					crumbly/dry rock (light brown)
H2063					crumbly/ dry rock (pale brown)
H2064					crumbly/ dry rock (pale brown)
H2065	PENDD009	8,9	10,9	1,01	crumbly/dry rock (light brown)
H2066					crumbly/dry rock (light brown)
H2067	PENDD010	122,5	127,3	3,62	crumbly/dry rock (pale brown)
H2068					crumbly/dry rock (pale brown)
H2069					crumbly/dry rock (light brown)
H2070					crumbly/dry rock (light brown)

Chemical analyses have been used to validate the mineralogical results obtained by Rietveld calculation. Calculation were made for 5 major elements (Zn, Pb, Mg, Ca, Fe) considering the amounts of minerals Zn, Pb, Mg, Ca, Fe-bearing: smithsonite and hemimorphite were used for total Zn% calculation; cerussite and plumbo-jarosite for the calculation of total Pb%; dolomite for calculation of total Mg%; calcite and dolomite for calculation of total Ca%; goethite and lepidocrocite were used for calculation of total Fe%.

Stable isotopes analysis (C-O) has been carried out, in order to investigate the nature of the fluids involved in nonsulfide mineralization. We sampled 5 concretionary smithsonite (Sm2) specimens, 2 host rock limestones, 2 sparry calcite crystals from hydrothermal veins and 2 sparry calcite crystals from supergene veins. We were not able to isolate the generation of replacive smithsonite (Sm1), because of practical difficulties.

Stable carbon and oxygen isotope analyses were carried out at the University of Erlangen-Nurenberg, Germany.

QEMSCAN® analysis and SIP file

QEMSCAN® analyses were carried out on 10 core samples of the Hakkari deposit, selected from those already analyzed in the study of Santoro et al. (2013), each one corresponding to 1 m-long core interval. The samples have been chosen on the basis of their higher zinc content. The analyses as well as the sample preparation were carried out at the Camborne School of Mines (University of Exeter, UK).

Initial sample preparation (see *chapter* 2 for more detailed information on sample preparation) was carried out at the University of Naples (Italy) and then finished at the Camborne School of Mines, University of Exeter (UK). Twenty grams of the two most Zn-rich samples were chemically concentrated by heavy-liquid separation using Na-polytungstate, QEMSCAN® analysis was carried out using the fieldscan analytical mode with 10μm grid resolution to obtain distribution maps of the mineral phases and a database containing all the information on the statistical distribution of the particles, grain sizes, mineral association and quantitative analyses for each samples. The analyses were carried out at the Camborne School of Mines, University of Exeter, UK. The data acquisition and the data processing were conducted by iMeasure v. 4.2 and iDiscover v. 4.2 software packages, respectively (see *chapter* 2 for more detailed analytical parameters). The modal mineralogy is expressed in mass % (wt.%).

The discrimination of the mineral species is by a modified SIP file (Species Identification Protocol). For this study, it was necessary to modify the default SIP file (LCU5) containing common minerals, by adding the nonsulfide ore compounds already detected by Santoro et al. (2013) and other. The final SIP file includes minerals already identified, as well as other mineral species and mineral compounds newly detected during the QEMSCAN® analyses.

The SIP modification encountered many issues and required repeated processing to render the final SIP file (and hence the final data) to be reliable in terms of chemistry, imagery and value estimation. The chemistry of the mineral species set in the SIP file is in line with the average composition of each known mineral (Webmineral, www.webmineral.com), considered as ''*pure minerals*''; for those species not respecting the stoichiometry (e.g. Fe-dolomite, Zn-dolomite) it was necessary to use a SEM-EDS to determine their average chemistry. The entries in the SIP file have been inserted as single minerals or categories, on the basis of their chemistry. For the ''*impure*'' minerals (containing several, not so far recorded, elements) it was necessary to split the mineral phases in different entries.

Smithsonite and hemimorphite are rather pure at Hakkari, and have been inserted in the SIP as single "*pure*" phases (Table 2). Zincite (ZnO), hydrozincite [$Zn_4Si_2O_7(OH)_2 \bullet H_2O$] and willemite ($Zn_2SiO_4$) have not been detected at Hakkari, either from previous mineralogical work (Santoro et al., 2013), or from QEMSCAN® analyses. Dolomite was subdivided into three categories: dolomite (devoid of metallic elements), Fe-dolomite (Fe≤5 wt.%), and Zn-dolomite (Zn≤10 wt.%). Calcite was also subdivided into two entries: calcite (almost stoichiometric, locally containing small amounts of Mg), and Cd

calcite (cadmium enriched ≤10 wt.%). Low Pb can be also present ≤5%, but the Pb-calcite, which had been observed using SEM by Santoro et al. (2013), was not clearly detected by QEMSCAN®. The Fe-(hydr)oxides group contains goethite>>lepidocrocite. The Fe-(hydr)oxides were split in two categories on the basis of their Zn content: Fe-(hydr)oxides (barren in metallic elements) and Zn-bearing Fe-(hydr)oxides (Zn≤10 wt.%). In the category named "pyrite/Fe-(hydr)oxides/jarosite" are grouped all the mineral compounds consisting of oxidized phases of Fe, S and O, plus some trace elements ≤5 wt.% . Under the entry "cerussite" there is only the Pb carbonate phase.

Table 2: Explanation of mineral phases detected by QEMSCAN®

Mineral Category	Mineral Description
Background	All resin related/edge effects, Others.
Smithsonite	Any phase with Zn, O, C and maybe OH.
Hemimorphite	Any phase with Zn, Si, O, H and maybe OH.
Fe-dolomite	Any phase with Ca, Mg, O, C and low Fe (approx. ≤5%).
Calcite	Any phase with Ca, O, C. May include Mg-rich Calcite (low Mg approx. ≤5%).
Fe-(hydr)oxides	Fe oxides such as Goethite, Lepidocrocite and Fe-(hydr)oxides.
Cerussite	Any phase with Pb, C, O. May include traces of Anglesite.
Barite	Any phase with Ba, S, O.
Pyrite/Fe-(hydr)oxides/Jarosite	Any phase with Fe, S, O. May include low amount of trace elements (<5%).
Pyrite	Includes Pyrite/Marcasite.
Coronadite	Any phase with Ba, Al, Mn, Pb, V and O. Includes a minor category of a mixture of Kaolinite-Coronadite (fine grained).
Hetaerolite	Any phase with Zn, Mn, O.
Chalcophanite	Any phase with Zn, Mn, Fe, O, H.
Quartz	Quartz and other silica minerals.
Muscovite/Illite	Includes Muscovite Mica and Illite (Al, K, Si, O).
Kaolinite	Kaolinite/Halloysite/Dickite.
Mixed Zn phases	Any phase with Zn, Si, Al, Na, O, H. Can be variable. May include Fe, C. Sauconite and tiny Kaolinite mixed with Smithsonite/Hemimorphite may occur.
Chlorite	Chlorite/Clinochlore, any phase with Fe, Al, Si, and Fe, Al, Si, Mg, O.
Gypsum	Any phase with Ca, S, O. Includes Gypsum and maybe Anhydrite.

The entry "mixed Zn-phases" includes all the phases containing Zn, Si, Al, Na, O, H, Fe, C and K. The Zn-smectite (sauconite) is the main phase in this category, together with tiny mixtures of kaolinite, smithsonite and hemimorphite. Further SEM-EDS analyses were carried out to resolve the issues linked to the scanning of small areas between two different minerals (boundaries). The presence of Fe-hydroxides intergrown with dolomite and Fe-dolomite had been previously considered as ankerite. The same is true for "Zn-ankerite" (most probably a mixture of very tiny smithsonite grains and Fe-dolomite). These values have been corrected after SEM-EDS validation.

QEMSCAN® mineralogical results have been compared with those of chemical analyses (ICP-MS) published in Santoro et al. (2013). The wt.% of 5 major elements (Zn, Pb, Mg, Ca, Fe) was calculated considering the amounts of Zn, Pb, Mg, Ca, and Fe-bearing minerals: smithsonite, hemimorphite, sphalerite, hetaerolite, chalcophanite, sauconite, Zn-dolomite (considering values around 10 wt.% Zn), Zn-rich Fe(hydr)oxides

(considering values around 8 wt.% Zn) and pyrite/Fe-(hydr)oxides/jarosite (5 wt.% Zn) for the calculation of total Zn%. For the calculation of total Pb% cerussite/anglesite, galena, coronadite and Pb-rich Fe-(hydr)oxides (around 5 wt.% Pb) were used. Dolomite, Fe-dolomite (with 20 wt.% Mg) and Zn-dolomite (with 14 wt.% Mg) was used for calculation of total Mg%. The total amount of Ca was calculated on the basis of calcite, dolomite, gypsum, Fe-dolomite (with 29 wt.% Ca) and Zn-dolomite (with 29 wt.% Ca). Fe-(hydr)oxides (i.e. goethite), Zn-rich Fe-(hydr)oxides (with 56 wt.% Fe), pyrite, chalcophanite and Fe-dolomite (with 1 wt.% Fe) were used for the total Fe% calculation.

3. 7. Results: Mineralogy and Petrography

Here follows a mineralogical and petrographic description of the minerals identified by OM, CL, SEM-EDS, and WDS analyses. WDS results for a few selected samples of smithsonite, hemimorphite and Fe-(hydr)oxides are shown in tables 3, 4, 5, while in table 6 are reported the EDS analytical data for the other detected mineral phases. Most data have been published in Santoro et al. (2013).

The most important economic and uneconomic mineral phases occurring at Hakkari were subdivided into four categories:

➢ Zinc nonsulfides
➢ Lead nonsulfides
➢ (Hydr)oxides
➢ Gangue and others

Zinc nonsulfides (carbonates and silicates)

These consist mainly of smithsonite ($ZnCO_3$) and hemimorphite [$Zn_4Si_2O7(OH)_2 \cdot H_2O$)]. Under cathodoluminescence microscope (CL), smithsonite shows two distinct generations with different colors. An earlier smithsonite (Sm1) generation (possibly replacing primary sulfides, and locally associated with Fe-(hydr)oxides, occurs in agglomerates of perfectly zoned concretions with a dark-red luminescence (Figures 3.10a, b). A second (Sm2) generation, growing as globular cryptocrystalline rims at the boundaries of druses and cavities, has a dark blue CL (Figures 3.10 c, d).

3D SEM images of smithsonite show that this mineral occurs as rhombohedral crystals, in concretions consisting of rhombohedral individuals or concretions (Figures 3.11a, b), or as massive agglomerates with a "knitted" pattern (Figure 3.11c). The smithsonite generations varieties are also shown in 2D BSE images Figures 3.11d and e. Calcium and iron appear to be the main geochemical variable between the different smithsonite generations (confirmed by EDS and WDS analyses). Smithsonite Zn–C–O ratio is always stoichiometric at Hakkari, although traces of other elements have been also detected: some smithsonites, in fact, contain small amounts of Fe (up to 1.6wt. % FeO) and Pb (up to 0.60 wt. % PbO), while Cd is very scarce (up to 0.2 wt.% CdO). Ca content in smithsonite is quite low, and can vary from 0.3 up to 2.40 wt. % CaO (table 3). The presence of CaO may reflect the fact that the calcite host rock is not completely replaced by smithsonite. Smithsonite is commonly replaced by hemimorphite (Figure 3.11f) and Fe-(hydr)oxides.
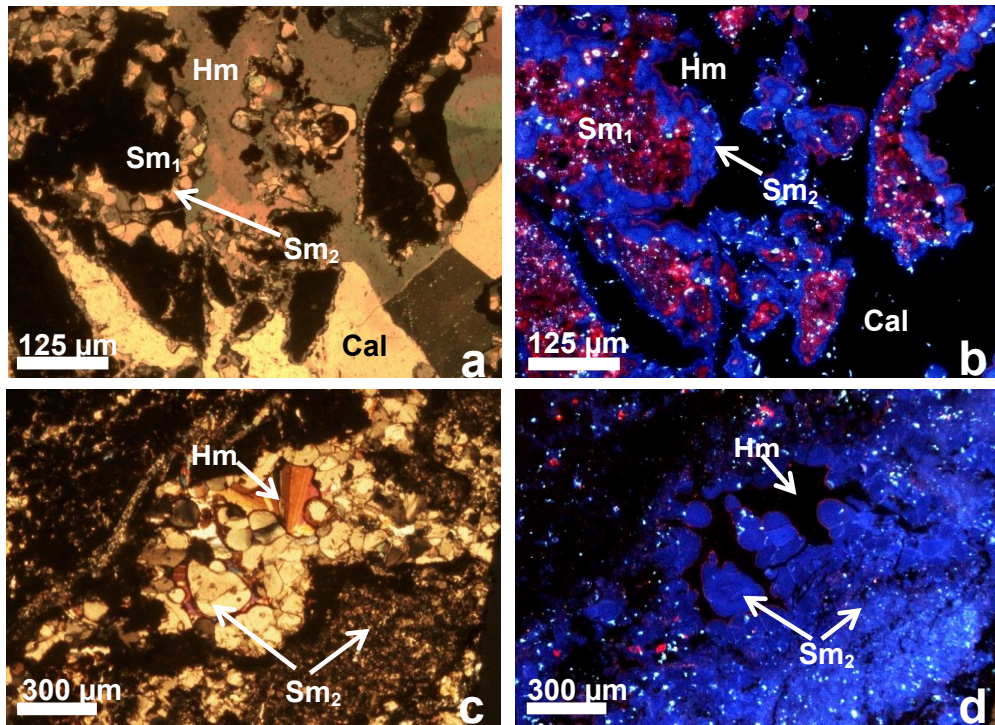
Figure 3.10: H2070: a) and c) smithsonite agglomerate in two generations: the older one (Sm1) is mixed with Fe-(hydr)oxides, the other (Sm2) is rather pure. The cement consists of sparry calcite and hemimorphite; thin section, N+; b) and d) under CL the Sm1 generation shows red luminescence colors, whereas Sm2 has blue luminescence. Sparry calcite and hemimorphite are not luminescent (Santoro et al., 2013).
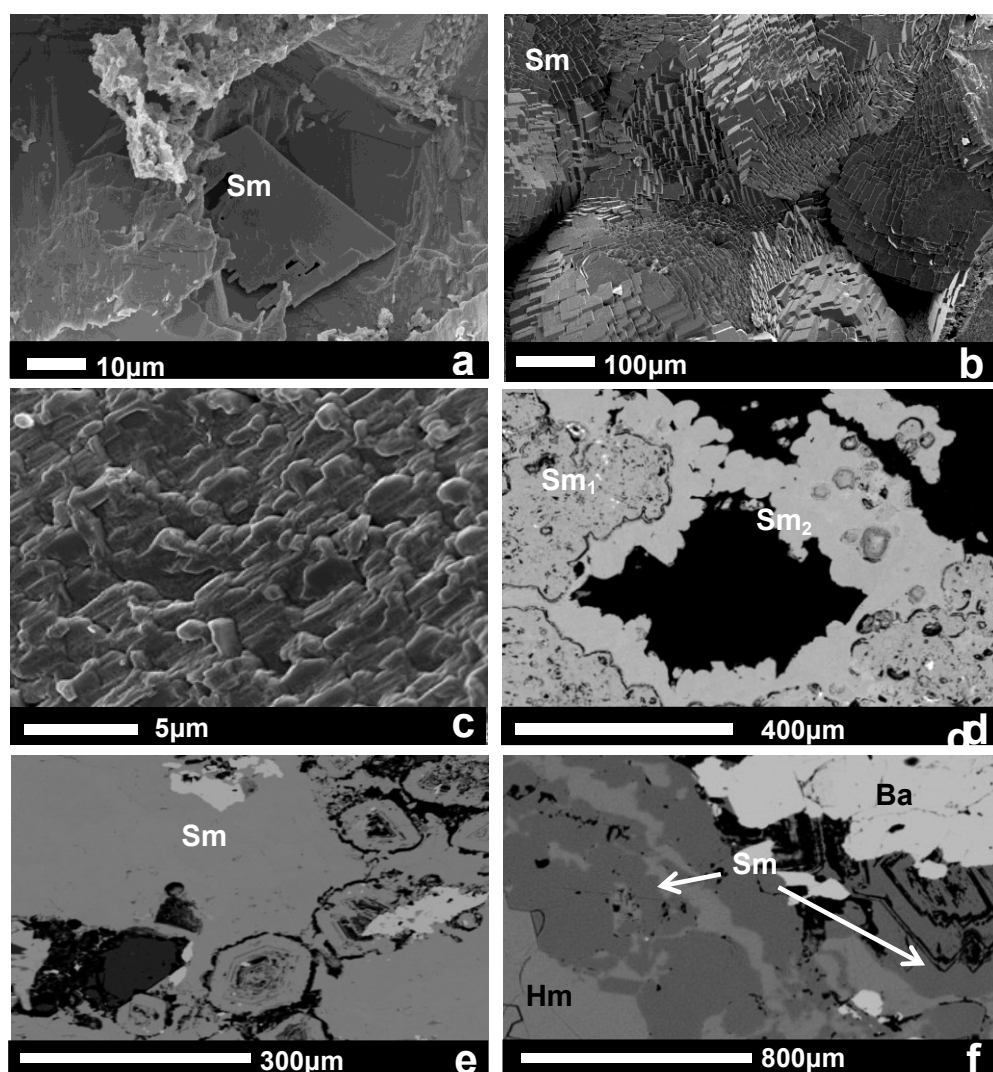
Figure 3.11: Scanning Electron Microscope 3D and 2D-images. a) H2065: smithsonite rhombohedron; b) H2066: globular concretions consisting of flat smithsonite crystals; c) H2065: smithsonite in a "*knitted*" pattern; d) same as c; e) H2067: smithsonite generations Sm1 and Sm2; f) H2070: H2070: hemimorphite replacing smithsonite layers. Top right: barite (Santoro et al., 2013).

Table 3: Wavelenght Dispersive Spectrometry (WDS) analyses of smithsonite

Sample	CaO	FeOt	ZnO	CdO	MgO	MnO	PbO	CO$_2$[1]	Total
H2067	1.11	n.d.	62.16	n.d.	n.d.	n.d.	0.12	34.66	98.05
	1.96	0.35	60.72	n.d.	n.d.	n.d.	n.d.	34.74	97.77
	1.53	n.d.	63.02	n.d.	0.13	n.d.	n.d.	35.27	99.93
	0.86	1.62	60.81	n.d.	0.51	0.22	0.50	35.48	99.98
	1.61	0.31	61.73	n.d.	0.16	n.d.	0.43	35.02	99.50
H2068	0.33	0.02	64.56	0.12	0.05	n.d.	0.49	35.40	100.97
	0.35	0.01	64.96	0.14	0.11	0.01	0.35	35.67	99.93
	0.41	0.02	64.73	0.02	0.04	n.d.	0.63	35.57	99.94
	0.31	n.d.	63.78	0.17	n.d.	n.d.	0.44	35.03	99.73

[1]calculated from stoichiometry; all results are expressed in oxides wt%; n.d.= not detected

Hemimorphite generally occurs as elongated lath-shaped crystals in cavities (Figures 3.12a and b), or it is replacing patchily smithsonite and/or other carbonates (Figures 3.12c, d and e). Locally, hemimorphite can also occur as zoned, globular-shaped concretions (Figure 3.12f) in association with Fe-(hydr)oxides, or filling veinlets and cavities in the massive nonsulfide ore. Hemimorphite does not show luminescence under CL microscopy (Figures 3.10b, d). Hemimorphite is rather pure at Hakkari: combined SEM-EDS and WDS analyses revealed that this mineral only contains small amounts of Fe (up to 3 wt.% FeO) and As (up to 0.8 wt.% AsO). Traces of Mn and Pb have also been detected in few samples (table 4).

Lead nonsulfides (carbonates)
The Pb minerals occurring in the Hakkari samples are scarce; they mainly consist of cerussite ($PbCO_3$), detected in small patches and locally as newly formed crystals in association with Fe-(hydr)oxides (Figures 3.12 g, h) Cerussite occurs in few specimens and, where present, it contains small amount of barium (up to 0.6 wt.% BaO) and locally zinc (up to 2 wt.% ZnO). No Pb-sulfates or galena were found in the samples examined in this study.
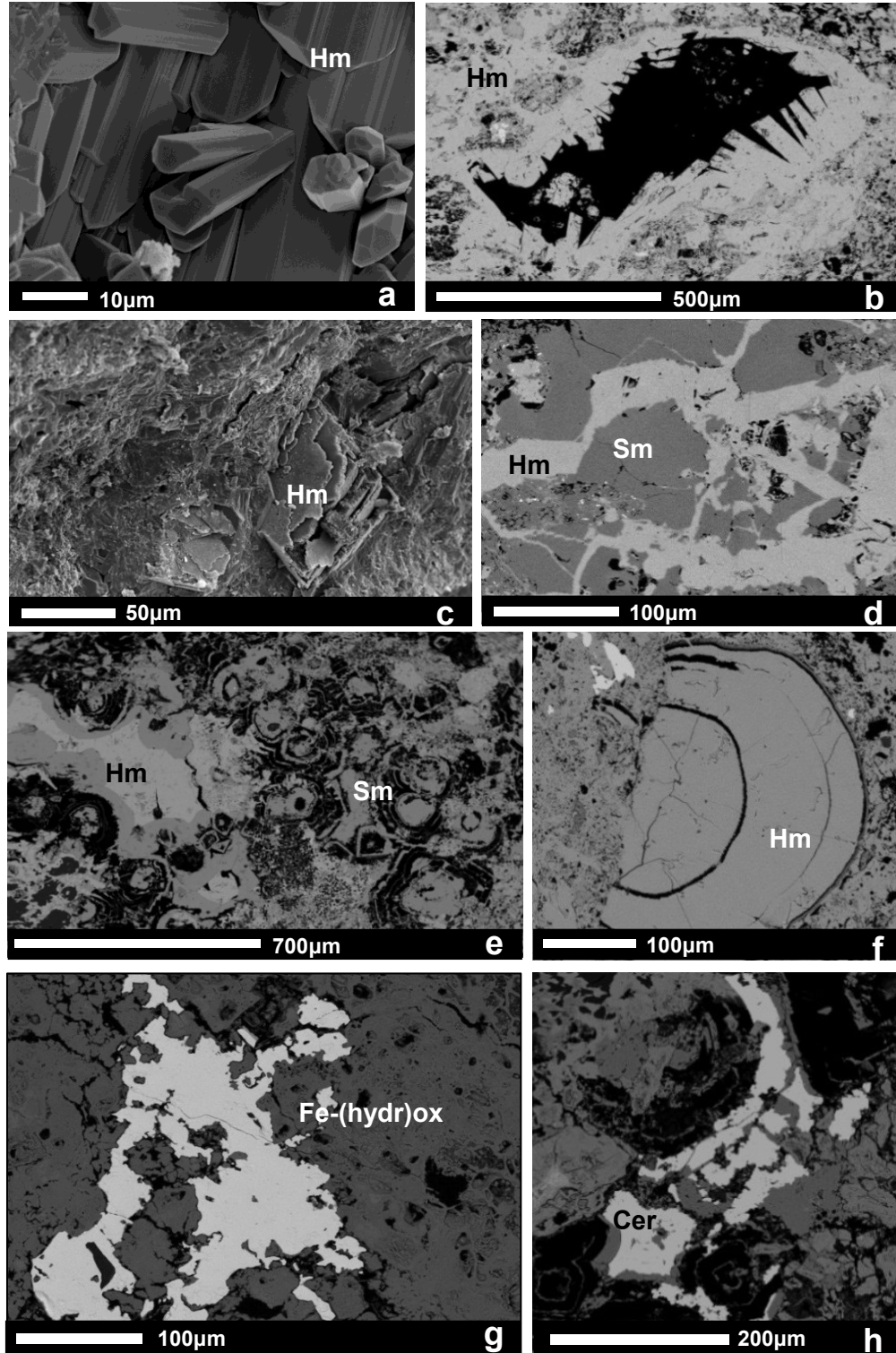
Figure 3.12: Scanning Electron Microscope 3D and 2D-images. a) H2062: hemimorphite crystals in cavity; b) H2058: hemimorphite crystals in cavity; c) H2062: hemimorphite replacing a smithsonite rhombohedron; d) H2070: hemimorphite veins cutting and partly replacing smithsonite; e) H2058: hemimorphite replacing smithsonite concretions; f) H2062: globular-shaped hemimorphite concretion; g) and h) H2058: cerussite and Fe-(hydr)oxides (Santoro et al., 2013).

Table 4: Wavelenght Dispersive Spectrometry (WDS) analyses of hemimorphite*

Sample	FeOt	ZnO	CdO	AsO	SrO	SiO_2	Total
H2068	0.03	73.31	n.d.	n.d.	n.d.	26.72	100.01
	0.05	75.63	0.05	n.d.	n.d.	24.99	100.66
	0.01	73.62	n.d.	n.d.	n.d.	26.31	99.90
H2065	0.06	70.45	0.18	0.49	0.71	26.29	98.18
	0.21	71.46	n.d.	0.83	0.61	26.09	99.21
H2070	0.19	71.58	0.18	0.51	0.68	26.26	99.40
	0.21	72.01	0.58	0.60	0.58	24.90	98.88

*all results are expressed in oxides wt%; n.d. = not detected

Fe- and Mn-(hydr)oxides

(Hydr)oxides are abundant in the Hakkari samples. Hard to distinguish under OM-CL, they are well recognizable under SEM-EDS, WDS. Generally, they have a concretionary and/or spongy texture (Figure 3.13a), and locally occur as vein fillings and crusts. Fe-(hydr)oxides can also be associated with smithsonite concretions (Figure 3.13b). The majority of them consist of Fe-(hydr)oxides like goethite in crusts (Figure 4.13c) or as intricate frameworks directly replacing pyrite (Figures 3.13d, e) and minor amounts of lepidocrocite. However, they are usually also enriched in other metals and Si. The Mn-(hydr)oxides are scarce and spongy, but they can be also perfectly zoned (Figure 3.13f). Fe and Mn-(hydr)oxides commonly contain high values of zinc and other metallic elements: zinc content in Fe-(hydr)oxides, for instance, ranges from 2 to 10 wt.% ZnO; lead (up to 5 wt.% PbO) and silica (from 3 to 10 wt.% SiO_2) are also commonly present. Iron is the main component in Fe-(hydr)oxides and generally ranges from 50 to 70 wt.% FeO. Arsenic (around 1–2 wt.% As_2O_3), as well as variable contents of antimony (Sb_2O_3), have also been detected in the (hydr)oxides. Mn-(hydr)oxides occur only in few samples: they have been detected using combined SEM-EDS analyses, but not any specific mineral has been found in the XRD patterns. The MnO content in the Mn-(hydr)oxides ranges between 22–26 wt.%. Other concurring elements are iron (6.50–7.50 wt.% FeO), silica, which is much lower than in the Fe-(hydr)oxides (1 wt.% SiO_2), and zinc (ranging from 3.7 to 6 wt.% ZnO). The Mn-(hydr)oxides are generally highly enriched in lead (25–30 wt.% PbO). Arsenic, silver, and cadmium have also been detected in traces (see Tables 5a and b). In many samples, high volumes of amorphous phases have been tentatively detected by QPA. Most of these phases can be attributed to poorly crystalline iron minerals.
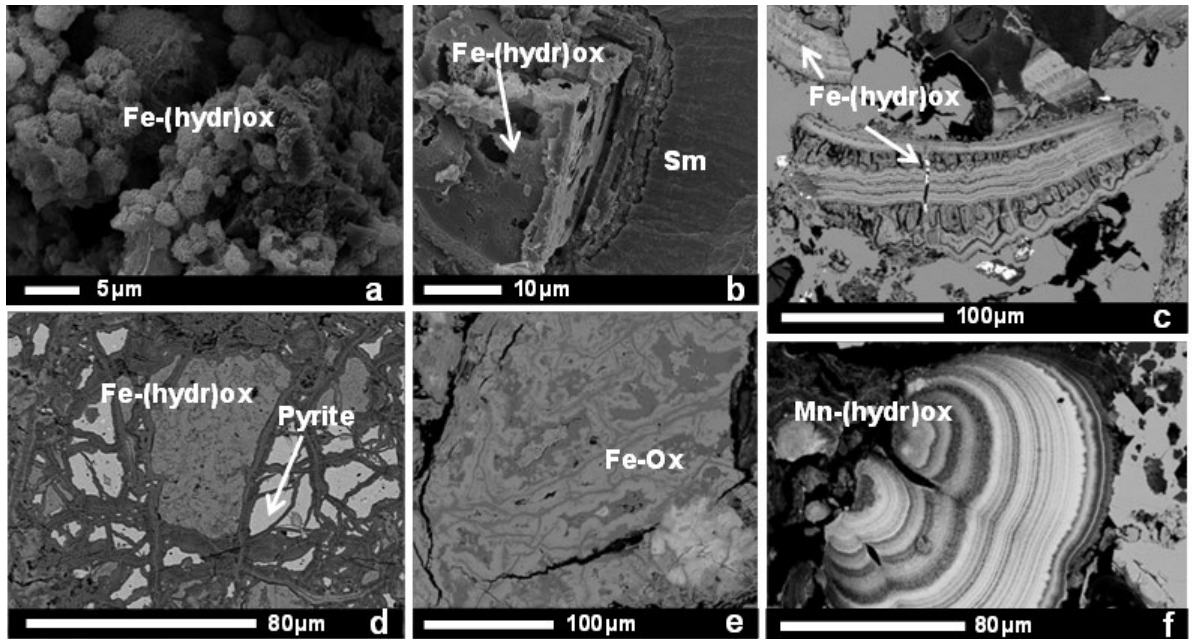
Figure 3.13: Scanning Electron Microscope 3D and 2D-images. a) H2061: Fe-(hydr)oxide concretions; b) H2067: Fe-(hydr)oxide replacing Smithsonite; c) H2070: zoned Fe-(hydr)oxides crusts in smithsonite; d) H2058: Fe-(hydr)oxides framework replacing pyrite; e) same as d; f) H2057: zoned Mn-(hydr)oxides concretion, strongly Pb-enriched (Santoro et al., 2013).

Table 5a: Wavelenght Dispersive Spectrometry (WDS) analyses of Fe-(hydr)oxides

Sample	FeOt	ZnO	CdO	AsO	MnO	PbO	AgO	SiO_2	Total
H2051	59.06	5.34	n.d.	1.16	0.01	4.01	n.d.	5.52	75.11
	58.52	5.42	0.28	1.41	n.d.	3.07	n.d.	4.41	73.11
	61.65	5.63	0.15	0.91	n.d.	3.66	n.d.	5.52	77.52
H2059	56.57	6.58	0.09	0.49	0.36	0.33	0.04	5.99	7.45
	75.14	3.93	0.25	n.d.	0.37	0.06	0.08	3.51	8.15
H2067	52.26	10.44	n.d.	0.35	0.03	0.76	0.03	6.93	70.89
	59.61	7.55	n.d.	0.31	n.d.	0.99	0.05	3.34	71.92

*all results are expressed in oxides wt%; n.d = not detected

Table 5b: Energy Dispersive Spectroscopy (EDS) Analyses of Mn-(hydr)oxides

	MnO	CaO	SiO_2	CdO	FeO	PbO	ZnO	AsO	SrO	AgO	Total
H2062	25.23	0.29	0.95	0.31	6.68	27.50	3.91	0.05	0.14	0.44	65.50
	22.6	n.d.	0.76	0.07	6.50	25.20	3.83	0.30	0.14	n.d.	59.40
	22.74	0.32	0.92	0.37	7.46	26.41	3.71	0.39	0.23	0.21	62.76
	26.22	0.15	0.86	n.d.	7.40	29.92	6.26	0.15	n.d.	n.d.	70.96

*all results are expressed in oxides wt%; n.d = not detected

Gangue and host rock minerals

Calcite is the main component of the host rock (thinly laminated limestone: Cal1), and occurs also as cement in the hydrothermal breccia (Cal2) (Figure 3.14a). Two more calcite generations (Cal3 and Cal4) are associated with the nonsulfide minerals (Figure 3.14b): they occur in small cavities, and do not show any luminescence under CL light. The occurrence of four calcite types has also been confirmed by combined SEM-EDS

analyses. The first type, dark gray in color (Cal1, Figure 3.14a), represents the host limestone. It is almost pure, mostly barren of metals, and has only local Mn- and Fe-enrichments (up to 0.9 wt.% MnO and up to 0.5 wt.% FeO). The second calcite type (Cal2, Figure 3.14a), representing the calcite cement of the primary hydrothermal breccia, is moderately Pb-enriched (up to 5.0 wt.% PbO) and contains traces of MgO. The third and fourth calcite generations grow at the rim of the cavities in the supergene ore and are associated to the nonsulfide mineral phases. The third calcite type (Cal3, Figure 3.14b) is highly enriched in lead (up to 6.90 wt.% PbO) and in cadmium (up to 10 wt.% CdO). Zinc (up to 1 wt.% ZnO) is commonly present in both the third (Cal3) and fourth (Cal4) (Figure 3.14b) calcite generation, as they are commonly related with hemimorphite and smithsonite. The element content of all the calcite types is reported in table 6.

Barite is a minor component but is commonly observed in a number of core samples. It occurs either as fragmented remnants of a likely primary mineral association (Ba1, Figure 3.14c), or as neoformed small laths and needles (Ba2) precipitated together with the oxidation minerals (preferentially smithsonite and hemimorphite) (Fig. 14d). The two barite types occurring at Hakkari do not differ in their elements content: they usually have low zinc values (up to 2.70 wt.% ZnO) and lead (up to 1.90 wt.% PbO) and are poor in strontium (about 1 wt.% SrO).

Pyrite has been detected only in traces. In the sample H2060 a fair amount of (detrital?) muscovite/sericite (15 wt.%) and some chlorite (3.50 wt.%) have been measured. Traces of descloizite [$(Pb,Zn)_2(OH)VO_4$], generally associated with hemimorphite have been detected in few samples. Quartz is also relatively scarce. Sphalerite and galena have been identified only in traces (table 7).

Dolomite [$CaMg(CO_3)_2$], is much less abundant and occurs mainly as detrital clasts. Dolomite has stoichiometric ratios; only low traces of iron, cadmium, antimony, manganese, lead and silica have been detected (always<1wt.%) (table 6). F-apatite has been observed locally (max 2 wt.%).
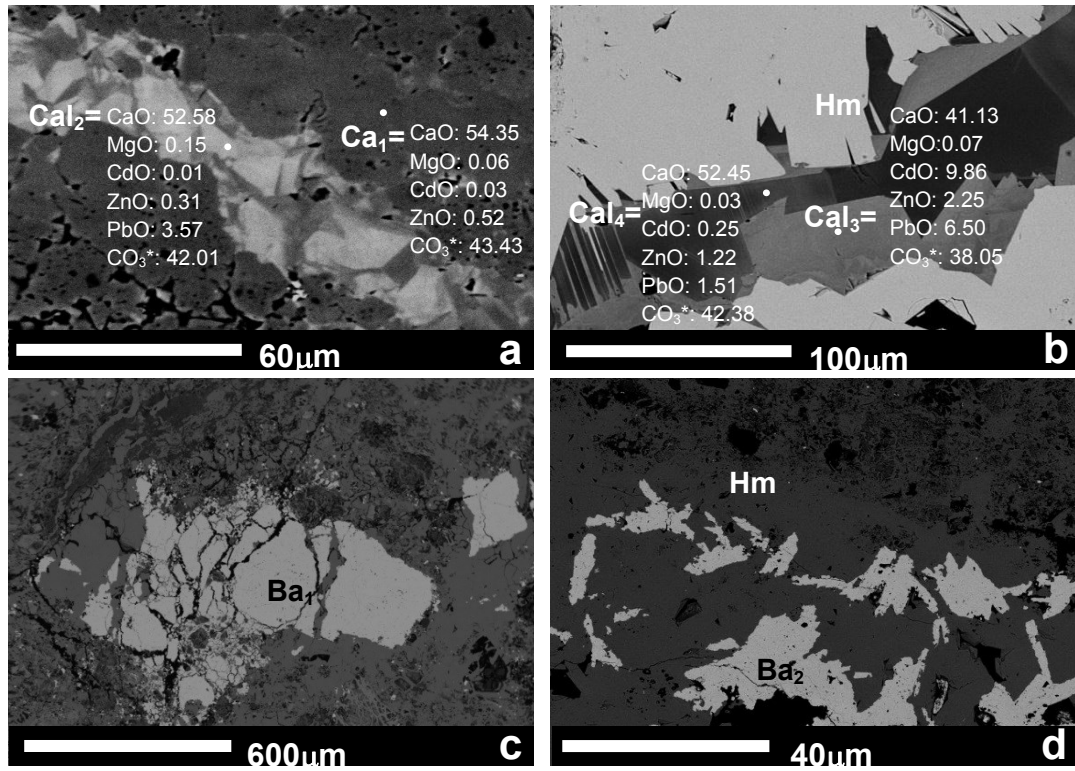
Figure 3.14. Scanning Electron Microscope 2D-images. a) H2076: H2076: host rock calcite (Cal1), cut by Pb-rich calcite veinlets (Cal2); b) H2062: calcite veinlet in hemimorphite ore: Cal3 contains up to 7% Pb and 10% Cd, Cal4 is quite barren; c) H2070: barite (Ba1) fragment surrounded by Fe-(hydr)oxides and cut by smithsonite veinlets; d) H2062: hemimorphite-hosted barite (Ba2) microcrystals (Santoro et al., 2013).

Table 6: Energy Dispersive Spectroscopy (EDS) Analyses of calcite

		CaO	*MnO*	*MgO*	*ZnO*	*PbO*	*CdO*	*CO_2[1]*	*Total*
Calcite 1	H2065	56.01	0.24	n.d.	n.d.	n.d.	n.d.	44.15	100.39
	H2067	55.39	n.d.	0.17	n.d.	n.d.	n.d.	43.71	99.27
	H2076	54.61	0.94	n.d.	n.d.	n.d.	n.d.	43.48	99.01
Calcite 2	H2062	50.63	n.d.	0.11	0.50	5.90	n.d.	41.36	98.50
	H2076	52.58	n.d.	n.d.	n.d.	3.57	n.d.	42.02	98.20
Calcite 3	H2062	41.13	n.d.	0.07	1.79	6.50	9.86	38.51	97.85
		41.56	0.14	0.11	1.22	6.86	10.35	38.56	98.80
Calcite 4	H2062	52.45	n.d.	0.03	1.22	1.51	0.25	42.38	97.84
		53.01	0.05	0.24	1.16	0.39	0.31	42.80	97.96
	H2067	52.87	n.d.	n.d.	2.31	1.44	n.d.	43.58	99.23
		52.15	n.d.	0.14	5.15	n.d.	n.d.	42.15	99.59

[1] calculated from stoichiometry; all results are expressed in oxides wt%; n.d. = not detected

Table 7: Energy Dispersive Spectroscopy (EDS) Analyses of barite and dolomite

	Barite					Dolomite		
	H2059	H2060	H2062				H2051	H2076
BaO	60.06	62.39	61.54	61.22	61.64	*MgO*	19.97	20.33
SiO₂	0.34	n.d.	n.d.	0.32	0.18	*CaO*	30.34	30.8
SO₃	33.65	33.21	34.84	33.16	33.13	*SiO₂*	0.28	0.35
PbO	1.29	1.49	1.8	1.13	1.21	*Sb₂O₃*	0.53	n.d.
ZnO	0.42	2.75	n.d.	0.58	0.37	*CdO*	0.22	n.d.
SrO	0.92	n.d.	1.33	0.9	0.69	*PbO*	n.d.	n.d.
FeO	1.16	0.26	n.d.	n.d.	n.d.	*ZnO*	0.11	n.d.
V₂O₃	0.23	n.d.	n.d.	0.5	n.d.	*MnO*	0.06	n.d.
						FeO	0.16	n.d.
						CO₂[1]	45.92	46.31
Total	98.07	100.01	99.51	98.81	97.22	*Total*	97.66	97.8

[1] calculated from stoichiometry; all results are expressed in oxides wt%; n.d. = not detected

3. 8. Results: Geochemistry

Chemical analyses

In Table 8 are listed the results of the chemical analyses carried out on the representative fractions of the core samples. The analyses are comprehensive of major element (expressed in wt.%): Ca, Fe, Mg, Mn, Pb, S, Zn; and minor elements (expressed in ppm): Ag, As, Ba, Cd, Cr, Cu, Hg, Mo, Ni, Sb, Sr, Tl, V.

The contents can be matched with XRD quantitative Rietveld phase analysis (QPA). Among the most abundant elements, Ca is higher in calcite-rich samples (H2054, H2059, H2067 and H2079), whilst Mg is high only in few dolomite specimens.

Zinc occurs with high values (ranging from 2 to 45 wt.%) in the core interval going from H2060 to H2070. The highest zinc content detected so far (45.60 wt.% Zn) is in sample H2069 and in sample H2068 (42.60 wt.% Zn). Consistent with the chemical analyses, Fe is the most abundant element in all mineralized samples (generally ranging between 2 and 50 wt.%, with average values around 30 wt.%). Locally the Fe amount can be >50wt.% (in the samples H2052, H2058, H2072, H2074, H2075). A small amount of zinc is always contained in the Fe-(hydr)oxides. Lead is less abundant at Hakkari, with values ranging between 0.30 and 9.50 wt.%. The highest values have been detected in the samples H2050, H2055, H2058 and H2061. Lead is mainly contained in the Mn-(hydr)oxides and in cerussite ($PbCO_3$). Barium can be quite abundant, ranging from negligible values in the barren carbonate rocks, up to 12 wt.% in the mineralized samples. Regarding the minor elements content: Ag (<5–88 ppm) is generally not correlated with Pb, with the exception of the samples H2055, H2061, H2065, H2068 and H2079, where Ag follows the relatively high Pb values. Copper is negligible in all samples (never reaching 50 ppm), as it is the case for many other metals (Ni, Cr etc.). Variable V amounts have been detected locally, with maximum values in the samples

H2052 (226 ppm), H2057 (253 ppm) and H2071 (252 ppm). These values are related to the small descloizite occurrences, associated with hemimorphite.

Table 8: Chemical analyses of major and minor elements of the Hakkari samples

	Ca	Fe	Mg	Mn	Pb	S	Zn	Ag	As	Ba	Cd	Cr	Cu	Hg	Mo	Ni	Sb	Sr	Tl	V
Sample n.					(wt.%)									(ppm)						
H2050	0.16	42.48	0.04	0.06	7.36	0.10	3.65	2.29	5128.89	32.86	49.57	11.50	13.02	15.14	170.32	14.21	805.70	90.22	83.25	90.91
H2051	9.07	27.60	5.20	0.17	3.72	0.08	2.41	3.86	4062.17	63.35	31.11	94.09	7.43	10.64	121.63	30.32	353.68	73.80	83.10	14.66
H2052	2.15	33.90	1.22	0.15	1.59	<.05	5.37	0.43	1091.35	98.22	42.36	48.57	38.97	3.44	47.47	56.38	25.50	72.22	63.35	225.70
H2053	1.35	41.45	0.12	0.78	0.25	0.55	4.85	2.77	656.20	5639.65	17.26	43.88	18.28	4.04	133.73	70.90	39.38	111.15	651.84	76.12
H2054	18.06	26.92	0.10	0.88	0.25	<.05	2.10	0.47	319.85	725.15	74.55	22.65	13.69	0.88	97.05	24.79	19.99	269.63	336.35	54.71
H2055	0.64	40.04	0.03	0.11	7.90	1.06	6.50	9.74	9549.81	47.75	40.02	53.91	14.46	3.13	154.51	9.69	926.37	38.92	556.68	20.82
H2056								0.78	131.12	336.76	109.14	15.05	9.59	5.64	36.83	30.78	24.08	299.70	62.03	48.60
H2057	1.92	6.79	0.45	2.52	2.46	0.05	29.79	1.58	688.81	447.40	1149.69	19.52	21.77	1.62	56.00	123.67	44.88	54.35	909.71	252.63
H2058	0.30	44.08	0.09	0.08	5.61	0.09	5.30	2.73	3605.02	44.13	51.92	49.34	8.47	22.56	173.36	27.10	140.72	40.45	93.02	29.69
H2059	10.28	28.00	0.21	0.94	0.38	0.41	3.82	6.38	1516.19	4820.77	71.93	49.73	25.37	5.69	99.35	129.68	61.51	220.92	598.09	93.08
H2060	0.68	6.63	0.31	0.03	0.88	1.14	15.90	4.19	496.54	6815.13	242.31	28.58	38.54	15.88	135.22	28.86	79.98	157.17	16.36	49.83
H2061	0.43	11.53	0.08	0.19	9.52	0.71	35.09	85.30	4815.46	1916.37	539.38	4.58	15.70	66.80	20.74	12.66	709.02	342.28	90.71	4.54
H2062	6.97	6.18	0.04	0.40	1.41	0.69	35.19	17.37	598.11	5389.40	691.89	5.79	46.80	64.69	327.97	11.62	101.46	85.47	119.58	9.08
H2063	7.49	5.10	1.59	0.46	0.57	0.71	30.45	7.11	130.57	5658.70	1063.23	<2	13.48	1.67	11.23	22.86	27.70	149.47	179.96	4.93
H2064	4.92	5.09	0.11	0.15	0.69	0.39	37.72	21.28	173.60	5348.43	114.17	5.37	13.67	4.08	11.61	9.77	20.25	151.22	62.72	7.45
H2065	0.05	12.20	0.01	0.08	2.32	0.17	40.89	22.61	2120.81	3567.87	33.14	11.38	12.70	6.63	108.35	8.17	18.58	28.61	60.22	6.38
H2066	0.54	31.39	0.10	0.63	0.48	0.09	21.22	1.36	1253.73	233.54	437.78	20.91	9.50	0.95	38.38	22.05	18.94	23.57	560.02	12.42
H2067	13.03	6.17	0.15	0.13	0.40	0.14	27.85	1.59	250.58	3336.12	85.50	<2	10.58	1.07	8.39	12.25	26.75	115.71	88.49	9.40
H2068	2.81	2.05	0.09	0.37	2.10	0.70	42.62	19.60	173.28	7265.83	834.31	<2	16.07	5.40	12.47	9.02	35.74	204.92	186.22	7.07
H2069	0.37	5.20	0.08	0.37	0.97	0.06	45.59	5.29	133.75	1900.10	1088.88	<2	13.85	14.97	8.87	12.33	43.93	45.03	146.10	6.85
H2070	0.25	13.25	0.06	0.01	2.04	0.79	31.86	9.61	1161.42	5732.97	411.51	16.20	13.83	45.51	243.35	12.20	73.80	100.67	43.51	16.08
H2071	0.11	37.54	0.08	0.03	1.15	<.05	2.80	0.42	2692.59	117.65	14.25	49.11	21.41	0.81	101.15	20.17	47.30	13.20	46.47	252.16
H2072	0.22	48.84	0.05	0.06	1.50	0.07	4.94	5.16	1571.60	60.30	63.43	52.08	12.62	5.51	170.69	45.26	70.89	21.55	132.03	23.34
H2073	0.16	37.59	0.29	0.05	0.22	<.05	2.17	2.41	1168.19	192.28	14.13	71.96	46.02	3.04	95.30	67.93	22.26	19.45	65.49	160.04
H2074	0.10	49.97	0.07	0.01	1.03	0.10	3.68	0.09	589.31	1754.59	46.76	7.63	5.04	0.33	146.73	29.81	14.29	28.11	104.39	4.40
H2075	0.60	46.62	0.15	0.06	0.36	0.32	4.51	2.76	2701.56	3047.35	11.65	72.50	15.88	5.79	180.12	39.26	47.07	72.95	164.17	70.61
H2076								1.82	272.96	54.60	70.24	9.75	4.15	7.64	7.26	3.71	89.07	292.85	7.74	7.91
H2077								1.09	639.12	76.34	17.51	19.42	30.10	2.13	43.35	17.95	50.97	244.40	10.33	84.91
H2078								0.97	15.94	2734.95	6.93	2.15	3.88	0.66	1.88	1.18	4.46	1188.37	1.57	13.31
H2079	33.87	2.59	0.22	0.13	1.02	0.43	2.33	47.13	427.66	5318.89	110.69	2.74	28.31	51.92	16.95	7.17	180.52	913.60	26.89	17.16
H2080	7.75	41.81	0.08	0.38	0.47	0.07	3.22	17.16	1907.66	236.03	48.79	12.82	12.50	41.90	145.77	14.57	33.93	30.79	125.09	27.51

It is interesting to note the high arsenic values occurring in some of the analyzed samples (table 8). These values range between 16 ppm (in pure limestone) and 9550 ppm in the mineralized cores, commonly averaging 1500 ppm. Antimony can be also anomalous (from 20 to 900 ppm): the highest values occur in H2050 (805 ppm), H2055 (926 ppm) and H2061 (710 ppm) (Table 2). Arsenic and antimony are moderately correlated and associated with Fe-(hydr)oxides.

Thallium is locally enriched at Hakkari, ranging between 7 to 910 ppm in the ore specimens (Table 8). The highest values have been detected in the samples: H2053 (652 ppm), H2054 (336 ppm), H2055 (556 ppm), H2057 (910 ppm), H2059 (598 ppm) and H2066 (560 ppm). Thallium values seem to be roughly correlated to Mn ones, as in other nonsulfide deposits (see Accha, Peru). Traces of Hg (up to 66 ppm) have been detected in some of the chemical analyses, although Hg residence has not been determined yet.

Stable isotope (carbon and oxygen) geochemistry
The results are based on several Zn-carbonates, as well as on calcite and dolomite samples. The samples originate from different drill cores and variable depths. The concretionary smithsonite samples were picked from samples H2061-H2063 (PENDD006), H2066 (PENDD006) and H2070 (PENDD010). Calcite host rock was measured in the samples H2076-H2077 (core 5DD009). Sparry calcite has been taken from samples H2062 and H2063 (core PENDD006) and samples H2076 and H2077 (core 5DD009).

In table 9 and Figure 3.15 are reported the $\delta^{18}O$ and $\delta^{13}C$ values of five smithsonites. The $\delta^{18}O$ values of smithsonite lie in a restricted interval comprised between 24.2‰ and 25.3 ‰ VSMOW. On the contrary, the $\delta^{13}C$ values are variable and range from -3.36‰ to -6.03‰ VPDB. These values are comprised in the characteristic $\delta^{13}C$ interval of supergene smithsonites (Gilg et al., 2008): they were encountered also in other supergene ore districts worldwide.

The $\delta^{18}O$ and $\delta^{13}C$ values for three calcite types are considered separately. The $\delta^{18}O$ values of the host rock limestone at Hakkari are around 24.9‰ VSMOW, whereas the $\delta^{13}C$ values range between −0.6‰ and −2.5‰ VPDB.

Sparry calcite from veins cutting the host rock shows a limited range of values for $\delta^{18}O$ and $\delta^{13}C$, which are ranging between 21.36‰ and 21.63‰ VSMOW, and between −1.83‰ and −2.04‰ VPDB respectively. Sparry calcite precipitated together with supergene smithsonite shows similar $\delta^{18}O$ values as the previous veins (21.48‰ and 22.57‰ VSMOW), but lower $\delta^{13}C$ ratios (−5.87‰ and −7.35‰ VPDB).

Table 9: Carbon and Oxygen stable isotopes of Hakkari
carbonates (smithsonite and calcite)

	Sample	$\delta^{18}O$ VSMOW	$\delta^{13}C$ VPDB
Smithsonite	H2061	24.61	-5.09
	H2063	24.23	-5.06
	H2066	24.51	-3.36
	H2066	25.35	-6.03
	H2070	24.28	-5.80
Host calcite	H2076	24.92	-0.66
	H2077	24.88	-2.54
Hydrothermal calcite	H2077	21.36	-2.04
	H2076	21.63	-1.83
Supergene calcite	H2063	22.57	-7.35
	H2062	21.48	-5.87
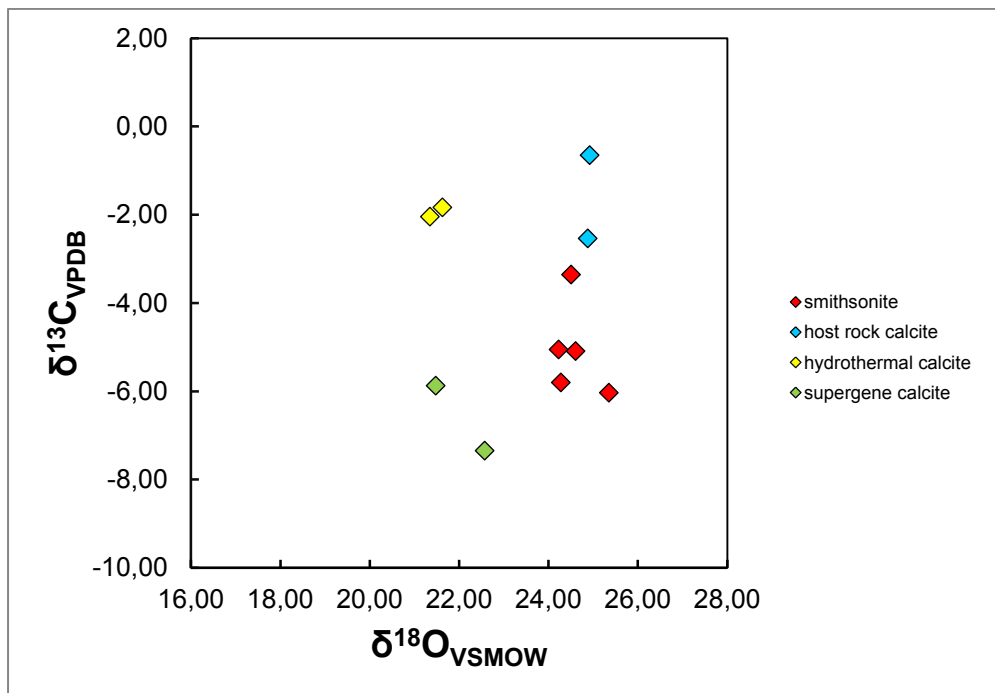
Figure 3.15: Carbon and Oxygen stable isotopes of Hakkari carbonates (smithsonite and calcite).

92

3. 9. Results: X-ray quantitative Rietveld phase (QPA)

The QPA analyses show that the best-mineralized samples (Zn≫ Pb) are those falling within the H2060 to H2070 core interval (table 10). This explains the high zinc values found in this interval. The principal economic minerals resulting from QPA are smithsonite (ZnCO$_3$, 52 wt.% Zn), up to ~86 wt% (H2069) and hemimorphite [Zn$_4$Si$_2$O$_7$(OH)$_2$H$_2$O, 54 wt.% Zn] up to 96 wt.% (H2065). Hydrozincite has not been detected in the core samples, but its presence was recognized in surface specimens (A. Clegg oral communication). Fe-(hydr)oxides (goethite and lepidocrocite) are abundant in almost all the samples ranging from few amounts (samples from H2060 to H2070) to up 80 wt.% (H2074).

In many samples with high iron content, a variable amount of not better-identified amorphous phases occur. It is possible, however, that part of the amorphous fractions correspond to non-crystalline silica phases. By SEM-EDS and WDS analyses (see *paragraph 3.7*) it resulted that most Fe-(hydr)oxides (as well as Mn-Pb-(hydr)oxides) are enriched in Zn. This is confirmed by chemical analyses shown in table 8, where are displayed variable % of zinc that are not only derived from the smithsonite- and hemimorphite-enriched samples.

Many analyzed core samples contain calcite, together with small amounts of dolomite. Quartz can have values ranging from <1% to 27 wt.%. Barite can be quite abundant, ranging from negligible values in the barren carbonate rocks, up to 12 wt.% in the mineralized samples. F-apatite has been observed in some samples (max 2 wt.%). Pyrite has been detected only in traces. In the sample H2060 a fair amount of (detrital?) muscovite/sericite (15 wt.%) and some chlorite (3.50 wt.%) have been measured.

Table 10: QPA-Rietveld of the Hakkari mineralized samples (H2050-H2080)

Sample n.	Sm	Hem	Cer	Cal	Dol	Qz	Ba	Lpc	Goe	F-Ap	Pb-Jrs	Ms	Chl	Py	Amorphous
								(wt.%)							
H2050						4.5			47.5		0.5				46.6
H2051			0.1		43.2	0.6			35.1						21.1
H2052					11.9	5.3		1.6	60.1			6.9			14.4
H2053				3.7		3.2	2.5		46.3						43.3
H2054				52.1					38.3						8.9
H2055		5.2	1.1	1.8					53.1		5.6				33.3
H2056				95.6	0.5	3.2			0.7						
H2057	45.1	27.1			7.2	17.7		0.7		2.3					
H2058		1.2	0.6			1.1			59.4						37.9
H2059				24.8		9.1	1.8		34.9			5.1			24.4
H2060	16.8	18.7			5.8	26.8	13.1					15.3	3.5		
H2061	57.5	26.1	8.4				2.2	1.4	4.4						
H2062	8.7	63.8		21.5			5.6	0.5							
H2063	61.6	3.6		14.5	12.7	1.4	6.2								
H2064	3.1	70.5		20.8			5.3	0.4							
H2065	2.1	96.3					1.6								
H2066	30.5	5.6				0.7			37.1						25.6
H2067	55.2	3.7		37.7	1.1	1.1			1.1						
H2068	54.5	32.2	0.9	7.8			4.5								
H2069	86.9	12.1						1.1							
H2070	51.7	15.6				25.5	6.2	1.1							
H2071						8.6			49.6			7.9			33.3
H2072						0.1			70.4						29.6
H2073						6.1			50.1			7.4	0.2		35.6
H2074									80.3						19.7
H2075				1.33		2.55	1.66		66.67						27.79
H2076				94.96	5.04										
H2077				75.01	2.22	0.08			22.01					0.04	
H2078				89.96	8.65	1.41									
H2079		2.59	0.26	93.89		1.77	1.49								
H2080				19.01					48.01						32.02

Sm = smithsonite, Hem = hemimorphite, Cer = cerussite, Cal = calcite, Dol = dolomite, Qz = quartz, Ba = barite, Lpc = lepidocroicite, Goe = goethite, F-Ap = fluoroapatite, Pb-Jrs = plumbojarosite, Ms = muscovite/sericite, Chl = chlorite, Py = pyrite.

3. 10. Results: QEMSCAN® quantitative phase analyses (QPA)

Table 11 shows the quantitative mineralogy (wt.%) of the Hakkari samples, obtained with QEMSCAN® analyses. The meaning of each entry is displayed in Table 2. QEMSCAN® false color fieldscan images of the crushed samples are shown in Figure 3.16 and Figure 3.17 displays the values of the concentrated samples alongside those of the un-concentrated ones. Calcite, which is the prevalent host rock at Hakkari, is less abundant in the mineralized samples chosen for QEMSCAN® analysis. It occurs essentially as two main phases: as almost pure calcite (from few wt.% up to 12.96 wt.%), and as Cd-calcite. In the analyzed samples, the latter is rare but, if processed, it may affect the metal quality. Moreover, due to the toxicity of the element, even small amounts of Cd (ppb) can be considered detrimental to the environment and human health.

Dolomite is scarce in the whole deposit (Santoro et al., 2013), but can reach up locally to 7.60 wt.% (H2063). Fe-dolomite is in even lower percentages, as well as Zn-dolomite (maximum up to 1.56 wt.%). Smithsonite and hemimorphite are abundant in almost all the samples.Smithsonite ranges from a few percentages (in samples most enriched in Fe-(hydr)oxides), up to 57.41 wt.% (H2063). Hemimorphite, as smithsonite, can be quite abundant, up to 44.98 wt.% (H2064), whereas it is relatively scarce in most samples enriched in Fe-(hydr)oxides. The Zn mixed phases belonging to the category that contains sauconite (not previously detected by Santoro et al., 2013), and kaolinite mixed with smithsonite or/and hemimorphite, occur in traces, which hardly reach 1 wt.%, except for two samples (H2060 -up to 3.35 wt.% - and H2070 –up to 1.49 wt.%). Sphalerite is always <~1wt.%, except for the sample H2060 (2.63 wt.%). Although galena is generally absent, a few secondary Pb compounds (cerussite) locally occur; in some samples they are only in traces, whereas in others they can reach values of ~5-10 wt.% (Table 11). Fe-(hydr)oxides have been detected in all samples, and range from few percentages (~4 wt.%) to much higher amounts (up to 57.45 wt.% in sample H2058). The Zn-rich Fe-(hydr)oxides are quite abundant, even if in minor percentages compared to the Zn-barren (hydr)oxides. The latter occur in variable quantities, and reach 20.86 wt.% in the sample H2066. Remarkable amounts of mixed pyrite, Fe-(hydr)oxides and jarosite (Pb-bearing) have also been detected: they range from low percentages (around 1 wt.%), to much higher amounts (up to 23.94 wt.%). Barite can be quite abundant (up to 15.61 wt.%, in sample H2060). Detrital quartz (Santoro et al., 2013) hardly reaches 1 wt.%, except in the sample H2060, where it is ~15 wt.%. Muscovite/illite occur in traces, with the only exception of sample H2060, where they reach 8.51 wt.%. Among the mineral species detected in traces, there are: hetaerolite, coronadite, chalcophanite, chlorite and kaolinite. QEMSCAN® analyses on the ore mineral concentrates showed, as expected, higher values for most Zn-Pb phases (e.g. smithsonite, hemimorphite), and lower contents of gangue minerals (e.g. dolomite, calcite) (Table 11). However, despite the effectiveness of the concentration process, the gangue mineral phases were not completely removed. In fact, many particles in the concentrate samples consist of economic minerals lying within or strictly adherent to gangue mineral phases.
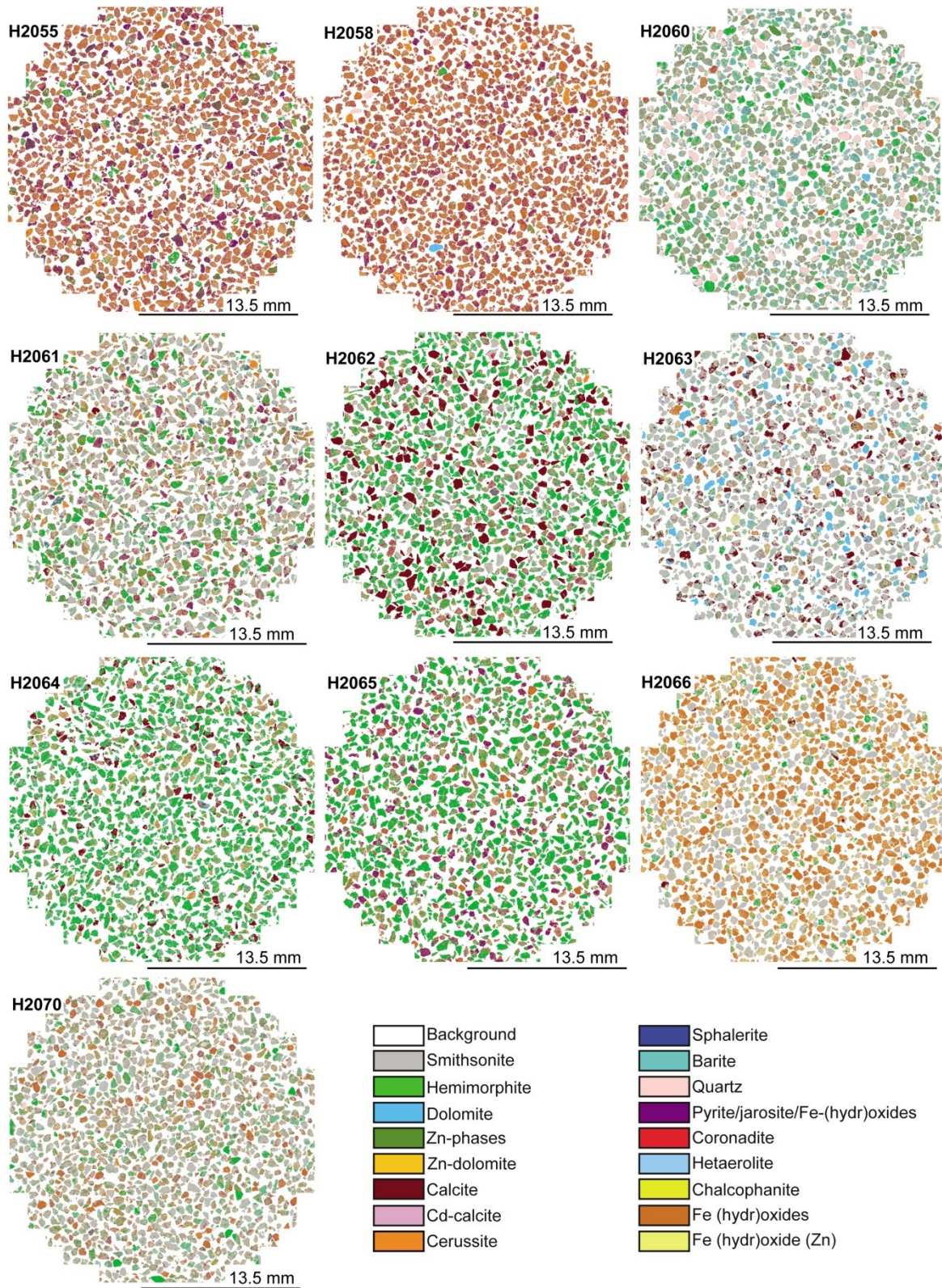
Figure 3.16: False-color fieldscan images of all selected samples analyzed by QEMSCAN®. Minor and trace minerals (i.e. Fe-dolomite, pyrite, ilmenite, rutile, kaolinite, K-feldspar, plagioclase feldspar, muscovite/illite, biotite, gypsum/anhydrite apatite, chlorite) are not visible in the figure, and therefore not represented in the color key (Santoro et al., 2014).

☐	Background	■	Calcite	■	Sphalerite
■	Smithsonite	■	Cd-calcite	■	Barite
■	Hemimorphite*	■	Cerussite	■	Quartz
■	Dolomite	■	Chalcophanite	■	Pyrite/jarosite/Fe-(hydr)oxides
■	Zn-phases	■	Fe (hydr)oxides	■	Coronadite
■	Zn-dolomite	■	Fe (hydr)oxide (Zn)	■	Hetaerolite
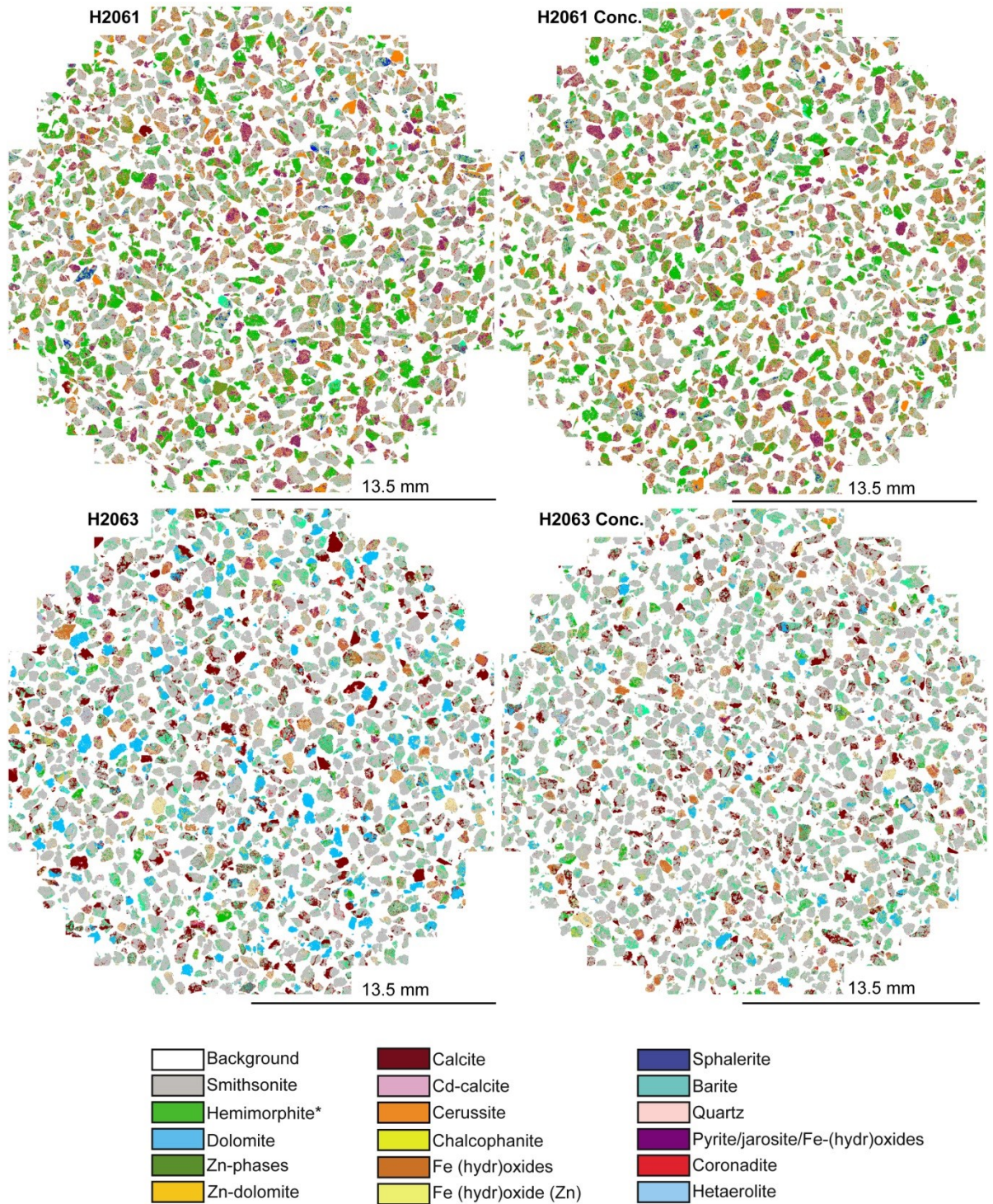
Figure 3.17: False-color fieldscan images of two selected samples and their concentrates analyzed by QEMSCAN®. Minor and trace minerals (i.e. Fe-dolomite, pyrite, ilmenite, rutile, kaolinite, K-feldspar, plagioclase feldspar, muscovite/illite, biotite, gypsum/anhydrite apatite, chlorite) are not visible in the figure, and therefore not represented in the color key (Santoro et al., 2014).

Table 11: Quantitative analyses of Hakkari samples by QEMSCAN®

Sample n	H2055	H2058	H2060	H2061	H2061 Conc*.	H2062	H2063	H2063 Conc.*	H2064	H2065	H2066	H2070
						wt.%						
Smithsonite	1.61	0.21	23.76	42.51	36.51	23.91	57.41	65.36	24.65	11.01	28.57	45.98
Hemimorphite	2.04	0.19	9.20	15.68	16.44	34.45	2.52	3.46	44.98	44.69	2.88	7.26
Dolomite	<0.01	0.18	0.72	<0.01	0.01	0.01	7.60	2.57	0.38	<0.01	<0.01	<0.01
Fe-dolomite	0.2	<0.01	0.01	<0.01	0.02	<0.01	0.55	0.30	0.09	<0.01	0.21	<0.01
Zn-dolomite	<0.01	nd	0.29	<0.01	0.01	0.09	1.56	1.19	0.40	<0.01	0.01	<0.01
Calcite	0.28	0.01	0.06	0.14	0.04	12.96	7.15	5.16	5.71	<0.01	0.28	0.01
Cd-Calcite	<0.01	<0.01	<0.01	<0.01	<0.01	0.17	0.07	0.05	0.01	<0.01	<0.01	<0.01
Fe-(hydr)oxides	44.95	57.45	10.33	10.05	12.37	8.74	4.61	4.57	8.34	18.72	42.64	17.30
Fe-(hydr)oxides (Zn)	14.35	12.73	2.78	8.92	10.55	6.97	5.33	5.06	6.40	9.54	20.86	11.90
Cerussite	5.00	5.75	0.61	9.03	10.36	0.67	0.10	0.22	0.16	1.79	0.07	1.34
Sphalerite	0.18	0.08	2.63	1.06	0.98	0.16	0.14	0.15	0.20	0.15	0.01	0.34
Barite	<0.01	<0.01	15.61	0.99	0.85	3.69	5.89	5.94	3.69	1.21	<0.01	6.93
Pyrite/Fe-(hydr)oxides/Jarosite	23.94	21.11	1.05	7.63	8.00	3.22	1.34	0.92	1.27	11.11	0.74	4.96
Pyrite	2.36	0.47	0.05	0.37	0.33	0.11	0.07	0.06	0.06	0.20	0.08	0.19
Coronadite	0.45	0.06	0.11	1.19	0.88	2.28	2.92	2.20	1.11	0.49	0.58	0.08
Hetaerolite	0.01	<0.01	0.01	0.12	0.10	0.42	1.65	1.75	0.38	0.04	1.76	<0.01
Chalcophanite	0.01	<0.01	<0.01	0.17	0.11	0.17	0.19	0.16	0.08	0.11	0.49	<0.01
Quartz	0.04	0.59	14.62	<0.01	<0.01	0.03	0.08	0.10	0.47	0.04	0.60	0.64
Muscovite/Illite	0.05	0.19	8.51	0.03	0.03	0.06	0.01	0.01	0.03	0.07	0.05	1.08
Kaolinite	0.01	<0.01	0.62	<0.01	<0.01	<0.01	<0.01	<0.01	<0.01	<0.01	<0.01	0.01
Mixed Zn phases	0.22	0.32	3.35	0.30	0.52	0.64	0.12	0.29	0.39	0.60	0.20	1.49
Apatite	<0.01	0.01	0.09	0.01	<0.01	0.03	0.01	0.01	0.02	<0.01	0.01	0.03
Chlorite	0.02	0.32	1.77	<0.01	<0.01	0.02	<0.01	<0.01	0.01	0.02	0.04	0.25
Gypsum	0.21	<0.01	0.04	0.03	0.01	1.08	0.48	0.32	1.04	<0.01	<0.01	0.03

Notes: QEMSCAN® measurement mode = field scan image: X-ray pixel spacing 10 μm; ilmenite, rutile, kaolinite, biotite, apatite, plagioclase feldspar, K-feldspar and other minerals occur in traces; *Concentrate samples.

3. 11. Results: QEMSCAN® Mineral association

In Figures 3.18 and 3.19 are shown the pie charts of the mineral association, plus a few enlargements of the crushed particles that synoptically show what the mineral association corresponds to (Santoro et al., 2014).

The charts have been drawn considering the percentage of contacts between the hemimorphite and smithsonite respectively, and all the other minerals detected by QEMSCAN®. Hemimorphite (Figure 3.18) is mostly associated with smithsonite from a minimum value of 38% (H2058) to a maximum of 67% (sample H2063), with an average percentage of ~56% of hemimorphite in contact with smithsonite. It can also be associated with Fe-(hydr)oxides (Figure 3.18) from 2% (H2063) to 43% (H2058), with an average of ~22%, and less with Zn-enriched Fe-(hydr)oxides from 1% (H2063) to 10% (H2066) with an average of ~ 5%. Another phase in contact with hemimorphite is barite (if present in the sample, Figure 3.18) from 0 % (in samples barren of barite) up to 23% (H2063). Quartz, where present in a sample, can also be associated with hemimorphite (up to 6% in H2066). Cerussite (Figure 3.18), Zn phases, sphalerite (up to ~3%), hetaerolite, coronadite and pyrite/jarosite/Fe-(hydr)oxides can be in contact with hemimorphite (up to ~1%), depending on their occurrence in the samples. Smithsonite (Figure 3.19) is associated with hemimorphite from a minimum of 10 % (H2060) to a maximum of 50 % (H2064); the average value is ~29%. As well as hemimorphite, smithsonite is also abundantly associated with Fe-(hydr)oxides (Figure 3.19), from 5 % (H2063) to 43 % (H2058) (average ~18 %); however it seems to be more associated with Zn-rich Fe-(hydr)oxides than with hemimorphite (from 6 % in H2060 to 29 % in H2070, with an average value of ~15 %). Other minerals in association with smithsonite are: barite (up to 16 % in H2060 with an average of ~4 %), heaterolite and sauconite (both up ~9 %); calcite and Zn-dolomite (up ~6.5 %), cerussite and pyrite/jarosite/Fe-(hydr)oxides (up to 4 %), quartz, chalcophanite and sphalerite (up to a maximum of 3 %) (Figure 3.19).
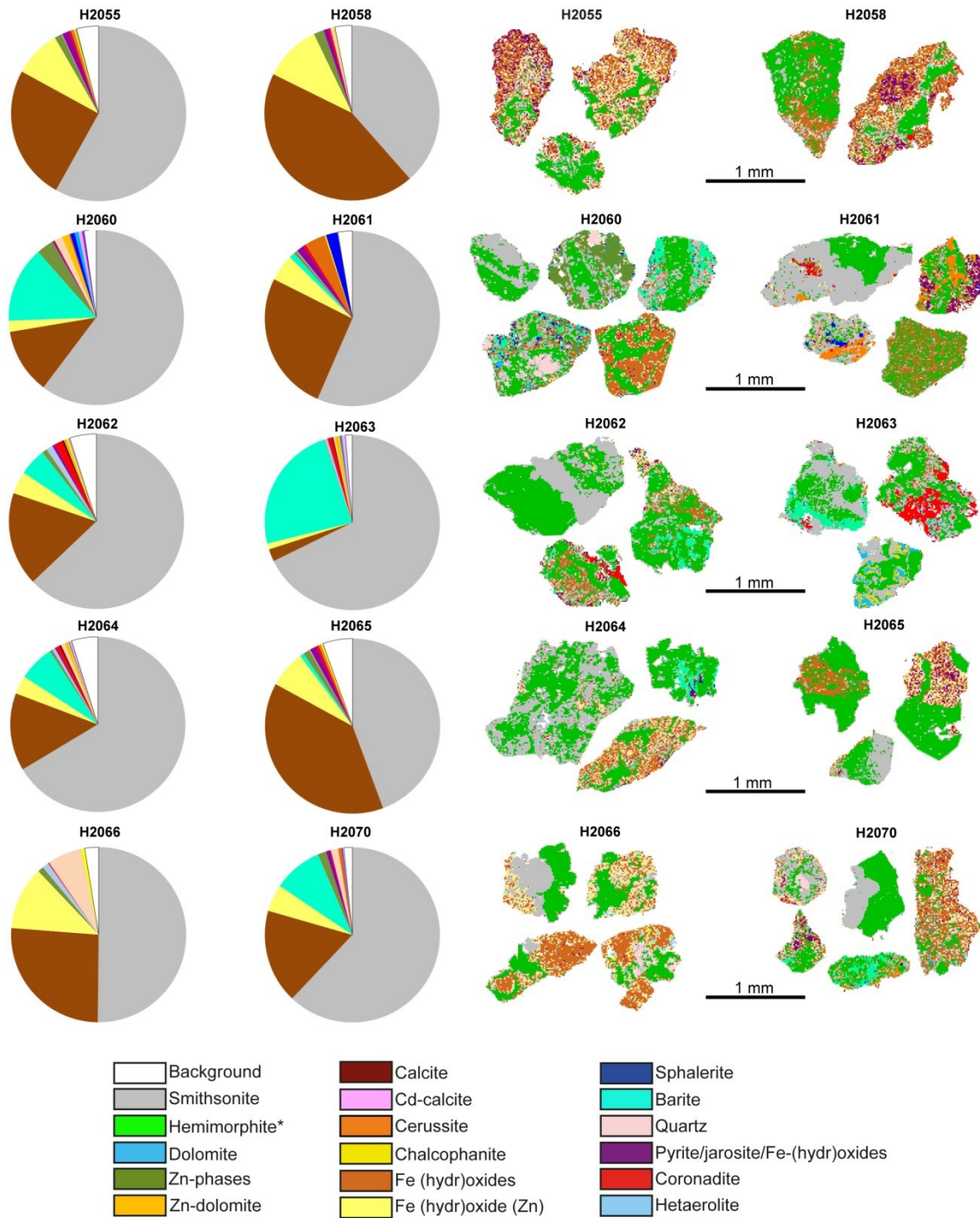
Figure 3.18: Pie diagrams of the mineral association for all the samples and enlargements of selected particles. The diagrams show the association between hemimorphite and the other minerals in percentages. The color keys indicate the mineral phases occurring. *Hemimorphite is inserted in the color key as it occurs in the enlarged particles (Santoro et al., 2014).
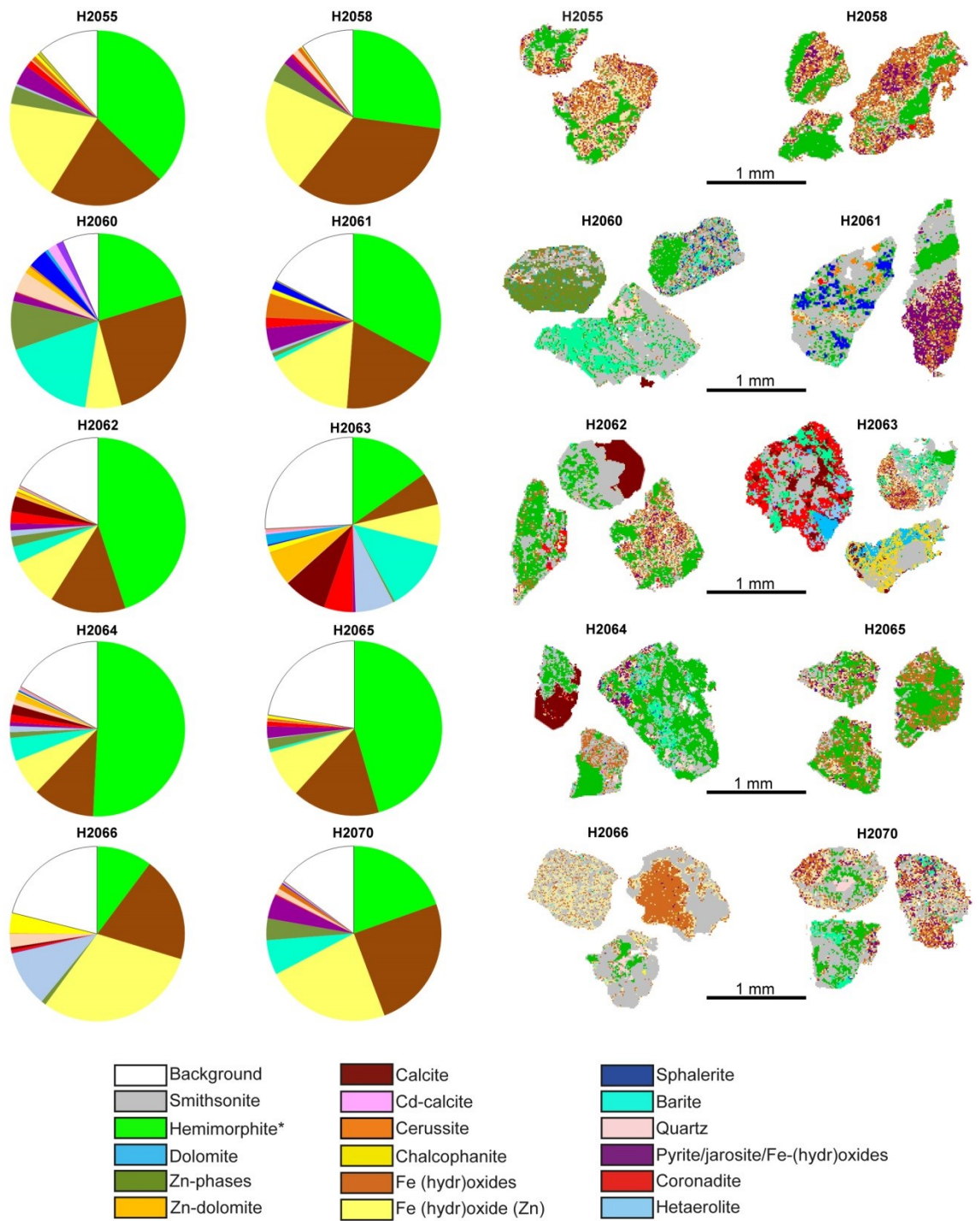
Figure 3.19: Pie diagrams of the mineral association for all the samples and enlargements of selected particles. The diagrams show the association between smithsonite and the other minerals in percentages. The color keys indicate the mineral phases occurring. *Smithsonite is inserted in the color key as it occurs in the enlarged particles (Santoro et al., 2014).

3. 12. Results: Calculation of elements from QPA (Rietveld and QEMSCAN®)

In table 12a and b are reported the attempts made to reconcile the elemental values of Zn, Pb, Ca, Mg and Fe calculated from the QPA data (both XRD-Rietveld and QEMSCAN® methods) with total Zn, Pb, Ca, Mg and Fe (all wt.%) obtained by chemical analyses. The calculation was done for only ten samples (the same analyzed by QEMSCAN® analyses), in order to carry out a comparison of the XRD-Rietveld and QEMSCAN® methods for the same samples (Santoro et al., 2014).

Here follows an element-per-element description of the results obtained by this calculation using the minerals quantities obtained with both the Rietveld and QEMSCAN® technology:

Zinc: The calculation was made using the contributions from only smithsonite and hemimorfite evaluated with XRD-QPA. It can be seen that using the standard parameters (52.15 wt.% Zn for smithsonite and 54.29 wt.% Zn for hemimorphite), there is generally an overestimation of the zinc grade between ~2 and ~12wt.%. However, sample H2066 shows a significant underestimation of zinc. The XRD-QPA for this sample indicates that it contains 37 % goethite, which from the WDS data this mineral has a content of up to 10 wt.% ZnO. It is very likely, therefore, that goethite can significantly contribute to the total Zn content in some samples. This has also been confirmed by QEMSCAN® analyses that clearly show the presence of Zn-enriched hydroxides in the Hakkari samples.

Even if we compare the assayed zinc amounts with the zinc values calculated from the QEMSCAN® quantitative mineral analyses (table 12b) it is possible to observe that they do not match perfectly, although we considered several minerals as being possible Zn sources (smithsonite, hemimorphite, Zn-dolomite, Zn-rich Fe-(hydr)oxides, sphalerite, hetaerolite, chalcophanite, and sauconite). In some samples, indeed, the Zn calculated is overestimated (up to ~4 wt.%), while in others it is underestimated (up to 9 wt.%). For the minor zinc phases detected by QEMSCAN® we used the average standard values also for sphalerite (64.06 wt.% Zn), hetaerolite (27.33 wt.% Zn), chalcophanite (17.02 wt.% Zn), sauconite (33.80 wt.% Zn), as well as the average values of ZnO found in the *"impure-mixed"* phases transformed as Zn element. The latter are: 8 wt.% Zn for Zn-dolomite and 8 wt.% Zn for Zn-rich Fe-(hydr)oxides (Santoro et al., 2014).

Lead: The same issues have been encountered for Pb calculated with the Rietveld analyses that is always underevaluated because, in the majority of the samples, no lead minerals were detected by X-rays. This does not mean that there are not Pb minerals at all, but that they were hardly detectable because of their low abundance in the analyzed samples. Another possibility is that lead is carried by no typical lead minerals (i.e. Fe-Mn(hydr)oxides). Lead minerals (cerussite and plumbojarosite) were only detected in three samples (H2061, H2055, H2058) but also for these minerals the evaluated Pb amount is lower than the one measured by chemical analyses. Also in this case the standard values for cerussite (77.54 wt.% Pb) and plumbojarosite (18.33 wt.% Pb) were used.

Lead calculation of QEMSCAN®-QPA analyses were made taking into account the standard values of Pb for cerussite, galena (86.60 wt. % Pb), coronadite (24.41 wt.% Pb), and the elemental value of lead for PbO in Fe-(hydr)oxides (10 wt.% Pb) and PbO in jarosite (3 wt.% Pb). In table 12b it is shown that the values of Pb measured and Pb calculated do not match perfectly as the Pb calculated in the majority of the samples is overestimated (even if in small amount) except for the three samples: H2055, H2060, H2061.

Calcium: The calculation of this element from XRD-QPA was made considering only calcite and dolomite as Ca sources, and using the stoichiometric values of Ca in dolomite (21.73 wt.% Ca) and calcite (40.04 wt.% Ca). The results indicate that calcium is always overestimated in those samples that contain dolomite or calcite, while they are underestimated in the samples where no calcium phases have been detected.

The QEMSCAN® calculations, instead, were carried out considering the contributions of dolomite and calcite (standard values above reported), of gypsum (32.57 wt.% Ca), apatite (53.54 wt.% Ca), and also of Fe-dolomite (29 wt.% Ca) and Zn-dolomite (22 wt.% Ca). The calcium content of the latter phases has been evaluated considering the standard value of Ca in dolomite, subtracted of the values of FeO and ZnO detected by SEM-EDS analyses respectively (1 wt.% Fe and 8 wt.% Zn). The results of this calculation show that Ca is always under-estimated, except in the sample H2062, in which there is an over-estimation of 0.68 wt.%.

Magnesium: Magnesium has been calculated taking into consideration only dolomite (21.86 wt.% Mg) by XRD-QPA values. It results that the Mg calculated is always under-estimated in samples where no dolomite was detected because of the detection limit, whereas it is over-estimated in the samples H2060 and H2061.

In the QEMSCAN® analyses, the Mg calculated is again under-estimated, except for the samples H2063 and H2064, but the discrepancy between Mg calculated and Mg measured is less marked than in the XRD-QPA. The dolomite standard value (21.86 wt.% Mg) and the impure phases as Zn-dolomite (20 wt.% Mg) and Fe-dolomite (14 wt.% Mg) were considered as sources for Mg. The Mg content of the latter phases was calculated with the same route used for Ca (see above).

Iron: Fe was calculated considering the standard values of lepidocrocite and goethite (62.85 wt.% Fe). By the calculation from XRD-QPA, it is possible to observe that the Fe calculated is always lower than that measured. This could be ascribed to the presence of Fe-bearing amorphous phases not identified by Rietveld.

In the calculation of the Fe by QEMSCAN®-QPA, it is possible to observe, instead, that Fe-calculated and Fe-measured have a better matching, if compared to the XRD-QPA. In the calculation we considered the contributions of Fe-(hydr)oxides with a standard Fe-content (see above), pyrite (46.55 wt.% Fe), chalcophanite (6.08 wt.% Fe), and also Zn-rich Fe-(hydr)oxides, mainly consisting of Zn-goethite (56 wt.% Fe).

Table 12a: Zinc, lead, calcium, magnesium, and iron amount (Zn%, Pb%, Ca%, Mg%, Fe%) calculated from whole rock chemical assays (CA), compared with the metal percentages derived from the Zn-bearing minerals measured by X-ray quantitative method (QPA-Rietveld)

Sample	Zn% QPA Sm	Zn% QPA Hm	Zn% ΣQPA1	Zn% CA2	Zn% ΣQPA-CA3	Pb% QPA Cer	Pb% QPA Pb-Jrs	Pb% ΣQPA1	Pb% CA2	Pb% ΣQPA-CA3	Ca% QPA Dol	Ca% QPA Cal	Ca% ΣQPA1	Ca% CA2	Ca% ΣQPA-CA3	Mg% ΣQPA1	Mg% CA2	Mg% ΣQPA-CA3	Fe% QPA Lpc	Fe% QPA Gth	Fe% ΣQPA1	Fe% CA2	Fe% ΣQPA-CA3
H2055		5.2	7.06	6.50	0.56	1.1	5.6	1.88	7.90	-6.02		1.8	1.01	0.64	0.37	0.00	0.03	-0.03		53.1	33.37	40.04	-6.67
H2058		1.2	5.40	5.30	0.10	0.6		0.47	5.61	-5.14			0.00	0.30	-0.30	0.00	0.09	-0.09		59.4	37.33	44.08	-6.75
H2060	16.8	18.7	18.83	15.90	2.93			0.00	0.88	-0.88	5.8		1.74	0.68	1.06	1.27	0.31	0.96			0.00	6.63	-6.63
H2061	57.5	26.1	44.35	35.09	9.26	8.4		6.51	9.52	-3.01			0.00	0.43	-0.43	0.00	0.08	-0.08		4.4	2.77	11.53	-8.76
H2062	8.7	63.8	38.98	35.19	3.79			0.00	1.41	-1.41		21.5	12.05	6.97	5.08	0.00	0.04	-0.04			0.00	6.18	-6.18
H2063	61.6	3.6	33.98	30.45	3.53			0.00	0.57	-0.57	12.7	14.5	11.93	7.49	4.44	2.78	1.59	1.19			0.00	5.10	-5.10
H2064	3.1	70.5	39.68	37.72	1.96			0.00	0.69	-0.69		20.8	11.65	4.92	6.73	0.00	0.11	-0.11			0.00	5.09	-5.09
H2065	2.1	96.3	53.09	40.89	12.20			0.00	2.32	-2.32			0.00	0.05	-0.05	0.00	0.01	-0.01			0.00	12.20	-12.20
H2066	30.5	5.6	21.85	21.22	0.63			0.00	0.48	-0.48			0.00	0.54	-0.54	0.00	0.10	-0.10		37.1	23.32	31.39	-8.07
H2070	51.7	15.6	35.31	31.86	3.45			0.00	2.04	-2.04			0.00	0.25	-0.25	0.00	0.06	-0.06	1.1		0.69	13.25	-12.56

Notes: Sm= smithsonite; Hm= hemimorphite; Cer=cerussite; Pb-Jrs=Plumbojarosite; Dol= dolomite; Cal=calcite; Lpc= lepidocrocite; Gth= goethite.
[1] Σ_{QPA}: is the sum of element (Zn, Pb, Ca, Mg, Fe) coming from Quantitative values of minerals detected in Rietveld analysis; [2]CA: is the element value from Chemical analyses;
[3]Σ_{QPA}-CA: is the difference between Σ_{QPA} and CA.

Table 12b: Zinc, lead, calcium, magnesium, and iron amount (Zn%, Pb%, Ca%, Mg%, Fe%) calculated from whole rock chemical assays (CA), compared with the metal percentages derived from the Zn-bearing minerals measured by X-ray quantitative method (QPA-QEMSCAN®).

Sample	Co	Sm	Hm	Dol	Fe-Dol	Zn-Dol	Cal	Gth	Fe-Gth	Cer	Sph	Py/Fe-(hydr)ox/Jrs	Py	Cor	Het	Cha	Sau	Gp	Zn% ΣQPA1	Zn% CA2	Zn% ΣQPA-CA3	Pb% ΣQPA1	Pb% CA2	Pb% ΣQPA-CA3	Mg% ΣQPA1	Mg% CA2	Mg% ΣQPA-CA3	Ca% ΣQPA1	Ca% CA2	Ca% ΣQPA-CA3	Fe% ΣQPA1	Fe% CA2	Fe% ΣQPA-CA3
H2055	1.33	2.04	0.01			0.01	0.28	44.95	14.35	5.00	0.18	23.94	2.36	0.45	0.01	0.01	0.22	0.21	4.38	6.50	-2.12	5.42	7.90	-2.48	0.00	0.03	-0.03	0.24	0.64	-0.40	37.14	40.04	-2.90
H2058	0.12	0.19	0.18	0.01	0.00		0.01	57.45	12.73	5.75	0.08	21.11	0.47	0.06	0.01	0.01	0.32	0.01	2.42	5.30	-2.88	5.75	5.61	0.14	0.04	0.09	-0.05	0.07	0.30	-0.23	43.15	44.08	-0.93
H2060	23.32	9.20	0.72	0.01	0.29		0.06	10.33	2.78	0.61	2.63	1.05	0.05	0.11	0.01	0.01	3.35	0.04	20.27	15.90	4.37	0.78	0.88	-0.10	0.20	0.31	-0.11	0.40	0.68	-0.28	8.02	6.63	1.39
H2061	42.42	15.68	0.01	0.01	0.01		0.14	10.05	8.92	9.03	1.06	7.63	0.37	1.19	0.12	0.17	0.30	0.03	32.48	35.09	-2.61	8.19	9.52	-1.33	0.01	0.08	-0.07	0.10	0.43	-0.33	11.44	11.53	-0.09
H2062	23.63	34.45	0.01	0.01	0.09		12.96	8.74	6.97	0.67	0.16	3.22	0.11	2.28	0.42	0.17	0.64	1.08	32.13	35.19	-3.06	1.78	1.41	0.37	0.02	0.04	-0.02	7.66	6.97	0.69	9.41	6.18	3.23
H2063	56.55	2.52	7.60	0.10	1.56		7.15	4.61	5.33	0.10	0.14	1.34	0.07	2.92	1.65	0.19	0.12	0.48	32.17	30.45	1.72	1.32	0.57	0.75	1.90	1.59	0.31	6.93	7.49	-0.56	5.90	5.10	0.80
H2064	24.29	44.98	0.38	0.01	0.40		5.71	8.34	6.40	0.16	0.20	1.27	0.06	1.11	0.38	0.08	0.39	1.04	37.97	37.72	0.25	1.03	0.69	0.34	0.14	0.11	0.03	3.78	4.92	-1.14	8.82	5.09	3.73
H2065	10.98	44.69	0.01			0.01	0.01	18.72	9.54	1.79	0.15	11.11	0.20	0.49	0.04	0.11	0.60	0.01	31.49	40.89	-9.40	2.46	2.32	0.14	0.00	0.01	-0.01	0.02	0.05	-0.03	17.11	12.20	4.91
H2066	28.32	2.88	0.01	0.01	0.01		0.28	42.64	20.86	0.07	0.01	0.74	0.08	0.58	1.76	0.49	0.20	0.01	18.65	21.22	-2.57	2.28	0.48	1.80	0.01	0.10	-0.09	0.18	0.54	-0.36	38.32	31.39	6.93
H2070	45.79	7.26	0.01	0.01	0.01		0.01	17.30	11.90	1.34	0.34	4.96	0.19	0.08	0.01	0.01	1.49	0.03	29.68	31.86	-2.18	2.25	2.04	0.21	0.01	0.06	-0.05	0.04	0.25	-0.21	17.54	13.25	4.29

Notes: Sm= smithsonite; Hm= hemimorphite; Dol= dolomite; Cal=calcite; Gth= goethite; Cer=cerussite; Sph= sphalerite; Jrs=jarosite; Py=pyrite; Cor= coronadite; hetaerolite; Cha=chalcophanite; Sau=sauconite; Gy=gypsum.
[1] Σ_{QPA}: is the sum of element (Zn, Pb, Ca, Mg, Fe) coming from Quantitative values of minerals detected in Rietveld analysis; [2]CA: is the element value from Chemical analyses; [3]Σ_{QPA}-CA: is the difference between Σ_{QPA} and CA.

3. 13. Discussion

This study focuses on a detailed mineralogical, petrographic and geochemical characterization of the Hakkari nonsulfide ore deposit. It is also comprehensive of a quantitative phases analysis evaluation pursued with two methods: XRD-Rietveld and QEMSCAN®.

The Hakkari deposit can be considered to belong both to the "*direct replacement*" and "*wall-rock replacement*" supergene zinc deposit types (Hitzman et al., 2003), as the nonsulfide Zn>>Pb minerals tends to replace both the sulfides and the host rock.

The nonsulfide Zn mineral association typically consists of smithsonite and hemimorphite. The former occurs in two generations: a first smithsonite (Sm1) commonly replaces both previous sphalerite crystals and host rock calcite, whereas a second smithsonite (Sm2) tends to precipitate as well zoned concretions in cavities, vugs and porosities of the host rock. Hemimorphite is younger than smithsonite, as it cuts and partially replaces smithsonite in veinlets. Both smithsonite and hemimorphite are commonly associated with Fe(Mn)-(hydr)oxides. Fe-(hydr)oxides are commonly Zn-enriched. Cerussite generally occurs in association with Zn-nonsulfides. Sulfide remnants are scarce. Calcite occurs in 3 generation at least: the first two generations are the host rock calcite (Cal1) and the vein calcite filling fractures, which is likely related to the hydrothermal breccia (Cal2). The latter generations (Cal3 and 4) correspond to sparry calcite crystals in veins, which are associated with the nonsulfide zinc minerals (Santoro et al., 2013). In Figure 3.20 is displayed a scheme summarizing the interpreted paragenesis of the main mineral phases occurring at Hakkari.

The results of the isotopic analyses of the Hakkari carbonates are revealing an interesting history of the mineralizing fluids. The $\delta^{18}O$ values of the host rock limestone are around 24.9‰ VSMOW, whereas the $\delta^{13}C$ values range between $-0.6‰$ and $-2.5‰$ VPDB. The $\delta^{13}C$ ratios fall in the range of upper Jurassic carbonates (Jenkyns et al., 2002), whereas the $\delta^{18}O$ values are significantly lower, pointing to diagenetic modifications. The $\delta^{18}O$ values of smithsonite lie in a restricted interval comprised between 24.2‰ and 25.3‰ VSMOW. The $\delta^{13}C$ smithsonite values are comprised in the characteristic interval of supergene smithsonites (Gilg et al., 2008), encountered also in other supergene ore districts worldwide. These valus are usually interpreted as a result of mixing between carbonate carbon from the host rock and soil/atmospheric CO_2 (Gilg et al., 2008). The $\delta^{18}O$ - $\delta^{13}C$ composition of supergene calcite veins is typical of a terrestrial carbonate precipitated from the same groundwaters that precipitated smithsonite at the same temperature (Boni et al., 2003).

If the $\delta^{18}O$ value of the solution from which smithsonite was formed can be approximated, the precipitation temperature can be calculated using the following equation (Gilg et al., 2008):

$$1000 \ln \alpha \text{smithsonite-water} = 3.10 \ (106/T2) - 3.50$$

Modern spring waters collected in two different areas around Hakkari have an oxygen isotope composition between -9.7‰ and -10.7‰ VSMOW (Multu et al., 2012).
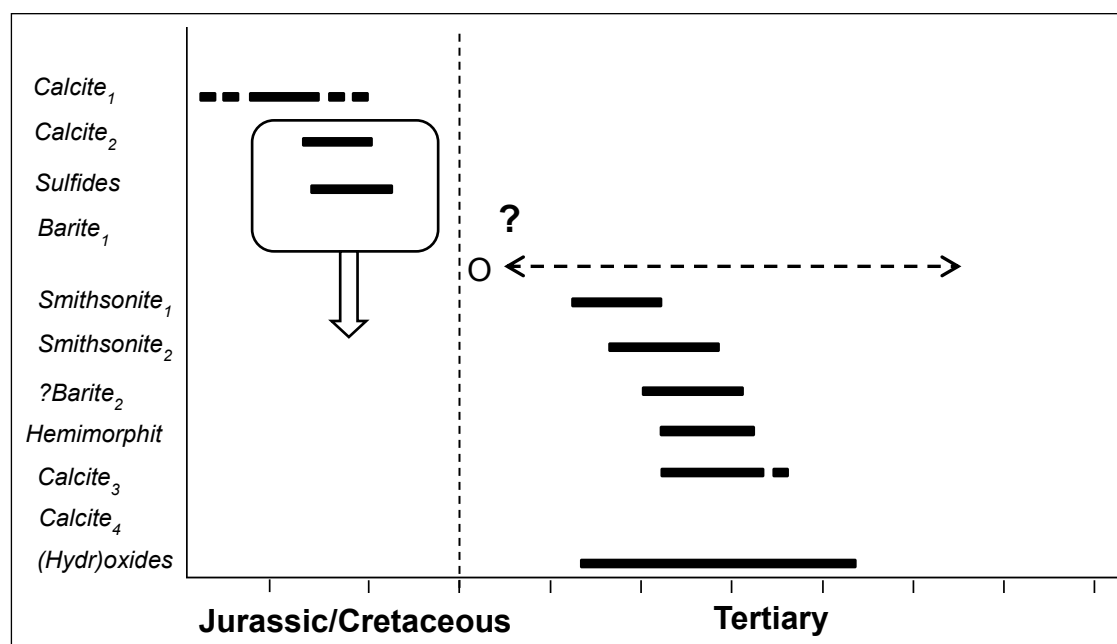
Figure 3.20: Interpreted mineralogical paragenesis for the Hakkari mineralization (Santoro et al., 2013).

The $\delta^{18}O$ values measured in the Pleistocene to Holocene speleothems from karstic caves of eastern Turkey, point to an oxygen isotope composition of dripwaters that range between -14.5‰ and -11‰ VSMOW (Rowe et al., 2012). If the Hakkari smithsonites were formed from a fluid with a $\delta^{18}O$ value comparable to modern groundwater, then the precipitation temperature would have been between ~10 and ~18°C (Figure 3.21). If they precipitated instead from a fluid with a $\delta^{18}O$ value comparable with that of Pleistocene to Holocene cave water, their precipitation temperature would have been between <0 and 10°C, which is generally a temperature too low for smithsonite precipitation.

The use of automated mineralogy combined with optical or electron beam techniques, provided benefits to the Hakkari ore characterization if compared to the results obtained by X-Ray quantitative phase analysis with Rietveld method, although some limitations must also be considered (Santoro et al., 2014). The QEMSCAN® analyses allowed the calculation of an accurate modal mineralogy for the economic and gangue minerals, and the definition of their spatial distribution.

In addition, detailed information on Zn deportment, and on the average mineral association for all the mineral compounds has also been collected, while the X-ray QPA (Rietveld) only evaluated the amount of mineral phases previously detected by the interpretation of the X-ray diffraction spectra. In the tables shown in the above paragraphs (Table 10 and 11), it is possible to synoptically understand the differences of the results obtained in term of modal mineralogy.

The QEMSCAN® analyses on the Hakkari samples, in fact, confirmed the occurrence of the mineral phases detected by the use of XRD-spectra interpretation, but also added new data about the mineral compounds that had not been previously identified, or quantified

by the XRD-Rietveld analyses. Moreover, QEMSCAN® was also able to distinguish and quantify metal-bearing, "*impure*" phases.
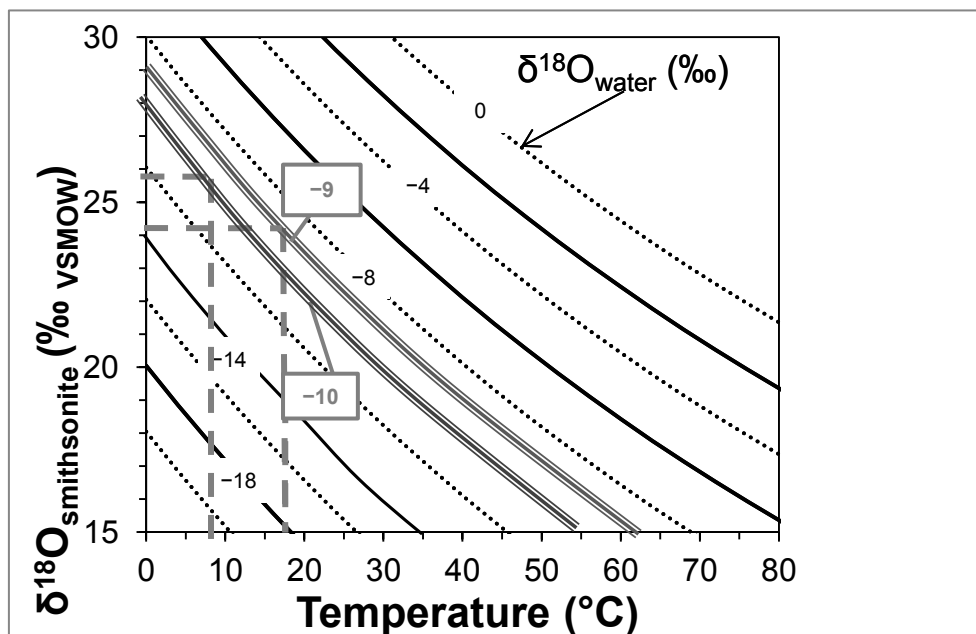
Figure 3.21: Graphical representation of oxygen isotope equilibrium curves between smithsonite and water according to Gilg et al. (2008), calculated for different $\delta^{18}O$ water values as a function of temperature. Calculated temperatures for smithsonite formation are based on the $\delta^{18}O$ value of -9 and -10 ‰ for the local meteoric groundwater and -14.5 and -11‰ of speleothemes. Note: dashed lines maximum and minimum $\delta^{18}O$ values.

The Cd- and Pb-calcites, for example, only locally observed in the previous SEM-EDS analyses, were easily distinguished from the "*pure calcite*" and quantified, though very scarce. The same applies to Zn-dolomite (Zn≤10 wt.%) and Fe-dolomite (Fe≤5 wt.%), clearly distinguished from "*pure dolomite*", and consequently quantified. Through QEMSCAN® analyses, it was also possible to distinguish between Fe-(hydr)oxides and Zn-bearing Fe-(hydr)oxides (Zn≤ 10wt.%), which can be locally abundant in the deposit. The QEMSCAN® analyses also allowed the discrimination of a previously un-identified amorphous phase, which had been roughly quantified by the XRD-Rietveld method using an internal standard. By the use of QEMSCAN® it was possible to reveal the nature of this amorphous phase, mainly consisting in a blend of pyrite mixed with Fe-(hydr)oxides and jarosite, whose percentage roughly corresponds to the quantities of the amorphous phase reported in calculated by XRD-Rietveld. However, from the point of view of a quantitative evaluation of the ore phases, it is very important to stress that several discrepancies have been found between the analyses carried out with the XRD-Rietveld method, and those obtained by QEMSCAN®. This must be ascribed to:

1) The differences between the analytical systems in use the two technologies, because QEMSCAN® analysis recognizes the minerals on the basis of their chemical composition, whereas XRD distinguishes the minerals on their crystal structure,

2) The two technologies have different detection limits, hence most of the trace mineral phases, detected and quantified in the current work had not been previously identified;

3) The samples analysed are not exactly the same of those analysed with the XRD-Rietveld. However, they come from the same core, and are in close proximity.

In Figures 3.22a and b are displayed the correlation diagrams of the calculated element amounts (Zn, Pb, Ca, Mg, Fe) plotted vs. the measured element concentrations both from XRD- and QEMSCAN®-QPA (Santoro et al., 2014). All the points in the diagrams represent the relationship between the amount of element calculated from QPA analyses and the element directly measured in the sample for each sample. In a hypothetical case of perfect stoichiometry for all the minerals occurring in the deposit, all the points should follow along the theoretical dotted line (considering the possible measurement errors) having a unitary coefficient. The samples falling below the lines, hence, contain less amount of element than corresponding calculated values and vice versa for samples above the line.

Looking at the diagrams obtained by the XRD-QPA calculation of the elements amount vs. measured element concentrations (Figure 3.22a), it is possible to observe no correlation between elements calculated and measured; in fact the amount of elements calculated is generally less than the effective values measured in the samples (see diagrams of Fe, Pb, Ca, Mg). This because during the XRD-QPA carried with the Rietveld method, it was impossible to measure the quantity of impure mineral phases bearing Fe (and the amorphous Fe-phases), Pb, Mg or Ca. Moreover, it was impossible to evaluate the mineral phases occurring in low percentages because of the XRD limit detection. This brought to an under-estimation of the elements. In the case of the iron, the impossibility to establish the amount of iron carried by the amorphous phases, led to a high under-estimation of Fe (Figure 3.22a)

On the contrary, there is a common over-stimation of Zn, probably due to analytical errors (sampling, preparation, homogenization issues).

If we consider the diagrams of Figure 3.22b, showing the calculated elements amounts from QEMSCAN®-QPA vs the measured element amounts, it is possible to observe a better correlation (compared to previous diagrams). However, the data do not match perfectly. This may be due to several reasons:

1) representativity issues: the quantity of the material analysed by QEMSCAN® (1gr) is lower than that used for chemical analyses (~10gr),

2) complex mineralogy issues: QEMSCAN® uses the average chemistry for each mineral but, if the mineralogy is complex (as in the case of Hakkari), the estimated average chemistry for each mineral could be incorrect,

3) homogenization issues: the coarser the particles, the less representative they are. The Hakkari block samples prepared for QEMSCAN® have particles around 450 μm in size, whereas the samples for chemical assays were ground to <50μ (good homogenization). This may cause strong discrepancies between the directly measured Zn amounts and the calculated values,

4) assaying technique: the samples were assayed using ICP-MS, which requires them to be dissolved using acids. It is possible that the method used (*Aqua Regia* digestion) may

not have been adequate to dissolve all the minerals, especially the Zn silicates. If this was the case, the Zn assays will be underestimated and could explain some of the differences. For a complex mineralogy that is silicate rich, a 4-acid attack or lithium metaborate fusion is preferred for IC-PMS analysis. Further investigation would be required to confirm this issue. Mis-matches of elemental assay data (XRF) versus QEMSCAN® calculated elemental data, have also been discussed by Anderson et al. (2014). The comparison between the non-concentrated and the concentrated samples showed only a weak increase of the economic mineral phases (smithsonite, hemimorphite) in the latter. As mentioned earlier, despite a decrease of the gangue mineral phases in the concentrates, these were not completely removed (Figure 3.16). This could be due either to the presence of heavy metallic elements within the structure of the uneconomic minerals (e.g. Zn, Fe in dolomite), or to liberation issues (e.g. light dolomite grains still attached to heavier smithsonite grains). This phenomenon must be carefully considered during processing, as it could decrease the effectiveness of the metal recovery, or might increase the processing costs (Santoro et al., 2014 abstract). One of the most powerful results of the QEMSCAN® analyses, are the mineral maps that can be used to identify the various associations of mineral phases (Figures. 3.14 and 3.16). Mineral association revealed that hemimorphite is mostly associated with smithsonite and Fe-(hydr)oxides and in minor % with barite (where present in sample). Specularly smithsonite is mostly associated mostly with hemimorphite, Fe-(hydr)oxides and Zn rich Fe-(hydr)oxides.
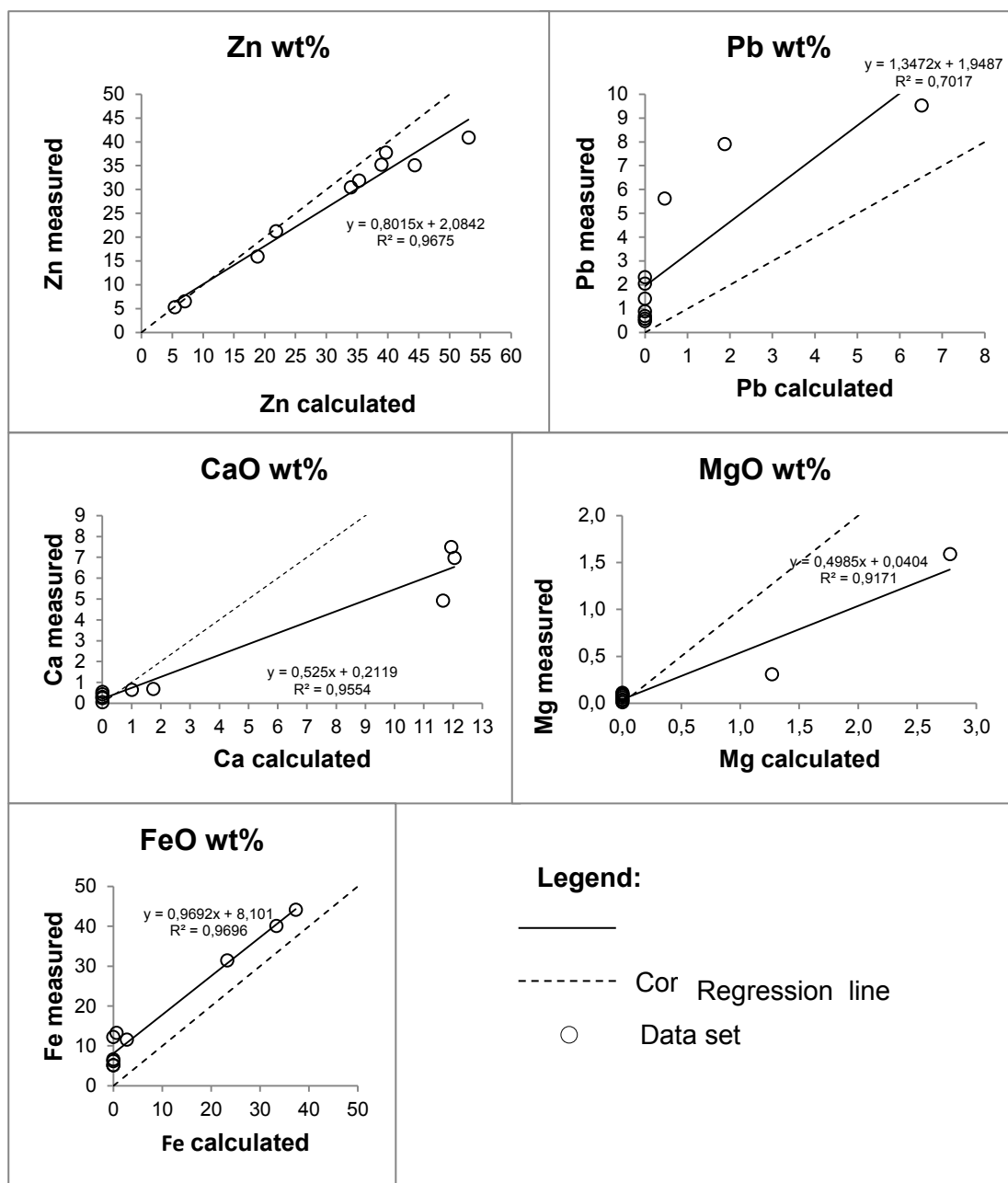
Figure 3.22a: Zinc, lead, calcium, magnesium and iron contents, calculated from the amounts of smithsonite, hemimorphite, dolomite, calcite, goethite and lepidocrocite determined by XRD-Rietveld QPA (the data are reported in table 11a), is plotted versus element contents measured in the chemical assays (data in table 7). The dotted line indicates the theoretical unitary correlation.
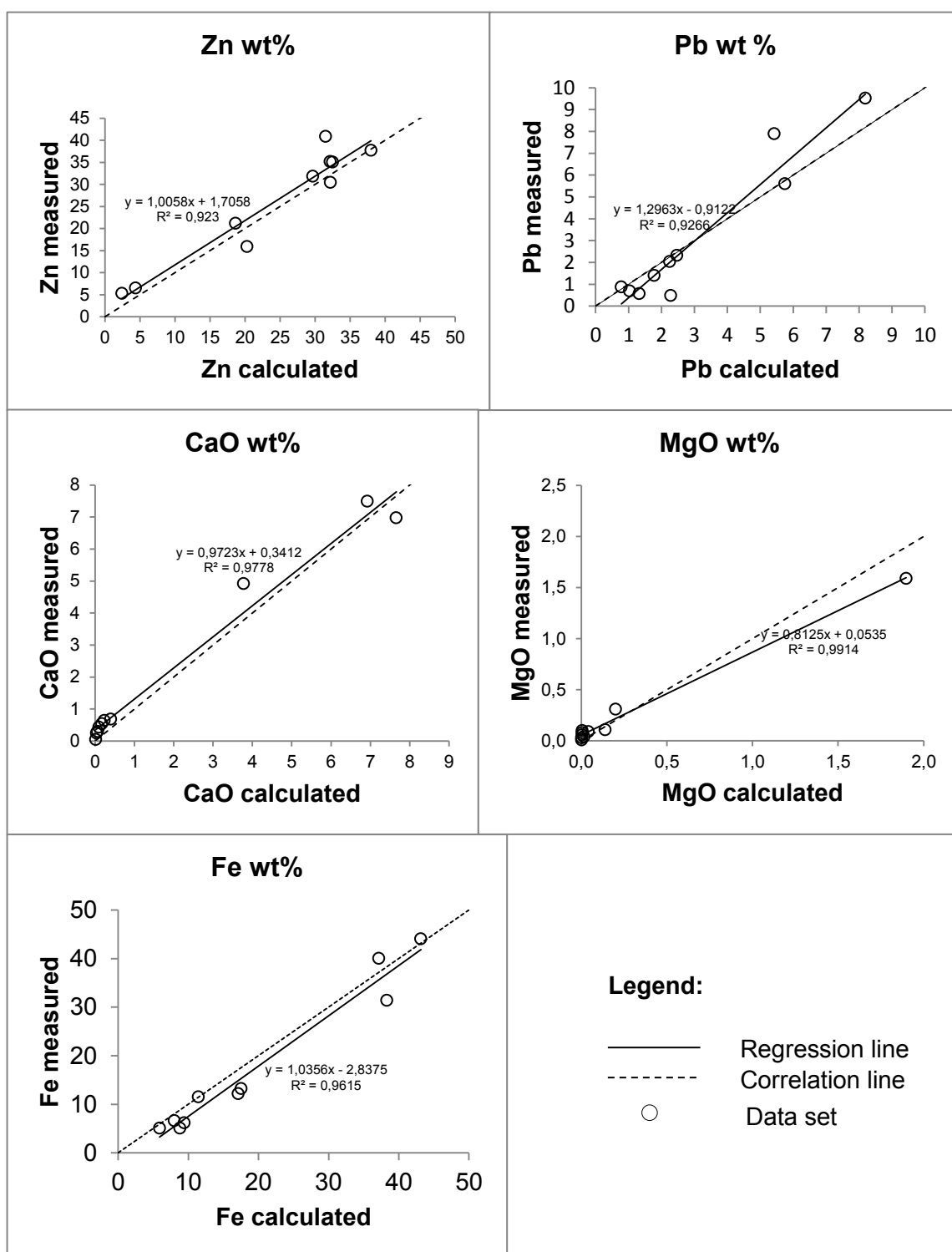
Figure 3.22b: Zinc, lead, calcium, magnesium and iron contents, calculated from the amounts of smithsonite, hemimorphite, dolomite, calcite, goethite and lepidocrocite determined by XRD and QEMSCAN®-QPA (the data are reported in table 11b), is plotted versus element contents measured in the chemical assays (data in table 7). The dotted line indicates the theoretical unitary correlation.

Conclusions

Both XRD-QPA Rietveld and QEMSCAN®-(QPA) analyses revealed that the amount of the identified minerals is: smithsonite and hemimorphite>>Fe-(hydr)oxides and calcite>>barite. Quartz, cerussite, dolomite, muscovite/illite with traces of sulfides remnants (sphalerite, pyrite) and chlorite occur. Coronadite, hetaerolite, chalcophanite and jarosite/plumbojarosite have been also detected. The use of QEMSCAN® technology enhanced the knowledge of the modal mineralogy, and the mineral association for the major, minor and trace mineral compounds. It, in fact, yield the possibility to distinguish and measure the amounts of the *"impure mineral phases"* occurring at Hakkari (e.g. Zn-dolomite, Fe-dolomite, Zn-rich Fe-(hydr)oxides). Moreover, the Mineral Maps allowed obtaining detailed information on the spatial relationships between minerals and mineral compounds. Smithsonite and hemimorphite are associated in all samples. Smithsonite is also well associated with Zn-rich Fe(hydr)oxides while hemimorphite is preferentially associated with Fe-(hydr)oxides and poor with Zn-rich Fe-(hydr)oxides.

The comparison between the non-concentrated and the concentrated samples showed only a weak increase of the economic mineral phases (smithsonite, hemimorphite) in the latter, this because the economic phases were not completely liberated during the separation process or because of the presence of heavy metallic elements within the structure of the uneconomic minerals.

Chemical analyses revealed that the most common elements are Zn and Fe, followed by Ca, Pb and Mg. Between the minor elements are important As and Sb, Tl and locally Hg (mostly in Fe-Mn-(hydr)oxides). The comparison between the elements measured (Zn, Pb, Ca, Mg and Fe) and the same elements calculated, using the mineral amounts analyzed both with XRD-QPA Rietveld and QEMSCAN®-QPA, revealed overestimation and underestimation of the elements amount from the calculated values with both quantitative methods. However, the correlation diagrams revealed a better matching for the elements calculated using the QEMSCAN® measurement method. This means that the QEMSCAN®-QPA analyses are more reliable than those obtained using XRD-QPA (though with some analytical errors and method limitations), as they play an important role in the accuracy of the quantitative evaluation of the phase minerals.

Chapter 4

The supergene nonsulfide Zn-Pb-Ag deposit of Jabali, Yemen

4. 1. Introduction

The Jabali is a Zn-Pb-Ag nonsulfide deposit, located 110 km northeast of Sana'a, the capital of Yemen along the western border of the Marib-Al-Jawf/Sab'atayn basin. The deposit covers an area of about 2 km^2, at an altitude comprised between 1,850 and 1,950 m.s.l. (15°37'N latitude, 44°46'W longitude).

The deposit is known since the antiquity for its silver and lead resources; the mining operations in this area are thought to be over 2,500 years old. During the Middle Ages Jabali was considered one of the most important mining areas for silver in the Muslim world. Modern exploration campaigns, which ended up in several research papers by French authors started from 1980 after a re-discovery of the site by the Bureau de Recherches Géologiques et Minières (BRGM) and by the Yemen Geological Survey and Mineral Resources Board (YGSMRB). The first pre-feasibility study was completed in 1993, and the licenses were sold during the time span from 1996-1998. The nonsulfide concentrations mainly consist of smithsonite with minor hydrozincite, hemimorphite, acanthite and greenockite hosted by carbonate rocks (Mondillo et al., 2011, 2014).

In 2004-2005 the English Company ZincOx, together with SRK Consulting, concluded the final feasibility study on the deposit, and reported total resources of 12.6 Mt at 8.9% Zn, 1.2% Pb, and 68 ppm Ag. The best-mineralized portion occurs in the oxidized levels, where the overall estimated resources amount at 8.7 million tonnes of ore at an average grade of 9.2% zinc. The final Jabali processing flowsheet was developed in two successive stages. At first (Woollett et al., 2002), it consisted of five main unit operations: ore crushing and screening, grinding and classification, desliming, lead/silver concentrate, and zinc concentrate production. Lead sulfide and carbonate minerals would have been recovered together using a mixture of xanthate, carbonate and clay dispersant and sulfidization reagents. Silver associated with lead would also have been recovered in this step. Oxidized zinc minerals (predominately smithsonite) would have been separated from dolomite using a reagent mixture consisting of primary amine acetate, xanthate, carbonate and clay dispersant. This flowsheet was efficient from a technical point of view, but the relatively small size of the Jabali resource in comparison to the high capital cost, and the lack of a cheap and abundant power supply in the area, resulted in unacceptable economic returns.

After extensive laboratory test work, a second more profitable proprietary metallurgical process (LTC technology) was identified in 2004 (Grist, 2006). As with the previous method, this route was also questionable in its ability to selectively discard dolomite (which is the main constituent of the host rock) from smithsonite. This continued to produce high and variable losses of Zn from samples containing <5 wt.% Zn, because it was not known that in these poorer parts of the deposit, Zn was contained also in dolomite (Zn-dolomite), and this "impure" mineral was discarded as waste together with the pure dolomite of the host rock. Despite this problem, the LTC process allowed good zinc recoveries, at lower costs than with the previous method (Grist, 2006): it enabled to recover up to 80% from the bulk ore, even if it was impossible to raise the recovery over this level. The reason of this are briefly reported in the following paragraphs and were fully discussed by Mondillo et al. (2011, 2014). In March 2013, after a few years of work

on the site, due to the realignment of the ZincOx strategy towards recycling instead of exploitation of primary natural resources (ZincOx press release, 2013), this Company sold its interest in the Jabali Project to Ansan Wikfs, which currently owns the deposit.

The Jabali deposit has been already subjected to scientific research in the past. The resulting data have been reported in: Christmann et al. (1989), Al Ganad (1991), Al Ganad et al. (1994), Mondillo et al. (2011, 2014), and in several unpublished reports for mining companies (e.g. Allen, 2000; SRK Consulting, 2005).

The Jabali deposit was already the subject of a PhD thesis (Mondillo, 2013) and a previous publication (Mondillo et al., 2013). In both papers the petrography, mineralogy and geochemistry of the supergene mineral assemblage was investigated with traditional methods (OM, CL, XRD, SEM-EDS). A quantitative XRD-Rietveld analysis was also been carried out, whose results are briefly described in the following paragraphs.

The aim of this chapter is to carry out a quantitative characterization of the Jabali deposit, obtained with the use of Automated Mineralogy by QEMSCAN®, in order to obtain a more accurate and reliable definition of the nonsulfide mineral assemblage, that could be useful to establish a processing route leading to metallurgy.

In conformity with the other chapters of this thesis, here will be listed:

1) The geological setting of the Jabali deposit, comprehensive of the general frame and the geological evolution of the whole district,

2) A brief resume of the previous studies on the petrography and mineralogy of the deposit (Mondillo et al., 2011, 2013) comprehensive of geochemical analyses of the mayor and minor elements. The results of the stable C-O isotope geochemistry will be also discussed, which constrain the genetical conditions of the Jabali supergene deposit.

3) Chemical analyses and Quantitative characterization of the nonsulfide ore assemblage and mineral composition of the deposit, mainly addressed to the feasibility study and metallurgy. This is the original part of this thesis, which has been carried out on the already sampled drill cores.

4. 2. Geological setting and tectonic of Yemen; stratigraphy of the Jabali area

Yemen is located in the southwestern corner of the Arabian Peninsula. The country is bordered by Saudi Arabia (north) and Oman (east), and by Red Sea (west) and Gulf of Aden (south) (Figure 4.1). The geology of Yemen comprises: 1) Precambrian basements, transected by a failed Jurassic rift system, formed during the break-up of the Gondwana supercontinent; 2) Jurassic pre-, syn-, and post-rift carbonate and clastic sediments; 3) Tertiary to Recent sediments and magmatic rocks, associated to the opening of the Gulf of Aden-Red Sea rift (Menzies et al., 1994).

The basement mainly consists of volcanic and sedimentary rocks, metamorphosed and intruded by granites and granodiorites (Whitehouse et al., 1998). At the end of the Proterozoic, this area was subjected to an extensional regime resulting in an uplift and erosion and in the formation of wrench –fault systems developing in several sedimentary basins (e.g. Najd fault-system; Ellis et al., 1996) filled by marine and deltaic clastic successions (Beydoun, 1997). As some of the terranes currently forming the Anatolian Peninsula, Yemen was part of the Gondwana (Triassic-Middle Jurassic) until the late Jurassic break-up, which caused the split up of the Arabian plate from the Gondwana

itself. This big event caused in Yemen the formation of five basins. One of them is the Sab'atayn basin, which hosts the Jabali deposit (As-Saruri et al., 2010).

Here follows a brief stratigraphic description of the Sab'atayn basin (Figure 4.2).

The succession starts with pre-rift continental clastic sediments (Kuhlan Fm.) passing upward to transgressive shallow-marine facies. Late Jurassic marine sediments of the Amran Group follow. The Amran Group occurs in all the Yemen territory, but generally differs from zone to zone in thickness and facies. This Group is subdivided from bottom to the top in several Formations (Figure 4.2)*: 1) Shuqra Fm., 2) Madbi Fm., 3) Sabatayn Fm.* and *4) Naifa Fm.* (Menzies et al., 1994; Beydoun *et al.*, 1998; Ahlbrandt, 2002).
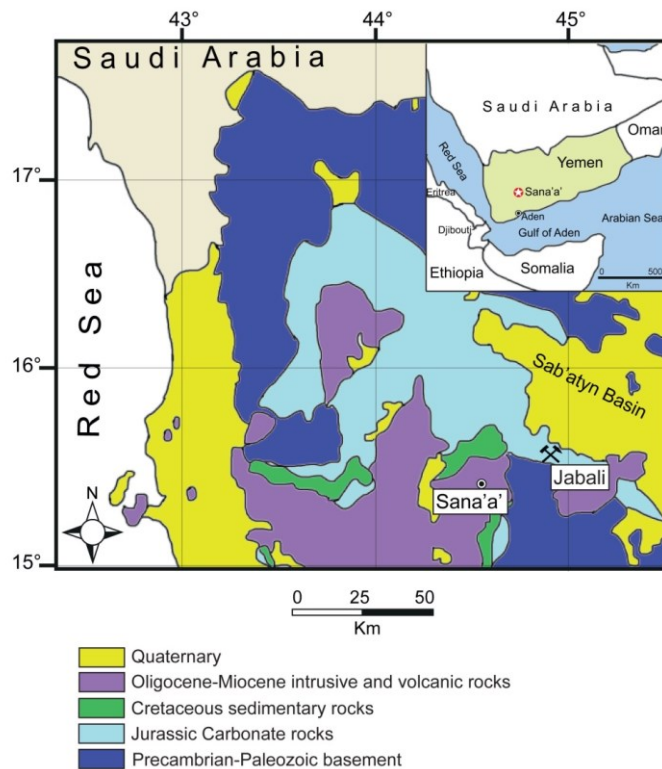
Figure 4.1: Geological map of western Yemen, with the location of the Jabali deposit (Santoro et al., in press).

1) Shuqra Fm. (Callovian-Oxfordian), is the most widespread Fm in Yemen, and represents the host formation of the Jabali deposit. It consists of marine fossiliferous limestones deposited directly on the Kuhlan Fm., during a pre-rift stage. Starting from the bottom we find several lithological units: 1) detrital intertidal limestone; 2) marls and thinly bedded carbonaceous biomicrite, 3) foraminiferal biomicrite interbedded with chert nodules, 4) dolomitic marl interbedded with dolostone, sandy oolitic-oncolitic limestone interbedded with fossiliferous argillaceous limestone and bioclastic sandstone, 5) coral-algal stromatolitic limestone, containing organic fragments, oncolite grains and black foraminiferal biomicrite (Youssef, 1998).

2) Madbi Fm. (Kimmeridgian-Tithonian), formed in a syn-rift stage. It consists of organic-rich-bituminous marine shales, sandstones, debris flow breccias, well-bedded limestones, and turbidites (As-Saruri et al., 2010).
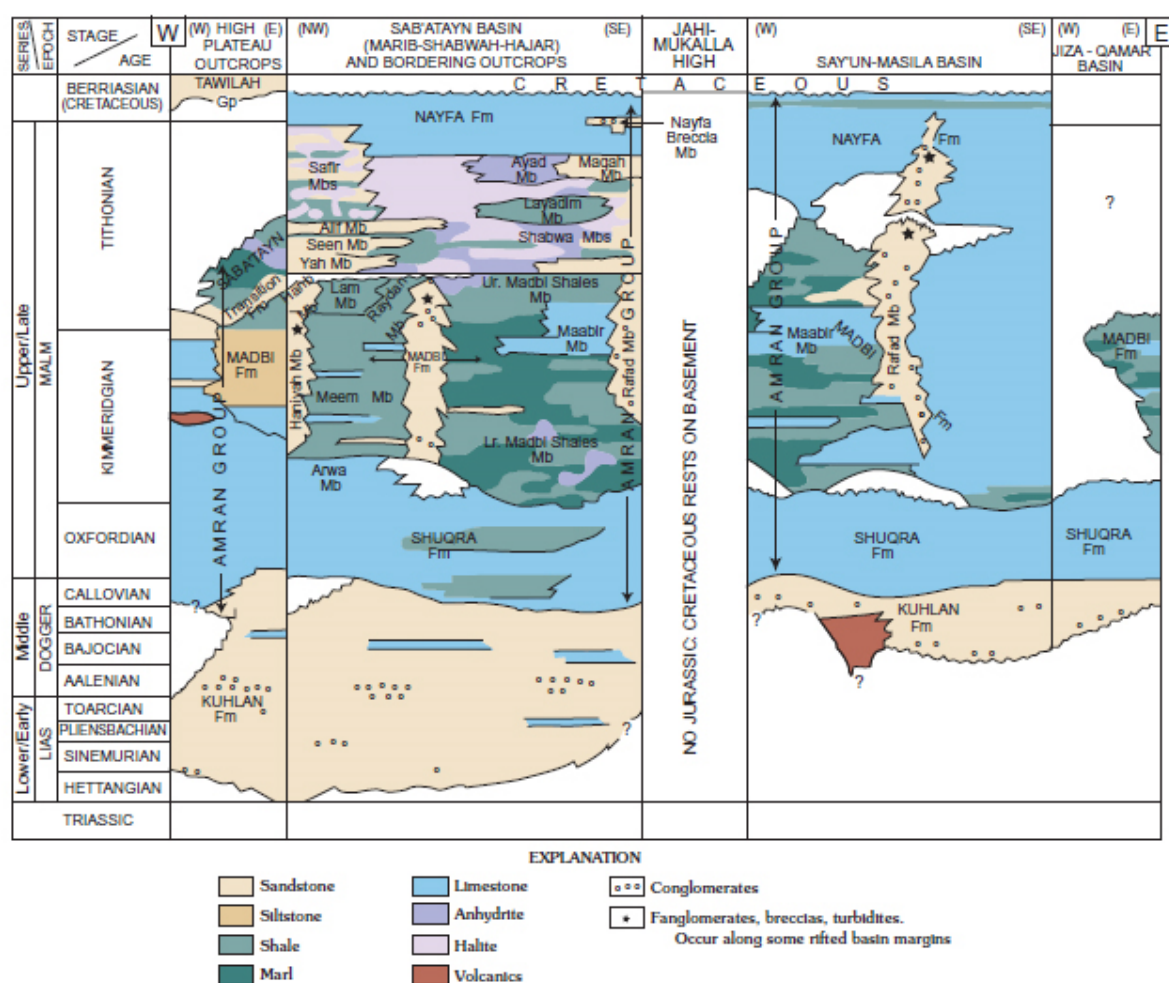
Figure 4.2: Jurassic lithostratigraphy, correlations, and spatial stratigraphic distribution for Yemen (Beydoun et al., 1998; Ahlbrandt, 2002).

3) *Sabatayn Fm*. (Tithonian) is also a syn-rift succession and consists mainly of evaporites, salts, and shales (Beydoun et al., 1998).

4) *Naifa Fm.* (upper Tithonian-Berriasian) is a post-rift deposit (Csato et al., 2001) consisting of marine platform carbonates and marine clastics, dolostones and dolomitic shales, marls and silts, and fine-grained shelly limestones, locally yielding a rich ammonite fauna (Menzies et al., 1994; Beydoun et al., 1998).

Cretaceous in Yemen is represented by the Tawilah Gp., which varies from Western to Eastern Yemen. In western Yemen it consists of continental facies typical of braided, fluvial-channel environments (cross-bedded sandstones interbedded with paleosols), while in the eastern zone there are several shales and limestones indicating a marine facies (Beydoun et al., 1998).

The Oligocene-Miocene is marked by another rifting phase associated to the opening of the Red Sea and the Gulf of Aden. A widespread volcanism affected all the Western Yemen, while the effects of this Rift stage are absent in Eastern Yemen.

The Early Miocene magmatic products consist of plutonic bodies and mafic and felsic dykes (Radfan area, age ~25-16 Ma). During this Rifting activity Yemen moved away

from the Gondwana supercontinent along the numerous faults related to the Red Sea opening (Menzies et al., 1997; Huchon et al., 2003). This movement caused a strong volcanic activity in Yemen during the Tertiary. In the Jabali area this volcanism resulted in the emplacement of trachytic dykes and sills, alkaline granites and in late Miocenic basaltic plateaus and volcanic centers (Capaldi et al., 1983; Huchon et al., 1991). During Plio-Quaternary a strong and widespread volcanism affected all the Yemen. This volcanism is also responsible for the genesis of several thermal springs, which triggered the deposition of thick travertine sequences in several districts (i.e. Sirwah area, Jabal as Saad, Weiss et al., 2009; Allen, 2000). During the Plio-Quaternary, furthermore, the western portion of Yemen (where the Jabali deposit is located) underwent considerable uplift (Menzies et al., 1997; Brannan et al., 1997). This uplift, most likely, favored the exhumation of the primary deposit, and hence its oxidation (Mondillo et al., 2011, 2014).

The Jabali deposit is located in correspondence of a small plateau, on the eastern flank of a NW-SE-elongated mountainous area, known as "Jabal Salab", that is a segment of the western boundary of the Sab'atayn basin. The plateau is delimited to SE by several valleys, which cut the mineralization that is exposed along their flanks.

The deposit is hosted in dolomitized Jurassic carbonate platform sediments of the Shuqra Fm., belonging to the Amran Gp. (Al Ganad et al., 1994). This formation in the Jabali zone overlies directly the Proterozoic basement (Figure 4.2).

The host rock of the Jabali mineralization corresponds to massive bioclastic and biomicritic limestone, locally oolitic with coral bioherms of homogeneous thickness (Kimmeridgian) partly dolomitized which directly underly the Madbi Fm. (Figure 4.2). The whole Jurassic succession was intruded by numerous trachytic dykes and sills, related to Tertiary alkaline volcanism of the area (early Miocene). This volcanism is also responsible for the widespread hydrothermal activity and the travertine deposits (Allen, 2000).

The whole area is affected by brittle deformation and by several faults. This fault set includes the main Jabal Salab fault that acts as a synthetic fault, and borders the shoulder of the plateau below the Jabal Salab peak, as well as the associated sub-parallel structures (antithetic faults).

4.3. Zinc–lead deposits in Yemen

Yemen, as the other countries in the Arabian Peninsula, has a high mineral potential, which includes industrial minerals (i.e. celestine, clays, dolomite, feldspar, gypsum, limestone, magnesite, perlite, sandstone, talc, and zeolite), gas and oil and metal resources (i.e. cobalt, copper, gold, nickel, silver, zinc, iron, titanium, REE, tungsten, tin, and radioactive elements) (Yemen Geological Survey and Mineral Resources Board 2009).

Zinc and lead mineralization in Yemen are generally hosted in Jurassic-to-Paleocene sedimentary rocks (dolomite, limestone) and associated with the rifts or rift-affected blocks related to the Gondwana break-up (Jurassic), or the Red Sea opening in Oligo-Miocene. Most ore concentrations have been considered to belong to MVT deposits (Robertson Research Minerals Ltd., 1993), due to the multiple mineralogical and depositional evidence (carbonate host rocks, stratabound mineralization, occurrence of

saddle dolomite). The map in Figure 4.3 shows the distribution of the Zn-Pb-(Ag) deposits in Yemen.

The major source of Zn-Pb-(Ag) is the Jabali district, where also minor deposits such as Barran, Al-Kwal and Haylan and Dhi Bin (75 km north of Sana'a) occur. A few sulfide orebodies are still present, but the most economic deposits correspond to their oxidized levels, where supergene nonsulfide minerals occur in association with Fe-(hydr)oxides (Yemen Geological Survey and Mineral Resources Board 1994, 2009).

The Tabaq district in southern Yemen is another example of MVT ore type (Robertson Research Minerals Ltd., 1993). It lies about 500 km east of Jabali, and is located in the same rift system. The mineralization consists of stratabound Zn-Pb orebodies hosted by a Jurassic-Paleocene carbonate platform sequence (Veslov, 1990; Al Ganad, 1992). In the same district of Tabaq there are also the Jabal Al-Jubal, Wadi Rama, Yab'uth, Ras Sharwyn, Wadi Jardan and Ras Ba Sa'd deposits, which are all hosted in locally dolomitized Paleocene limestone, and are generally related to fault zones (Yemen Geological Survey and Mineral Resources Board 2009).

Also in these mineralizations, as in the Jabali district, the most economic parts are in correspondence of the oxidized zone.

A peculiar deposit in Yemen is Wadi al Masylah, located in the Mukalla area. Here the mineralization is rather different from those quoted above and consists galena and barite veins structurally controlled by faults. The secondary mineralization also contains willemite, smithsonite, cerussite, descloizite, calcite, pyrolusite and celestine.
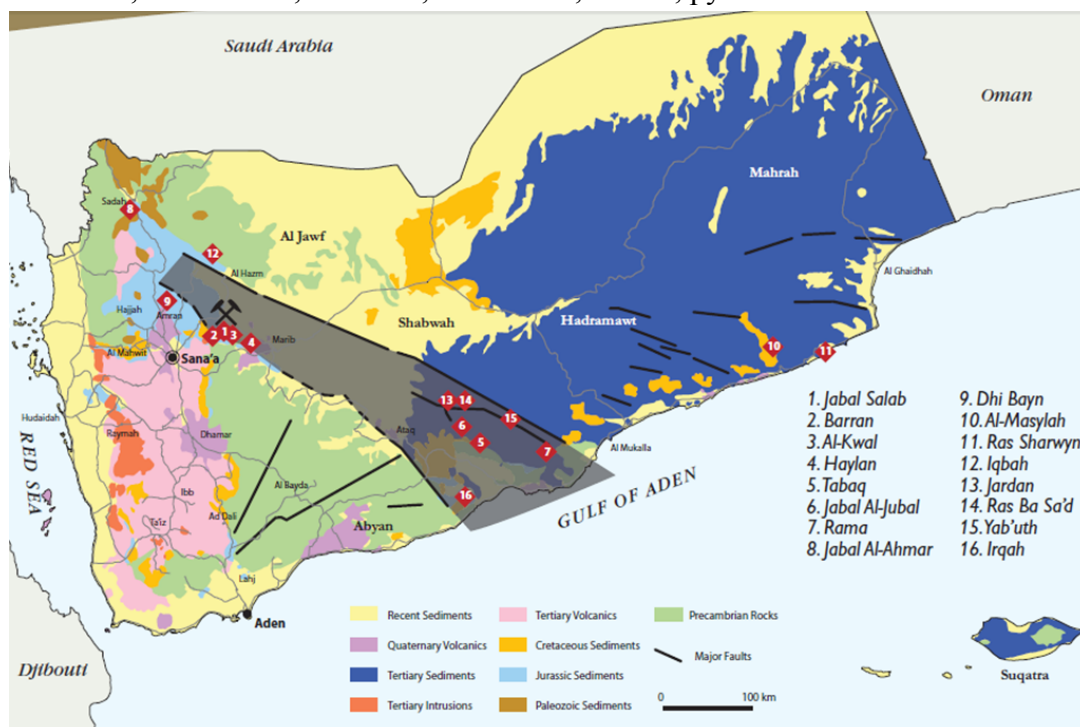
Figure 4.3: Geological sketch map of Yemen with zinc-lead occurrences, most of which are concentrated in a rift valley (shaded). Jabal Salab mine marked with hammers (Yemen Geological Survey and Mineral Resources Board, 2009).

4.4. Jabali Mineralization

The Jabali mineralization is hosted in Jurassic limestone, partly dolomitized of the Shuqra Fm. (SRK Consulting, 2005). The deposition of the orebodies, as well as the dolomitization seems to have been driven by faults orientation. The ore is almost completely oxidized with only a small portion unaltered thanks to a black mudstone and argillite cover (Al Ganad et al., 1994). The orebodies are both tabular and parallel to stratigraphy, and vertical along fractures, faults and at the intersection of these structures. The Jabali deposit is only partly exposed, since at least half of the mineralized lithologies occur in the subsurface below the hill called Jabal Barrik.

The nonsulfide ore is massive, semi-massive and disseminated, and is characterized by vuggy to highly porous, brown-orange to white zinc nonsulfide minerals. Smithsonite is the main zinc mineral, while less common are hemimorphite and hydrozincite (only in outcrops). Cerussite and anglesite also occur as main lead minerals. Iron staining is common throughout the mining area, resulting in variable concentrations of goethite, hematite, and Mn-(hydr)oxides. Ag-sulfide and native silver are also present. Gypsum was observed through the entire mineralized area. Remnants of the primary sulfide association can be observed in outcrop and drillcores and consist of sphalerite (predominant), galena, and pyrite/marcasite.

Different hypotheses on the nature of the primary sulfide concentrations have been formulated:

Al Ganad et al. (1994) considers the primary mineralization as a paleokarst-hosted Mississippi Valley deposit formed from fluids migrating from the Sab'atayn basin during Late Jurassic (Kimmeridgian) rifting, whereas, Allen (2000), hypothesizes a sulfide mineralization generated by the emplacement of CRD-MVT hybrid fluids along extensional structures related to Red Sea rifting, contemporarily to the development of magmatic activity in the region (~22 Ma). On the basis of the chemistry of the deposit (low content in As, Mo, Bi, and Sb) and of the temperatures and salinity of the fluid inclusions in sphalerite (Al Ganad et al., 1994) and Mondillo et al. (2011, 2014) consider the MVT hypothesis to be more realistic.

Also different views have been expressed on the age and genesis of the supergene mineralization. Al Ganad et al. (1994) propose a long period of oxidation, extended from Cretaceous to Present, whereas Allen (2000) believes that there has been a single oxidation stage, which started in Miocene and continues until present time. According to more recent research (Mondillo et al., 2011, 2014), the most favorable setting for the development of the Jabali secondary deposit could be placed in early Miocene (~17 Ma), when supergene alteration was favored by major uplift and exhumation, resulting from the main phase of Red Sea extension. Low-temperature hydrothermal fluids may have also circulated at the same time, through the magmatically-induced geothermal activity in the area.

4.5. Previous studies

Mineralogy and petrography

Several studies have been already conducted on the Jabali deposit by various authors (Al Ganad 1994; Allen, 2000). More recently Mondillo et al. (2011; 2014) carried out a complete mineralogical, petrographic, and geochemical analysis on 40 samples (each one consisting of 1m core) from 3 drill-cores considered representative of the whole orebody (Figures 4.4 and 4.5). The analyses were mainly carried out by the use of OM, CL, SEM-EDS, and XRD methods.

An attempt to obtain quantitative phase analyses has been done (Mondillo et al., 2011) using the XRD-Rietveld method (Rietveld, 1969). A geochemical study on the C-O stable isotopes of the carbonate host rock and of the supergene zinc minerals has also been carried out in order to constrain the conditions for the precipitation of the supergene mineralization.

According to petrographic investigations, dolomite occurs in 4 generations (Al Ganad, 1994; Mondillo et al., 2011): the first two phases are interpreted as early diagenetic and replace the primary limestone. The last two generations show the typical "saddle" features and generally crosscut the previous generations (Al Ganad et al., 1994). By SEM-EDS it was verified that *saddle* dolomite contains Mn (up to 2 wt.% MnO), which is responsible for its red cathodoluminescence color, Fe (up to 6 wt.% FeO) and Cd (up to 1.5 wt.% CdO). All the dolomite phases are partly affected by a de-dolomitization process, transforming dolomite into calcite (Al Ganad, 1994). Under SEM-EDS analyses, a ZnO enrichment (up to 22 wt.%) was observed in dolomite, which is inversely correlated to its MgO content. The Zn-dolomite is also recognizable under CL, as it shows red-yellow colors.

The Zn-carbonate smithsonite is generally intergrown with Fe-(hydr)oxides in reddish concretional agglomerates, as well as with thin layers of clays. It occurs in two different generations: one replacing both the dolomite host rock (generally the *saddle* dolomite) and the Zn-bearing dolomite, and another precipitated in vugs and cavities or as vein fillings, neo-formed crystals and/or zoned concretions (Mondillo et al., 2011). Replacive smithsonite consists of very small rhombohedral/scalenohedral microcrystals (also <10μm), which form agglomerates mimicking the original macrocrystalline habit of dolomite. The replacive smithsonite generally have high Mg amounts locally reaching 8-10 wt.% MgO, Mn (up to ~3 wt.% MnO), Fe (up to 5-6 wt.% FeO), and Ca (up to 6 wt.% CaO), while concretionary smithsonite can be characterized by up to 20 wt.% MgO amounts (corresponding to a substitution of Mg for Zn in the smithsonite lattice around 70%), up to ~2 wt.% MnO, up to ~2wt.% CdO, up to ~1.5 wt.% CaO, up to ~1.5 wt.% PbO.

Hydrozincite occurs in outcrop as smithsonite replacement, vein and porosity filling, and crusts. Hemimorphite is rare and, where occurs, it is in cavities, voids and in veins (Mondillo et al., 2011, 2014).

The (hydr)oxides are quite abundant at Jabali: Fe-(hydr)oxides generally contain high values of FeO (around 60 wt.%) ZnO (up to 12 wt.%), PbO (up to 7 wt.%) and SiO_2 (up to 6 wt.%). Also most Mn-(hydr)oxides consist not only of chalcophanite (which should

contain only MnO and ZnO), but of possibly amorphous phases containing Mn-Pb-Fe in variable proportions (PbO ~20-30 wt.%, FeO ~10 wt.%).

Galena and sphalerite remnants also occur; galena is generally coated by cerussite and anglesite. Sphalerite occurs in two generations (Al Ganad, 1994): a first dark colored, and a second more abundant and represented by zoned euhedral to subhedral honey-colored or brownish-red crystals. Sphalerite contains iron and silver, cadmium, copper, germanium and mercury. It is often replaced by smithsonite and gypsum.

At the boundary between sphalerite and smithsonite, secondary sulfides were also detected: abundant greenockite [CdS], and rare covellite [CuS].

Silver sulfide is also a quite common mineral at Jabali, even though it occurs in very small inclusions in other minerals. It has been observed commonly in association with concretionary smithsonite, gypsum, greenockite, and also as small spots within hemimorphite.

Among other minerals Zn-smectite, locally associated with kaolinite and illite, also occurs as fill of the porosity of the host rock.
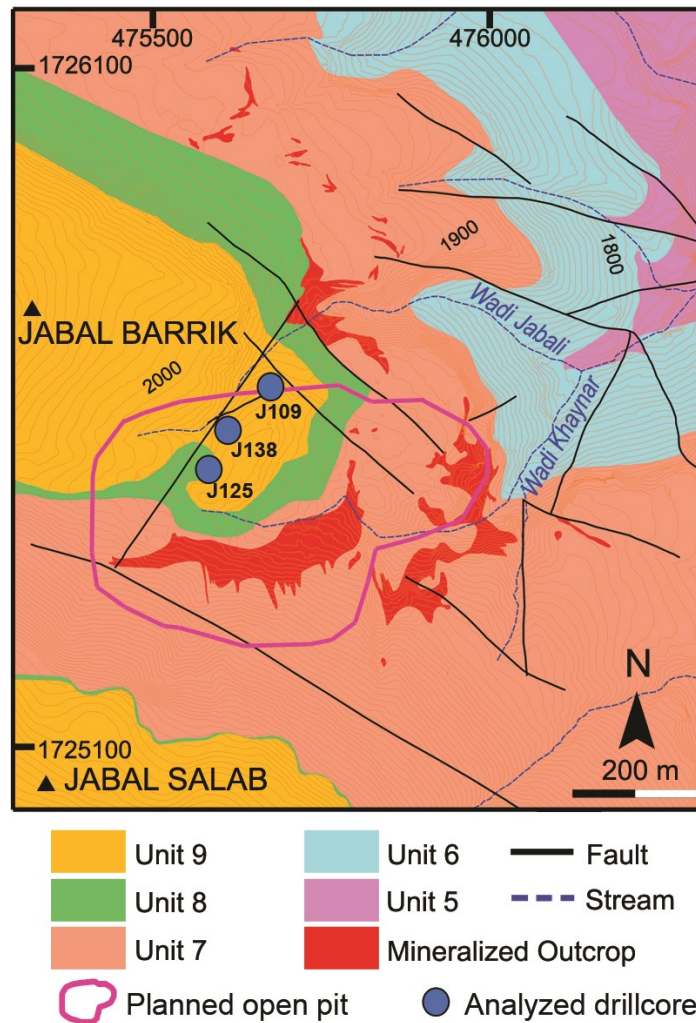
Figure 4.4: Geological map of the Jabali mining site with the location of analyzed drill holes, and the planned open pit area (modified from SRK Consulting, 2005). Stratigraphy of the Jabali area. Shuqra Formation - Unit 1: sandstone and conglomerate, transgressive on the Late Proterozoic basement; Unit 2: gypsiferous mudstone overlain by dolomitized calcarenite, marl and nodular limestone; Unit 3: micritic-biomicritic limestone (Callovian), with nodular concretions and chert layers; Unit 4: (not on the map) micritic limestone and lagoonal/lacustrine dolomite; Unit 5: partly dolomitized bryozoan calcarenite (Late Oxfordian- Early Kimmeridgian), overlain by coral-bearing oolitic limestone; Unit 6: gypsiferous mudstone grading into micritic limestone (Kimmeridgian) and marl; Unit 7: massive bioclastic-biomicritic limestone, locally oolitic with coral bioherms (Kimmeridgian). Madbi Formation - Unit 8: black mudstone and argillite with gypsum crystals and dolomite intercalations, grading laterally into micritic ammonite-bearing limestone (Late Kimmeridgian-Tithonian). Sab'atayn Formation – Unit 9: biomicrite with oncolites and bio-oocalcarenite (Late Jurassic) (Mondillo et al., 2014).
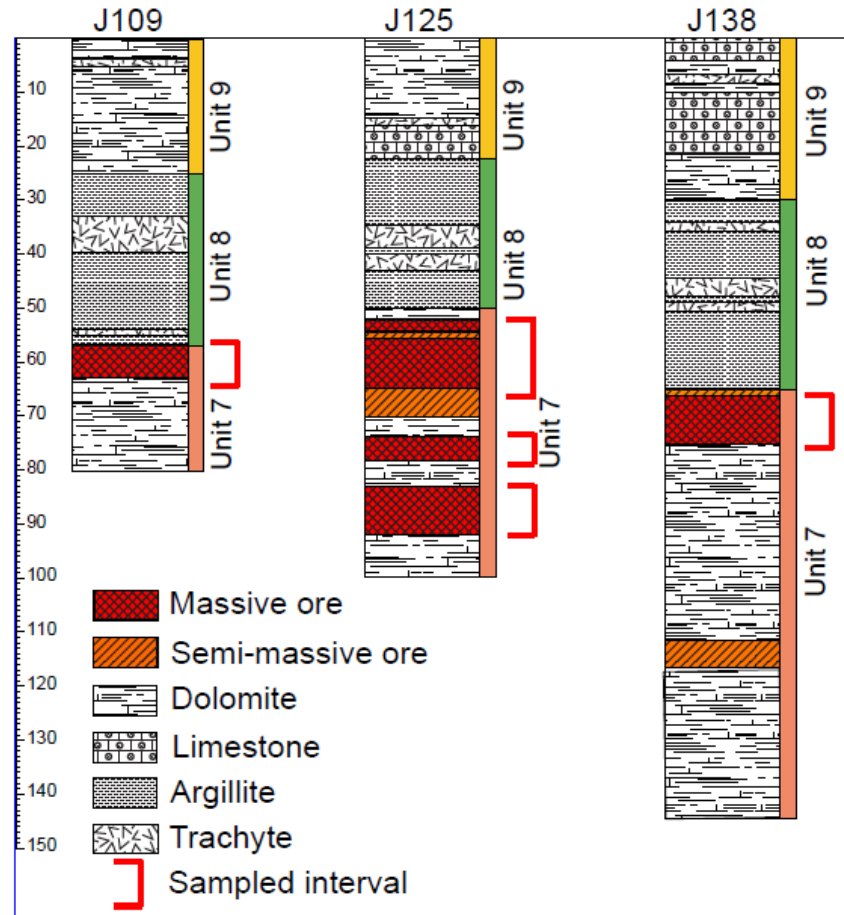
Figure 4.5: Stratigraphic logs of selected drill holes. The selected intervals are indicated in red. The color bars on the right of the logs indicate the corresponding stratigraphic Units. Explanation for the Units is in Figure 5.4 (Mondillo et al., 2014).

X-ray quantitative Rietveld phase (QPA)

In table 1 are reported the Quantitative analyses obtained by the Rietveld method (Mondillo et al., 2011). The analyses show that smithsonite at Jabali ranges from a few % to 20 wt.%, with a maximum of ~ 82 wt.%. Sphalerite occurs in much lower amounts (up to 8 wt.%), as well as galena (up to 3 wt.%), cerussite and anglesite (both up to 4 wt.%). Hemimorphite and hydrozincite were not detected in the drillcore samples, while sauconite and other clay minerals, though having been identified, are in low amounts. Dolomite, being the host rock of the Jabali deposit, is quite abundant, even in the mineralized samples (up to 50 wt.%). Gypsum, Fe-oxides and hydroxides (hematite and goethite) and Pb-Mn-(hydr)oxides (chalcophanite) occur in many samples with variable values.

Table 1: X -Ray-QPA by Rietveld method (Mondillo et al., 2011)

Sample n	J109-3	J109-5	J125-2	J125-3	J125-5	J125-6	J125-8	J125-9	J125-10	J125-15	J125-20 wt.%	J125-21	J125-22	J125-30	J125-31	J125-32	J125-33	J138-8	J138-9	J138-10
Dolomite	76.9	78.6	83.6	2.7	77.9	19.5		2.6	61.1	95.7	56.4	15.6	30.6	55	85.6	16.9	59.4	89.4	83.8	62.1
Calcite	15.3	1.3			0.2					0.1	32.9		38.1			0.1	0.1			29.7
Smithsonite	5.2	17.7	3.3	38	5.9	63.3	82.5	82.8	34.5	2.9	5.8	45.4	10.4	39	10.5	78.1	35.6	6.4	10.1	2
Cerussite	0.7							4	0.9					0.4		0.3	0.4	0.1	1.8	0.7
Gypsum			7.8	52.5	7.7	8.7	8.9	5.1	1.7	0.1										
Anglesite				3.7		2.6	2.6	3.1												
Sphalerite			4.7	0.1	7.6	0.7														0.6
Galena	0.8		0.3		0.5	0.4								0.2				0.1	2.3	0.9
Chalcophanite		0.2							0.2	0.1										
Hematite					0.1											0.1	0.2	1.6		
Goethite	1.2	2.1	0.3	3		3.2	3.8	2.4	1.7	1.2	4.4	7.7	5.5	2.1	3.8	4.6	4.3	2.3	2.1	3.9
Kaolinite						1.6	2.2				0.5	30.8	15	3.3						
Sauconite												0.4	0.3							
Illite												0.5	0.3							
Quartz																				

4. 6. Analytical Methods

Twenty mineralized samples were chosen for this thesis, in order to carry out a renewed petrographic and mineralogical characterization, as well as quantitative analyses using QEMSCAN®. The samples, which are the same analyzed by Mondillo et al. (2011), consist of 1 m-long quarter core sections (Table 2). For this study it was necessary to carry out new chemical analyses on the selected samples, as the analyses already reported in Mondillo et al. (2011), corresponded to the commercial assays carried out by ZincOx plc.

The new chemical analyses were performed by Actlabs, Ancaster (Ontario), using ICP-MS. Forty elements were analyzed: Si, Al, Fe, Mn, Mg, Ca, Na, K, Ti, P, Zn, Pb, S, Ba, Sr, Y, Sc, Zr, Be, V, As, Bi, Co, Cs, Cu, Ga, Ge, In, Li, Mo, Nb, Ni, Re, Se, Sn, Ta, Te, Th, Tl, U, W).

Table 2: Location of the drillcores depicted in Figure 5.5

Drillcore n.	From (m)	To (m)	Sample n.
J109	59.3	60.3	J109-3
	61.65	62.7	J109-5
J125	51.78	53.1	J125-2
	53.1	54.73	J125-3
	55.73	56.73	J125-5
	57.92	59.45	J125-6
	60.97	62	J125-8
	62	64	J125-9
	64	65	J125-10
	69	70	J125-15
	75.5	76.5	J125-20
	76.5	77.5	J125-21
	77.5	78.5	J125-22
	85.5	86.5	J125-30
	86.5	87.5	J125-31
	87.5	88.5	J125-32
	88.5	89.5	J125-33
J138	72	73	J138-8
	73	74	J138-9
	74	75	J138-10

For the analysis of major elements, the samples were mixed with a flux of lithium metaborate and lithium tetraborate and fused in an induction furnace. The melt was poured into a solution of 5 % nitric acid containing an internal standard, and mixed until completely dissolved. The samples were measured for major oxides and selected trace elements. The calibration was performed using 7 prepared USGS and CANMET certified reference materials. Total sulfur analysis was carried out by a combustion technique. Sulfur was measured as sulfur dioxide in the infrared cell using an Eltra CS-800. The metallic elements (Pb, Zn, Cu, Co, Ni, Mo, As, Sn, Bi, In, Li) were evaluated after a fusion-sintering process using sodium peroxide. The samples were sintered at 650° C in a

muffle furnace, and then dissolved in a solution of 5 % nitric acid. Fused samples were diluted and analyzed by Perkin Elmer Sciex ELAN ICP/MS. The fusion sintering process using sodium peroxide was preferred, in order to dissolve Zn from this type of ore, as aqua regia may not have been fully effective (Walsh et al., 1997).

QEMSCAN® analysis and SIP file
Sample preparation was carried out first at the University of Naples (Italy) and then completed at the Camborne School of Mines, University of Exeter (UK) (*see chapter 2* for more detailed information on sample preparation). All the samples correspond to 1 m-long quarter core sections.

Thirty grams of the five most Zn-rich samples were chemically treated to simulate a concentration process by heavy-liquid separation, using Na-polytungstate. Two uncrushed mineralized fragments from the cores were also analyzed with QEMSCAN®, in order to visualize the texture of the ore, to serve as a guide for the interpretation of the granulated material.

QEMSCAN® analyses were carried out at the Camborne School of Mines, University of Exeter, UK, using a QEMSCAN® 4300. The QEMSCAN® software version used in this study was iMeasure v. 4.2 for the data acquisition and iDiscover v. 4.2 for the spectral interpretation and data processing. X-ray data were collected in fieldscan analytical mode every 10μm spacing across the polished sample surfaces (~3 cm^2 per sample), with 1000 total X-Ray counts per spectrum acquired (see *chapter 2* for more detailed analytical parameters). The output data consisted in distribution maps of the mineral phases and in a database containing all the information on the statistical distribution of the particles, grain sizes, mineral association and quantitative analyses for each sample.

The QEMSCAN® modal mineralogy was output in both mass % (wt.%).

A Species Identification Protocol (SIP) is required, in order to discriminate the mineral species by QEMSCAN® (see *chapter 2* for more detailed information).

A modified species identification protocol was created specifically for this study, by developing the SIP created by Rollinson et al. (2011), to which were added the nonsulfide ore compounds typical of the Jabali deposit. Part of the newly added phases were already known from previous studies (Mondillo et al., 2011, 2014); other mineral compounds detected by QEMSCAN® during this study have also been included in the species identification protocol.

The chemistry of the mineral species set in the SIP file is in line with the average composition of each known mineral (Webmineral, www.webmineral.com), considered as ''*pure*'', and the mass conversion was automatically done by the software after average chemistry and density data were input for each mineral. For those species not respecting the stoichiometry and considered as "*impure*" minerals (e.g. Fe-dolomite, Zn-dolomite) it was necessary to use a SEM-EDS to determine their average chemistry. The density data were evaluated considering the backscattered electron intensity of these compounds, relative to pure phases with known density, and the concentration of the elements they contained. The entries in the SIP file have been inserted as single minerals or categories, on the basis of their chemistry. For the ''*impure*'' minerals (containing several, not so far recorded, elements) it was necessary to split the mineral phases in different entries.

Smithsonite was subdivided in two categories, related to its Mg content: smithsonite (containing <5 wt.% Mg), and Mg-smithsonite (containing >5 wt.% Mg) (Table 3).

A category named "Zn-clays" comprises all the clay mineral phases (not structurally classified), containing Al, Si, Na and Zn, as well as sauconite or Zn-bearing illite and kaolinite.

Dolomite was subdivided into four categories on the basis of its Zn, Fe, and Mn content: dolomite (Fe, Zn, Mn< 5wt.%), Fe-dolomite (Fe> 5 wt.%, Zn and Mn <5 wt.%), Zn-dolomite (Zn>5 wt.%, Fe and Mn <5 wt.%), Zn-Mn-dolomite (Zn and Mn >5 wt.%, Fe <5 wt.%).

The Pb minerals anglesite ($PbSO_4$) and cerussite ($PbCO_3$) were grouped together in a single category, named anglesite/cerussite, because these phases are commonly misidentified by QEMSCAN®. This is due to an X-ray interference caused by the resolution of the EDS detectors (the overlap of Pb and S peaks affects the analysis), the unclear detection of the carbon peak and similar backscattered electron intensities of the two minerals.

Hematite and goethite were grouped in a single category [Fe-(hydr)oxides] because the distinction between them is based on X-ray spectra dominated by the Fe and O lines. Hence, although 1000 X-ray counts per spectra is an acceptable value in order to recognize most minerals, it is typically not enough to precisely distinguish between the above Fe oxidized phases. We added a specific category of Zn-bearing Fe-(hydr)oxides (Zn> 5wt.%), named as Fe-(hydr)oxides (Zn) in the SIP. Another single category was also added for mixtures of Fe- and Mn-(hydr)oxides [Fe-Mn-(hydr)oxides].

Minerals of the SIP file have been validated using a Zeiss EVO 50 SEM with Bruker 4010 EDS SDD detectors, and with Bruker Esprit 1.8 software applied for the standard-less EDS analysis (approx. ±1%), at the Camborne School of Mines. Information gained was used to help to develop the SIP, and in particular boundary categories.

Chemical analyses (ICP-MS) have been used to validate the mineralogical results obtained by QEMSCAN® analysis. Calcium amounts were calculated on the basis of the Ca-bearing minerals: calcite, dolomite, gypsum, apatite (standard CaO contents), Fe-dolomite (30 wt.% CaO), Zn-dolomite (30 wt.% CaO), Zn-Mn-dolomite (30 wt.% CaO). Magnesium was evaluated from the amounts contained in pure dolomite (Fe-dolomite (20 wt.% MgO), Zn-dolomite (14 wt.% MgO), Zn-Mn-dolomite (15 wt.% MgO) and Mg-smithsonite (8 wt.% MgO).

The calculation of the Zn amounts was carried out on the basis of the Zn contents of the pure Zn minerals as smithsonite, sphalerite, hetaerolite, chalcophanite, sauconite (standard composition), Mg-smithsonite (45 wt.% Zn), Zn-dolomite (7 wt.% Zn), Zn-Mn-dolomite (5 wt.% Zn) and Zn-enriched (5 wt.% Zn) Fe-(hydr)oxides. The evaluation of Pb was based on cerussite, galena and coronadite (standard composition), while the Fe amount was calculated using pyrite, chalcophanite, Fe-(hydr)oxides (mainly goethite, 62.32 wt.% Fe), Fe-(hydr)oxides Zn-enriched (56 wt.% Fe), Fe-Mn-(hydr)oxides (8 wt.% Fe).

Table 3: Explanation of the mineral phases detected by QEMSCAN®.

Mineral Category	Mineral Description
Background	All resin related/edge effects, Others.
Dolomite	Any phase with Ca, Mg, O, C.
Fe-dolomite	Any phase with Ca, Mg, O, C and low Fe (approx. ≤5%). May contain small grains of goethite.
Zn-dolomite	Any phase with Ca, Mg, O, C and Zn (approx. ≤10%).
Zn-Mn-dolomite	Any phase with Ca, Mg, O, C with Mn and Zn (approx. ≤10%).
Calcite	Any phase with Ca, O, C. May include Mg-rich Calcite %), (low Mg approx. ≤5%).
Smithsonite	Any phase with Zn, O, C and maybe OH. May include Hydrozincite.
Mg-smithsonite	Any phase with Zn, O, C and maybe OH with Mg (approx. ≤5%).
Fe-(hydr)oxides	Fe oxides such as Hematite, Magnetite, and Fe-hydroxides (Goethite). May contain small grains of other mineral phases.
Fe-(hydr)oxides (Zn)	Zinc rich: Fe oxides such as Hematite, Magnetite, Goethite and Fe-hydroxides. Zn≥10%.
Cerussite/Anglesite	Any phase with Pb, C, O, or Pb, O, S. Most likely Anglesite (Pb, S, O, weathered Galena).
Galena	Any phase with Pb, S.
Sphalerite	Any phase with Zn, S, with minor Fe. Includes Cd rich sphalerite,trace amounts in some samples.
Pyrite	Includes Pyrite/Marcasite, trace Pyrrhotite and Jarosite.
Coronadite	Any phase with Ba, Al, Mn, Pb, V and O. Includes a minor category of a mixture of Kaolinite-Coronadite (fine grained).
Hetaerolite	Any phase with Zn, Mn, O.
Fe-Mn-(hydr)oxides	Any phase with Mn, Fe, O with possible minor Pb,S, Zn.
Chalcophanite	Any phase with Zn, Mn, Fe, O, H.
Zn-clay	Kaolinite/Halloysite/Dickite and any other with Zn (≤ 5%). May include Trace/Minor Sauconite.
Gypsum	Any phase with Ca, S, O. Includes Gypsum and maybe Anhydrite.

4.7. Results: Geochemistry

Chemical analyses

The chemical analyses of major and minor elements (published in Mondillo et al., 2011) show that Zn is highest in the Upper zone of the J125 drillcore (38.02 wt.%) and less abundant in other cores (J109 and J138), where it hardly reaches 10 wt%. Calcium and magnesium are locally abundant, the main host rock being dolomite. Lead reaches a maximum of 13 wt.%. Sulfur (up to ~5-7 wt.%) is related to the occurrence of sulfide remnants or gypsum. Iron is always < ~5% wt. and Mn < ~1 wt%. Among minor elements the highest values have been detected for Ag (up to ~400 ppm) and Cd (up to ~2000 ppm) (Mondillo et al., 2011).

In table 4a,b and c are instead reported the results of the chemical analyses carried out for this thesis on the representative fractions of the core samples (20 samples + 5 concentrates). The analyses are comprehensive of major elements (expressed in oxide compounds wt.%): CaO, ZnO, PbO, SiO_2, Al_2O_3, Fe_2O_3 (total), MnO, MgO, Na_2O, K_2O, TiO_2, P_2O_5; the calculation of LOI has also been reported.

Analyses on minor elements consist of: Ba, Sr, Y, Sc, Zr, Be, V (expressed in ppm) and As, Bi, Co, Cs, Cu, Ga, Ge, In, Li, Mo, Nb, Ni, Re, Se, Sn, Ta, Te, Th, Tl, U, W (expressed in wt.%).

The contents can be roughly compared with the quantitative phase analysis (QPA) obtained with QEMSCAN® in table 5 (*see next paragraphs*).

Calcium ranges from few values up to 30.82 wt.% (J125-20), MgO occurs in lower % (up to ~15% in sample J125-15). The calcium source can come both from calcite and dolomite host rock while, as shown by Mondillo et al. (2014), Mg is not only contained in dolomite, but can occur also in smithsonite.

Zinc occurs with high values in almost all the selected samples from a minimum of 4.58 wt.% ZnO (J125-15) to a maximum of 47.05 wt.% ZnO (sample J125-9). Lead occurs with variable %, generally lower than 10 wt.% except in sample J125-9 (12.50 wt.%

PbO). Chemical analyses on concentrates show interesting results: ZnO can have a significant increase (e.g. from 44.81 wt.% in sample J125-8 to 52.15 wt.% in sample J125-8 Conc., or from 24.15 wt.% in sample J125-10 to 45.80 wt.% in sample J125-10 conc.). The same can be said for lead, even if the increase is less significant, due to the lower presence of lead minerals compared to zinc minerals: e.g. PbO increases from 12.50 wt.% in sample J125-9 to 18.96 wt.% in its concentrate (Table 4a).

Iron is generally low (around ~3 wt.%). In sample J125-21 and J125-22, where higher amounts of Fe-(hydr)oxides have been detected by QPA analyses (table 5), higher amount of Fe_2O_3 are reported (respectively 7.31 wt.% and 6.28 wt.%).

Silica can be present with values ranging from <1 wt.% to ~3 wt.% (except for sample J125-21, where it is up to ~8 wt.%), while MnO is very low and, as well as Al_2O_3 it hardly reaches 1 wt.% (table 4a). Sodium and K_2O, TiO_2 and PO_2 are always lower than 0.5 wt.%.

Total S is generally low, except for the samples where more sulfide remnants occur. The higher values have been detected in the samples J125-3 and J125-5: respectively 7.09 wt.% and 4.5 wt.%.

Among minor elements, the most abundant are: Ba (up to 157 ppm in sample J125-22), Sr (up to 55 ppm in sample J109-3), and V (up to 52 ppm in sample J125-21). Other minor elements occur in negligible amounts (table 4b). All the other elements are reported in table 4c and occur in very low quantities: most of them, in fact, hardly reach <0.001 wt.%.

Table 4a: Chemical analyses of the major elements of the Jabali drillcore samples

Sample n.	SiO_2	Al_2O_3	Fe_2O_3(tot)	MnO	MgO	CaO	Na_2O	K_2O	TiO_2	P_2O_5	ZnO	PbO	S(total)	LOI
							(Wt.%)							
J138-8	0.34	0.11	3.98	0.485	12.37	20.72	0.02	0.01	0.013	0.04	10.36	1.09	0.05	41.9
J138-9	0.49	0.2	3.02	0.476	11.58	19.11	0.05	0.03	0.022	0.03	11.74	7.29	0.53	38.77
J138-10	0.38	0.13	3.3	0.731	8.96	29.56	< 0.01	< 0.01	0.008	0.03	5.07	2.84	0.17	41.53
J125-2	0.21	0.1	2.88	0.695	13.8	22.8	0.03	0.02	0.006	0.03	7.98	0.25	2.75	37.62
J125-3	0.26	0.1	3.36	0.15	0.77	10.94	0.02	0.01	0.005	0.02	29.87	4.68	7.09	29.54
J125-5	0.3	0.16	2.46	0.494	12.09	19.89	0.03	0.02	0.01	0.02	14.31	1.95	4.5	31.35
J125-6	3.26	1.29	2.64	0.941	4.45	7.03	0.02	0.04	0.059	0.03	36.10	3.64	3	31.53
J125-8	0.9	0.36	2.46	0.409	2.38	7.18	0.02	0.03	0.019	0.03	44.81	4.46	1.98	34.13
J125-9	2.85	0.8	1.83	0.232	0.79	1.22	0.06	0.11	0.01	0.03	47.05	12.50	1	33.09
J125-10	0.26	0.08	2.87	0.468	10.04	13.59	0.02	0.01	0.004	0.03	24.15	1.44	0.22	39.88
J125-15	0.25	0.11	2.65	0.609	15.28	23.65	0.03	0.02	0.007	0.02	4.58	0.11	0.06	44.47
J125-20	0.46	0.2	3.03	0.479	8.73	30.82	0.03	0.03	0.012	0.04	6.61	0.25	< 0.01	42.58
J125-21	8.07	3.35	7.31	0.299	2.59	3.2	0.03	0.06	0.177	0.09	41.45	0.54	< 0.01	27.88
J125-22	4.32	1.73	6.28	1.261	2.83	21.79	< 0.01	< 0.01	0.086	0.08	15.43	1.26	0.04	34.29
J125-30	0.72	0.33	2.4	0.31	5.45	8.82	0.02	0.03	0.015	0.03	33.73	1.86	0.04	37.67
J125-31	0.36	0.14	3.63	0.454	9.81	17.48	0.02	0.02	0.007	0.04	16.06	0.87	< 0.01	41.31
J125-32	0.33	0.08	3.1	0.349	3.47	6.74	0.02	< 0.01	0.003	0.03	51.03	0.95	< 0.01	35.4
J125-33	0.38	0.13	4.11	0.353	6.75	10.07	0.03	0.01	0.004	0.05	32.86	1.92	< 0.01	37.86
J109-3	0.26	0.1	2.41	0.571	11.62	28.19	0.03	0.01	0.003	0.02	6.24	4.27	0.28	41.82
J109-5	0.33	0.11	2.43	0.516	10.65	17.27	0.02	0.01	0.005	0.03	16.43	0.07	< 0.01	42.37
J125-8 (conc.)	2.28	0.77	2.66	0.368	1.08	1.65	0.05	0.06	0.028	0.03	52.15	5.00	1.42	34.58
J125-9 (conc.)	3.57	1.09	1.75	0.219	0.58	0.48	0.08	0.13	0.008	0.03	44.93	18.96	1.05	31.69
J125-10 (conc.)	3.1	0.76	2.84	0.437	4.36	4.32	0.03	0.05	0.006	0.03	45.80	2.89	0.16	35.26
J125-32 (conc.)	0.75	0.18	3.3	0.27	1.66	1.05	< 0.01	< 0.01	0.002	0.03	56.26	1.21	0.02	34.56
J125-33 (conc.)	0.77	0.27	5.93	0.288	3.44	3.71	0.08	0.04	0.014	0.05	46.30	3.10	0.02	0.02

Table 4b: Chemical analyses of the minor elements of the Jabali drillcore samples.

Sample n.	Ba	Sr	Y	Sc	Zr	Be	V
				(ppm)			
J138-8	2	32	5	< 1	8	< 1	9
J138-9	4	33	5	< 1	10	< 1	8
J138-10	78	24	6	< 1	4	< 1	< 5
J125-2	75	37	4	< 1	6	< 1	< 5
J125-3	2	24	1	< 1	4	< 1	< 5
J125-5	3	31	4	< 1	4	< 1	< 5
J125-6	29	49	5	1	14	< 1	21
J125-8	22	10	3	< 1	7	< 1	11
J125-9	18	17	3	< 1	8	< 1	7
J125-10	5	20	4	< 1	3	< 1	6
J125-15	14	32	3	< 1	4	< 1	8
J125-20	121	22	5	< 1	5	< 1	9
J125-21	31	17	7	3	57	< 1	52
J125-22	157	16	7	2	28	< 1	46
J125-30	3	11	4	< 1	7	< 1	12
J125-31	3	15	4	< 1	4	< 1	10
J125-32	14	8	3	< 1	4	< 1	6
J125-33	2	12	4	< 1	3	< 1	7
J109-3	10	55	7	< 1	4	< 1	5
J109-5	12	18	8	< 1	3	< 1	9
J125-8(conc.)	24	9	3	< 1	9	< 1	13
J125-9(conc.)	23	18	3	< 1	6	< 1	6
J125-10(conc.)	23	23	5	< 1	6	< 1	8
J125-32(conc.)	5	5	2	< 1	2	< 1	9
J125-33(conc.)	3	9	3	< 1	10	< 1	8

Table 4c: Chemical analyses of the Jabali drillcore samples

Sample n	As	Bi	Co	Cs	Cu	Ga	Ge	In	Li	Mo	Nb	Ni
							(Wt.%)					
J138-8	< 0.001	< 0.001	< 0.001	< 0.001	0.005	< 0.001	0.003	< 0.001	< 0.001	< 0.001	< 0.001	0.002
J138-9	< 0.001	< 0.001	< 0.001	< 0.001	0.006	< 0.001	0.003	< 0.001	< 0.001	< 0.001	< 0.001	0.002
J138-10	< 0.001	< 0.001	< 0.001	< 0.001	0.003	< 0.001	0.002	< 0.001	< 0.001	< 0.001	< 0.001	0.002
J125-2	< 0.001	< 0.001	< 0.001	< 0.001	0.004	< 0.001	0.003	< 0.001	< 0.001	< 0.001	< 0.001	0.001
J125-3	< 0.001	< 0.001	< 0.001	< 0.001	0.026	0.001	0.024	< 0.001	0.001	< 0.001	< 0.001	< 0.001
J125-5	< 0.001	< 0.001	< 0.001	< 0.001	0.005	< 0.001	0.006	< 0.001	< 0.001	< 0.001	< 0.001	0.001
J125-6	< 0.001	< 0.001	0.002	< 0.001	0.008	< 0.001	0.007	< 0.001	< 0.001	< 0.001	< 0.001	0.003
J125-8	< 0.001	< 0.001	< 0.001	< 0.001	0.014	< 0.001	0.013	< 0.001	< 0.001	< 0.001	< 0.001	0.002
J125-9	< 0.001	< 0.001	< 0.001	< 0.001	0.024	< 0.001	0.012	< 0.001	< 0.001	< 0.001	< 0.001	0.002
J125-10	< 0.001	< 0.001	< 0.001	< 0.001	0.006	< 0.001	0.012	< 0.001	< 0.001	< 0.001	< 0.001	0.002
J125-15	< 0.001	< 0.001	< 0.001	< 0.001	< 0.001	< 0.001	< 0.001	< 0.001	< 0.001	< 0.001	< 0.001	0.001
J125-20	< 0.001	< 0.001	< 0.001	< 0.001	< 0.001	< 0.001	< 0.001	< 0.001	< 0.001	< 0.001	< 0.001	0.002
J125-21	0.002	< 0.001	< 0.001	< 0.001	0.005	< 0.001	0.004	< 0.001	< 0.001	< 0.001	< 0.001	0.032
J125-22	0.002	< 0.001	< 0.001	< 0.001	0.004	< 0.001	0.004	< 0.001	< 0.001	< 0.001	< 0.001	0.004
J125-30	< 0.001	< 0.001	< 0.001	< 0.001	0.009	< 0.001	0.003	< 0.001	< 0.001	< 0.001	< 0.001	0.002
J125-31	< 0.001	< 0.001	< 0.001	< 0.001	0.004	< 0.001	0.004	< 0.001	< 0.001	< 0.001	< 0.001	0.002
J125-32	< 0.001	< 0.001	< 0.001	< 0.001	0.009	< 0.001	0.009	< 0.001	< 0.001	< 0.001	< 0.001	0.002
J125-33	0.005	< 0.001	< 0.001	< 0.001	0.003	< 0.001	0.012	< 0.001	< 0.001	< 0.001	< 0.001	0.003
J109-3	< 0.001	< 0.001	< 0.001	< 0.001	0.003	< 0.001	< 0.001	< 0.001	< 0.001	< 0.001	< 0.001	0.001
J109-5	< 0.001	< 0.001	< 0.001	< 0.001	0.007	0.002	0.003	< 0.001	< 0.001	< 0.001	< 0.001	0.001
J125-8 (conc.)	< 0.001	< 0.001	< 0.001	< 0.001	0.015	< 0.001	0.015	< 0.001	< 0.001	< 0.001	< 0.001	0.002
J125-9 (conc.)	< 0.001	< 0.001	< 0.001	< 0.001	0.02	< 0.001	0.012	< 0.001	< 0.001	< 0.001	< 0.001	0.001
J125-10 (conc.)	< 0.001	< 0.001	< 0.001	< 0.001	0.01	< 0.001	0.019	< 0.001	< 0.001	< 0.001	< 0.001	0.003
J125-32 (conc.)	< 0.001	< 0.001	< 0.001	< 0.001	0.01	< 0.001	0.01	< 0.001	< 0.001	< 0.001	< 0.001	0.001
J125-33 (conc.)	< 0.001	< 0.001	< 0.001	< 0.001	0.004	< 0.001	0.017	< 0.001	< 0.001	< 0.001	< 0.001	0.003

Stable Isotopes (C-O) Geochemistry

By the study of stable isotopes (C-O) in carbonates (saddle dolomite, Zn-dolomite, smithsonite and hydrozincite) Mondillo et al. (2014) defined the genetic conditions for the formation of the supergene ore minerals at Jabali (temperature of precipitation, source waters, source of the carbon), also defining a possible age for the supergene mineralization. In Figure 4.6 are reported the C-O results. The main findings, which result from the isotope study are:

- *saddle* dolomite shows $\delta^{13}C$ and $\delta^{18}O$ ratios typical of other hydrothermal dolomites in the world (Diehl et al., 2010).
- Zn-dolomite is characterized by $\delta^{18}O$ compositions that are broadly in a hydrothermal range, whereas the $e^{13}C$ compositions are slightly lower than those of *saddle* dolomites.
- The carbon and oxygen isotopic values for smithsonite vary along the length of the core. The $\delta^{13}C$ values are in the range of supergene smithsonites worldwide (Gilg et al., 2008) and point to a mixed source of carbon (organic matter in the soil, atmospheric CO_2, and host rocks). The $g^{18}O$ values, instead, indicate the effects of temperature-related fractionation along the core. This is probably due to variable precipitation temperatures of the Zn-carbonate at different depths, or to different periods/stages of alteration and smithsonite formation.
- Hydrozincite has stable isotope ratios in the range of most supergene hydrozincites quoted in literature (Gilg et al., 2008).
- Precipitation temperatures were calculated with the equation published by Gilg et al. (2008) and using modern groundwater, modern rainwater and/or Pleistocene-Holocene speleothemes. Mondillo et al. (2014) hypothesized a precipitation temperature between ~55° and ~65°C when using $\delta^{18}O$ values of thermal water in the region, and a temperature between 20° and 45°C using $\delta^{18}O$ values of rainwater and cave water.
- A possible initial age for the oxidation stage could be around 17 Ma (Miocene), when extensional tectonics caused the opening of the Red Sea also determining a strong uplift phase in Yemen. An additional evidence for this age and relationship to the Red Sea rifting is the occurrence of a widespread hydrothermal activity, associated to Miocene-Holocene magmatism.
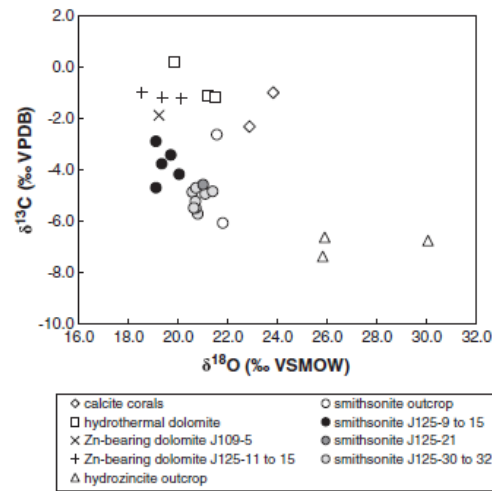
Figure 4.6: δ^{18}O-PDB vs. δ^{13}C-PDB compositions of Jabali Zn-carbonates and of smithsonites from other nonsulfide deposits/districts: Iglesias, Sardinia, Italy (Boni et al., 2003); Angouran, Iran (Boni et al., 2007); Silesia-Cracow district, Poland (Coppola et al., 2009); Sierra Mojada, Mexico (Hye In Ahn, 2010) (from Mondillo et al., 2014).

4.8. Results: QEMSCAN®

Analysis on the Jabali texture

  In Figure 4.7 are displayed the QEMSCAN® false color images of two thin sections from the core sample J109-5 and the surface sample Js-Mon 2, which are useful to understand the Jabali rock texture. The dolomite host rock is porous and locally fractured; broad fronts of Zn-dolomite, evidenced through their yellow color, replace the pure dolomite (pale blue color). Smithsonite (pale grey), locally Mg-enriched, generally occurs in the porosity of the host rock, in major vugs, and/or at the border of weathered sphalerite. Galena (Figure 4.6 Js-Mon 2) is surrounded by secondary phases, whereas the Fe-Mn-(hydr)oxides (Figure 4.6 J109-5) are either scattered throughout the host rock, or concentrated in small veins. Their presence is generally associated with the Zn-dolomite patches.

Figure 4.7: False color fieldscan images of two thin sections analyzed by QEMSCAN®: J109-5 from a core sample and Js-Mon 2 from a surface specimen. Less abundant and trace minerals are not represented in the color key. The latter phases comprise: Fe-dolomite, pyrite, hetaerolite, Fe-Mn-(hydr)oxides, chalcophanite, chlorargyrite, plagioclase feldspar, apatite, chlorite (Santoro et al., in press).

Quantitative QEMSCAN® analyses (QPA)

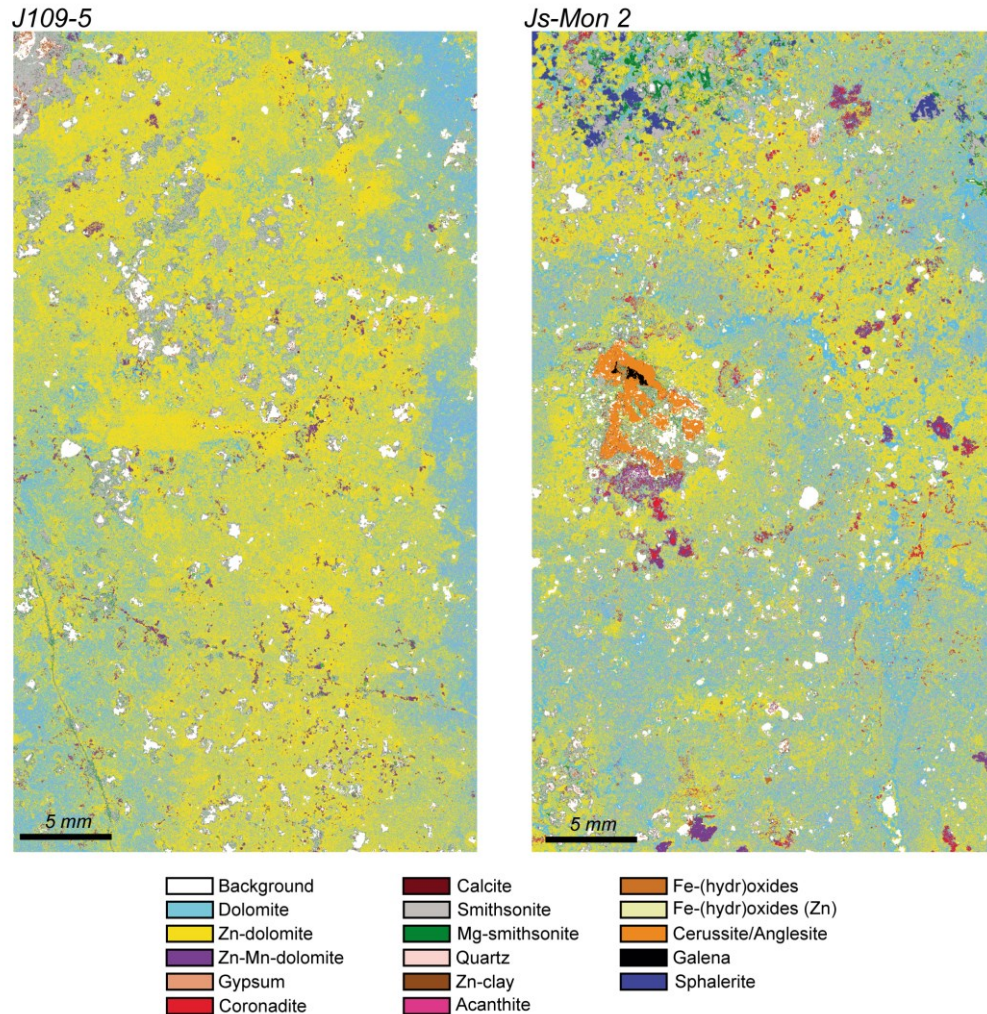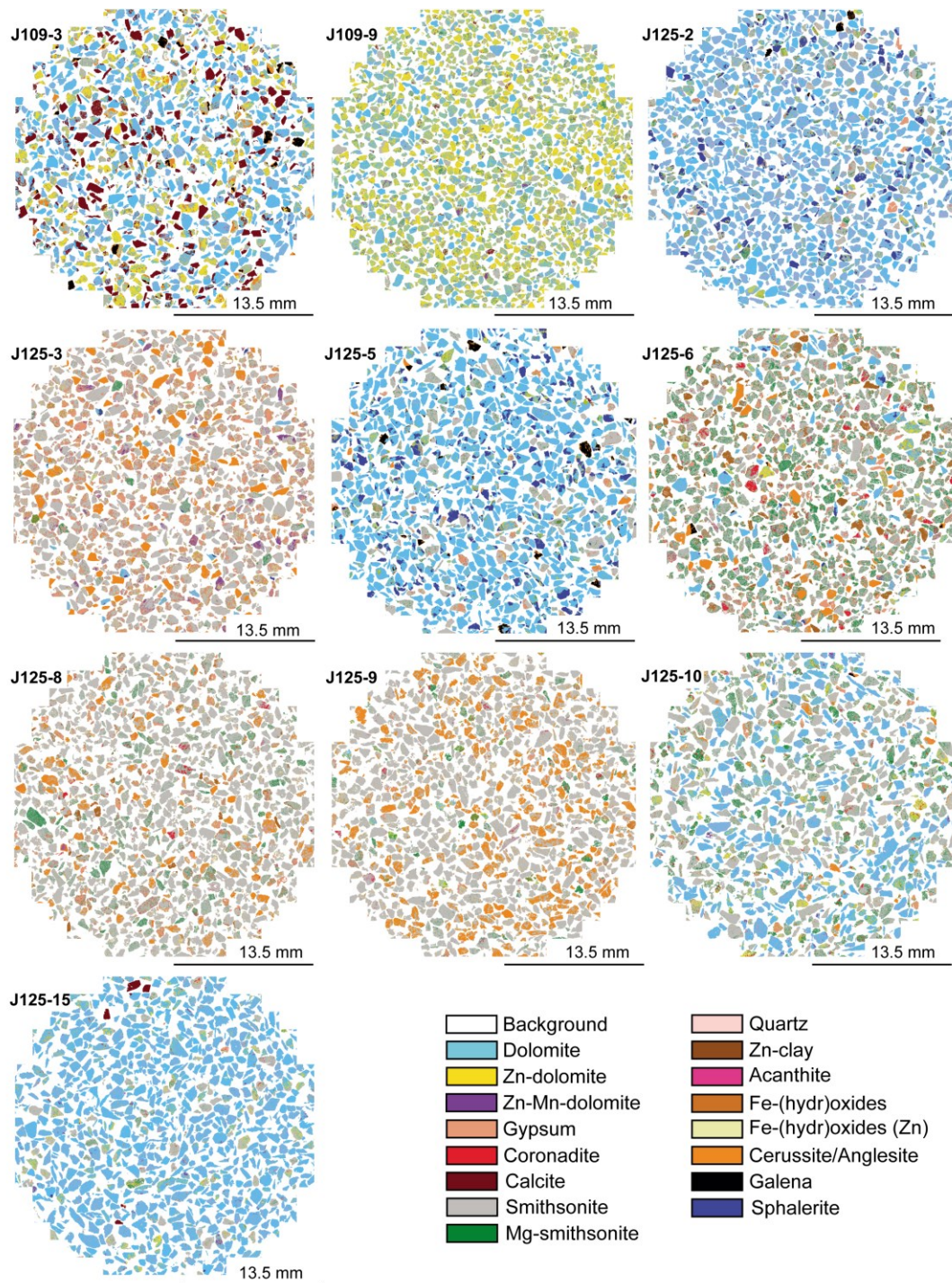Table 5 shows the quantitative mineralogical data (wt.%) of the Jabali samples, obtained from QEMSCAN® modal analysis. False color QEMSCAN® mineral maps for all the 20 samples are displayed in Figures 4.8. A few enlargements of the crushed samples are shown in Figure 4.9, while in Figure 4.10 are depicted the false color images for the 5 concentrates.

Dolomite in the host rock occurs essentially as two main phases: as almost pure dolomite (from few wt.% up to 68 wt.%), and as Zn-dolomite, which appears to be a widespread phase, up to 44 wt.% throughout the deposit (Table 5). The relationships between these two phases are visible in the thin sections of Figure 4.7, where Zn-dolomite substitutes for the precursor dolomite along broad replacement fronts. Zn-Mn- and Fe-dolomites are only minor components of the host rock (their average concentration being ≤5 wt%), and are strictly associated with Zn-dolomite.

The main Zn-mineral at Jabali is smithsonite (up to 79 wt.%), which generally occurs in the host rock porosity, as filling of major vugs or as dolomite replacement. Smithsonite is commonly associated with Fe-(hydr)oxides (Figure 4.9b), Mg-smithsonite, Zn-dolomite (Figure 4.9c) and with cerussite/anglesite (Figure 4.9d). The Mg-bearing smithsonite phase can contain up to 15 wt.% Mg, and occurs in variable amounts, generally from a few wt.% up to 16 wt.%. In a few samples (J125-3, J125-6 and J125-8), smithsonite occurs together with gypsum (Figure 4.9e).

Sphalerite and galena occur in the samples as unweathered, though not very abundant (up to 12 wt.% and 8 wt.% respectively) remnants. Sphalerite is commonly rimmed by replacive smithsonite (Fig. 4.9a). Galena is locally surrounded by thin layers of acanthite (Figure 4.9f) and chlorargyrite. Cerussite/anglesite are generally scarce, but can reach values between 8 and 27 wt.% in the samples J125-3, J125-6, J125-8, J125-9 and J138-8.

Zn-clays can be locally abundant as in the samples J125-6, J125-21 and J125-22 (Table 5). Fe-Mn-(hydr)oxides are quite scarce. They may also contain Zn (up to 10-20 wt.% Zn). Minor amounts of the Mn minerals hetaerolite, chalcophanite and coronadite have also been detected. Other non-economic mineral phases are: calcite (maximum 31 wt.% in the mineralized samples), and quartz that can be locally abundant.

QEMSCAN® analyses on the ore mineral concentrates (Figures 4.10) also showed interesting results. As expected, they have higher abundances of the Zn-Pb-rich phases (e.g. smithsonite, cerussite/anglesite), and lower contents of gangue minerals (e.g. dolomite, gypsum) (Table 5). However, despite the effectiveness of the concentration process, the gangue mineral phases were not completely removed. Specifically, in samples J125-10 and J125-33, the dolomite amount decreases ~80 relative percent from the original samples to the concentrated ones (25.06 wt.% to 4.90 wt.%, and 11.52 wt.% and 2.71 wt.% respectively). This is due to the fact that many particles in the concentrate samples consist of a mixture of pure dolomite and smithsonite-Zn-dolomite, which, at this grain size, are not liberated.

J109-3 · J109-9 · J125-2
J125-3 · J125-5 · J125-6
J125-8 · J125-9 · J125-10
J125-15

13.5 mm

Background | Quartz
Dolomite | Zn-clay
Zn-dolomite | Acanthite
Zn-Mn-dolomite | Fe-(hydr)oxides
Gypsum | Fe-(hydr)oxides (Zn)
Coronadite | Cerussite/Anglesite
Calcite | Galena
Smithsonite | Sphalerite
Mg-smithsonite

Continued...
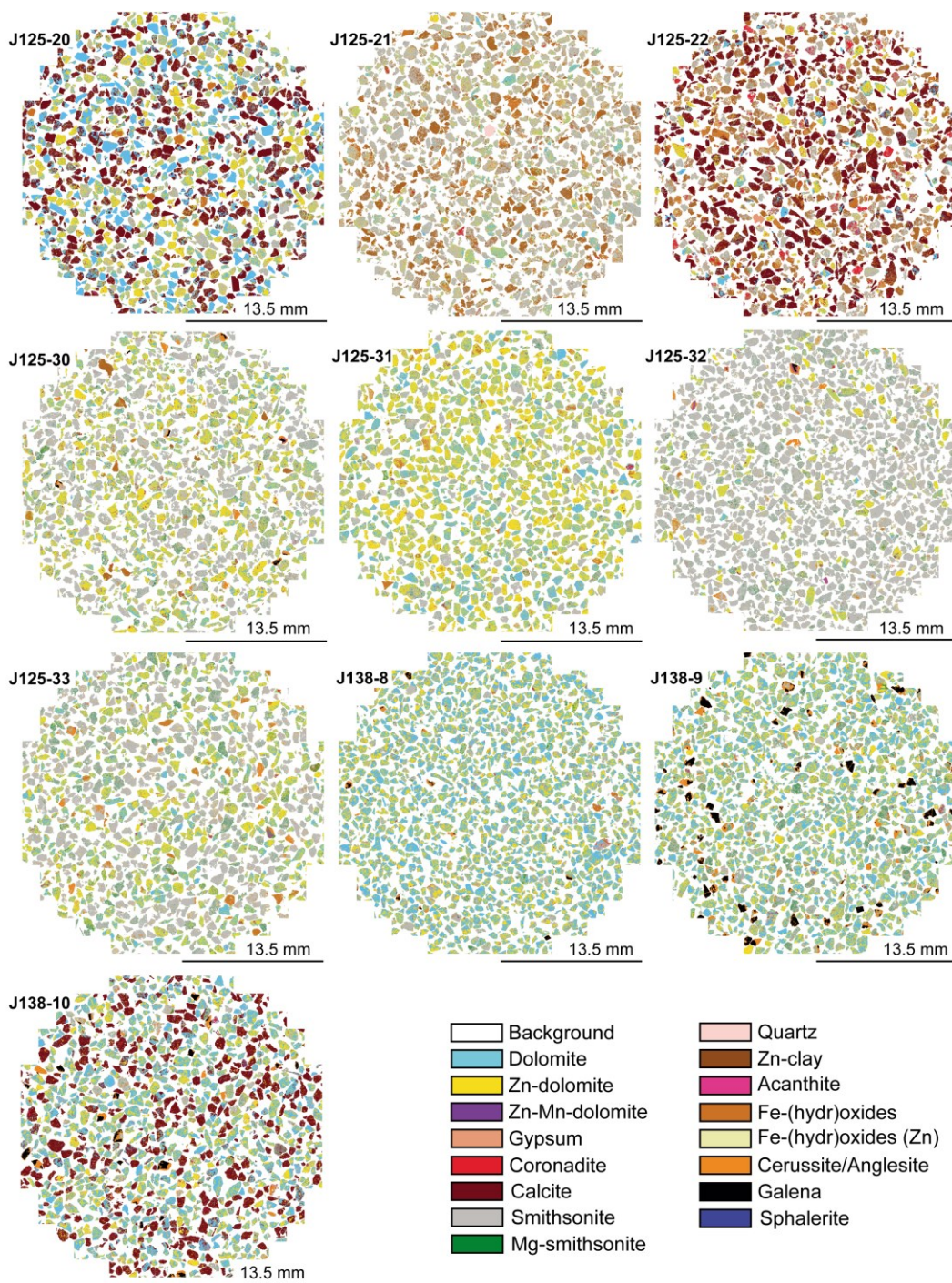
Figure 4.8: False color fieldscan images of selected samples, analyzed by QEMSCAN®. Less abundant and trace minerals are not visible in the figure, and are therefore not represented in the color key. The latter phases comprise: Fe-dolomite, pyrite, hetaerolite, Fe-Mn-(hydr)oxides, chalcophanite, chlorargyrite, plagioclase feldspar, apatite, chlorite (Santoro et al., in press).
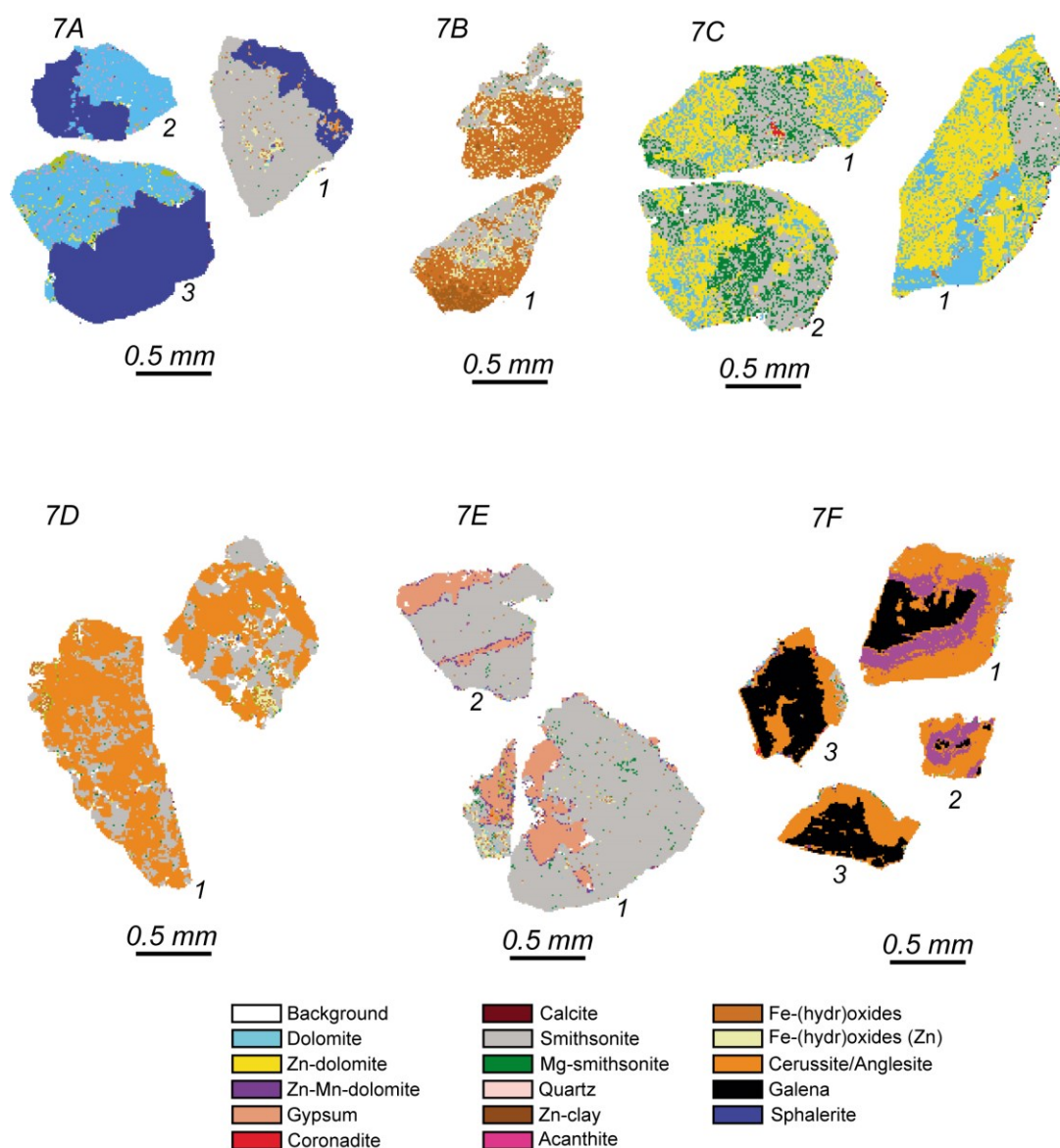
Figure 4.9: Enlargements of the mineral particles from the original blocks (Figures 5.7) analyzed by QEMSCAN® using fieldscan mode: (a) J125-5: sphalerite associated with host rock dolomite and smithsonite. Some Zn-dolomite and sauconite occur within the host rock; (b) J125-21: smithsonite with Fe-(hydr)oxides and Zn bearing Fe-(hydr)oxides. Small amounts of Zn-clays also occur; (c) J109-5: smithsonite in association with Mg-smithsonite and Zn-dolomite; it can be seen how Zn-dolomite replaces previous dolomite. In some pixels, traces of coronadite and Fe-(hydr)oxides can be detected; (d) J125-9: association of smithsonite and cerussite/anglesite; several pixels show the occurrence of Fe-(hydr)oxides (Zn) in smithsonite and cerussite/anglesite; (E) J125-3: gypsum patches within smithsonite; some pixels show the occurrence of Zn-bearing Fe-(hydr)oxides, Mg-smithsonite, dolomite and Zn-Mn-dolomite. (F) J138-9: galena as remnant core surrounded by anglesite/cerussite. In a different sample (J125-32) acanthite can be seen at the border between galena and secondary Pb-phases (cerussite/anglesite). Other minerals of lesser abundance and in traces are not represented in the color key. The latter phases comprise: Fe-dolomite, pyrite, hetaerolite, Fe-Mn-(hydr)oxides, chalcophanite, chlorargyrite, plagioclase feldspar, apatite, and chlorite (Santoro et al., in press).

☐ Background	■ Calcite	■ Fe-(hydr)oxides
■ Dolomite	■ Smithsonite	■ Fe-(hydr)oxides (Zn)
■ Zn-dolomite	■ Mg-smithsonite	■ Cerussite/Anglesite
■ Zn-Mn-dolomite	■ Quartz	■ Galena
■ Gypsum	■ Zn-clay	■ Sphalerite
■ Coronadite	■ Acanthite	

Continued...

154

Figure 4.10: False color fieldscan images of selected samples and their concentrates, analyzed by QEMSCAN®. Less abundant and trace minerals are not visible in the figure and are not represented in the color key. Theses phases comprise: Fe-dolomite, pyrite, hetaerolite, Fe-Mn-(hydr)oxides, chalcophanite, chlorargyrite, plagioclase feldspar, apatite, and chlorite (Santoro et al., in press).
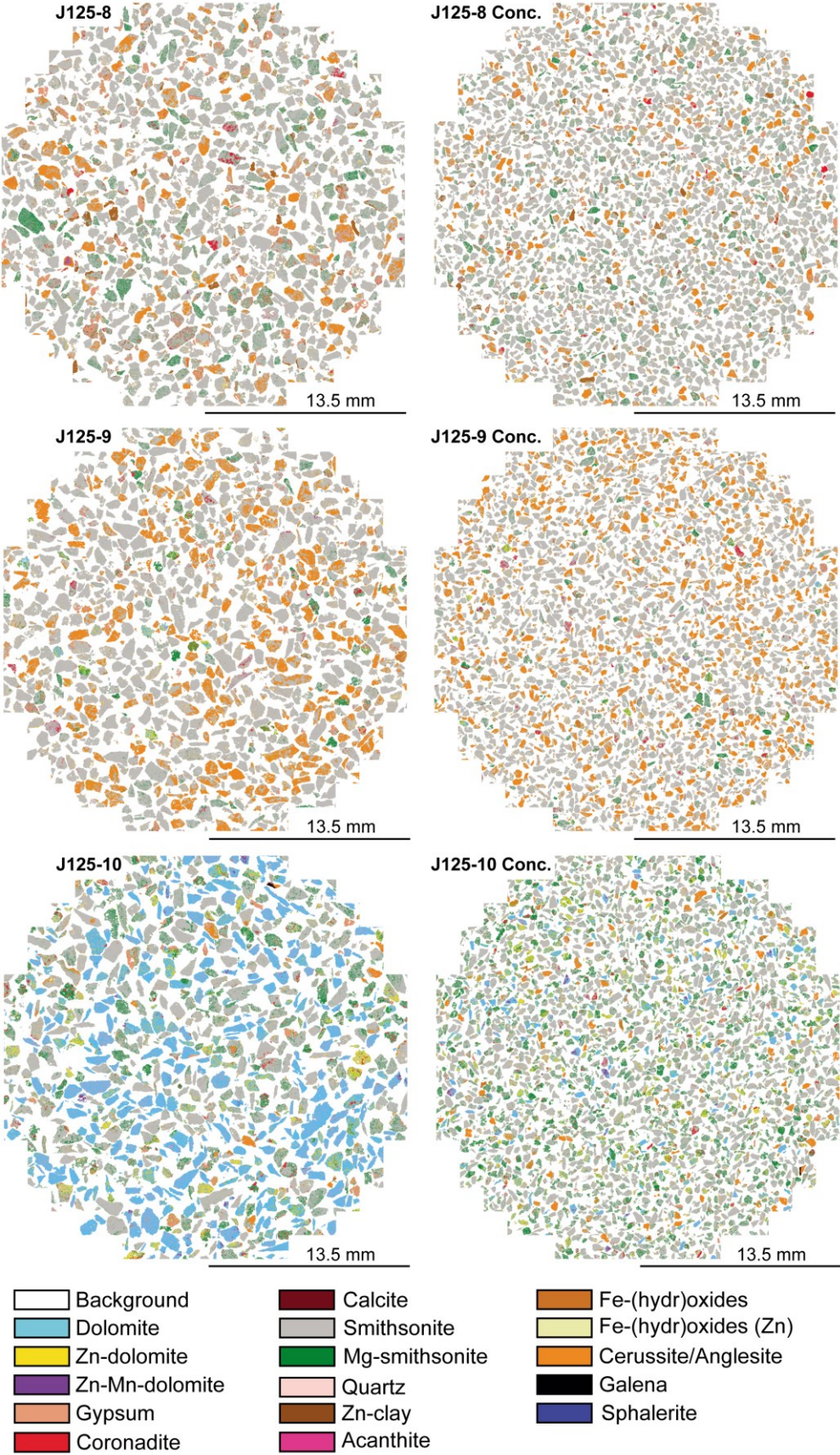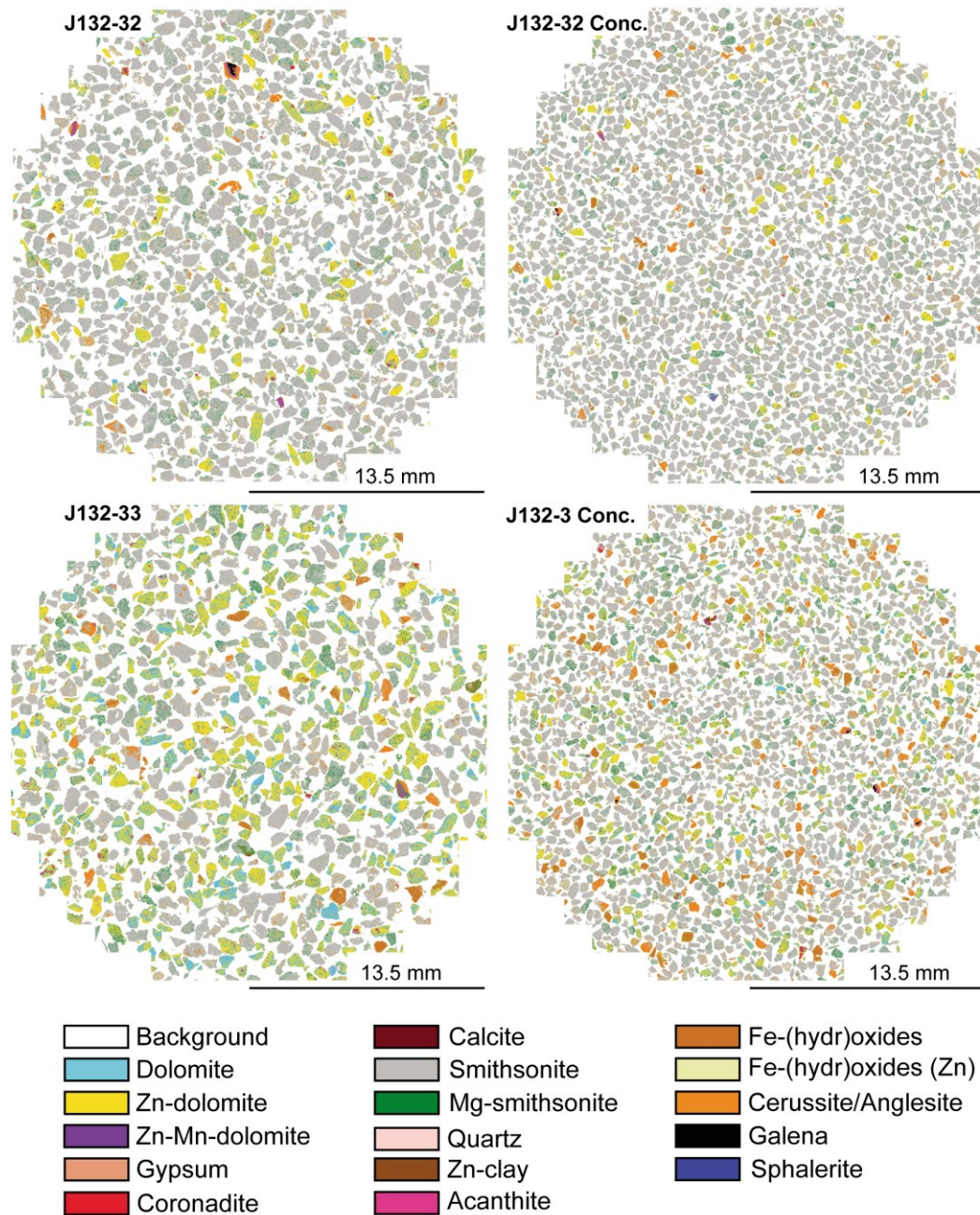
Table 5: Quantitative analyses of the Jabali drillcore samples by QEMSCAN®

Sample n	J109-3	J109-5	J125-2	J125-3	J125-5	J125-6	J125-8	J125-8*	J125-9	J125-9*	J125-10	J125-10*	J125-15	J125-20	J125-21	J125-22	J125-30	J125-31	J125-32	J125-32*	J125-33	J125-33*	J138-8	J138-9	J138-10
													wt%												
Dolomite	40.94	30.77	55.59	0.66	53.84	6.09	<0.01	<0.01	0.25	0.14	25.06	4.90	68.03	28.73	3.99	4.78	9.87	23.84	1.55	0.54	11.52	2.71	43.34	32.44	29.82
Fe-dolomite	6.57	5.61	17.78	0.18	3.55	0.81	<0.01	<0.01	0.04	0.02	5.15	0.77	12.59	2.52	0.11	0.75	0.59	2.68	0.05	0.02	0.65	0.15	4.17	2.29	2.94
Zn-dolomite	14.87	35.93	3.28	2.12	2.66	2.31	0.38	0.28	0.39	0.31	3.81	4.05	3.86	21.56	7.20	8.44	23.49	44.37	5.76	2.70	18.81	6.66	32.21	26.49	22.31
Zn-Mn-dolomite	0.59	1.41	0.59	5.09	0.76	1.17	0.59	0.35	0.17	0.09	0.44	0.30	0.75	0.65	0.07	0.62	0.54	0.78	0.08	0.04	0.36	0.12	0.57	0.72	0.90
Calcite	13.86	0.78	0.44	0.16	0.25	0.13	0.03	0.02	0.03	0.02	0.19	0.15	0.80	29.45	0.11	31.72	0.48	0.84	0.05	0.03	0.31	0.11	0.85	0.77	25.22
Smithsonite	10.04	19.14	8.07	56.24	15.88	48.01	70.32	73.53	62.49	60.96	46.47	61.17	11.54	10.26	59.23	21.61	51.38	19.57	79.79	84.57	50.82	66.68	10.29	13.38	5.03
Mg-smithsonite	1.22	4.91	1.90	1.44	1.84	16.58	6.00	5.67	2.53	2.57	10.18	15.04	1.01	0.70	1.87	0.93	4.85	2.23	5.16	5.02	6.26	6.77	2.04	3.73	0.55
Fe-(hydr) oxides	0.68	0.54	0.34	2.61	0.35	3.25	2.68	2.45	2.09	1.94	1.85	2.55	0.37	4.72	12.04	13.34	2.64	3.29	2.53	2.58	4.39	5.79	3.43	1.54	4.17
Fe-(hydr) oxides/(Zn)	0.21	0.41	0.20	3.10	0.28	1.00	2.36	2.12	2.15	2.03	1.76	2.51	0.06	0.44	2.97	1.70	1.57	1.11	2.63	2.64	3.04	4.08	0.49	0.59	0.16
Cerussite/Anglesite	5.92		0.27	15.23	1.97	7.75	11.66	11.79	27.10	29.65	1.74	5.38			0.02	0.03	1.60	0.04	1.10	1.16	2.20	5.72	0.99	8.38	3.72
Galena	4.03		0.90		3.35	0.28					0.06	0.03					0.47		0.11	0.01		0.08	0.61	8.14	3.05
Sphalerite	0.29	0.01	8.69	0.64	12.20	0.99	0.11	0.09	0.09	0.06	0.09	0.10	0.04		0.03	0.04	0.06	0.03	0.02	0.04	0.01	0.03	0.02	0.06	0.01
Pyrite	0.05		0.47	1.08	1.14	0.26	0.39	0.27	0.38	0.33	0.26	0.32	0.04	0.03	0.10	0.12	0.13	0.08	0.09		0.25	0.34	0.16	0.15	0.14
Coronadite	0.46	0.12	0.04	0.09	0.06	2.90	1.04	0.95	0.70	0.86	1.41	1.56	0.32	0.39	0.86	5.60	0.96	0.81	0.34	0.20	0.63	0.35	0.52	0.75	1.32
Hetaerolite	0.03	0.18	0.02	0.01	0.01	0.60	0.24	0.18	0.30	0.36	0.19	0.27	0.24	0.04	0.17	0.65	0.13	0.06	0.16	0.14	0.08	0.08	0.05	0.06	0.09
Fe-Mn-(hydr)oxides	0.10	0.01		0.02	0.01	0.10	0.08	0.05	0.03	0.03	0.16	0.16	0.04	0.13	0.12	0.20	0.08	0.05	0.02	0.01	0.05	0.02	0.06	0.05	0.18
Chalcophanite	0.02	0.07	0.01	0.04		0.19	0.13	0.13	0.13	0.15	0.28	0.34	0.03	0.04	0.27	0.19	0.17	0.05	0.12	0.10	0.09	0.10	0.04	0.10	0.02
Zn-clays	0.02	0.06	0.04	0.13	0.17	3.80	1.20	0.89	0.23	0.16	0.04	0.06	0.06	0.16	10.51	8.23	0.84	0.06	0.01	0.01	0.14	0.03	0.01	0.14	0.11
Gypsum	0.06	0.01	1.31	11.04	1.60	3.50	2.60	1.13	0.79	0.27	0.82	0.29	0.15	0.03	<0.01	0.34	0.02	0.03	0.01		0.03	0.01	0.04	0.17	0.08
Others/Undiff	0.01	0.01	0.01	0.02	0.02	0.04	0.02	0.02	0.01	0.01	0.01	0.01	0.02	0.03	0.05	0.09	0.01	0.02			0.01		0.03	0.02	0.04

Notes: QEMSCAN® measurement mode = field scan image: X-ray pixel spacing 10 µm; chlorargyrite, muscovite/illite, chlorite, apatite, quartz, acanthite, plagioclase feldspar and others minerals occur in traces; - = below detection limit.
* concentrate samples.
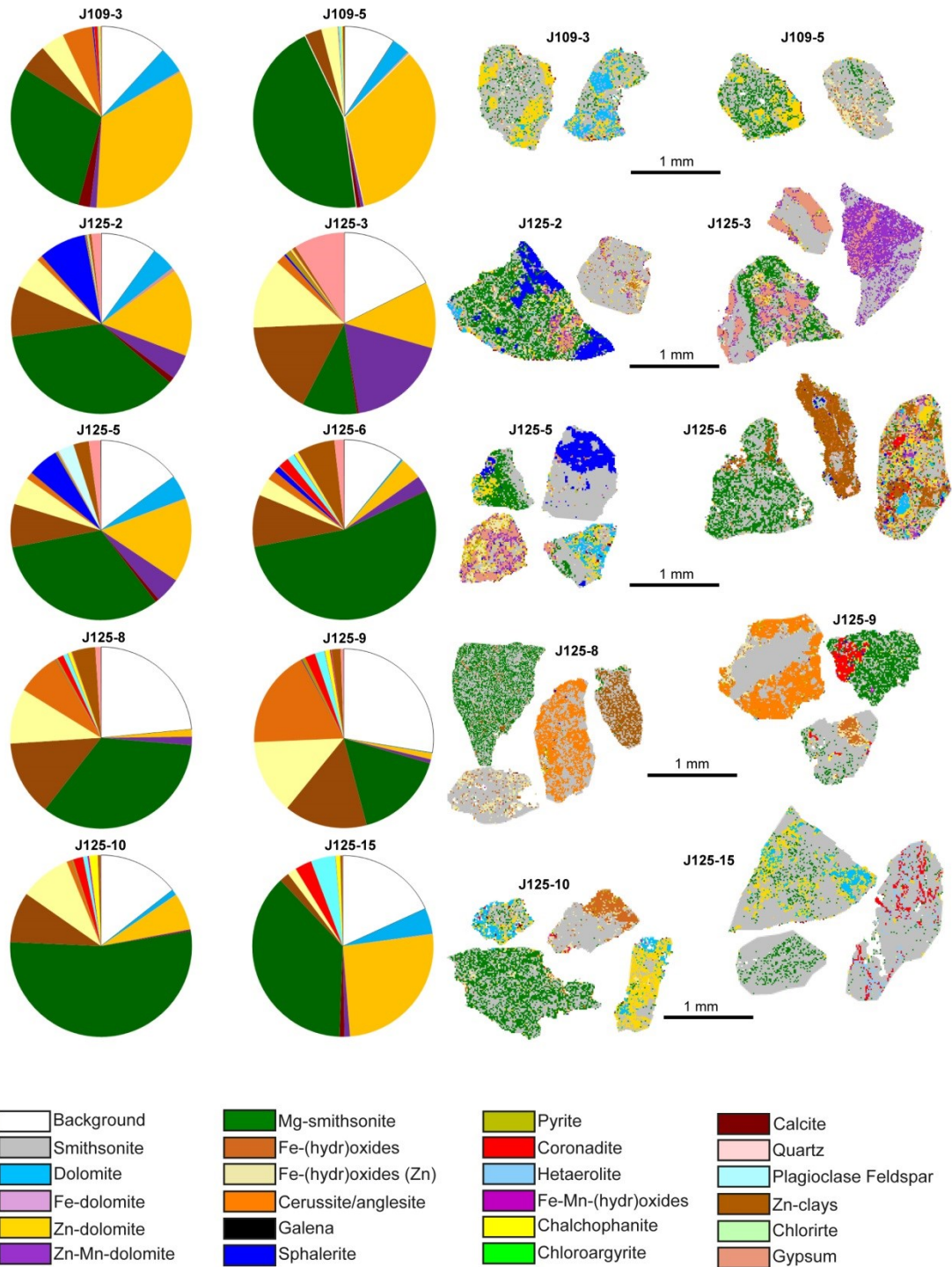
QEMSCAN® mineral association

In Figure 4.11 are shown the pie charts of the mineral associations, plus a few enlargements of the crushed particles that synoptically show what the mineral association corresponds to.

The diagrams have been drawn considering the percentage of contacts between smithsonite (which is the most important economic phase) and all the other minerals detected by QEMSCAN®. As it can be observed, smithsonite is mostly associated with Mg-smithsonite from a minimum of 8.10 % (sample J125-22) to a maximum of 54.04 % (sample J125-6), and with Zn-dolomite from 1.11 % (sample J125-9) up to 52.32 % (sample J125-20). Nevertheless, even though the dolomite is the main host rock, its association with smithsonite is quite low (up to a maximum of 7.28 % in sample J125-20). This means that, in the most enriched intervals, smithsonite tends to be associated more with Zn-dolomite than with pure dolomite itself. Fe-dolomite is poorly associated with smithsonite (up to 0.90 % in sample J138-8); the same is for Zn-Mn-dolomite, which is poorly associated with smithsonite (except for sample J125-3, up to 18.10 %).

Smithsonite is also commonly associated with Fe-(hydr)oxides from 1.74 % (sample J125-15) to 25 % (sample J125-22), and less associated with Zn-rich Fe-(hydr)oxides; indeed smithsonite is associated with the latter from 1.61 % (sample J-125-15) up to a maximum of 13.45 % (sample J125-9).

Zn-clays are commonly associated with smithsonite in a wide range of values: from few percentages (<1 %) up to 29.01 % (sample J125-22).

Cerussite/anglesite (from few percentages up to a maximum of 17.79 % in sample J125-9), sphalerite (up to 8.54 % in sample J125-2), gypsum (up to 9.05 % in sample J125-3), and calcite (up to 4.51 % in sample J138-10) are also associated with smithsonite. Among the minor phases in association with smithsonite, there are also chalcophanite, hetaerolite and coronadite (always <~2 %); pyrite and Fe-Mn-(hydr)oxides are always <1 %.
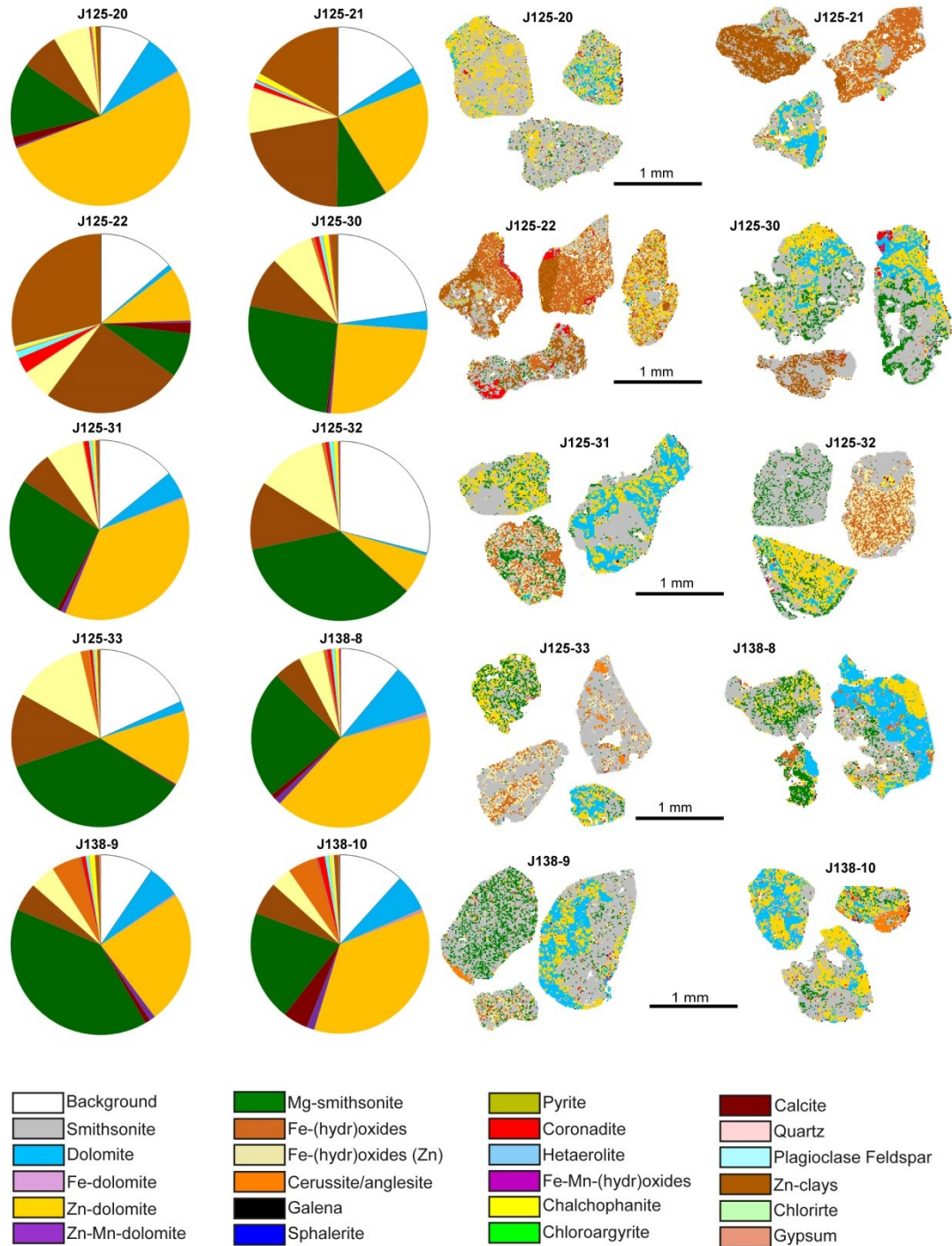
Continue...

Figure 4.11: Pie diagrams of the mineral association for all the samples and enlargements of selected particles. The diagrams show the association between the smithsonite and the other minerals in percentages. The color keys indicate the mineral phases occurring. Smithsonite is inserted in the color key as it occurs in the enlarged particles (Santoro et al., in press).

Calculation of elements from QPA (QEMSCAN®)

In table 6 is reported an attempt to reconcile the elemental values of Zn, Pb, Ca, Mg and Fe calculated from the QPA data (QEMSCAN® method), with the total Zn, Pb, Ca, Mg and Fe (all wt.%) obtained by the new chemical analyses. The calculation was done for all the 20 samples analyzed by QEMSCAN®, and also for the concentrate ones.

Here follows an element-per-element description of the results obtained by the calculation using the minerals quantities, obtained both with the Rietveld and QEMSCAN® technologies:

Zinc: The calculation was made using the contributions from *"pure"* phases i.e. smithsonite, sphalerite, hetaerolite, chalcophanite, and sauconite (that have standard values in Zn content) and "*impure mixed*" phases i.e. Zn-dolomite (7 wt.% Zn), Zn-Mn-dolomite (5 wt.% Zn), Zn-rich Fe-(hydr)oxides (5 wt.% Zn) and Mg-smithsonite (45 wt.% Zn). As reported in table 6, it is possible to note that the Zn calculated from the QEMSCAN®-QPA is almost always over-evaluated (from few % to up 10 wt.%), except in the samples J125-9 and J125-21, where the calculated zinc % are under-estimated compared to the values of the chemical analyses. Even if the two sets of data do not match perfectly, we can say that for the samples more enriched in smithsonite the discrepancy between the two is not so significant. Interesting results have been observed for the concentrate samples, where the two values match almost perfectly (table 6).

Lead: it has been calculated considering the contribution of only "*pure*" minerals, like cerussite/anglesite, galena and coronadite, and using Pb stoichiometric values (Webmineral, www.webmineral.com). The results show that Pb is generally over-evaluated compared to the chemical analyses, and for only few samples it is under-estimated (table 6). The reasons of this discrepancy could be due to sample preparation issues, or to the complex and variable mineralogy of the Jabali deposit, and are fully discussed in the next paragraph.

Iron: it was calculated considering the standard values of goethite, pyrite and chalcophanite, reported in Webmineral, www.webmineral.com., but also the contribution of Zn-enriched Fe-(hydr)oxides (56 wt.% Fe) and of Fe-Mn-(hydr)oxides (8 wt.% Fe) has been considered. The comparison between Calculated and Measured Fe shows that the discrepancy between the two values is generally variable and difficult to explain, as there is not a general trend. The reasons of this discrepancy may be: 1) the fine grain size of Fe-(hydr)oxides that could create a misidentification of the Fe-phases, or 2) the impossibility to distinguish between the different types of Fe-(hydr)oxides, and hence the different Fe wt.% values that should be considered.

Calcium: it has been evaluated from the contribution of calcite, dolomite, gypsum, and apatite according the standard CaO (Webmineral, www.webmineral.com), but also considering the amounts contained in Fe-dolomite, Zn-Mn-dolomite and Zn-dolomite (it has been considered for all three 30 wt.% CaO). The results show a general under-estimation of Ca, compared to that measured in chemical analyses.

Magnesium: the calculation of magnesium was done considering the *pure* dolomite (21.86 wt.% MgO, according the standard composition), but also Fe-dolomite (20 wt.% MgO), Zn-dolomite (14 wt.% MgO), Zn-Mn-dolomite (15 wt.% MgO), and Mg-

162

smithsonite (8 wt.% MgO). The results in table 6 show that even though a general under-estimation of MgO in the calculation from QEMSCAN®-QPA exists, the data fit quite well with those of the chemical analyses.

Table 6: Calculation of the % of total element amounts (Zn, Pb, Fe, Mg, Ca) from whole rock chemical assays (CA) compared with metal percentages from Zn, Pb, Fe, Mg, Ca-bearing minerals measured with QEMSCAN®-QPA calculation

Sample n	Zn% Σ_{QPA}[1]	Zn% CA[2]	Zn% Σ_{QPA}-CA[3]	Pb% Σ_{QPA}[1]	Pb% CA[2]	Pb% Σ_{QPA}-CA[3]	Fe% Σ_{QPA}[1]	Fe% CA[2]	Fe% Σ_{QPA}-CA[3]	MgO Σ_{QPA}[1]	MgO CA[2]	MgO Σ_{QPA}-CA[3]	CaO Σ_{QPA}[1]	CaO CA[2]	CaO Σ_{QPA}-CA[3]
J109-3	7.1	5.0	2.1	8.2	4.0	4.2	0.6	1.7	-1.1	12.5	11.7	0.9	26.7	29.8	-3.1
J109-5	14.9	13.2	1.7	0.0	0.1	0.0	0.6	2.1	-1.5	13.5	14.0	-0.5	22.6	22.8	-0.2
J125-2	10.9	6.4	4.5	1.0	0.2	0.8	0.7	2.3	-1.6	16.4	15.3	1.1	23.9	25.2	-1.3
J125-3	31.0	24.0	7.0	11.8	4.3	7.5	3.9	2.7	1.2	1.4	0.9	0.5	6.1	12.1	-6.0
J125-5	17.2	11.5	5.7	4.5	1.8	2.6	0.9	2.1	-1.1	13.1	14.1	-1.0	18.9	23.2	-4.3
J125-6	33.6	29.0	4.6	7.0	3.4	3.6	2.7	2.2	0.5	3.3	5.3	-2.0	4.3	8.4	-4.0
J125-8	39.7	36.0	3.7	9.3	4.1	5.2	3.2	2.4	0.8	0.6	1.4	-0.8	1.2	3.1	-2.0
J125-9	34.1	37.8	-3.7	21.2	11.6	9.6	2.7	2.2	0.5	0.3	1.3	-1.0	0.5	2.0	-1.5
J125-10	29.4	19.4	10.0	1.7	1.3	0.4	2.3	2.4	-0.1	7.9	11.9	-3.9	10.7	16.1	-5.3
J125-15	6.9	3.7	3.2	0.1	0.1	0.0	0.4	2.1	-1.7	18.1	17.0	1.2	26.1	26.7	-0.7
J125-20	7.3	5.3	2.0	0.1	0.2	-0.1	3.2	2.1	1.1	10.0	9.3	0.6	32.6	35.1	-2.5
J125-21	32.5	33.3	-0.8	0.2	0.5	-0.3	9.2	6.2	3.0	2.1	3.2	-1.1	3.5	4.0	-0.5
J125-22	12.6	12.4	0.2	1.4	1.2	0.2	9.4	5.5	3.9	2.5	3.4	-0.9	22.3	27.4	-5.1
J125-30	30.8	27.1	3.7	1.9	1.7	0.2	2.6	2.5	0.1	6.0	7.9	-1.9	10.6	13.2	-2.6
J125-31	14.5	12.9	1.6	0.2	0.8	-0.6	2.8	3.2	-0.4	12.3	12.2	0.1	22.0	21.8	0.1
J125-32	44.6	41.0	3.6	1.0	0.9	0.2	3.1	2.9	0.2	1.6	3.3	-1.7	2.3	3.6	-1.4
J125-33	30.9	26.4	4.5	1.9	1.8	0.1	4.6	3.7	0.9	5.8	8.5	-2.7	9.6	12.9	-3.3
J138-8	8.6	8.3	0.3	1.4	1.0	0.4	2.5	3.1	-0.6	15.1	14.0	1.1	24.6	23.4	1.2
J138-9	10.7	9.4	1.3	13.8	6.8	7.0	1.4	2.5	-1.1	11.7	13.4	-1.7	19.1	22.9	-3.8
J138-10	4.5	4.1	0.5	5.9	2.6	3.2	2.8	2.2	0.6	10.4	8.3	2.2	31.0	34.4	-3.5
J125-8 (Conc.)	41.2	41.9	-0.7	9.4	4.6	4.7	2.9	2.3	0.6	0.5	1.3	-0.8	0.6	2.0	-1.5
J125-9 (Conc.)	33.3	36.1	-2.8	23.2	17.6	5.6	2.5	1.9	0.6	0.3	0.9	-0.6	0.3	0.7	-0.5
J125-10 (Conc.)	39.3	36.8	2.5	4.6	2.7	1.9	3.2	2.5	0.7	3.0	5.1	-2.1	3.2	5.2	-2.0
J125-32 (Conc.)	46.8	45.2	1.6	1.0	1.1	-0.2	3.1	2.9	0.3	0.9	2.0	-1.1	1.0	1.3	-0.3
J125-33 (Conc.)	38.6	37.2	1.4	4.6	2.9	1.7	6.1	4.1	1.9	2.1	3.4	-1.3	3.0	3.7	-0.8

[1] Σ_{QPA}: is the sum of element (Zn, Pb, Ca, Mg, Fe) coming from Quantitative values of minerals detected in Rietveld analysis; [2] CA: is the element value from Chemical analyses; [3] Σ_{QPA}-CA: is the difference between Σ_{QPA} and CA .

4.9. Discussion

A complete study on the texture of the supergene deposit was already carried out by Mondillo (2013) and Mondillo et al. (2011, 2014) by the use of OM, CL and SEM images; even if the QEMSCAN® textural study was carried out only on two thin sections, the results obtained are in agreement with previous works.

QEMSCAN® analysis of the Jabali supergene ore has also allowed the quantification of the economic and noneconomic minerals in the deposit and the evaluation of their textures. A comparison of these results with those obtained in previous studies shows both positive and negative points that should be discussed. The most important advantage of QEMSCAN® (compared to traditional methods) is the possibility to obtain in less than 3 hours, false color images synoptically showing the texture of the sample (in the current study: dolomite replaced by broad fronts of Zn-dolomite and smithsonite; smithsonite in cavities and veins, in association with Fe-(hydr)oxides, and remnant of sulfides surrounded by secondary phases).

Another important point is that QEMSCAN® was able to reveal, classify, and quantify different compounds with compositions near to dolomite and smithsonite: dolomite (Fe, Zn, Mn <5 wt.%), Fe-dolomite (Fe>5 wt.%, Zn and Mn <5 wt.%), Zn-dolomite (Zn>5 wt.%, Fe and Mn <5 wt.%), Zn-Mn-dolomite (Zn and Mn >5 wt.%, Fe <5 wt.%), smithsonite (containing <5 wt.% Mg), and Mg-smithsonite (containing >5 wt.% Mg).

In the analyzed samples, Zn-dolomite is on average 12 wt.% of the bulk, whereas smithsonite is ~ 41 wt.% on average. Considering that our samples have an average grade of 24 wt.% Zn, about 1 wt.% of Zn is hosted in Zn-dolomite and 23 wt.% Zn in smithsonite. This means that if we normalize these amounts to 100 wt.% of all zinc minerals, Zn-dolomite represents ~20 wt.%, while smithsonite plus Mg-smithsonite represent the other ~75 wt.% (Figure 4.12a). It follows that normalizing the measured Zn to 100 wt.%, smithsonite contains 85 wt.% of the total zinc, whereas Zn-dolomite only carries 3 wt.% of the total zinc (Figure 4.12b). However, as previously mentioned, this distribution is not uniform within the samples: for instance, in sample J109-5, Zn-dolomite amounts to 35.93 wt.% of the bulk ore, whereas smithsonite is only 19.14 wt.% (table 3). This means that in this sample Zn-dolomite represents 65 wt.% of the Zn-minerals, while smithsonite, the remnant 35 wt.%. Hence, in this sample, Zn is mostly contained in Zn-dolomite rather than in smithsonite; this ZnO enrichment in dolomite was considered the reason of the difficulty in overcome the 80% of Zn from the bulk ore using the AmmLeach[®] processing route (Mondillo et al., 2011).

It is also necessary to stress that the mineral abundances obtained by QEMSCAN® are only roughly comparable with those derived from X-ray diffraction quantitative analyses using the Rietveld method (table 1) (Mondillo et al., 2011). The reason is a consequence of the technical approach of the QEMSCAN® methodology: several mineral compounds discriminated by QEMSCAN® are not minerals *sensu stricto,* and are not classified on the basis of their crystal structure, so it was impossible to calculate them by the Rietveld method. For instance, if we want to make a rough comparison between the results obtained by XRD-QPA (Rietveld) and those resulting from QEMSCAN®-QPA (table 2 and table 5) in a sample (i.e. J109-3), we must note that, because QEMSCAN® detects a

───

higher number of mineral phases, the wt.% of the main minerals, which are in common with the Rietveld analyses will vary comformably.

In this study, when chemical analyses have been used to validate the mineral amounts determined by QEMSCAN®, contrasting results have arisen (Figure 4.13).
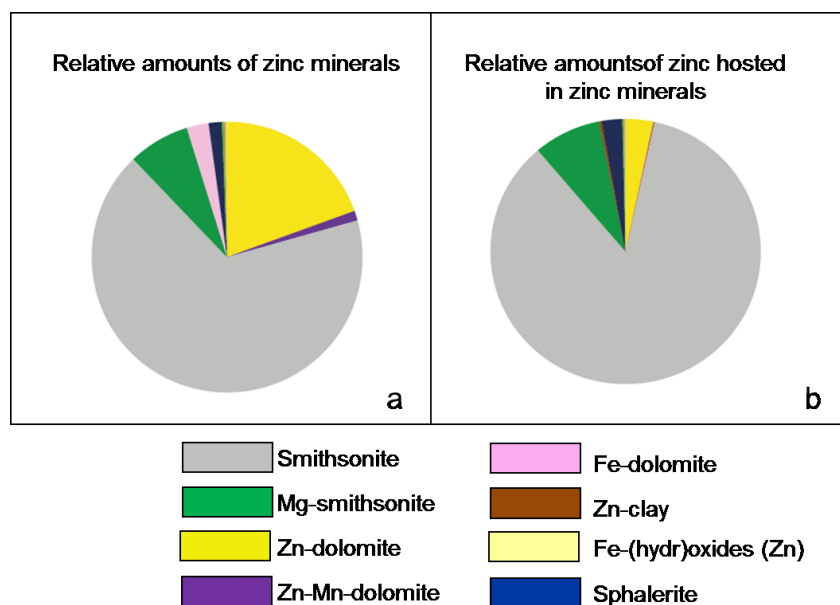

Figure 4.12: Pie chart showing the amount of Zn in the various Zn minerals at Jabali: (a) Normalized amounts (wt.%) of zinc minerals occurring in the Jabali samples; (b) Normalized amounts (wt.%) of total zinc hosted in the various zinc minerals occurring in the Jabali samples (Santoro et al., in press).

In particular, it is evident that the calculation of the most abundant elements from the mineral phases results typically in a slight under-estimation of Ca. On the other hand Zn and Pb were over-estimated, whereas Fe values show a more complex correlation. Magnesium is the only element that on average appears in good agreement between the two methods.

When comparing the geochemical data with the mineral-based data (Figure 4.13), there are differences. However, this was expected, as the chemical analyses of the elements and those of minerals were not carried out on exactly the same sub-samples (sample variation), and the analytical techniques are different (detection sensitivity differences). However, it is obvious that several samples show notable differences between the amounts of elements measured and those calculated. For example, the Pb and Fe minerals seem to be consistently and incorrectly evaluated relative to the measured element concentrations. Specifically, Pb mineral compounds correspond to a Pb amount double than that chemically measured. One possible explanation is that sample preparation may have affected the Pb-rich samples, concentrating the Pb minerals in the QEMSCAN® samples, relative to the real samples. As mentioned in the paragraph on the analytical methods, during epoxy resin block preparation, the heaviest particles (Pb-containing) that are mixed into the resin may accumulate preferentially at the base of the mould (which is the surface that is analyzed by QEMSCAN®), and this may result in an increase of the Pb ratio affecting the analysis. However, this possibility is already known, when working

with grain mount samples containing Pb-ores or any samples that have a large density variation (Pascoe et al., 2007).
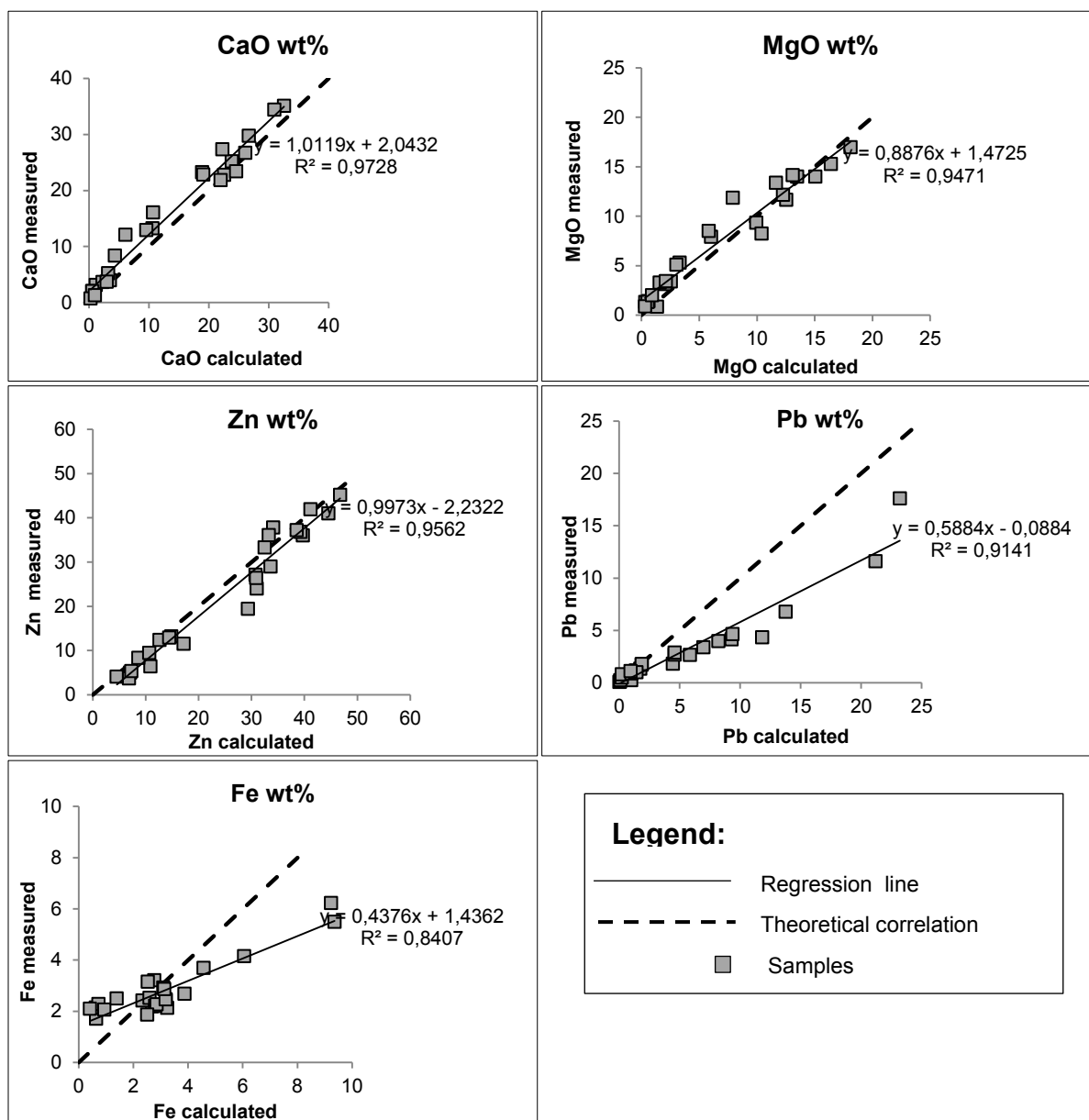

Figure 5.12: Diagrams of calculated element amounts from QEMSCAN® analyses plotted vs. measured element concentrations. (A) CaO wt% calculated from the minerals on QEMSCAN® analyses vs. CaO wt.% calculated by chemical analyses; (B) MgO wt.% calculated from mineral QEMSCAN® analyses vs. MgO wt.% from chemical analyses; (C) Zn wt.% calculated from mineral QEMSCAN® analyses vs. Zn wt.% from chemical analyses; (D) Pb wt.% from mineral QEMSCAN® analyses vs. Pb wt.% from chemical analyses; (E) Fe wt.% calculated from mineral QEMSCAN® analyses vs. Fe wt.% from chemical analyses (Santoro et al., in press).

Another explanation might be the complex and variable mineralogy of the samples: thus calculating real "*accurate*" chemical values from minerals, based on average theoretical values is a difficult task.

Iron was also expected to be poorly constrained, because in nonsulfide deposits it is mainly contained in hydroxides, which, as mentioned, can be poorly distinguished by the

use of QEMSCAN® because of the similarity of their spectra on rapidly acquired energy dispersive X-ray spectra (Anderson et al., 2014). Another issue is related to the grain size of the Fe-(hydr)oxides. In fact, in this study, we could observe that tiny grains (<10μm) of Fe-(hydr)oxides, scattered throughout both dolomite and Zn-dolomite (Figure 4.14) were commonly misidentified by QEMSCAN®: combined with the dolomite background they were evaluated as Fe-dolomite.
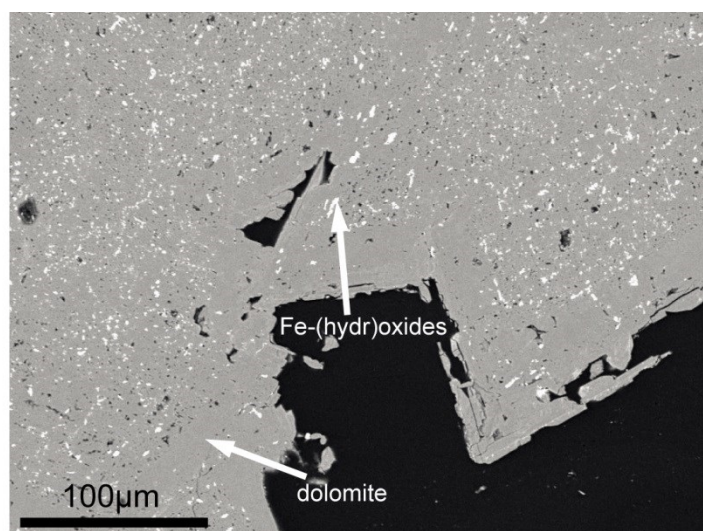

Figure 5.14: Scanning Electron Microscopy (SEM) image (BSE mode) of Fe-(hydr)oxides grains scattered within the dolomite (Santoro et al., in press).

Indeed, comparing samples where Fe-calculated is lower than Fe-measured, it can be deduced that the Fe-dolomite amount (table 5) is quite high. If 1/3 of the Fe values are subtracted from the Fe-dolomite (e.g. 3 wt.% Fe-dolomite at 5 wt.% Fe), and they are reassigned to Fe-(hydr)oxides (3 wt.% at ~60 wt.% Fe), the amount of Fe-calculated is very similar to Fe-measured. On the contrary, for phases <10 μm (grid size used), i.e. smithsonite, surrounded by or scattered throughout Fe-(hydr)oxides, QEMSCAN® detects them together as Zn-enriched Fe-(hydr)oxides. This results in an over-estimation of the calculated Fe. Therefore, if a particular deposit is characterized by mineral grains smaller than the scan resolution normally used for analyses (e.g. by SEM validation), it may be worth running QEMSCAN® analyses using a smaller grid size/resolution to ascertain the reliability of the data. Another point that needs considering is that the evaluation of calculated Fe was done using a fixed value for goethite (68.88 wt.% Fe). If other trace elements are present in goethite (in the current study: Pb, Mn, Zn, Si), the percentage of Fe in this mineral decreases. Hence, for a better evaluation of Fe calculated from the modal mineralogy, it is more reliable to check the composition of a mineral phase in each sample, but this increases the time and thus the costs of the work.

The problem in QEMSCAN® analysis, related to the occurrence of mineral phases smaller than the employed 10 μm resolution, or smaller than the beam size excitation volume (e.g., clays), which are misidentified because they produce a mixed X-ray spectrum (Chapman, 1986), was encountered also in other cases. For example, kaolinite

at Jabali is finely intergrown with sauconite (Zn-smectite), and as such it was impossible to distinguish between the two. Also the identification of sauconite itself, instead of a rough smithsonite-kaolinite mixture, was challenging because of the fine size of these clay mineral particles. Other examples of this type of problem encountered in the current QEMSCAN® study relate to Cd-sphalerite, Pb-acanthite, and Ag-smithsonite. In Figure 4.15A it can be seen that what was previously considered as Cd-sphalerite by QEMSCAN® analyses, corresponds instead to small patches of greenockite at the border and within sphalerite. Moreover, galena specks can be detected in acanthite, which is contained in turn within an anglesite patch (Figure 4.15B). These cases may be technically resolved by increasing the X-ray resolution from 10 μm to 5 μm or less. However, the very low amount of the above mentioned phases (greenockite <0.05 wt.%, acanthite <0.20 wt.%, and galena rarely up to 4 wt.%), and hence their negligible importance in a feasibility study, means that the higher cost of these more accurate analyses is likely prohibitive. In our case, the best option was to corroborate these data, solely for a scientific purpose, with a scanning electron microscope.

As regards to the analyses of the concentrate samples, it was determined that, despite the effectiveness of the concentration process, several uneconomic phases (e.g., pure dolomite from the host rock, Fe-(hydr)oxides) were not completely removed. This result, which should be carefully considered during processing, can be related to: (1) very fine-grained textures (0.5 mm or even lower); or (2) liberation issues, as some less dense phases can still occur together with heavy phases (i.e., composite particles with associated dolomite and smithsonite).

The data of the mineral association indicate that the smithsonite is, in these samples, mostly associated with a Mg-rich smithsonite and Zn-rich dolomite. This is an important information for the possibility of Zn recovery; in fact SRK consulting (2005) already reported the inexplicable impossibility to recover all the Zn from the bulk ore by the use of LTC (Ammleach®). Mondillo et al. (2011, 2014) solved the issue, ascribing this not-recoverable Zn to the presence of Zn-dolomite (not quantified). The quantitative analyses carried out in this thesis and the mineral association directly reveal not only the occurrence of abundant Zn-dolomite (in agreement with Mondillo's analyses), but also to which phase it is associated (smithsonite). Hence follows that, by the use of QEMSCAN® it was possible to predict a certain loss of zinc with the use of Ammleach®, and the impossibility to recover the zinc trapped in the dolomite lattice unless a more effective technology should be used.
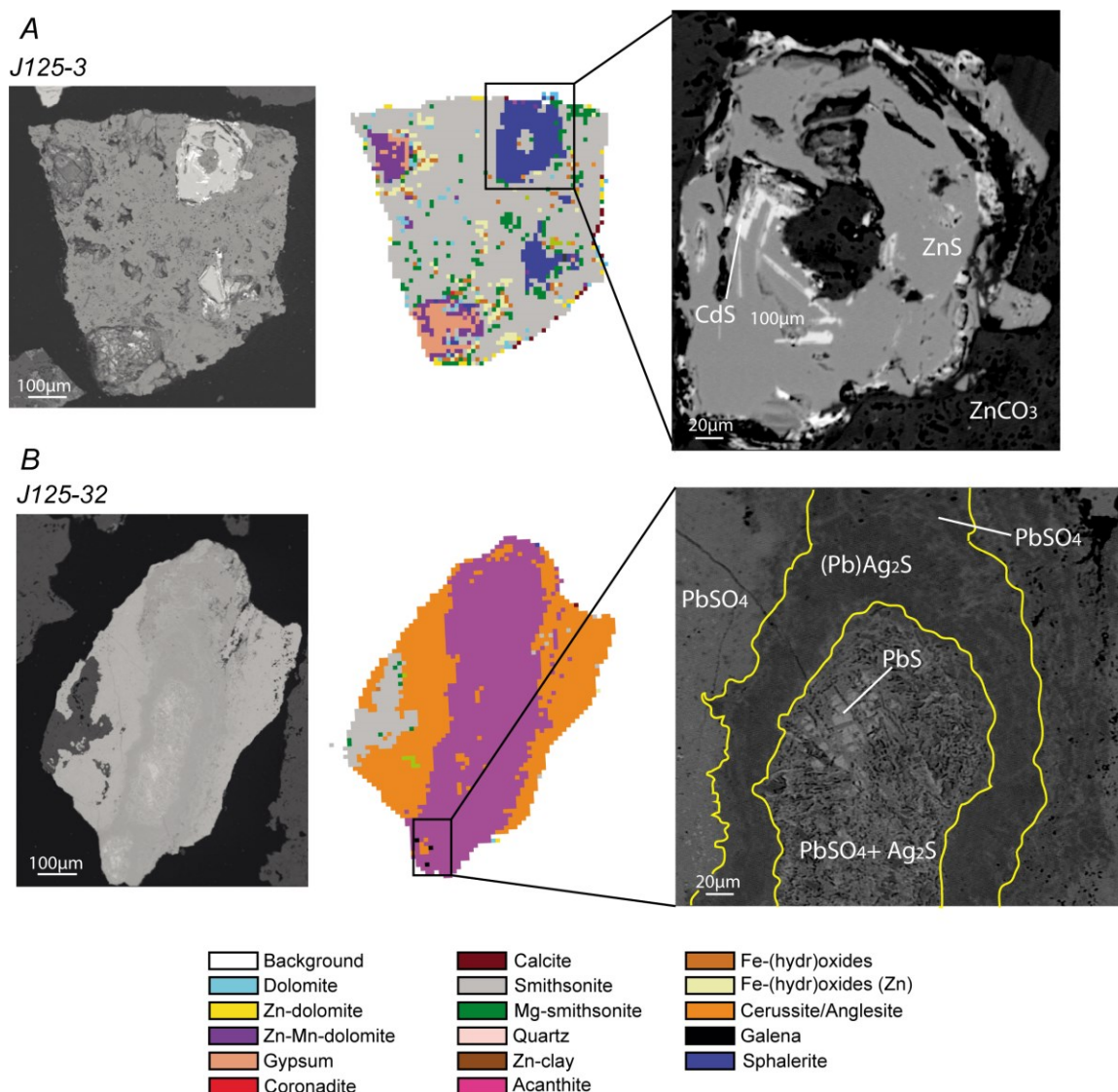
Figure 4.15: SEM backscattered electron images compared with QEMSCAN® enlarged false color images (fieldscan mode). (A) J125-3: sphalerite (ZnS) remnant within smithsonite (ZnCO$_3$). Greenockite exsolution (CdS) within a sphalerite remnant. The inner part consists of smithsonite; (B) J125-32: galena (PbS) grains in anglesite (PbSO$_4$); acanthite (Ag$_2$S) mixed with anglesite surrounds the galena cores. Less abundant and trace minerals are not visible in the figure and are therefore not represented in the color key; the latter comprise: Fe-dolomite, pyrite, hetaerolite, Fe-Mn-(hydr)oxides, chalcophanite, chlorargyrite, plagioclase feldspar, apatite, and chlorite (Santoro et al., in press).

Conclusions

The complex mineralogy of the Jabali nonsulfide ores had been investigated with different methods: the most important findings have been quoted from the recent literature. In this thesis the mineral association has been carefully investigated by QEMSCAN®. Here are resumed briefly the main results of this research:

1. The mineralogy of the Jabali deposit consists of major (dolomite, smithsonite), minor (calcite, cerussite/anglesite, Fe-(hydr)oxides) and trace minerals (chlorargyrite, acanthite); new accurate information has also been gained on the quantitative modal mineralogy, as it was possible to quantify the amount of the "*impure*" phases, such as Mg-smithsonite (up to ~16% in sample J125-6) and Zn-dolomite (up to ~36% in sample J109-5).

2. The Zn amount occurring in the Zn minerals is on average 3 wt.% carried by Zn-dolomite (~1 wt.% of measured Zn), 85 wt.% (~23 wt.% measured Zn) in smithsonite, and 12% in other Zn-phases, but it is not uniformly distributed through the samples. In some samples, which contain more Zn-dolomite than smithsonite (e.g., J109-5), the above proportion can be inverse. Its presence, considered to be the main cause of the irregular Zn recovery for the samples containing <5 wt % in the metallurgical tests, had been previously detected (Mondillo et al., 2011), but never quantified. The evaluation of the amount of Zn-dolomite in the Jabali deposit is therefore useful to enhance its mineralogical characterization, because it defines how much of the total Zn calculated from the chemical assays could be lost during processing and hence improves reconciliation data for Zn metal. In the case of nonsulfide Zn deposits like Jabali, a preliminary study like this carried out in this thesis, can better predict the results of metallurgical tests, especially if there are non-economic minerals in the deposit, which contain economic elements that would usually be discarded as waste.

4. Careful sample preparation and the combined use of complementary mineralogical techniques are necessary to obtain accurate results. Specifically, the outcomes of the comparison between chemical assays and calculated elements values show that QEMSCAN® analyses were accurate and effective for the characterization and quantification of Zn-, Ca- and Mg-bearing phases at Jabali, whereas the Pb and Fe phases require further refinement. The discrepancy between Pb and Fe calculated through QEMSCAN® modal mineralogy and that measured by chemical analyses, is probably due to a lack of focus on the Pb- and Fe bearing phases, related to the application of routine modes for sample preparation and analysis.

Chapter 5

The supergene nonsulfide Zn-Pb prospect of Reef Ridge, Alaska

5.1. Introduction

The Reef Ridge nonsulfide Zn>>(Pb) prospect is located in the Kuskokwim Mountains in the Yukon-Koyukuk region of west central Alaska (US) (Medfra Quadrangle B3), northeast of the McGrath village (63°23'2"N latitude 154°21'50"W longitude, 561 m elevation 50 a.s.l.).

The deposit is part of Doyon lands (Figure 5.1) and is under the management of Doyon Ltd., which is an Alaska Native regional corporation, created by the Congress in 1971 under the terms of the Alaska Native Claims Settlement Act (ANCSA).
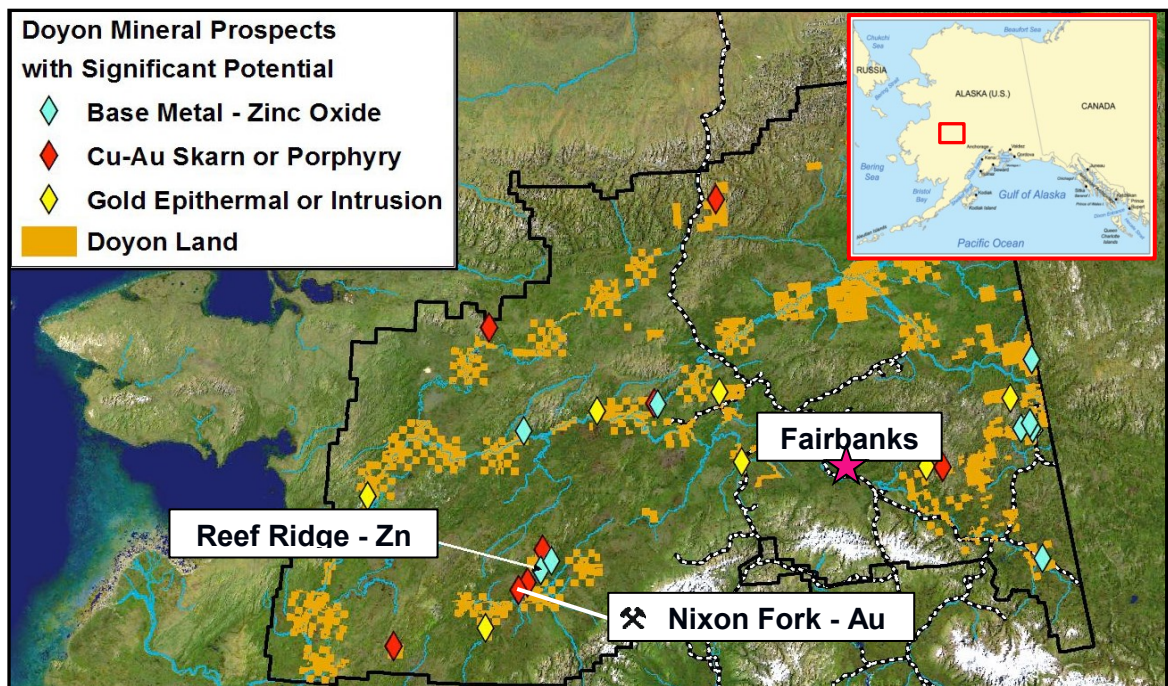

Figure 5.1: Doyon lands and main mineral resources occurring in it.

A first exploration campaign (Annual Progress Report, 1975) discovered anomalous concentrations of Zn and Pb in soils around the Reef Ridge area: this discovery was interpreted as a possible evidence for massive sulfide deposits. Since 1975, therefore, several exploration campaigns were conducted each year (1976, 1977, 1978, 1979), with the aim to define the mineral potential of the whole area. From 1980 to 1984 exploration activities were conducted by Patino Inc. The findings of this intense exploration brought to define a larger area comprising several prospect zones (Figure 5.2), in which a common mineralization style consisting in Zn and Pb sulfides was recognized.

In a Progress Report of 1981 by Patino staff, fourteen Zn>Pb sulfide prospects were mentioned, with different economic potential. The Reef Ridge, Beaver Creek, Soda Creek and Spring Ridge (Figure 5.2) prospects were considered to have the highest potential, whereas Saddle, Cache Creek, Bear Pass, Hillside and Big Gate (Figure 5.2) had a moderate potential, and Starship and Atoll the lowest one. The Bimini, Bermuda and Midway prospects (Figure 5.2) were hardly considered to be of any importance. The

Asmyrahha, discovered shortly afterwards, seemed not to held a great mineral potential either (Figure 5.2).

In 1989-1990 the exploration rights passed to Pasminco Exploration Ltd., which stated that the whole area of the belt had been thoroughly investigated and that the results showed that all the known occurrences, with the exception of Reef Ridge itself (where a limited drilling campaign had already taken place), were of inconsequential size. The estimated grade of the ore in the main prospect of Reef Ridge (1.8 Mt at 6.5% zinc, Andrews and Rishel, 1982; Fair and Bright, 1989; Schmidt, 1997b; Mosher 1990) was not economic either, considering the operating and capital costs. As a consequence, the exploration ceased and all further activities in the area were abandoned.
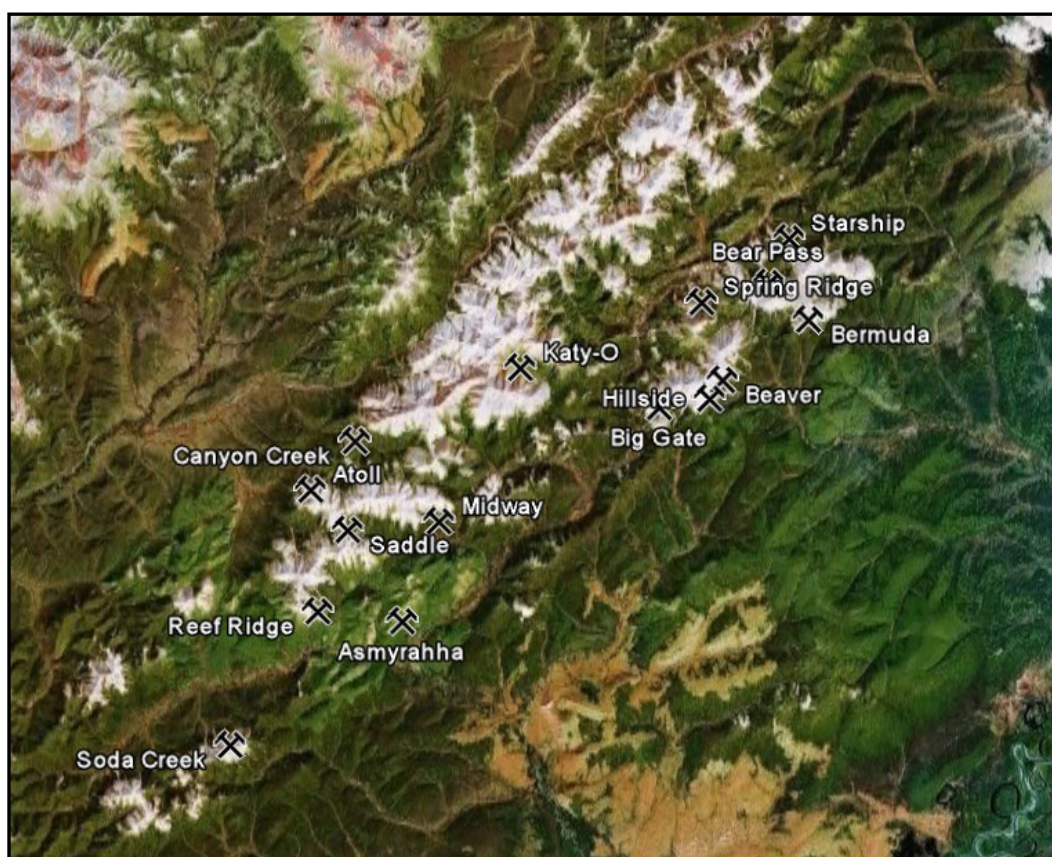

Figure 5.2: Distribution of several Zn>Pb prospects discovered from 1975 to 1990 in the Reef Ridge area.

In 2010-2011 Doyon Ltd. promoted a new drilling campaign on the Reef Ridge property, in order to re-evaluate the real potential of the site. Based on the 2011 drilling, the Reef Ridge reserves were adjourned to 460,330 metric tons at an average grade of 17.4% zinc (J. Woodman, personal communication). More attention was addressed to the oxidized portion of the deposit consisting of supergene nonsulfide Zn minerals (smithsonite, hydrozincite), mixed with Fe-(hydr)oxides. The samples from a selected number of cores were subjected to a complete petrographic, mineralogical, geochemical and quantitative mineral evaluation (which is part of this thesis), using a series of analytical techniques, in order to better characterize the supergene mineralization. In addition, Doyon Ltd. carried

out a new soil sampling campaign during the summer of 2012. The aim was the investigation around three magnetic anomalies revealed during an extensive aeromagnetic exploration of Newmont Mining in this part of Alaska.

The scientific literature on the Reef Ridge deposit is extremely scarce; the big part of the knowledge on Reef Ridge geology and mineralization comes from the numerous annual reports held in the archives of Doyon Ltd. and from few published papers.

After Schmidt (1997b), the primary mineralization not only at Reef Ridge, but also at other prospects of the belt may genetically represent Mississippi Valley-type deposits that formed between Late Cretaceous and Early Tertiary in the Selwyn basin. In all existing reports and literature items the Reef Ridge primary ores are always mentioned as belonging to the "Mississippi Valley-type" (Nockleberg *et al.*, 1994). Neither a spatial or genetic relationship with the Late Cretaceous-Tertiary magmatism has been observed so far (Patton et al., 1980; Andrews and Rishel, 1982). However, considering the proximity to the porphyry systems of the Mystery Mountain area (Copenhagen Hill, Frozen Creek, and Tarn Von Frank prospects), and to the Nixon Fork mineralization, it cannot be excluded that the primary deposit of the Reef Ridge belt could be seen as distal polymetallic ore concentrations associated with the magmatic processes and to the Idiatroot-Denali faults displacement, during Late Cretaceous-Early Tertiary (Santoro et al., 2014 aggiungi abstract).

No certainty exists about the age of Reef Ridge nonsulfide ores, which have been considered economically more important than the small concentrations of primary sulfides; recent stable C-O isotopic studies on the carbonate minerals suggest that they formed during modern summer periods or a Pliocene or Holocene age.

In the following paragraphs are reported the results of a study on the Reef Ridge nonsulfide concentrations, carried out with different analytical techniques, in order to obtain a complete and reliable characterization of the deposit (Santoro et al., in press). A complete bibliographic evaluation of the geology and tectonics of the area has been also performed, to provide a frame for the genesis of the mineralization.

In conformity to our aims this chapter reports on:

1) the geological setting of the Reef Ridge prospect, also comprehensive of the geological evolution of the whole district,

2) a complete mineralogical (also quantitative), petrographic and geochemical characterization of the nonsulfide ore association, to gain information aimed to the formulation of processing strategies.

5.2. Geology of Alaska

The current geological and tectonic setting of Alaska is the result of a complex history consisting of a continuous alternance of extensive and compressive regimes, during a time span lasting from Neoproterozoic to Late Mesozoic.

Alaska represents the extreme Northern portion of the American Cordillera, an accretionary orogen (Cawood et al., 2009) formed by the "collage" of authoctonous and parauthoctonous sequences of the Laurentian Craton with allocthonous portions of both crustal and oceanic lithosphere (Coney et al., 1980, Nelson et al., 2013). The Alaska

framework consists of numerous fault-bounded lithospheric blocks known as "terranes" (or lithospheric fragments) (Jones et al., 1983) with distinct origins (magmatic arcs, microcontinents, island arc, floors of ocean basins) that amalgamated and accreted to the western margin of the Ancestral North America (Plafker and Berg, 1994) in Middle Jurassic-Cretaceous (Coney et al., 1980; Box, 1985; Box et al., 1990). For simplicity, these terranes have been grouped in four major paleogeographic realms (Nelson and Colpron 2007; Nelson et al., 2013; Colpron et al., 2007a, b) showing affinity with the Laurentia, Baltica and in minor part with the Siberian domains (Figure 5.3) (Miller et al., 2011; Bradley et al., 2003; Nelson et al., 2013 and references therein). They are: 1) *Laurentian Realm, 2) Peri-Laurentian Realm, 3) Arctic North-Eastern Pacific Realm and Insular belt, 4) Coastal Realm* (Colpron et al., 2007a,b; Nelson et al., 2007, 2013).

1) The *Laurentian Realm* (Ancestral North America) includes the Neoproterozoic to Paleozoic autocthonous and parautocthonous sequences of the Ancestral North America belonging to the western border of the ancient Laurentia craton. The rocks belonging to this realm are confined to the north-eastern and central-eastern Alaska, and to the eastern part of the Alaskan Range (in the Yukon-Tanana upland, Foster et al., 1973). They consist of parautocthonous Devonian successions of slope-to-basinal facies and of plutons formed during the Rodinia break-up in Late Neoproterozoic-Middle Paleozoic (Colpron et al., 2006). These sequences were strongly deformed and metamorphosed during the Middle Mesozoic accretionary orogeny (Dusel-Bacon et al., 2006; Nelson et al., 2006; Dusel-Bacon and Williams, 2009). The Alaskan lithologies, in fact, show evidence of extensional deformation typical of exhumation and voluminous felsic plutonism, whereas no signs of these phenomena are registered in the Selwyn basin successions. This is explained with the fact that the Alaska basinal successions represent an exhumed core during the accretionary event of the allochtonous terrane on the western Ancestral North America, whereas the western Selwyn Basin represents an immediate northeastern salient to the exhumed core (Mair et al., 2006 and references therein). The current position of both areas depends on a destral movement of the Tintina Fault in Late Cretaceous-Early Tertiary (Figure 5.3), which displaced the Selwyn Basin in the Yukon region (Canada) (Mair et al., 2006).

2) The *Peri-Laurentian realm* (or Intermontane terranes, Monger et al., 1982) consists of allocthonous terranes having affinity with the Laurentia craton and boarding the boundary of the western Ancestral North America.

They comprehend: the Yukon-Tanana, Slide Mountain, Quesnel, Stikine, Cache Creek, Bridge River (and other minor) allochtonous terranes (Nelson et al., 2013) (Figure 5.3). Generally, these terranes consist of sequences of sedimentary rocks of Laurentian affinity, ocean floor, ridge flood basalts, arc magmatic rocks, the latter related to the subduction of the Panthalassa Oceanic crust beneath the Ancestral North America and to the development of a magmatic arc and a back arc rift basin, during the Middle-Late Devonian to Mississipian (Rubin et al., 1990; Colopron et al., 2007a, b).

Rocks belonging to the Peri-Laurentian realm crop out in the extreme eastern Alaska, at the border with Canada.

Figure 5.3: Terranes of the Alaska Cordillera. The terranes are grouped in the legend according to paleogeographic affinities. Inset shows morphogeologic belts of the northern Cordillera after Gabrielse et al. (1991). Fault abbreviations: CF = Cassiar fault, CSF = Chatham Strait fault, FF = Fraser fault, FwF = Farewell fault, KF = Kechika fault, NFF = Nixon Fork-Iditarod fault, PF = Pinch fault, PSF = Peril Strait fault, NMRT = northern Rocky Mountain trench, TkF = Takla-Finlay- Ingenika fault system, TT = Talkeetna thrust, YF = Yalakom fault (Colpron and Nelson, 2011a).

They belong to the Yukon–Tanana terrane consisting of sedimentary rocks of the Snowcap assemblage, which originated along the distal western Ancestral North America (Colpron et al., 2007a, b), followed by magmatic arc succession. Two different types of magmatism affected the Yukon-Tanana terrane: a) bimodal volcanism during the back arc rift onset (Piercy et al., 2006), similar to that occurring along the Laurentia Margin (Late Devonian-Early Mississipian), b) intermediate magmatism (Simard et al., 2003; Gunning et al., 2006) during the spreading of the Slide Mountain Ocean and after that the Yukon-

Tanana terrane was rifted apart from the western North America border (Upper Carboniferous-Early Permian).

3) The *Arctic North-eastern Pacific and Insular belt* (North Alaska and Insular Terrane) comprises several crustal blocks, which lack evidence of North American affinity and display similarities in term of faunas and isotopic values with other paleocontinents such as Siberia and/or Baltica (Bazard et al., 1995; Bradley et al., 2003; Amato et al., 2009; Colpron et al., 2007a, b, 2009; Miller et al., 2011; Beranek et al., 2013 a, b). These terranes occur in the whole Alaska (Figure 5.3.) and comprise the Arctic Alaska-Chukotka terrane (Moore et al., 1994) including the Brook Range, the North Slope of Alaska and the Seward Peninsula. It represents a composite pericratonic area with a crystalline basement (Neoproterozoic), continental carbonate shelves and siliciclastic sedimentary sequences (Paleozoic-Mesozoic) followed by magmatic and metamorphic rocks (Late Jurassic-Cretaceous). A paleogeographic reconstruction locates the Arctic Alaska- Chukotka terrane in an exotic position from the Laurentia; during the Neoproterozoic break-up of Rodinia, in fact, it likely rifted from Siberia (Dumoulin et al., 2002) and set to the north-east of ancient Laurentian near the Baltica Paleo continent (Amato et al., 2009; Miller et al., 2010, 2011). The current position was reached later, in Middle Mesozoic. The Ruby terrane is located in northern and central Alaska. It is a pericratonic terrane consisting of siliciclastic units intruded by Devonian plutons that have undergone extensive deformation and metamorphism. There is no certainty about its paleogeographic position, but the affinity with both western Laurentia and Brooks Range (Arctic Alaska), make it a possible composite structure of both elements that amalgamated during the Late Jurassic-Early Cretaceous accretion of the Koyoukuk-Togiak-Nyac terranes with the Arctic Alaska during the Brookian Orogeny (Roeske et al., 2006). The Angayucham Terrane is located in northern-central Alaska and represents large sheets of Devonian-Jurassic oceanic crust obducted and thrusted over the Arctic Alaska terrane during the Brookina Orogeny (Moore et al., 1994). The Farewell Terrane lies in central Alaska and consists of a Proterozoic crystalline basement overlain by Paleozoic carbonate and siliciclastic sequences depositated along a late Neoproterozoic to Devonian passive margin. Faunal and isotopic evidences (Blodgett et al., 2002; Bradley et al., 2003,) revealed that this terrane was a microcontinental fragment with affinity with both Laurentia and Siberia. For this reason, the Farewell terrane is believed to be somewhere in between these two cratonic areas from Cambrian to Early Permian (Bradley et al., 2003). A late Permian orogeny led to the assemblage of this terrane with the Arctic Alaska-Chukotka terrane (Bradley et al., 2003). The Kilbuk terrane (Box et al., 1990;) crops out in southwestern Alaska. It comprises the oldest known rocks of Alaska, dated to Early Proterozoic (2050 to 2084 Ma). It mainly consists of metamorphic rocks including a variety of intermediate to felsic orthogneisses, subordinate amphibolites, and rare pelitic schists and marbles. The Kilbuck terrane is now known to include at least one younger granite dated at 849 Ma (Bradley et al., 2007), strongly suggesting commonality with parts of the Farewell terrane. Previously regarded as a displaced fragment of the North American craton or as a piece dislodged from central and western Australia, from the Baltic shield of Finland or from Guiana and west African shields (Box et al., 1990

Bowring and Podosek, 1989), it is now considered to have a Siberian Craton origin, because of a detrital zircon population with affinity to that craton (Bradley et al. in 2007). The Peninsular terrane comprehends the Peninsula delimited by the Border Ranger fault (to the South) and the Castle Mtn. Fault (to the North) (Figure 5.3). It consists of Paleozoic metamorphic rocks occurring as roof pendants in the Brooke Ranges ultramafic-mafic assemblage, Late Paleozoic through Late Triassic, Jurassic and Cretaceous sedimentary and volcanic rocks correlated with Wrangellia terrane, Jurassic plutonic rocks of the Alaska-Aleutian Range Batolith. Paleomagnetic and stratigraphic data suggest that it may have shared its geologic history with the Wrangellia terrane since Late Triassic and possibly even since Late Paleozoic (Nokleberg et al., 1994). The Alexander and Wrangellia terranes belong to the Insular Belt; these are located in the south-easternmost Alaska. These two terranes were born as individual ones, and then were amalgamated before the Midde Jurassic accretion (Nelson et al., 2013 and references therein), probably in Middle Pennsylvenian (Gardner et al., 1988; Nokleberg et al., 1994). The Alexander terrane is older and has been considered as a fragment of early and middle Paleozoic Island arc (Gehrels and Saleeby, 1987; Gehrels and Berg, 1994). It consists of Late Precambrian-to-Early Paleozoic pericratonic continental shelves and Paleozoic volcanic arc related rocks (Nelson et al., 2007), but with some continentally derived sedimentary strata that contain Precambrian detrital zircon populations (Gehrels et al., 1996). Wrangellia is a Devonian and younger arc terrane. Alexander and Wrangellia experienced non-arc mafic volcanism in Late Triassic, which has been interpreted as the product of oceanic plateau volcanism in a rift zone. Peninsular Wrangellia and Alexander Terranes amalgamated prior to their accretion to south-central, southeastern Alaska (Colpron et al., 2007a, b).

4) *The Coastal Realm*: the terranes forming the Coastal Realm represent the outermost coastal belt occurring in Alaska, which is currently situated in the extreme southern Alaska and comprises also the Kenai Peninsula (Figure 5.3). This Realm developed in the Eastern Pacific near or along the Cordilleran margin. The terranes forming the Coastal Realm are relatively young (Mesozoic to Paleogene) and include accreted Paleocene-Eocene seamounts of Crescent terranes and Accretionary complex filled with sediments eroded from the emerging Cordillera. Although they originated along the more-or-less present margin of North America, some of the terranes have undergone a significant northward translation of 13° to 23°, indicated by paleomagnetic data (Bol et al., 1992; Gallen, 2008, Housen et al., 2008), but also by detrital zircon population; some of them derives from southwestern North America (Garver J. personal communication, 2013), other are of local origin.

5.3. Zinc–lead deposits in Alaska; primary sulfides and associated supergene concentrations

The metallogenic evolution of Alaska has been strongly influenced by the complex tectonics affecting the whole area. The numerous ore deposits occurring in Alaska are in relation with the pre-, syn-, and post accretionary evolution of this portion of the Northern American Cordillera (Goldfarb, 1997). The mineralization history in Alaska spans over 1.6 Ga from the Mesoproterozoic to Present, i.e. from the break-up of the

supercontinent Rodinia (Late Proterozoic-Early Cambrian) through the collision of several discrete terranes of different affinity (Early-Middle Mesozoic) to the nowadays setting (Late Mesozoic-Tertiary).

Several mineral deposits occur in Alaska: Porphyry Cu-Au, Cu-Mo, Mo, Epithermal and Intrusion-related gold, Orogenic gold, Carlin-type gold, Volcanogenic massive sulfides (VMS), sedimentary exhalative (SEDEX), Mississipi Valley-type (MVT), Zn-Pb Skarns, Carbonatites (REE) and Iron-oxide copper-gold (IOCG) deposits.

Generally, the mineralization styles in Alaska change according to the tectonic regimes active during the various ages: the Paleozoic is known as "the age of syngenetic sulfides" (Nelson et al., 2013), because of the many VMS and SEDEX deposited in this period, all of them related to extensional tectonic, which led to the rifting of continental margins. From Late Triassic to Paleocene, Alaska experienced instead a compressional tectonic regime leading to the deposition of big porphyry systems: from here the name of "age of porphyries" (Nelson et al., 2013).

Many of Alaska's significant base metal deposits generally formed both within and at some distance to the continental margins, subsequent to the initial opening of the Pacific Ocean at about 700 Ma (Goldfarb, 1997). These deposits include the late Paleozoic shale-hosted, base metal concentrations (Schmidt, 1997a; Leach et al., 2004; Kelly et al., 2000, 2004a), such as Red Dog in the western Brooks Range, and the polymetallic volcanogenic massive sulfide deposits of several ages (Newberry et al., 1997), occurring within the Brooks Range, east-central Alaska, and south-eastern Alaska. These deposits also developed farther from North America, and now occur in Wrangellia, Alexander, and Peninsular terranes, which were amalgamated together prior to Late Triassic (Goldfarb 1997; Nokleberg et al., 1994).

Volcanic hosted massive sulfides (VHMS or VMS) deposits

Most VMS in Alaska have a pre-Devonian to Late Triassic age, with minor occurrences of Tertiary deposits (Paleocene, Eocene).

Pre-Devonian VMS deposits occur in the allochthonous lithologies of Prince of Wales Island in the southernmost part of southeastern Alaska (Figure 5.4). The mineralization, consisting in Cu- and Zn-rich massive sulfides, is hosted in felsic to mafic volcanic units and in shallow-marine sedimentary rocks of the Alexander terrane (Goldfarb, 1997). The mineralization event should be ascribed to two episodes ranging from Late Proterozoic trough Silurian submarine-arc volcanism, in an intra-oceanic region far south(?) of the present craton (Plafker and Berg, 1994), which was developed during the Appalachian-Caledonic orogeny due to the closure of the Iapetus ocean (van Staal, 2007\). The recent location was reached prior of Late Triassic. Most deposits, such as Niblack, Khayyam, Stumble-On, and Copper City (Figure 5.4), are located in rocks of the Late Proterozoic and Early Cambrian(?). A few occurrences, (one of the most important is Trocadero Bay, Figure 5.4, are hosted by Early Ordovician to Early Silurian units (Newberry et al., 1997a).

Late-Devonian to Carboniferous VMS, as well as SEDEX deposits are widely distributed in the Brooks Range (east-central and south-eastern Alaska). They are generally related to a big rifting event immediatly following the Appalachian-Caledonian orogeny. The

Ambler district (Devonian-Mississipian) is a big Zn-Pb-Cu cluster of deposits occurring in the southern Brooks Range (Figure 5.4). These are supposed to have been deposited at relatively shallow-water depths above submarine vents (Hitzman et al., 1986), because of the presence of shallow-water fossils, abundant carbonate rocks, and possibly subaerial volcanics.

Other VMS deposits occur in Central-eastern Alaska, in the Yukon-Tanana Upland, hosted in Alaska basinal sequences (Late Neoproterozoic-Middle Paleozoic, Colpron et al., 2006) of the Laurentia Realm (Ancestral North America). Their origin is considered to be related to a proximal back-arc and intra-arc setting contemporaneous/after the formation of the Slide Mountain Ocean, in latest Devonian to Early Mississipian (Nelson et al., 2002).

Many VMS deposits once located close to the Selwyn Basin (Lange et al., 1993), are now distributed along the north side of the Denali fault system: among them we can mention Bonnifield, Delta and Kantishna Hills District (Figure 5.4), which are all hosted in felsic parautochtonous successions of the Alaskan Range (Dusel-Bacon et al., 2006). Additional Devono-Mississippian Cu-Pb-, and Zn-rich VMS prospects continue to the east in the Yukon-Tanana terrane. In the western part of the Yukon-Tanana terrane, other Cu-Zn VMS occur. They are generally hosted by marine sedimentary rocks, spatially associated with pillow basalts of the Mystic sequence (Triassic) in the Farewell terrane. In central and

southeastern Alaska other Devonian to Mississipian Zn-Pb-Cu VMS districts have been recognized (Tracy Arm, Sumdum, and Sweetheart Ridge) (Figure 5.4).

Important VMS deposits formed in Late Triassic are related to a rifting stage of the Alexander terrane starting from Early Mesozoic. This rifting event led to a bimodal magmatism, responsible of high grade Cu-Pb, Zn, and Au-Ag VMS (Goldfarb, 1997), which extend throughout the Alexander terrane for 400 km. Among these we mention Greens Creek (Figure 5.4), which is one of the most enriched in Zn-Pb with Cu and minor Au and Ag.

The Johnson River (Figure 5.4), is also a highly enriched Zn-Au(Cu-Pb) VMS deposit (Early-Middle Jurassic) (Rockingham, 1993). It is related to the arc magmatism developed contemporaneously or shortly after the amalgamation between the Arctic-Northeastern Pacific Realm and the Peri-Laurentiam Realms.

In the Prince William area (Figure 5.4), in southern Alaska several Cyprus-and Besshi-type VMS deposits occur. They are related to the sea-floor volcanism associated with the spreading of the Kula plate, contemporaneous to its subduction under the North-America Plate (Goldfarb, 1997). Among these we mention the Midas deposit (Late Jurassic), and the Beatson-Duchess, Rua Cove, Ellamar, Schlosser and Threeman mineralizations (Paleocene-Early Eocene).
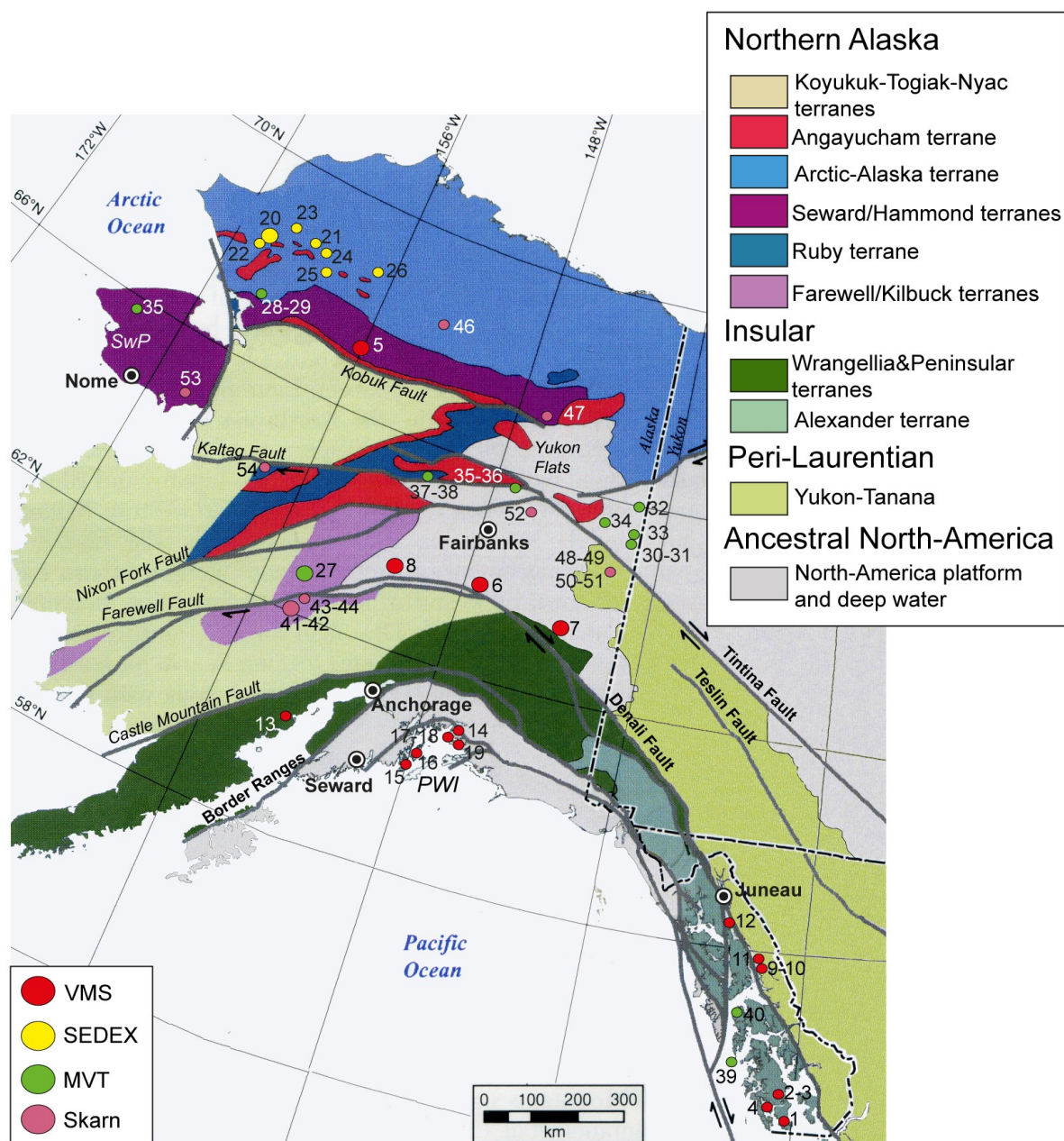
Figure 5.4: Zn-Pb deposit in Alaska (modified from Nelson et al 2013). VMS deposits: 1 = Niblack, 2-3 =Khayyam and Stumble-On, 4 = Copper City, 5 = Ambler District, 6 = Bonnifield, 7 = Delta, 8 = Kantishna Hills, 9-10 = Tracy Arm and Sumdum, 11 = Sweetheart Ridge, 12 = Greens Creek, 13 = Johnson River, 14 = Midas, 15 = Beatson-Duchess, 16 = Rua Cove, 17-18 = Ellamar and Threeman, 19 = Schlosser. SEDEX deposits: 20 = Red Dog, 21 = Drenchwater, 22 = Lik, 23 = Ginny Creek, 24 = Story Creek, 25 = Whoopee Creeks, 26 = Kady. MVT deposits: 27 = Reef Ridge, 28-29 = Frost and Powdermilk, 30-31 = Three Castle Mountain and Pleasant Creek, 32 = Midnight Hill, 33 = VABM Casca, 34 = Snowy Peak, 35-36 = Mo and Udall, 37-38 = Little Rosa Creek and Windy Creek, 39 = Coronation Island, 40 = Cornwallis Peninsula. Skarn deposits: 41-42 = Bowser Creek and Tin Creek, 43-44 = Rat Fork and Saturn Prospects, 45 = Eielson, 46 = Wiseman district, 47 = Chandalar district, 48- 48-50-51 = Happy, Oscar, Iron Creek and Deer Creek, 52 = Cleary, 53 = Omilak, 54 = Illinois Creek. Abbreviations: SwP = Seward Peninsula; PWI = Prince William Island (modified from Nelson et al., 2013).

Sediment-hosted massive sulfide (SHMS or SEDEX) deposits
The main part of the sediment-hosted (SEDEX) deposits in Alaska are Devonian-Carboniferous, related to a big rifting event, which began in Middle or Late Devonian, near to the end or immediately after the Appalachian-Caledonian orogeny (Goldfarb, 1997). The Late Devonian extensional tectonic led to the formation of several sedimentary basins, along the south-facing continental margin shelf-platforms (Einaudi and Hitzman, 1986; Moore et al., 1994). At the same time a widespread, perhaps 100 Ma long period of base metal-rich syngenetic ore deposition occurred in the newly-formed basins. The main part of the SEDEX deposits occur in the north-central Brooks Range, in the Arctic Alaska terrane. The ore deposits, mainly consisting of Zn-Pb-Ag massive sulfides, commonly associated with significant barite, are generally hosted in black siliceous shales, silicified calcareous black shales, and deep water siliceous successions (Schmidt, 1997a). Their age is from Devonian to Mississipian.
The biggest SEDEX deposit in Alaska is Red Dog (Figure 5.4) (Bundtzen et al., 1994, Ayuso et al., 2004, Leach et al., 2005; Kelly et al., 2004a), which was also the larger Zn producer in the world since 1989 (Nelson et al., 2013). Other examples include the nearby Lik deposit (Forrest, 1983) and the Drenchwater mine, about 150 km east of Red Dog (Figure 5.4) (Nokleberg and Winkler, 1982; Werdon, 1996). Most of these deposits are early diagenetic, as evidenced by the stratiform laminated sulfides, vent fauna, monomineralic banding, resedimented sulfide conglomerates, replacement textures and associated barite (Young, 1989).
Red Dog (Figure 5.4) is a peculiar SEDEX deposit: it has a high Zn/Pb ratio, lower Fe-sulfides (pyrite) content, high amounts of barite and a siliceous gangue. The mineralization is not laminated and the host rock is highly bioturbated (Schmidt, 1997a). Host sediment and sulfides are commonly replaced, and several banded or brecciated feeder zones are common: the multiple-vein episodes and breccia developments, the silicification fronts, and replacement textures indicate that ore deposition formed during the basin deposition but continued also during and after diagenesis (Young, 1989). A thick extensive barite-rich layer (Kelly et al., 2000, 2004a and b) suggests that the deposit formed under relatively oxidizing conditions and Schmidt and Zierenberg (1987) suggested that the Red Dog orebody may have formed beneath an impermeable silicified barite cap. The possible metal sources could have been provided by the leaching of clay minerals underlying the Late Devonian to Early Mississipian shale during basin dewatering (Schmidt and Werdon, 1993).
Lik (figure 5.4) deposit (Kelly et al., 2003) is a typical SEDEX: it has a low Zn/Pb ratio, high pyrite/marcasite amounts with less sphalerite, minor galena and rare barite. The main ore texture is laminar. Locally the sulfides occur in massive or nodular textures and only rarely in breccia. The feeder systems are absent or poorly developed. The environment of deposition was dysaerobic to euxinic (Schmidt, 1997a).
Other minor SEDEX ore concentration are: Drenchwater (Noklemberg and Winkler, 1982), Ginny Creek (Mayfield et al., 1979), Story Creek, Whoopee Creeks (Ellersieck et al., 1982) and Kady in figure 5.4 (Duttweiler, 1987); they are hosted by Late Devonian to Early Mississippian clastic units.

Mississippi Valley-type (MVT) deposits

Large Mississippi Valley-type deposits have not been identified in Alaska, but Schmidt (l997b) suggests that numerous, poorly studied Zn-Pb±Ag occurrences in Northern (Brooks Range), East-central and Southwestern Alaska could be MVT concentrations. They have several characteristics in common: simple mineralogy (prevailing Zn, Pb sulfides and less abundant Fe sulfides), no apparent igneous association, partial dolomitization or silicification of the host limestone, variable minor barite or fluorite, and structural preparation (i.e. brecciation) of the host rocks. Some of them show a big oxidized zone with a high concentration of supergene minerals (i.e. smithsonite, hydrozincite associated with Fe-hydroxides). Many of these MVT deposits are hosted in Proterozoic to Permian lithotypes, but the age of most Alaskan MVT deposits is poorly defined (Schmidt, 1997b).

The Reef Ridge district (Figure 5.4) is the best-known MVT cluster of deposits in Alaska. It consists of many prospect areas hosted in Paleozoic carbonate platform sediments of the Farewell terrane (Patton, 1980). The mineralization is more consistent at Reef Ridge itself (subject of this thesis), where the primary deposit consists of sphalerite, minor pyrite and galena as cement of a hydrothermal breccia. The sulfides are generally oxidized resulting in smithsonite, minor hydrozincite and cerussite concentrations. The age of emplacement of the Reef Ridge primary mineralization is supposed to be Late Cretaceous to Tertiary (Schmidt, 1997b).

In northwestern Alaska, in the Brooks Range, the Powdermilk and the Frost prospects (Figure 5.4), occur in an Ordovician dolostone. The mineralization consists here of a locally zoned dissemination of sphalerite, galena and pyrite. The age of mineralization has again not been defined (Schmidt, 1997b).

In the Charley River-Black River area in eastern Alaska (Figure 5.4), Proterozoic to Permian carbonate rocks host a number of Zn-Pb±Ag prospects (Mosher, 1990). Other prospects in the area are also hosted by Proterozoic dolostone (Three Castle Mountain North, Pleasant Creek, Midnight Hill), in Cambrian limestone (VABM Casca, Three Castle Mountain West), in Devonian crinoidal limestone (Salmontrout River area), and in poorly dated Proterozoic-to-Paleozoic limestone (Snowy Peak) (Schmidt, 1997b).

In central Alaska the Mo and Udall MVT prospects occur, both hosted in Cambrian and Silurian-Devonian limestone (Dobson, 1979). The mineralization, consisting of minor pyrite and abundant sphalerite, occurs in a solution breccia (Dobson, 1979) or shatter breccia, accompanied by silicification and dolomitization. Smithsonite and cerussite occur, indicating an oxidation process affecting the primary mineralization. The age of the mineralization is not well constrained, but a post-Cretaceous age has been suggested by Schmidt (1997b).

Other minor deposits are Little Rosa Creek and Windy Creek in central Alaska, Coronation Island and Cornwallis peninsula in southeastern Alaska (Figure 5.4). Minor MVT prospect have been recognised in the Seward Peninsula (SwP, Figure 5.4).

Skarn-Carbonate Replacement Deposits (CRD)

Skarn rich in Zn and Pb sulfides are widespread from the Brooks Range to southern Alaska (Figure 5.4). They occur in the more distal areas to major plutonic-related-hydrothermal systems, indipendently by the chemistry of the system. They can indeed be present around both plutons of volcanic arc affinity (Zn-Pb skarns distal to Cu-porphyry and with Cu, Fe and W skarns) and within plate affinity (Zn-Pb skarn distal to Sn and W greisen or Porphyry Mo deposits and Sn skarns) (Newberry et al., 1997). The age of mineralization is dependent on the age of the plutons to whom they are associated. In Alaska, the plutons associated with Zn-Pb skarns range in age from Proterozoic to Miocene, and are generally tonalite-granodiorite in character.

The biggest Zn-Pb skarn replacement bodies are located in the Farewell and peninsular terranes, on the northeastern flank of the Alaska Range (Figure 5.4). These mineralizations are associated with Tertiary porphyry dykes (Szumigala, 1986), related to the magmatism developed in Southern Alaska during the subduction of Kula, Farallon and Resurrection Plates under the North American Plate (Nelson et al., 2013).

The highest-grade prospect is Bowser Creek (Figure 5.4), adjacent to the Bowser igneous complex consisting in felsic dykes (Bundtzen et al., 1988) The mineralization consists of pyroxene-rich skarns with replacement pods, lenses and veins of Fe-rich sphalerite (marmatite), galena, pyrrhotite, and minor chalcopyrite, marcasite, and pyrite. However, an important fissure-controlled, silver-rich galena, tetrahedrite, pyrrhotite, and calcite mineralization occurs in marble away from the skarn itself (USGS mineral resources on-line spatial http://mrdata.usgs.gov/ardf/show-ardf.php?ardf_num=MG068). Sulfide-rich masses with Ag-rich galena and calcite veins occur at the marble front (Newberry et al., 1997).

At the Tin Creek prospect (Szumigala, 1986) the mineralization (an Ag-base-metal rich skarn) is associated with the emplacement of a granodiorite dyke generating calc-silicate metasomatism. The ore concentrations consist of chalcopyrite-rich skarns (proximal to the dyke swarm) and pyroxene-sphalerite rich skarns (in more distal zones).

Other similar deposits in Farewell terranes are Rat Fork and Saturn Prospects, and Eielson in Norteast of Farewell Terranes (Figure 5.4). These latter are all associated to granodioritic dykes (USGS mineral resources on-line spatial http://mrdata.usgs.gov/ardf/show-ardf.php?ardf_num=MG059; http://mrdata.usgs.gov/ardf/show-ardf.php?ardf_num=MG089; http://mrdata.usgs.gov/ardf/show-ardf.php?ardf_num=MM166).

The oldest Zn-Pb skarns known in Alaska are related to Proterozoic granite plutons (Wiseman district) to the south of Brooks Range (Figure 5.4). In the same area, other old Zn-Pb skarns dated to Devonian (Chandalar district, Figure 5.4) occur (Newberry et al., 1997). Other Devonian deposits are in Interior Alaska (Happy, Oscar, Iron Creek, Deer Creek, Figure 5.4) and are associated with Cu and W skarns (Cleary, in the Fairbanks area, Figure 5.4) (Newberry et al., 1997).

Polymetallic vein and carbonate replacement deposits also occur in the Seward Peninsula (Gamble and Till 1993). They are spatially associated with Cretaceous plutons. Silver-bearing base metal-rich veins hosted by high–grade metamorphic rocks occur in the and

Omilak deposits. In the Ruby terrane, the Illinois Creek base metal-rich polymetallic deposit is associated with middle Cretaceous plutonism (Goldfarb, 1997).

5. 4. Geology and stratigraphy of Reef Ridge

The Reef Ridge Prospect, located in the in the Yukon-Koyukuk region of west central Alaska (US), is hosted in the Paleozoic carbonate platform of the Farewell Terrane.

This terrane was long regarded as a piece of the Paleozoic passive margin of western Canada, dislodged from its original position but not exotic to North America (Coney et al., 1980; Box, 1985; Plafker and Berg, 1994). It is now considered a micro-continent located between Siberian and Laurentia during the early Paleozoic (Blodgett et al., 2002; Dumoulin et al., 2002), and was amalgamated with the northernmost portion of the North American Cordillera during the Mesozoic (Bradley et al., 2003) prior to Middle Cretaceous time (Nokleberg et al., 1994; Decker et al., 1994; Patton et al., 1994).

The Farewell Terrane consists of three genetically related subterranes: the 1) *Nixon Fork*, the 2) *Dillinger* and the 3) *Mystic* subterranes (Figure 5.5) (Decker et al., 1994; Bundtzen and Miller, 1997). These subterranes form a typical shallow carbonate platform - deep-water basin system.
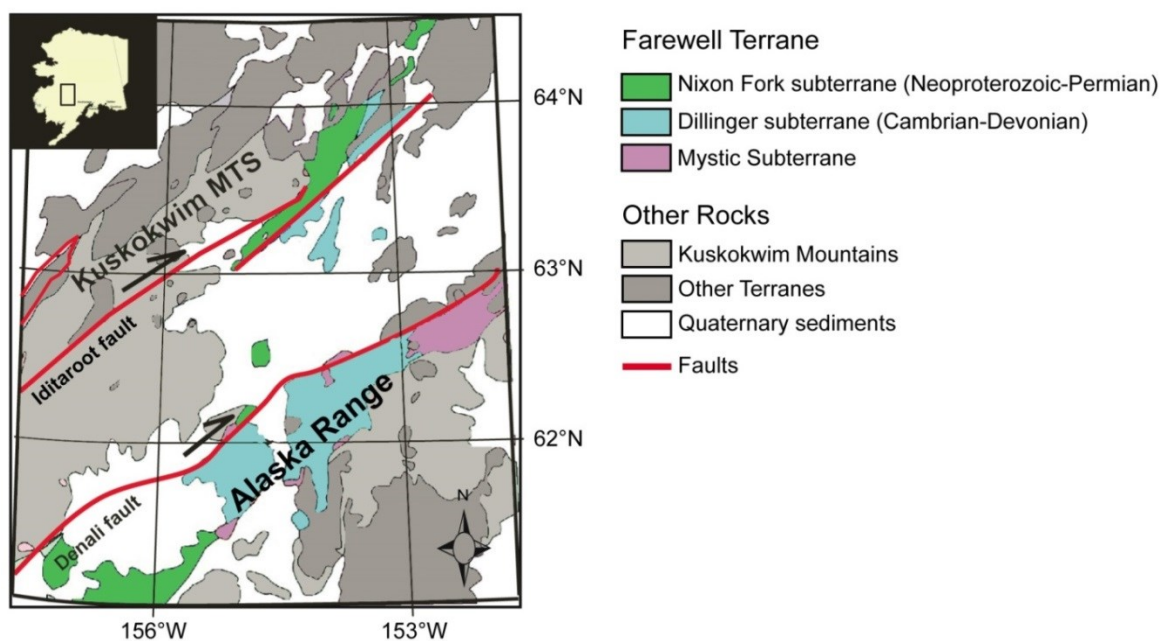

Figure 5.5: Geologic map of the Farewell Terrane and surrounding areas, Alaska (modified from Bradley et al., 2003).

1) The *Nixon Fork* subterrane mainly consists of a Paleozoic carbonate platform sequence lying on a Neoproterozoic metamorphic basement (McClelland et al., 1999), with affinity with the Siberia Craton (Blodgett et al., 2002; Dumoulin et al., 2002).
2) The *Dillinger* subterrane interfingers with the Nixon Fork, and is represented by a deep-water turbidite succession (Bradley et al., 2003 and references therein).
3) The *Mystic* subterrane consists of Late Paleozoic to Triassic-Jurassic shallow water successions (Bundtzen and Miller, 1997).

All these subterranes were subsequently eroded and partly covered by younger terrigenous clastic rocks deposited into the Kuskokwim basin. Late Cretaceous to Early Tertiary plutons and subvolcanic dyke and sill swarms of variable compositions (gabbro to alkali granite) (Bundtzen and Miller, 1997), related to the strong tectonic activity affecting the Reef Ridge area, intruded the older rocks. The Denali Fault system to the South and the Iditarod Fault to the North (Figure 5.5), which represent two major northeast trending regional structures, produced a Cretaceous-Tertiary offset of less than 150 km (Decker et al., 1994). Numerous northeast- and northwest-trending subsidiary structures (minor faults and folds), related to the Denali and Iditarod Faults, occur in the Farewell Terrane and possibly influenced the emplacement of intrusive bodies in the area. Tectonic activity controlled also the metallogeny in the Farewell Terrane. For example, the Nixon Fork project (Dutro and Patton 1982), located in the Kuskokwim Belt (Bundtzen and Miller, 1997), approximately 56 km northeast of McGrath and southwest of the Reef ridge area, consists of both disseminated and vein-style copper-gold-silver and skarn orebodies. The mineralization is hosted by Cambrian to Devonian shallow water carbonate rocks of the Nixon Fork subterrane and was formed in conjunction with Late Cretaceous to Early Tertiary volcanic activity.

Near the Reef Ridge area (within ~20 kms), several Cu-Au porphyry prospects (Bundtzen and Miller, 1997) i.e. Copenhagen Hill, Mystery Mountains-East, Frozen Creek, Von Frank and Tarn prospects, whose metallogenesis is related to Late Cretaceous tectonics, have an inferred Late Cretaceous age (based on an isotopic age of the Mystery Mountains intrusive complex, Moll et al. 1981). These prospects, as well as the Reef Ridge precursor sulfide mineralization, are considered to have been emplaced in the Nixon Fork subterrane during the Denali-Iditarod faults displacement in Late Cretaceous to Early Tertiary. Unconsolidated Late Tertiary to Holocene fluvial, colluvial, and aeolian deposits cover at least 50 percent of the maturely eroded Kuskokwim Mountains.

The Reef Ridge deposit is hosted in a Middle Paleozoic shallow water carbonate platform (Dutro and Patton, 1982; Clautice et al., 1993) belonging to the Nixon Fork subterrane, subdivided by Dutro and Patton (1982) into four main formations that from bottom to top are (Figure 5.6):

1) Novi Mountain Formation (Lower Ordovician), mainly consisting of shallow water limestone, locally intercalated with micritic limestone and siltstone.

2) Telestina Formation (Middle-Upper Ordovician), composed of dolomite with minor thin-layered limestone and silty interbeds at the base of the formation. At the top of the succession, the limestone beds decrease in thickness and include chert nodules and fossiliferous lenses.

3) Paradise Fork Formation (Silurian), which overlays the Telestina Formation with an angular unconformity. The whole succession reflects a change to a deep-water depositional environment, which consists of dark fossiliferous limestone and black shale.

4) Whirlwind Creek Formation (Upper Silurian-Late Devonian) that is well exposed in several outcrops in the Medfra Quadrangle. The base of the Formation consists of laminated algal dolostone deposited in a shallow water platform. The dolostone is

overlain unconformably by dark-grey limestone, intercalated with shale and marly limestone (Soda Creek Limestone).

The Reef Ridge prospect occurs in the algal dolomitic succession of the Whirlwind Creek Formation (Fig. 2). Schmidt (1997b and references therein) characterized the deposit as Mississippi Valley-type, whose fluid sources originated from Paleozoic sedimentary rocks and from the Jurassic/Cretaceous flysch of the Kahiltna terrane. Late-Cretaceous regional folding (Miller and Bundtzen, 1992), related to the Denali-Iditarod fault displacement, provided the possible mechanisms for the dewatering of sedimentary basins and the emplacement of the Reef Ridge mineralization (Schmidt, 1997b).
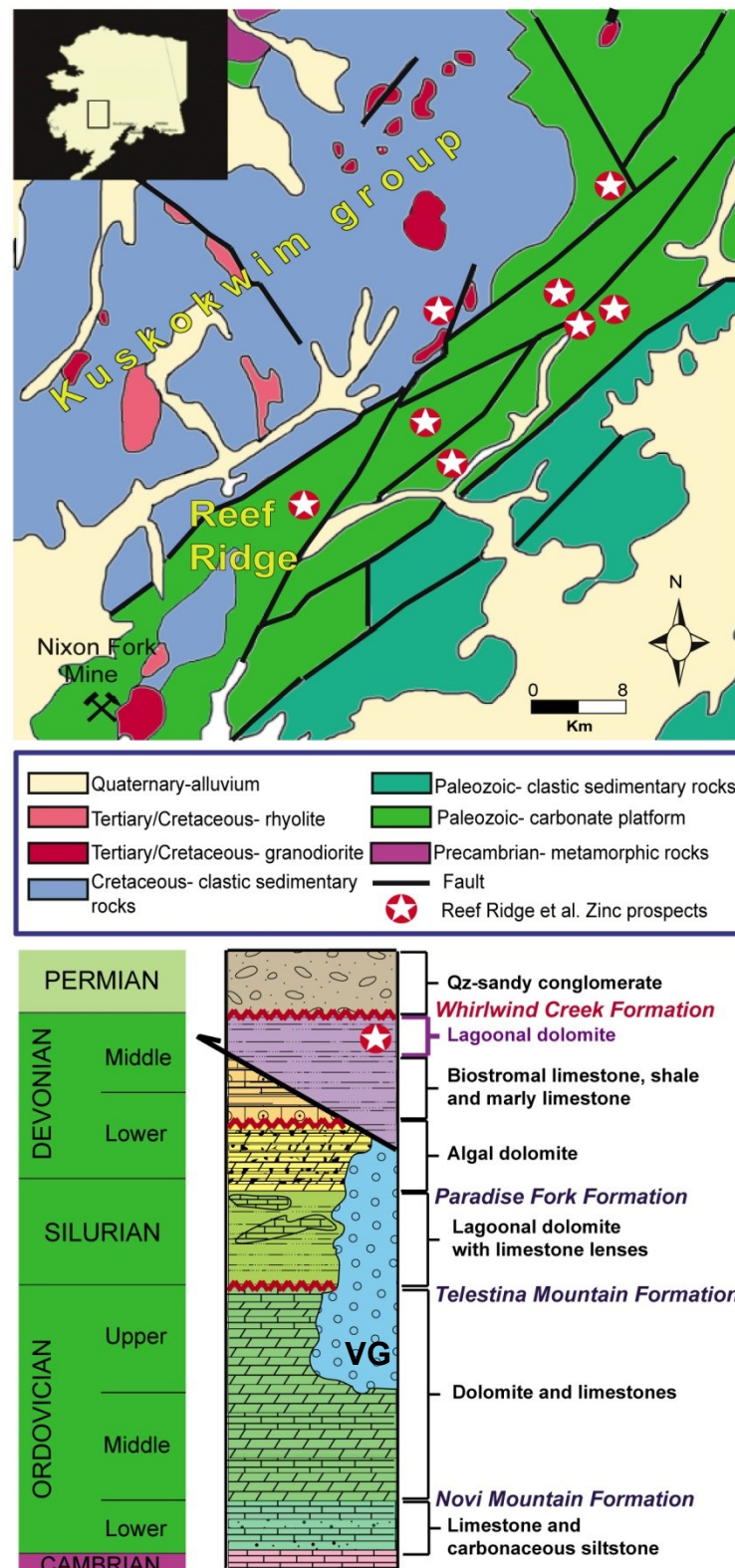
Figure 5.6: Geologic map of the Upper Kuskokwim area showing Zn prospects and mines. Below is shown the stratigraphic column of the Cambrian to Permian strata (modified from Wilson et al., 1998).

5.5. Geomorphology of the Reef ridge area

The current landscape of the Kuskokwim Mountains is dominated by two morphological features: (i) the Georgetown Summit Level, and (ii) the Sleetmute Upland Surface (Fernald, 1960; T. Bundtzen, personal communication). The Georgetown Summit Level is the erosional level with maximum elevation occurring in the Kuskokwim Mountains. It averages from 600 to 762 m a.s.l., and is considered to be Late Tertiary (Cady et al., 1955). The Sleetmute Upland Surface (Figure 5.7) is a predominantly late-mature upland, formed chiefly by frost action. It is typical of the central Kuskokwim region (Cady et al., 1955; Fernald, 1960), and corresponds to a surface located between 300 and 600 m a.s.l. In many areas, it has been documented at lower altitudes. Although it typically caps shale and sandstone bedrock, the Sleetmute Surface can also partially occur on dolomite and limestone, if these carbonate rocks have undergone strong uplift. The Sleetmute Upland Surface generally slopes in smooth open S-curves, from the upland summits to the stream bottoms (Fernald, 1960). This S-shape was generated by the creep of the residual deposits, directed by the force of gravity and exacerbated by frost heaving. The Sleetmute Surface is considered to have initially started to form in Late Tertiary (Pliocene?), and continued to evolve up to the present (Fernald, 1960). In the Reef Ridge area, the features of the Sleetmute shape are well distinguishable on the ground, as well as from the air (Figure 5.7). In the sub-Arctic environment, the continuous freeze-thaw cycles responsible for the formation of the Sleetmute Surface break up the bedrock resulting in the substrate oxidation. It is highly probable that the weathering level of at least part of the nonsulfide mineralization at Reef Ridge (and at many other prospects around the area) is related to the Sleetmute Upland Surface (Santoro et al., in press).
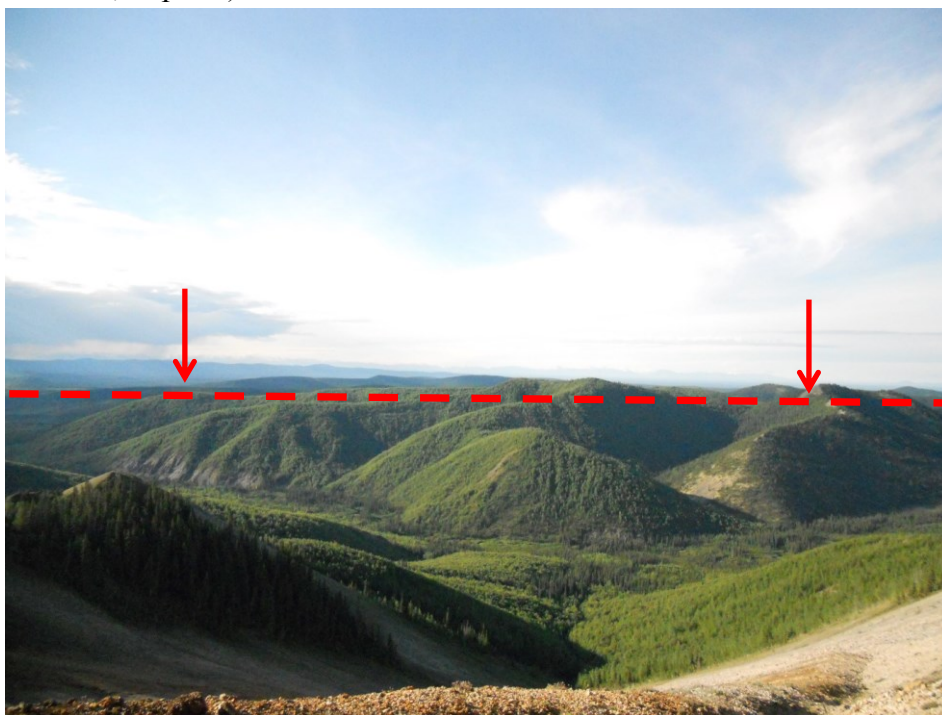

Figure 5.7: Landscape showing the Sleetmute surface (red dotted line) from Reef Ridge (Santoro et al., in press).

5. 6. Reef Ridge Mineralization

The Reef Ridge prospect covers a surface of approximately ~213 x 366 m. Reef Ridge is inaccessible by roads and can be reached only by helicopter. The prospect is hosted in the uppermost section of the Whirlwind Creek Formation of Late Silurian-Middle Devonian age (Dutro and Patton, 1982; Clautice et al., 1993). In the prospect area, highly brecciated dolomite ("solution breccias", "tectonic breccias"), interbedded with laminated *Amphipora*-rich, algal limestone and calcareous mudstone, a distinctive carbonate conglomerate with black chert pebbles, and reefal carbonates occur. Part of the brecciated dolomite may also be related to slope facies, grading from the platform to the basinal domains located to the east. Most carbonate rocks show the effects of hydrothermal dolomitization associated with the deposition of the primary sulfide ores (*vuggy* dolomite). As mentioned, the primary mineralization of Reef Ridge may genetically represent a MVT deposit formed between Late Cretaceous and Early Tertiary in the Selwyn basin (e.g. Nokleberg et al., 1994). However, considering the proximity of the primary Reef Ridge orebody and of other deposits in the Reef Ridge belt to the porphyry systems of the Mystery Mountain area and to the Nixon Fork mineralization, another genetic mechanism should also be considered: it can be considered as a distal polymetallic mineralization related both to magmatic processes, and to the Iditarod-Denali faults displacement.

The supergene Reef Ridge deposit, considered economically more important than the small primary sulfide concentrations, has been subdivided in two zones: the Eastern Zone (blue dotted line in Figure 5.8) approximately 137 m long and 18 m wide, and the Western Zone (yellow dotted line in Figure 5.8), approximately 213 m long and up to 49 m wide (Figure 5.8). Both areas have been widely explored by trenching (Figure 5.8 red tracks) and drillings (RRDH11-RRDH12-RRDH13-RRDH14). Most surface samples are typical gossans (Figure 5.9a), very porous and fractured, with black-brown to red, orange and ochre colors reflecting a high Fe-(hydr)oxides content. Goethite and hematite are the main oxidized phases. Locally calcite and hydrozincite concretions can be seen outcropping on dolomite.

In the drill core samples two main different mineralized facies have been considered: (i) primary sulfides, which consist mainly of pyrite/marcasite, sphalerite and rare galena in the cement of brecciated dolostone. Sphalerite occurs either as small crystals or as colloform bands (Figure 5.9b); (ii) secondary nonsulfides (Figure 5.9c), in a highly brecciated and vuggy dolomite host rock, cemented by calcite and nonsulfide minerals (i.e. smithsonite), intergrown with Fe-(hydr)oxides. Secondary mineral phases were observed in concretionary form in pores and veins, and as precipitates from oxidized fluids trickling through the vadose zone. Nonsulfide drill cores contain gossanous intercalations at several depths. Again, the color, ranging from black to red-ochre is due to the high Fe-(hydr)oxides content.
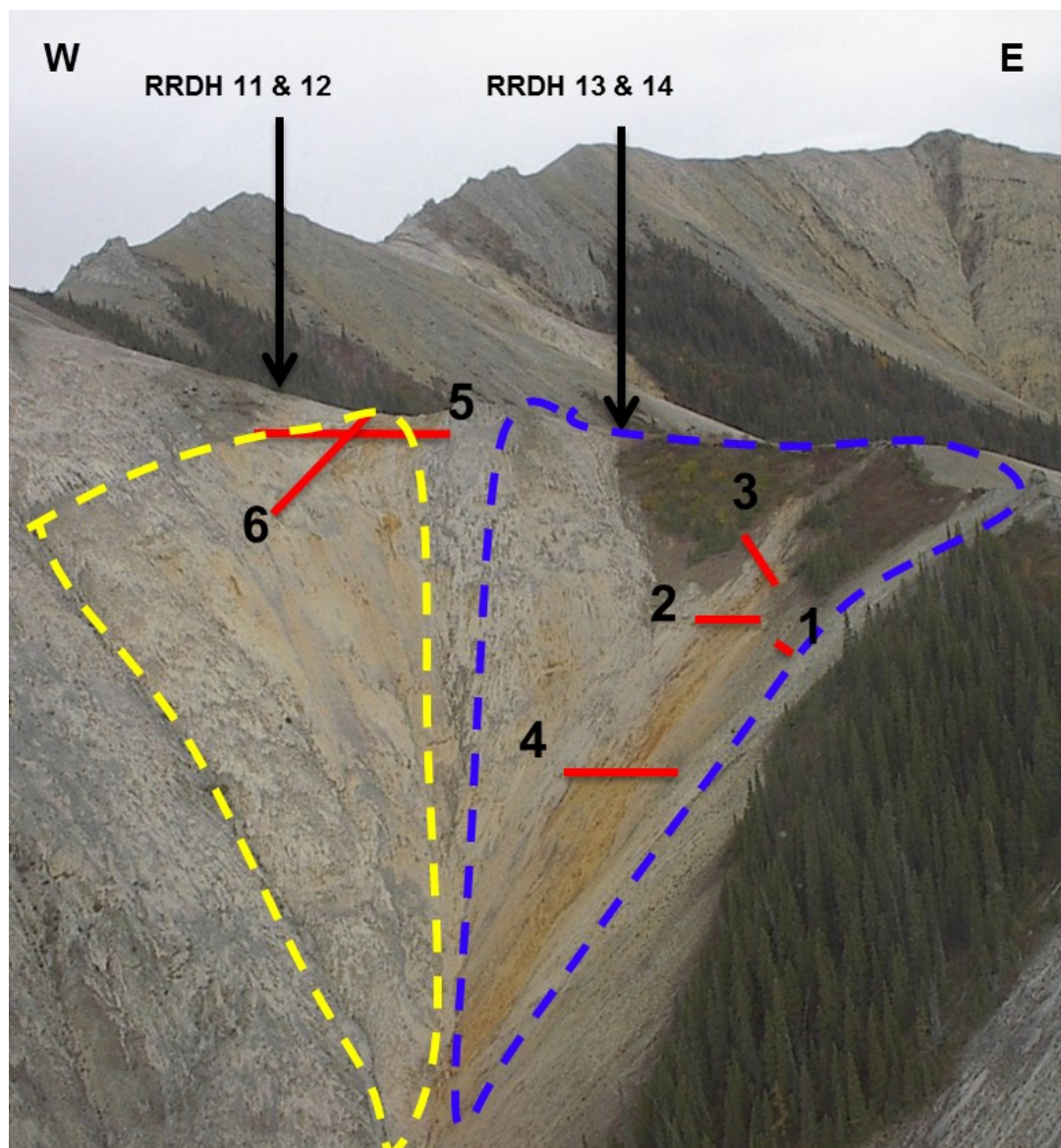
Figure 5.8: Southern slope of the Reef Ridge prospect, with indicated the position of the main drill holes and trenches (in red) (Santoro et al., in press).
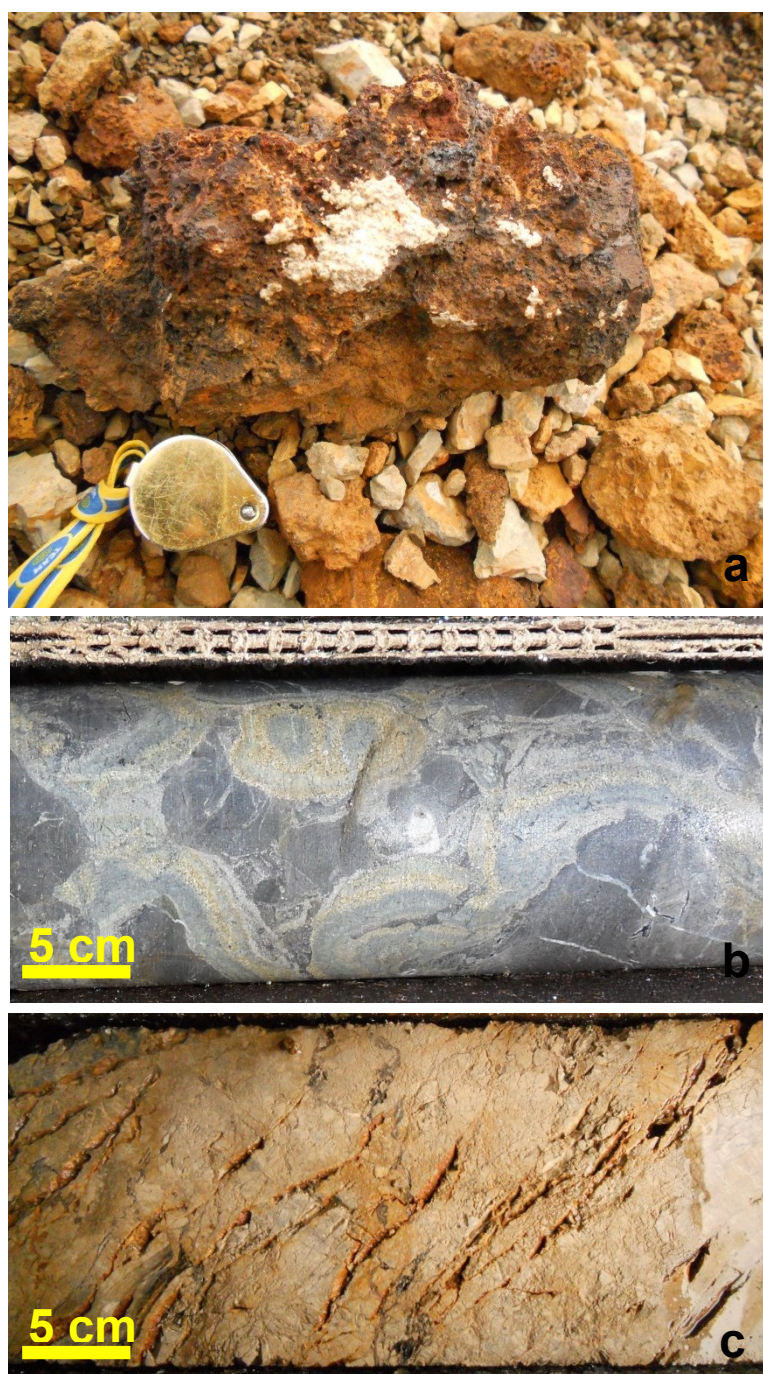
Figure 5.9: a) Reef Ridge gossan rubble with hydrozincite; b) Core RRDH12, 55-60 feet: dolomite-hosted banded sulfides (sphalerite); c) Core RRH12, 35-40 feet: oxidized nonsulfides (Santoro et al., in press).

5. 7. Analytical Methods

A mineralogical, petrographic, and geochemical study was conducted on 20 drill core samples, collected by the Doyon, Ltd. personnel from the Reef Ridge project area (Figure 5.10). The better mineralized nonsulfide cores, as well as the less enriched samples from both the Western (13 samples) and Eastern Zone (7 samples), were chosen for analysis (Table 1). The samples were cut in small slabs, to make polished thin sections used for petrographic and mineralogical analysis: the blocks were then prepared to obtain thin sections of ~30 μm of thickness in a commercial laboratory specialized in soft sediments (OMT, Aosta, Italy). Most of the material was impregnated with Araldite D and Raku Hardener EH 2950.

Figure 5.10: Core samples from Reef Ridge.

Optical Microscopy (OM) observation under polarized and reflected light was carried out at the University of Naples using a Nikon Eclipse E200 microscope.

Cathodoluminescence (CL) observation was carried out at the Geologisch-Paläontologisches Institut of the Heidelberg University (Germany), using a CITL 8200 Mk3 hot cathode instrument operating at 23–25 kV voltage and 400–450 μÅ beam current.

Scanning Electron Microscopy with Energy Dispersive X-Ray spectroscopy (SEM-EDS) analyses have been performed with a Jeol JSM 5310 (CISAG, Università di Napoli, Italy). The operating conditions were: 20 mm objective lens to specimen working distance with 15 kV acceleration voltage. Qualitative energy-dispersive (EDS) spectra and quantitative analyses were obtained with the INCA X-stream pulse processor and the 4.08 version Inca software (Oxford Instruments detector), interfaced with the Jeol JSM 5310. The following reference standards were used: albite (Si, Al, Na), orthoclase (K), wollastonite (Ca), diopside (Mg), almandine (Fe), rutile (Ti), barite (Ba), strontianite (Sr), Cr_2O_3 (Cr), rhodonite (Mn), sulphur (pyrite), sphalerite (Zn), galena (Pb), fluorite (F),

apatite (P), chlorine (sylvite), smithsonian phosphates (La, Ce, Nd, Sm, Y), pure vanadium (V) and Cornig glass (Th and U). Analytical errors are 1% rel. for major elements and 3% rel. for minor elements.

X-Ray Powder Diffraction (XRPD) analyses were carried out by the use of a Philips PW 3020 automated diffractometer (XRD) at the University of Heidelberg, with CuKα radiation, 40 kV and 30 mA, 10 s/step and a step scan of 0.02° 2θ. The data were collected from 3 to 110° 2θ.

Spectra were interpreted by the use of RayfleX software package (GE Inspection Technologies). The XDATA program (part of the XDAL 3000 software package from Rich. Seifert & Co.) has been used to evaluate the obtained profiles, and to permit the comparison with JCPDS-ICDD database. Regarding the analyses carried out with Co radiation, we have used for interpretation the XPowder software package.

The first quantitative phase analysis was performed on the XRD patterns using the Rietveld method (Rietveld, 1969; Bish and Howard, 1988; Bish and Post, 1993; Hill, 1991) on four selected samples (RRMB1, RRMB2, RRMB10, RRMB12). The samples were chosen on the basis of their oxidization stage: from less oxidized to highly oxidized. X-ray powder diffraction data were analyzed using the GSAS package (General Structure Analysis System, Larson and Von Dreele, 2000) and its graphical interface EXPGUI (Toby, 2001). The XRD patterns were converted to ASCII format using ConvX software.

Whole rock chemical analyses of major (Zn, Fe, Ca, Mg, Al, K, S) and minor (V, Co, Ni, Cu, Sr, Y, Zr, Nb, Ba, Pb, P, As, Cd, Tl, Na, Sb, Mo, Rb, Li, Sn, Cr, La, Ce, Th, U) elements were carried out at the ACME Laboratories, Ltd. (Vancouver, Canada), on identical powder splits to those used for XRD analyses. Ten grams of pulp of each sample was used for chemical analysis (ICP-ES and ICP-MS/hot 4-acid digestion).

Stable isotopes geochemical analyses (C-O) have been performed at University of Erlangen-Nuremberg (Germany), with the purpose of investigate the nature of the fluids involved in nonsulfide mineralization: 7 concretionary smithsonite and 13 dolomite fragments were selected by mechanical hand picking from the Reef Ridge core samples (RRDH-11, RRDH-12 and RRDH-13) at 5 feet intervals. Because of the small crystal sizes, the generation of fine smithsonite impregnating the host rock could not be isolated. The powdered samples were allowed to react at least for 36 hours with 103% phosphoric acid at 70°C using a Gasbench II connected to a Thermo Finnigan Five Plus Isotope Ratio Mass Spectrometer. Carbon and oxygen isotope values are reported in per mil (‰) relative to VPDB and VSMOW, respectively, by assigning a δ^{13}C value of +1.95‰ and a δ^{18}O value of -2.20‰ to standard NBS19.

Reproducibility was checked by replicate analysis of laboratory standards and was better than ± 0.07 ‰ (1σ) for both carbon and oxygen isotope analyses. Oxygen isotope values of dolomite and smithsonite were corrected using the phosphoric acid fractionation factors given by Kim et al. (2007), Rosenbaum and Sheppard (1986) and Gilg et al. (2008) respectively.

Table 1: List of the analyzed samples with depth and description.

Sample ID	Drill Hole	Sample Depth (Feet)	Lithology	Description
Western Zone				
RRMB1	RRDH-11	22.9 - 25	Dolomite	Fe-(hydr)oxide-stained dolomite and gossan
RRMB2	RRDH-11	27 - 28.5	Dolomite (?)	Gossan rubble with nonsulfide zinc minerals
RRMB3	RRDH-11	43.5 - 44.5	Dolomite	Solution breccia with Fe-(hydr)oxide veins
RRMB4	RRDH-11	47 - 48.5	Dolomite (?)	Gossan rubble with hydrozincite, smithsonite
RRMB5	RRDH-13	88 - 89.5	Silty dolomite	Tectonic breccia. Dolomite clasts in cataclastic matrix
RRMB6	RRDH-13	63 - 64.5	Dolomite	Tectonic & solution breccia. Dolomite clasts in dolomite, gossan, nonsulfide cement
RRMB7	RRDH-13	57 - 58.2	Dolomite (?)	Rubble of Fe-(hydr)oxides-dolomite, gossan, calcite, hydrozincite
RRMB8	RRDH-14	58 - 59.5	Dolomite	Massive dark grey dolomite cut by calcite veins
RRMB9	RRDH-14	26.5 - 29	Calcareous argillite	Carbonaceous mudstone-dolomite
RRMB10	RRDH-12	125 - 126	Dolomite>Limestone	Solution breccia. Grey to Fe-(hydr)oxide-stained dolomite clasts in gossan, calcite, nonsulfides
RRMB11	RRDH-12	55 - 56	Dolomite	Silicified Breccia. Nonsulfide zinc minerals with sphalerite remnants
RRMB12	RRDH-12	24 - 25	Dolomite	Orange-brown gossan rubble with nonsulfide zinc minerals
RRMB14	Hand Sample	Surface	Dolomite	Silicified solution breccia
Eastern Zone				
RRMB13	Hand Sample	Surface	Dolomite	Vesicular gossan on dolomite
RRMB15*	DDH-6	104-105	Dolomite	Tectonic breccia/stockwork. Dolomite clasts in cataclastic matrix with Fe-(hydr)oxides
RRMB16	Hand Sample	Surface	Dolomite?	Iron-rich gossan. No recognizable protolith
RRMB17	Hand Sample	Surface	Dolomite	Iron-rich gossan. 40% pore space
RRMB18	Hand Sample	Surface	Dolomite	Breccia cemented by Fe-(hydr)oxides. Local slickensides
RRMB19	Hand Sample	Surface	Dolomite	Rounded dolomite clasts in Fe-(hydr)oxides matrix
RRMB20	Hand Sample	Surface	Dolomite	Iron-rich gossan. 40% porosity with vesicles

*RRMB 15 belongs to an older drillcore.

5. 8. Results: Mineralogy and Petrography

Here follows a mineralogical and petrographic description of the minerals identified by OM, CL and SEM-EDS. The most important economic and uneconomic mineral phases occurring at Reef Ridge were subdivided in four categories (Santoro et al., 2013, in press):

- Zinc nonsulfides (smithsonite)
- Fe-(hydr)oxides
- Gangue and others

Zinc nonsulfides (smithsonite)

The secondary mineral association is dominated by smithsonite. Two different generations of smithsonite have been identified at Reef Ridge categories (Santoro et al., 2013, in press). The most common smithsonite (1) occurs as direct replacement of primary sphalerite (Figure 5.10a, b) and of all dolomite phases. Smithsonite replaces sphalerite partially (Figure 5.10a) or totally (Figure 5.10b), and part of the dolomite crystals after a dissolution-precipitation process (Figure 5.10c). The latter smithsonite is also associated with replacement fronts in the dolomite host rock, and may contain sauconite (Figure 5.10d). Under cathodoluminescence microscopy, this "replacive" smithsonite exhibits an intense blue luminescence (Figure 5.11a, b). Smithsonite (2) can occur also as concretions in the porosity and fractures of the host rock (Figure 5.10e), as well as in veinlets (Figure 5.10f). This smithsonite generation is commonly zoned, and shows a red-pink and blue luminescence (Figure 5.11c, d). The zonation is strongly dependent on the MgO content, with higher amounts of Mg in the darker rims (Figure 5.10 g). In general, the Zn-carbonate at Reef Ridge is characterized by variable Ca and Mg contents (up to 2.6 wt.% CaO, and up to 8.2 wt.% MgO), as well as by different Fe amounts (up to a maximum of 12 wt.% FeO), low MnO (below 1 wt.%) and also low Pb (up to 0.7 wt.% PbO), and Cd (up to 1 wt.% CdO). In Table 2 are reported a few selected EDS analyses, in order to show the average elements content in smithsonite.

Table 2: Selected EDS analyses of smithsonite.

Sample	MgO	SO₃	CaO	FeOt	ZnO	AsO	CdO	PbO	Total
RRMB 1a	0.39	n.d	0.64	0.33	62.19	0.38	0.52	n.d	64.94
RRMB 1b	0.25	n.d	0.23	n.d	64.07	0.80	0.19	0.31	65.86
RRMB 1c	0.18	n.d	0.44	n.d	63.48	0.13	0.12	0.27	64.60
RRMB 2a	n.d	0.06	0.62	0.11	61.17	0.55	0.39	n.d	62.90
RRMB 2b	n.d	0.05	0.68	0.15	62.71	0.53	0.94	0.06	65.12
RRMB 2c	0.19	n.d	0.21	0.12	65.75	0.34	0.13	0.16	66.90
RRMB 1d	2.42	n.d	0.11	0.33	59.90	0.13	0.18	0.08	63.13
RRMB 3a	1.18	n.d	0.24	n.d	60.74	0.19	0.45	n.d	62.79
RRMB 3b	4.78	0.31	0.26	n.d	53.98	0.56	0.00	0.03	59.93
RRMB 3c	7.02	0.24	0.09	n.d	51.93	n.d	0.04	0.04	59.35

* all results are expressed in oxides wt%; n.d = not detected
EDS analyses also detected traces of SiO_2 (0.03-0.14); TiO (0.01-0.23); SrO (0.04-0.28); MnO (0.06-0.22);
The last four samples (shaded) are Mg-rich smithsonite. The analyses were carried out in several points of the same samples (RRMB1a, RRMB1b, RRMB1c, etc.).
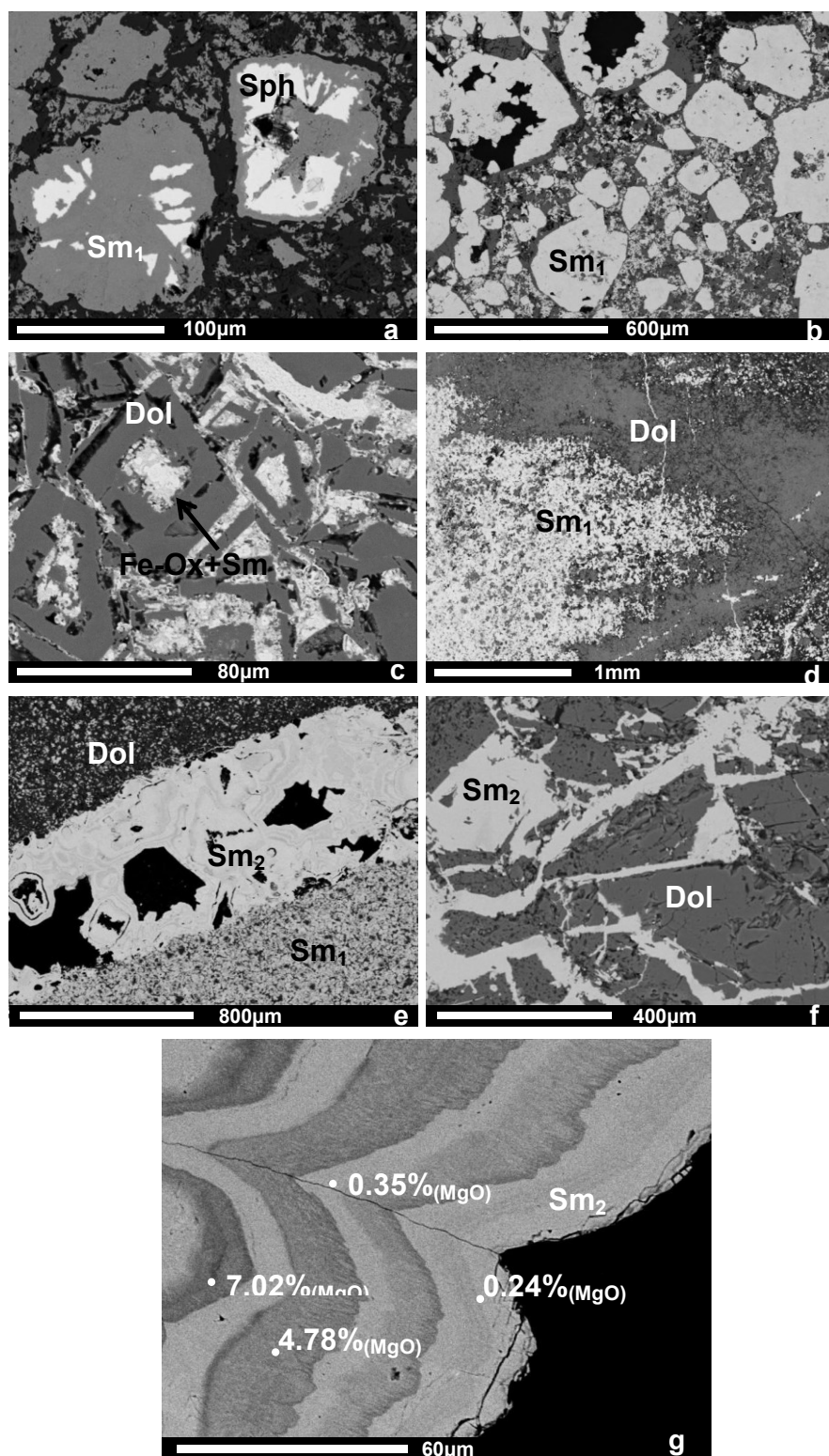
Figure 5.10: a) (sample RRMB3) Sphalerite crystals, partly replaced by smithsonite 1; b) (sample RRMB3) Smithsonite 1 totally replacing sphalerite crystals; c) (sample RRMB19) Dolomite crystals, with smithsonite1 and Fe-(hydr)oxides in the nucleus; d) (sample RRMB5) Front of smithsonite 1 replacing dolomite; e) (sample RRMB3) Concretions of smithsonite 2 in a vein cutting smithsonite 1 replacing dolomite; f) (sample RRMB1) Veins of smithsonite 2 cutting dolomite; g) (sample RRMB3) Banded smithsonite 2, with different values of MgO. Dol= dolomite; Sm_1 = smithsonite 1; Sm_2 = smithsonite 2.
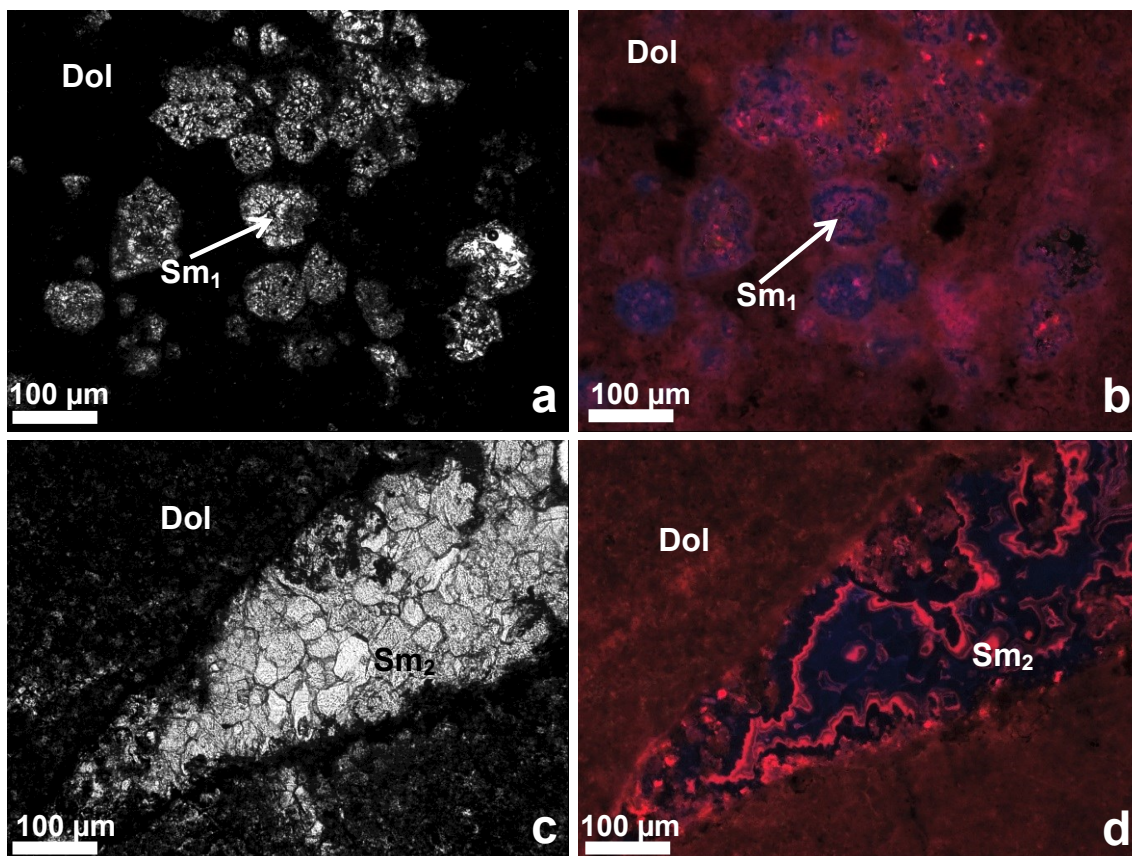
Figure 5.11: a) Smithsonite 1 replacing sphalerite crystals in dolomite (NII; sample RRMB3); b) Same as a) in CL (NII); c) Smithsonite 2 filling vug in dolomite (NII; sample RRMB3); d) Same as f) in CL (NII). Dol = dolomite; Sm= smithsonite.

Fe-(hydr)oxides

Fe-oxides and hydroxides are relatively abundant in the samples from the Western and Eastern Zone of the Reef Ridge prospect categories (Santoro et al., 2013, in press). The Fe-(hydr)oxides consist of vuggy hematite and goethite that locally occur as direct replacement of pyrite/marcasite through a network of veinlets (Figure 5.12a, b). Fe-(hydr)oxides have been also detected as concretions, vein fillings and crusts (Figure 5.12c, d), associated with concretionary smithsonite (2). In the more gossanous samples, some early generations of Fe-(hydr)oxides are covered by a thin veneer of smithsonite crystals. In goethite, Fe generally ranges from 45 to 75 wt.%, with maximum contents of 83 wt.% FeO. Silica is always present with 0.2 to 4 wt.% and maximum contents of 10 wt.% SiO_2. Zinc concentrations range from low amounts to a maximum of 13 wt.% ZnO, and Pb contents from 0.1 up to 7 wt.% PbO locally. In Table 3 are listed a few EDS analyses of Fe-(hydr)oxides in selected samples.
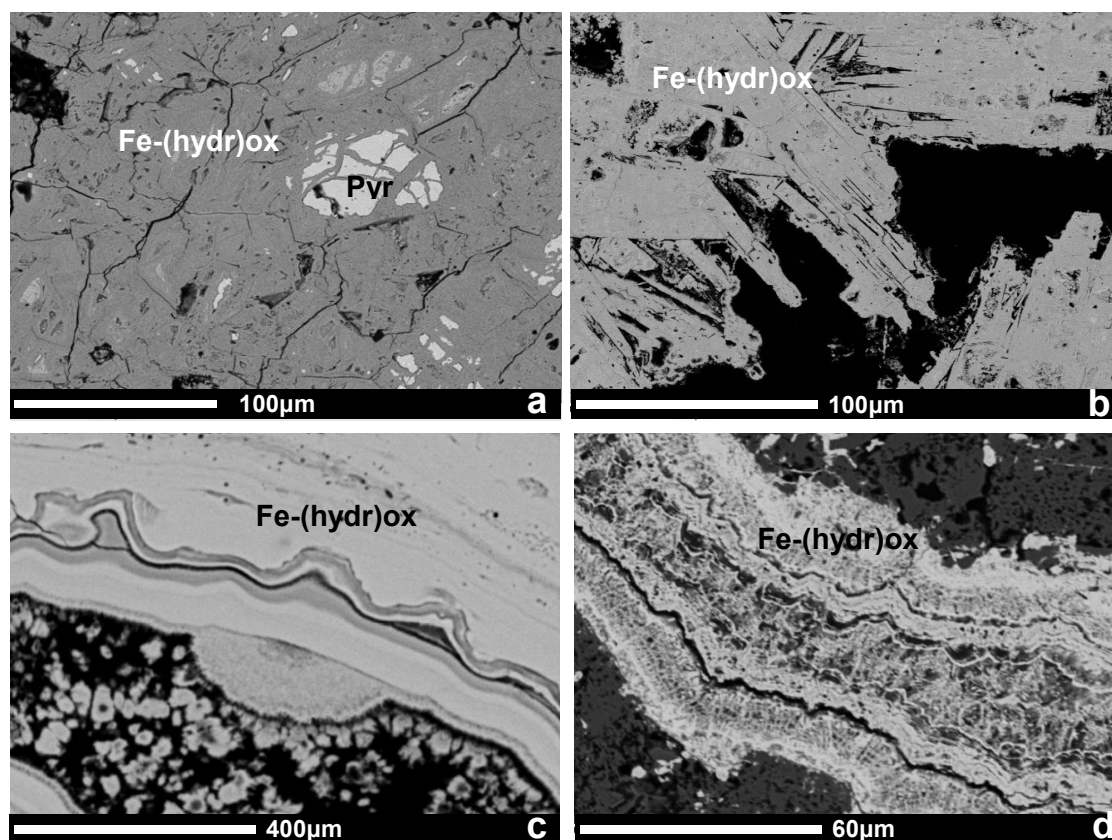
Figure 5.12: a) (sample RRMB10) Pyrite being replaced by Fe-(hydr)oxides; b) (sample RRMB13) Fe-(hydr)oxides completely replace marcasite crystals; c) (sample RRMB16) zoned Fe-(hydr)oxide concretions (sample RRMB20); d) Fe-(hydr)oxide concretion and crust.

Table 3: Selected EDS analyses of Fe-(hydr)oxides.

Sample	MgO	SiO$_2$	P$_2$O$_5$	SO$_3$	CaO	FeOt	ZnO	CdO	PbO	Total
RRMB 2	0.19	4.72	0.67	0.74	1.10	61.52	5.36		3.32	77.62
RRMB 4	0.34	1.19	0.10	0.60	0.17	73.06	3.13	0.01	0.51	79.10
RRMB 15	0.25	3.05	0.84	1.12	1.06	58.10	8.42		0.59	73.44
RRMB17	0.07	2.23		0.31	0.08	61.97	11.35	0.23	0.33	76.57
RRMB18	0.18	2.08	0.10		0.70	61.82	8.81	0.18		73.87
RRMB19	0.13	1.97		0.04	0.08	65.70	6.81	0.10	0.16	74.99
RRMB20	0.22	1.70		0.50	0.04	63.39	5.83	0.30		71.98

*[1]calculated from stoichiometry; all results are expressed in oxides wt%; n.d.= not detected
EDS analyses also detected traces of Al$_2$O3 (0.04-0.93); MnO (0.07-0.20); V$_2$O$_5$ (0.07-0.25); AgO (0.06-0.32); BaO (0.18-0.42); CuO (0.16-0.32) and SrO (0.05-0.62)

Gangue minerals/others

The host rock at Reef Ridge is a highly brecciated, microcrystalline algal dolostone. This first generation is cut by an epigenetic dolomite phase occurring in veins and cavities (Santoro et al., in press) (Figure 5.13a). The epigenetic dolomite can be both micro- and macrocrystalline. Macrocrystalline dolomite is represented by well-zoned rhombohedral macrocrystals having locally abundant fluid inclusions.

Under cathodoluminescence microscope, the epigenetic dolomite shows an intense red luminescence, which is considered as being activated by even very low Mn contents

(Götze, 2012.) In fact, MnO in the epigenetic dolomite phase rarely overcome 1%. In the same dolomite, Fe (around 1.5% FeO), and Zn (up to 3% ZnO) are in low amounts. Rare calcite veins have been also observed. Reef Ridge epigenetic dolomite shows the typical characteristics of hydrothermal "*saddle*" dolomites, which are generally associated with MVT deposits, and is commonly replaced by smithsonite (Figure 5.10c, d).

In some samples (i.e RRMB8, RRMB9) the early microcrystalline dolomites are highly fossiliferous and may contain organic matter and apatite (Figure 5.13b), but most of them are thinly laminated and seem barren. Several clay layers, consisting of either kaolinite, or muscovite/illite also occur in the Reef Ridge host rock.

Remnants of pyrite/marcasite and sphalerite have been locally detected (Figure 5.13c); early pyrite has generally a framboidal texture (Figure 5.13d).
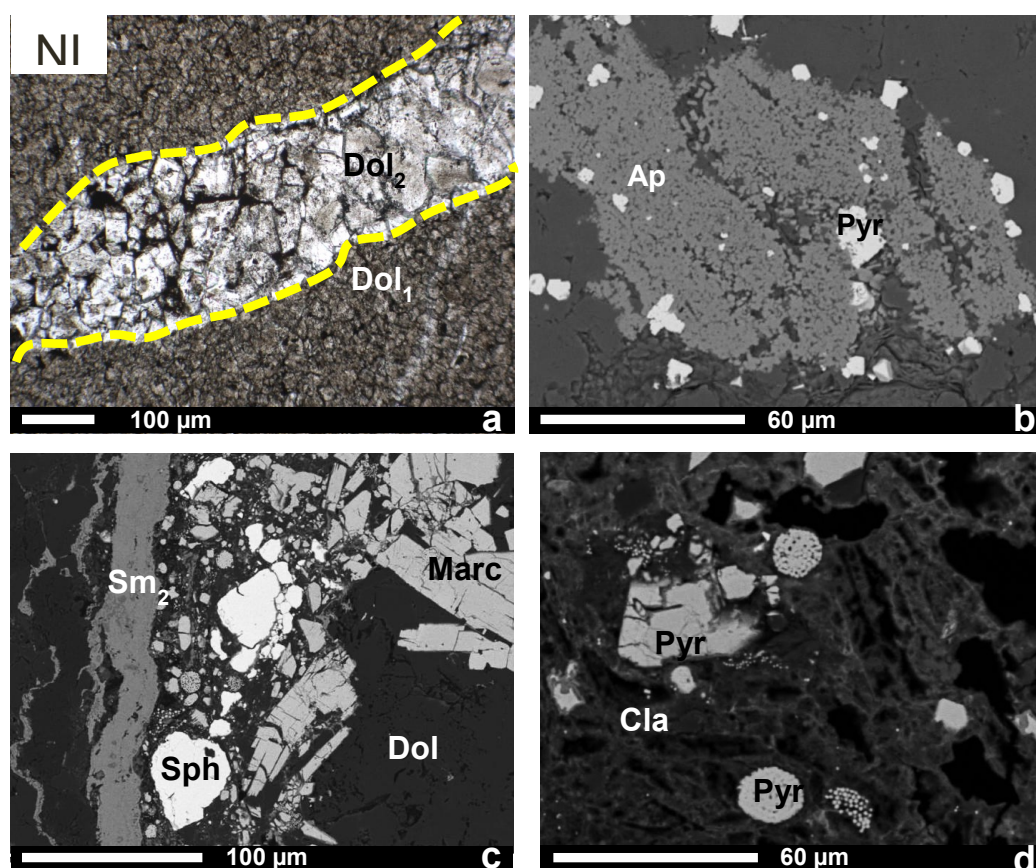

Figure 5.13: a) (sample RRMB3) host dolomite cut by macrocrystals of epigenetic dolomite; b) (sample RRMB3) pyrite and apatite in dolomite; c) (RRMB6) remnants of sphalerite and marcasite ina dolomite; smithsonite veins occur; d) (sample RRMB6) framboidal and crystalline pyrite in clay matrix.

5. 9. Results: Geochemistry

Chemical analyses

Chemical analyses of the major and minor elements are shown in Table 4. In the Western Zone, Zn contents range from 0.1 to 34 wt.% Zn, with the highest values measured in the samples RRMB1, RRMB3 and RRMB12. Iron content ranges between 0.4 and 54 wt.% Fe, with average values around 30 wt.%, and is particularly high in gossanous samples. Sulfur contents are high in samples RRMB6 and RRMB11 where sulfides occur, but these high values can be locally related also to gypsum veins. Aluminum, which is mostly related to clays, is relatively scarce (from 0.2 to 1.6 wt.% Al).

Lead abundances are generally low (16 to 2,000 ppm), with the higher values recorded in the gossan samples (2057 ppm in RRMB4). Barium (maximum 76 ppm), copper (maximum 25 ppm) and nickel (maximum 56 ppm) amounts are negligible. Arsenic is slightly more abundant (maximum value 154 ppm in RRMB1).

Cadmium values are high (up to 2430 ppm), because Cd content seems to be well correlated in most samples with the Zn amount. Strontium values (up to 215 ppm) are correlated with those of Ca and Mg in the host carbonates. Phosphorus occurs in variable amounts (up to 1800 ppm) and is related to the apatite occurrence. Manganese, which at Reef Ridge occurs as oxides and hydroxides, is never higher than 300 ppm. Thallium is generally below 10 ppm, with the only exception of sample RRMB12 (15 ppm Tl). The other analyzed elements (i.e. V, Sb, Mo, Th, Rb, Sn etc.) rarely reach values higher than 100 ppm. In the Eastern Zone (Table 4), the Zn contents are quite high (up to 11 wt.% and 33 wt.% in samples RRMB19 and RRMB17, respectively). In the other samples, Zn values are lower (from 1.3 to 6.50 wt.%). In sample RRMB20, which apparently does not contain smithsonite, the 3.7 wt.% of Zn measured may be totally contained within the Fe-(hydr)oxide. Similarly to the Western zone, the iron content in the Eastern Zone is high in gossanous samples, ranging from 12.6 to 51 wt.%. Lead (Table 5) is never above 2980 ppm. Phosphorus concentrations are lower than in the Western Zone, as less apatite occurs in this part of the prospect. Nickel (below 56 ppm), manganese (up to ~50 ppm) and arsenic (up to 188 ppm) values are very low, though generally higher in the Eastern than in the Western Zone. Cadmium has lower values in comparison with the Western Zone, except in RRMB17 (up to 1338 ppm). The values of other minor and trace elements are not significant.

206

Table 4: Chemical analyses of mayor and minor elements of Reef Ridge samples

	Western Zone													Eastern Zone						
	RRMB1	RRMB2	RRMB3	RRMB4	RRMB5	RRMB6	RRMB7	RRMB8	RRMB9	RRMB10	RRMB11	RRMB12	RRMB14	RRMB13	RRMB15	RRMB16	RRMB17	RRMB18	RRMB19	RRMB20
	wt%																			
Zn	34	22.79	29	15.63	0.04	6.62	1.65	0.1	0.05	9.9	19.94	32.87	45.73	4.03	1.27	5.08	33.01	6.5	10.74	3.67
Fe	6.71	5.38	1.93	33.2	0.46	7.4	4.42	0.62	0.87	2.43	0.62	22.61	3.97	54.28	1.8	50.01	20.31	42.98	12.57	51.19
Ca	3.54	9.57	9.01	2.06	21.4	14.69	19.59	23.31	21.59	17.31	11.74	0.27	1.68	0.26	21.21	0.16	0.19	1.35	12.13	0.56
Mg	2.05	5.23	4.82	1.18	10.79	7.02	9.63	10.62	7.57	8.5	5.79	0.24	1.13	0.12	11.03	0.09	0.37	0.83	6.69	0.31
Al	1.55	0.74	0.28	0.44	0.52	0.77	0.56	0.22	1.39	0.24	0.14	0.15	0.67	0.21	0.16	0.4	0.29	0.54	0.4	0.3
K	0.38	0.17	0.1	0.12	0.21	0.2	0.18	0.06	0.63	0.09	0.06	0.06	0.25	0.07	0.06	0.07	0.07	0.18	0.08	0.07
S	<0.05	0.14	0.14	0.14	0.64	5.4	0.31	0.3	0.29	0.36	10.21	<0.05	1.72	0.15	0.05	0.14	0.05	0.11	0.05	0.19
	ppm																			
V	85.0	38.0	13.0	37.0	<10	17.0	<10	<10	23.0	<10	11.0	16.0	17.0	29.0	10.0	56.0	23.0	56.0	21.0	55.0
Co	7.0	8.0	2.0	6.0	2.0	2.0	2.0	1.0	4.0	1.0	<1	2.0	2.0	2.0	1.0	3.0	6.0	3.0	6.0	1.0
Ni	24.4	11.6	7.7	56.5	3.2	7.8	7.1	3.7	15.0	4.3	3.9	18.5	15.9	35.0	7.6	45.5	51.8	52.7	41.6	16.1
Cu	19.8	9.7	5.5	16.9	9.2	18.2	10.0	6.9	25.6	4.5	3.0	7.0	17.3	12.6	4.5	16.1	11.7	11.6	8.1	7.7
Sr	40.0	42.0	55.0	20.0	119.0	98.0	121.0	215.0	130.0	118.0	58.0	<5	11.0	<5	138.0	5.0	5.0	7.0	51.0	5.0
Y	5.4	4.5	3.4	7.7	6.5	13.5	6.3	3.5	7.5	3.5	2.3	3.9	7.0	6.2	3.4	8.2	6.0	5.1	4.8	1.1
Zr	24.9	11.8	4.8	8.5	7.6	12.4	9.4	2.9	21.1	4.0	2.0	2.5	15.7	4.1	2.7	5.9	4.6	9.7	10.3	6.6
Nb	2.5	1.1	0.7	0.9	0.9	1.5	1.2	0.6	2.7	<0.5	<0.5	<0.5	1.7	0.5	0.5	0.6	0.5	0.7	0.8	0.6
Ba	45.0	20.0	10.0	15.0	68.0	76.0	20.0	18.0	66.0	11.0	9.0	6.0	19.0	10.0	12.0	13.0	10.0	27.0	17.0	12.0
Pb	1239.0	680.9	778.0	2057.5	16.5	347.0	281.1	29.7	18.2	240.6	477.9	1415.9	1583.7	2980.6	55.7	2378.0	1240.4	1645.7	171.6	1259.1
P	530.0	300.0	310.0	1130.0	1435.0	1800.0	1105.0	<100	<100	301.0	116.0	205.0	1200.0	200.0	301.0	310.0	210.0	200.0	202.0	203.0
Mn	142.0	200.0	128.0	304.0	134.0	132.0	198.0	92.0	169.0	103.0	75.0	237.0	86.0	139.0	112.0	78.0	458.0	181.0	492.0	45.0
As	154.0	61.0	<5	86.0	6.0	27.0	10.0	<5	15.0	6.0	7.0	21.0	45.0	102.0	10.0	188.0	67.0	154.0	72.0	86.0
Cd	1943.3	1331.2	1336.7	569.1	1.0	215.9	42.9	4.5	0.9	450.9	921.2	1054.4	2430.0	58.2	44.9	107.0	1338.7	49.0	213.3	63.0
Tl	6.9	3.8	2.5	10.6	0.3	1.1	1.3	0.2	0.1	2.6	3.3	14.9		6.9						
Na	110.0	123.0	112.0	123.0	230.0	205.0	301.0	202.0	205.0	212.0	110.0	<100	120.0	<110	201.0	101.0	110.0	101.0	106.0	108.0
Sb	5.1	3.5	1.9	7.2	<0.5	0.9	0.8	0.6	0.6	0.7	<0.5	1.6	1.3	7.3	0.5	4.6	2.2	6.5	2.5	2.6
Mo	16.1	8.1	1.5	31.1	1.8	5.2	2.7	2.3	4.2	1.2	3.2	9.2	10.0	31.7	2.0	31.4	8.1	16.6	4.1	11.9
Rb	15.6	5.5	3.5	4.1	7.4	6.8	6.6	2.8	25.3	3.6	2.1	2.1	9.6	3.0	2.4	3.3	2.6	7.5	3.4	3.1
Li	5.0	3.5	2.0	1.3	3.6	3.0	2.8	1.8	4.5	2.1	0.7	1.5	2.6	1.0	1.8	0.8	0.9	1.1	1.0	0.9
Sn	3.9	1.8	0.9	0.9	<0.5	<0.5	<0.5	<0.5	<0.5	<0.5	<0.5	<0.5	1.2	<0.5	0.5	0.6	0.5	0.5	0.5	0.5
Cr	22.0	11.0	8.0	12.0	9.0	11.0	11.0	7.0	24.0	8.0	7.0	11.0	17.0	11.0	9.0	17.0	10.0	14.0	7.0	30.0
La	7.6	5.0	2.6	4.3	5.2	8.9	5.0	2.6	7.8	2.7	1.5	1.9	5.4	4.4	1.8	4.2	3.4	3.2	3.8	0.8
Ce	13.0	8.0	<5	8.0	9.0	17.0	8.0	<5	14.0	<5	<5	<5	12.0	0.5	5.0	7.0	6.0	6.0	7.0	5.0
Th	2.8	1.7	0.7	0.9	1.1	1.9	1.5	<0.5	2.0	0.5	<0.5	<0.5	2.6	0.5	0.5	0.9	0.6	1.0	0.8	0.5
U	5.4	3.5	2.0	8.1	5.3	8.8	4.9	2.4	4.8	3.0	2.0	4.7	5.2	8.9	2.2	14.3	5.9	6.6	3.7	8.1

Stable isotopes geochemistry (carbon and oxygen)

Carbon and oxygen stable isotope analyses of Zn-carbonate minerals and of the host dolostone were used to characterize the fluid that precipitated the secondary mineralization (Santoro et al., in press). The genesis of the supergene deposits is related to the physical-chemical characteristics of meteoric, surficial and ground waters, and hence to the climatic conditions in the area at the time of formation. Thus, the study of the isotopic composition of the carbonate phases is important to fully understand the genetic conditions of the supergene ores.

Carbon and oxygen isotope analyses were conducted on the Upper Silurian-Late Devonian dolostone of the Whirlwind Creek Formation, host of Reef Ridge mineralization, and on several smithsonite samples (drillcores and outcrop). During sampling, however, it was not possible to distinguish between the two dolomite generations (early diagenetic and hydrothermal). The $\delta^{18}O$ values of dolomite range between 25.5 and 28.1‰ VSMOW, whereas their $\delta^{13}C$ ratios are relatively constant in the range between 0.3‰ and 1.6‰ VPDB. The $\delta^{18}O$ values of smithsonite range from 19.1 to 21.9‰ VSMOW (Table 5, Figure 5.14). On the contrary, their $\delta^{13}C$ values show a high variability and are between –0.7 and 2.1‰ VPDB.

As shown in Figure 5.14 the $\delta^{13}C$ and $\delta^{18}O$ values of Reef Ridge dolomite are similar to those of the Devonian dolomite (slightly hydrothermally altered), whereas the isotopic values of C-O of smithsonite differ from those of supergene smithsonites worldwide.
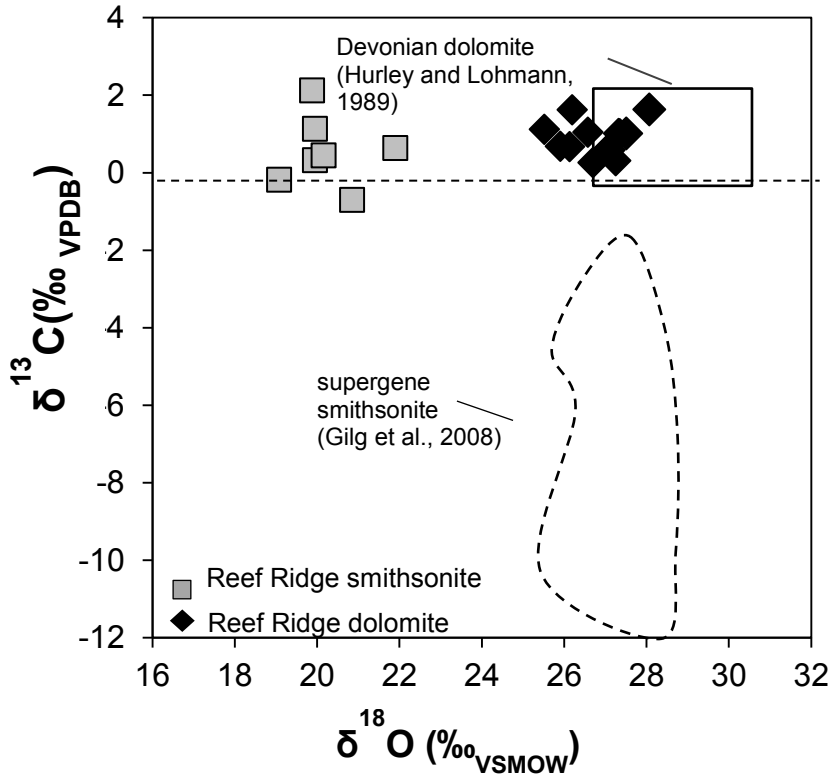

Figure 5.14: $\delta^{18}O$ vs. $\delta^{13}C$ of Reef Ridge carbonates (values in Table 5).

Table 5: Carbon and Oxygen isotopes of Reef Ridge carbonates

	Core ID	Sample Depth (Feet)	δ¹³C VPDB	δ¹⁸O VSMOW
Smithsonite	RRDH-11	23-25	-0.19	19.09
	RRDH-11	23-25	0.44	20.16
	RRDH-11	43 - 45	1.12	19.96
	RRDH-12	24 - 25	0.31	19.96
	RRDH-12	40-45	2.12	19.89
	RRDH-12	45-50	-0.71	20.86
	RRDH-12	45-50	0.63	21.91
Dolomite	RRDH12	25-30	0.67	26.14
	RRDH12	45-50	1.00	27.36
	RRDH12	50-55	1.62	26.20
	RRDH12	55-60	1.01	27.32
	RRDH12	55 - 56	1.00	27.52
	RRDH12	60-65	1.04	26.58
	RRDH12	75-80	0.58	27.06
	RRDH12	80-85	1.12	25.53
	RRDH12	85-90	0.31	27.26
	RRDH12	105-110	0.68	25.91
	RRDH12	115-120	0.25	26.71
	RRDH12	125 - 126	1.63	28.07
	RRDH-13	63 - 64	0.58	27.09

The δ¹³C values are relative to VPDB and δ¹⁸O values relative to VSMOW.

5. 10. Results: X-ray mineralogy

The most common minerals detected by XRD in the host rock are dolomite>>>calcite (RRMB6, RRMB7, RRMB8, RRMB9, RRMB10, RRMB15, and RRMB19) (table 6). The main ore phase is smithsonite, with the richest samples being RRMB1, RRMB2, RRMB3, RRMB4, RRMB5, RRMB10, RRMB12 (Western Zone), and RRMB14, RRMB17, RRMB18, RRMB19 (Eastern Zone). Abundant sphalerite and pyrite remnants have been identified in the samples RRMB6 and RRMB11 (Western Zone) (Santoro et al., in press). Goethite and local traces of hematite have been detected mostly in the gossanous Eastern Zone. Other mineral species are scarce: kaolinite occurs in a few samples (RRMB1, RRMB2, RRMB4, RRMB6) of the Eastern Zone, and in RRMB16 and RRMB19 from the Western Zone. Muscovite/illite has been observed locally (RRMB5, RRMB6 and RRMB14) in the Western Zone). Low quartz values are present in the samples from the Western Zone (RRMB2, RRMB5, RRMB6, RRMB7, RRMB9).

Table 6: Semiquantitative analyses (XRD).

Sample no	Sm	Dol	Cal	Qz	Bar	Kaol	Sph	Gyps	Goeth	Musc	Pyr	Hm
Western Zone												
RRMB1	xxxxx	xx	-	-	-	x	-	-	x	-	-	-
RRMB2	xxxx	xxx	-	xx	-	x	-	-	x	-	-	-
RRMB3	xxxxx	xxx	x	x	-	-	-	-	x	-	-	-
RRMB4	xxxx	xx	-	-	-	xx	-	-	xxx	-	-	-
RRMB5	xxxxx	x	xx	x	x	-	-	-	-	x	-	-
RRMB6	xx	xxxx	-	xx	x	-	xx	xx	x	x	-	-
RRMB7	xx	xxxxx	x	xx	-	-	-	-	x	-	-	-
RRMB8	x	xxxxx	xx	x	-	-	-	-	-	-	-	-
RRMB9	-	xxxx	xxx	xx	x	-	-	-	-	-	-	-
RRMB10	xxx	xxxxx	x	x	-	-	-	-	-	-	-	-
RRMB11	x	xxx	x	-	-	-	xxxx	xx	-	-	x	-
RRMB12	xxxxx	x	-	-	-	-	-	-	xx	-	-	-
RRMB14	xxxxx	xx	-	x	-	-	xx	-	-	x	-	-
Eastern Zone												
RRMB13	-	-	-	-	-	-	-	-	xxxx	-	-	xxx
RRMB15	x	xxxxx	x	-	-	-	-	-	x	-	-	-
RRMB16	xx	x	-	-	-	xx	-	-	xxxxx	-	-	-
RRMB17	xxxxx	x	-	-	-	-	-	-	xx	-	-	-
RRMB18	xxx	xxx	-	-	-	-	-	-	xxxx	-	-	-
RRMB19	xxx	xxxx	x	-	-	x	-	-	xx	-	-	-
RRMB20	-	xx	-	-	-	-	-	-	xxxxx	-	-	-

Sm=smithsonite; Dol=dolomite; Cal=calcite; Qz=quartz; Bar=barite; Kaol=kaolinite; Sph=sphalerite; Gyps=Gypsum; Goeth=goethite; Musc=muscovite; Pyr=pyrite; Hm=hematite;
*"-" not found, "x"<5wt%, "xx"5< <20wt%, "xxx"20< <40wt%, "xxxx"49< <60wt%, "xxxxx">60wt%

5. 11. Results: X-ray quantitative Rietveld phase (QPA)

In Table 7 are reported the X-ray quantitative analyses (Rietveld method) for four samples (RRMB1, RRMB2, RRMB10, RRMB12) selected on the basis of the oxidization stage, from less oxidized (RRMB2, RRMB10) to more oxidized (RRMB1, RRMB12). Only few minerals have been detected and quantified for these four selected samples. As expected, the less oxidized sample (RRMB10) has a high dolomite amount (up to ~84 %) and few wt.% of smithsonite (~14 wt.%). In sample RRMB2, in which the oxidation is more evident the smithsonite amount increases up to ~36 wt.%, and goethite occurs in low amounts (~7 wt.%). Minor phases also occur (detrital quartz and kaolinite up to 3.6 wt.%). RRMB1 and RRMB12 represent the most oxidized samples, in which smithsonite can reach up to ~66 wt.% (RRMB1) and goethite up to ~37 wt.% (RRMB12), while dolomite, as expected, occur in lower percentages (1.5 wt.% in sample RRMB12), probably because partially or completely replaced by smithsonite. Clays (kaolinite) can locally occur in the oxidized samples.

Table 7: X-ray quantitative analyses for 4 selected samples (Rietveld method).

Sample no	RRMB1	RRMB2	RRMB10	RRMB12
			wt.%	
Smithsonite	66.43	36.43	14.26	60.8
Dolomite	18.75	51.07	84.29	1.5
Calcite			0.074	
Goethite	11.05	7.11		37.54
Quartz		1.6	0.07	
Kaolinite	3.5	3.6		

5. 12. Results: Quantitative mineralogical characterization by QEMSCAN®

QEMSCAN® analysis and SIP file

A selected number of samples (8) were quantitatively characterized for mineralogy using QEMSCAN®. The analyses were performed at the Camborne School of Mines, University of Exeter, UK. The samples for QEMSCAN® quantitative mineralogical analysis were selected from the Reef Ridge Western Zone (which is the most enriched area), on the basis of their zinc content. The selection included seven oxidized samples (Zn-nonsulfides enriched) and one almost unweathered sample (RRMB11, rich in sulfides). The selected samples were prepared to obtain ~3 cm^2 diameter blocks. Twenty grams of the two most Zn-rich samples were chemically concentrated by heavy-liquid separation, using Na-polytungstate.

The analyses were carried out using the fieldscan analytical mode (Gottlieb et al., 2000; Pirrie et al., 2004; Goodall and Scales, 2007) with 10μm image resolution. Data acquisition and processing were conducted by iMeasure v. 4.2 and iDiscover v. 4.2 software packages, respectively.

The modal mineralogy data was output in mass% (wt.%) using the iDiscover software. QEMSCAN® mineralogical results were compared with those of the chemical analyses (ICP-MS/ ICP-ES).

The discrimination of the mineral species is carried out by a SIP file (Species Identification Protocol, see below for more detailed information). For this study, it was necessary to modify the LCU5 default SIP file containing common minerals, by adding the nonsulfide ore compounds. The final SIP file includes minerals identified by other analytical methods, as well as mineral species and mineral compounds newly detected by QEMSCAN® during the analyses. The chemistry of the mineral species set in the SIP file is in line with the average composition of each known mineral (Webmineral, www.webmineral.com) considered as *"pure"* minerals; for those species not respecting the stoichiometry (*"impure"* minerals, e.g. Fe-dolomite, Zn-dolomite) it was necessary to probe their average chemistry, and split the mineral phases in different entries. Smithsonite is rather pure at Reef Ridge, and has been inserted in the SIP as single *"pure"* phase. Dolomite was subdivided into three categories (table 8): dolomite (devoid of metallic elements), Fe-dolomite (Fe≤5 wt.%), and Zn-dolomite (Zn≤10 wt.%). The Fe-(hydr)oxides were split in two categories on the basis of their Zn content: Fe-(hydr)oxides (barren in metallic elements), and Zn-bearing Fe-(hydr)oxides (Zn≤10 wt.%).

The validation measurements were performed on a Zeiss EVO 50 SEM with Bruker 4010 EDS SDD detectors, and with Bruker Esprit 1.8 software (standard-less EDS analysis approx. ±1 %).

The wt.% of 4 major elements (Zn, Fe, Ca, Mg) was calculated considering the amounts of Zn, Mg, Ca, and Fe-bearing minerals: smithsonite, sphalerite, Zn-dolomite (considering values around 7 wt.% ZnO), Zn-rich Fe-(hydr)oxides (considering values around 5 wt.% Zn) for the calculation of total Zn%.

Dolomite, Fe-dolomite (with 20 wt.% MgO), and Zn-dolomite (with 14 wt.% MgO) were used for calculation of total Mg%. The total amount of Ca was calculated on the basis of calcite, dolomite, gypsum, Fe-dolomite (with 28 wt.% CaO) and Zn-dolomite (with 30 wt.% CaO). Fe-(hydr)oxides (i.e. goethite), Zn-rich Fe-(hydr)oxides (with 56 wt.% FeO), pyrite, and Fe-dolomite (with 3 wt.% FeO) were used for the total Fe% calculation.

In Table 9 it is shown the quantitative modal mineralogy (mass %) of 8 Reef Ridge selected samples, obtained with QEMSCAN® analyses. The meaning of each entry is displayed in Table 8. The QEMSCAN® false color fieldscan images of the crushed samples are shown in Figures 5.15. Concentrates are in Figure 5.16.

Dolomite, which is the prevailing host rock at Reef Ridge, occurs essentially in three main phases: as almost pure dolomite (from few wt. % up to 58.61 wt. %); as Fe-dolomite, which hardly reaches an amount of 2 wt.% except in the samples RRMB2 (3.33 wt.%) and RRMB6 (4.28 wt.%) as Zn-dolomite. The latter has been detected in very low amounts, with a maximum of 15 wt.% in sample RRMB3. Smithsonite can range from a minimum of ~1 wt.% (in sample RRMB11) up to a maximum of 62.33 wt.% (RRMB1). Fe-(hydr)oxides have been detected in all samples; they range from few

percentages (~2 wt.%) to high amounts up to ~54 wt.% (samples RRMB4 and RRMB12).

Table 8: Explanation of mineral phases detected by QEMSCAN®.

Mineral Category	Mineral Description
Smithsonite	Any phase with Zn, O, C and maybe OH. May include hydrozincite.
Dolomite	Any phase with Ca, Mg, O, C.
Fe-dolomite	Any phase with Ca, Mg, O, C and low Fe (approx. ≤5%).
Zn-dolomite	Any phase with Ca, Mg, O, C and Zn (approx. ≤10%).
Fe-(hydr)oxides	Fe-oxides such as hematite and Fe-(hydr)oxides (goethite).
Fe-(hydr)oxides (Zn)	Zinc-rich Fe-oxides such as hematite, magnetite, and Fe-(hydr)oxides (goethite). Zn (approx. ≤10%).
Sphalerite	Any phase with Zn, S, with minor Fe.
Pyrite/Marcasite	Includes pyrite/marcasite (Fe, S).
Quartz	Quartz and other silica minerals.
Kaolinite	Kaolinite/halloysite/dickite and any other Al-silicates (such as kyanite/sillimanite/andalusite).
Muscovite/illite	Includes muscovite and illite (Al, K, Si, O). May include biotite/flogopite
Chlorite	Chlorite/clinochlore, any phase with Fe, Al, Si, and Fe, Al, Si, Mg, O.
Gypsum	Any phase with Ca, S, O. Includes gypsum and anhydrite.

Zinc-rich Fe-(hydr)oxides are quite abundant even if in minor percentages compared to the zinc-barren (hydr)oxides. The latter occur in variable quantities, but generally not above 10 wt.%. An exception is sample RRMB4, where they reach 16.75 wt.%.

The only two samples containing measurable sphalerite contents are RRMB6 (up to 3.29 wt.%) and the completely unweathered RRMB11 (up to 48.08 wt.%). Pyrite/marcasite hardly reaches 1 wt.%, except in sample RRMB6, where pyrite amounts to 8.85 wt.%. Among the clay minerals, kaolinite is quite scarce and, where present never overcomes 2 wt.% (Table 9), whereas muscovite/illite can reach values up to 6 wt.% (RRMB1). Other minor phases occurring in the analyzed samples are quartz (up to 2.07 wt. % in sample RRMB6), chlorite (up to ~1wt.%) and gypsum (up to ~3wt.%). Concentrated samples showed only a weak increase of the economic mineral phases (smithsonite) (Table 9).

Table 9: Quantitative analyses of the Jabali samples by QEMSCAN®

Sample n	RRMB1	RRMB1 Conc.'	RRMB2	RRMB3	RRMB4	RRMB6	RRMB10	RRMB11	RRMB12	RRMB12 Conc.*
						wt.%				
Smithsonite	62.33	75.31	42.58	57.53	19.55	9.29	21.36	1.27	34.27	38.83
Dolomite	4.85	2.47	27.87	19.59	4.01	46.44	58.61	44.46	0.11	0.03
Fe-Dolomite	0.67	0.17	3.33	1.66	1.34	4.28	0.60	0.27	<0.01	<0.01
Zn-Dolomite	7.00	7.26	9.22	15.14	2.30	5.57	10.23	3.93	0.15	0.22
Fe-(hydr)-oxides	9.01	6.10	6.73	2.56	53.64	4.99	3.47	0.06	54.71	49.65
Fe-(hydr)-oxides (Zn)	6.65	5.93	4.24	1.85	16.75	1.30	2.37	0.03	9.75	10.43
Sphalerite	0.02	0.01	0.01	0.03	0.01	3.29	0.03	48.08	<0.01	0.01
Pyrite/Marcasite	0.01	0.01	0.01	0.01	0.08	8.85	0.21	0.28	0.10	0.10
Quartz	0.07	0.04	0.15	0.09	0.05	1.32	0.08	0.08	0.01	<0.01
Kaolinite	1.97	0.87	1.45	0.26	0.27	0.91	0.06	0.03	0.06	0.05
Muscovite/illite	5.59	1.33	2.97	0.81	0.96	2.07	0.64	0.30	0.34	0.18
Chlorite	0.99	0.27	0.46	0.08	0.61	1.01	0.06	0.01	0.10	0.07
Gypsum	0.01	<0.01	0.02	<0.01	<0.01	3.03	0.03	0.88	0.01	<0.01

Notes: QEMSCAN® measurement mode = field scan image: X-ray pixel spacing 10 μm; Jarosite/Coquimbite, K-feldspar, plagioclase feldspar, barite and other minerals occur in traces; *Concentrates samples.
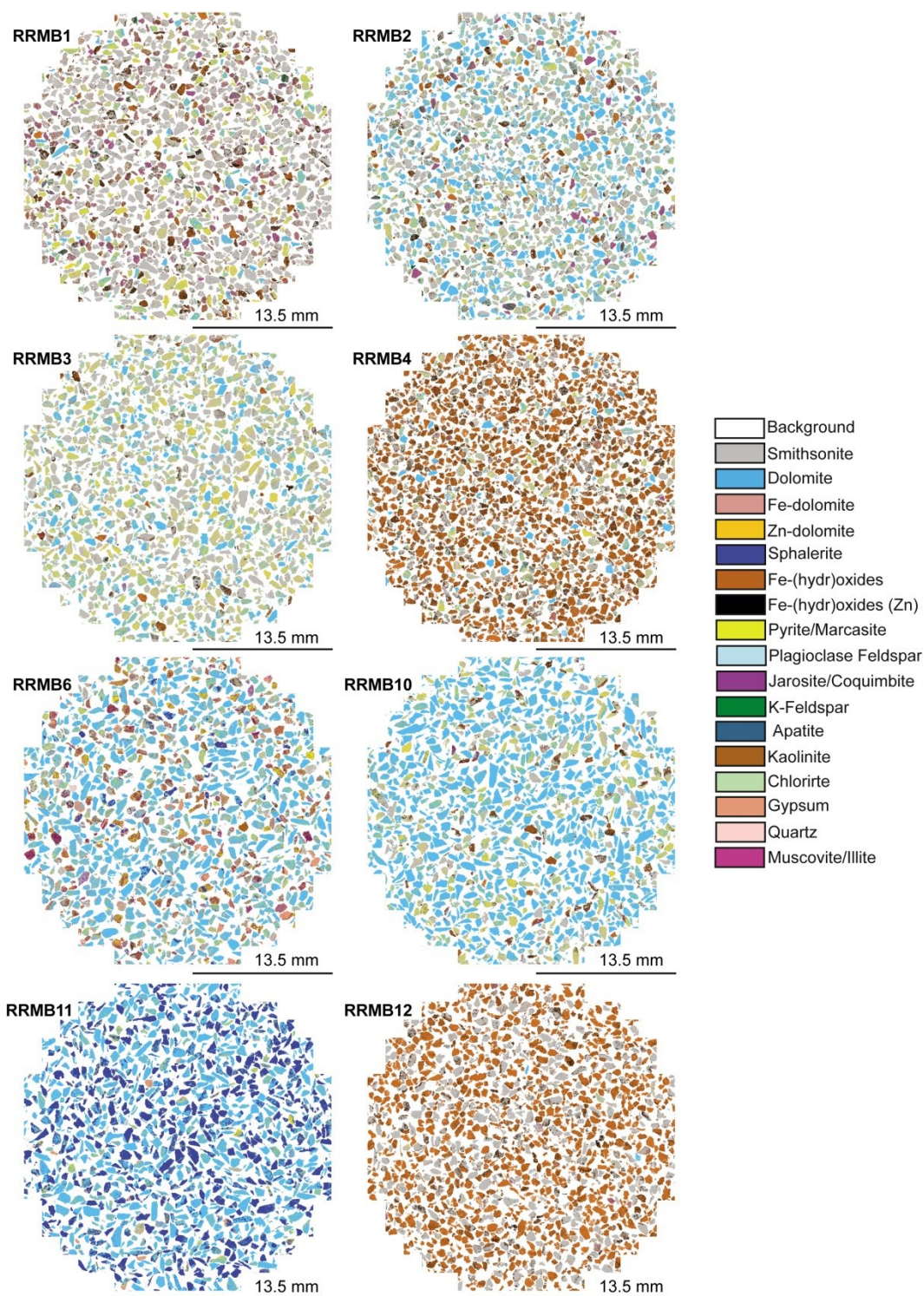
Figure 5.15: False-color fieldscan images of all the selected samples analyzed by QEMSCAN®.
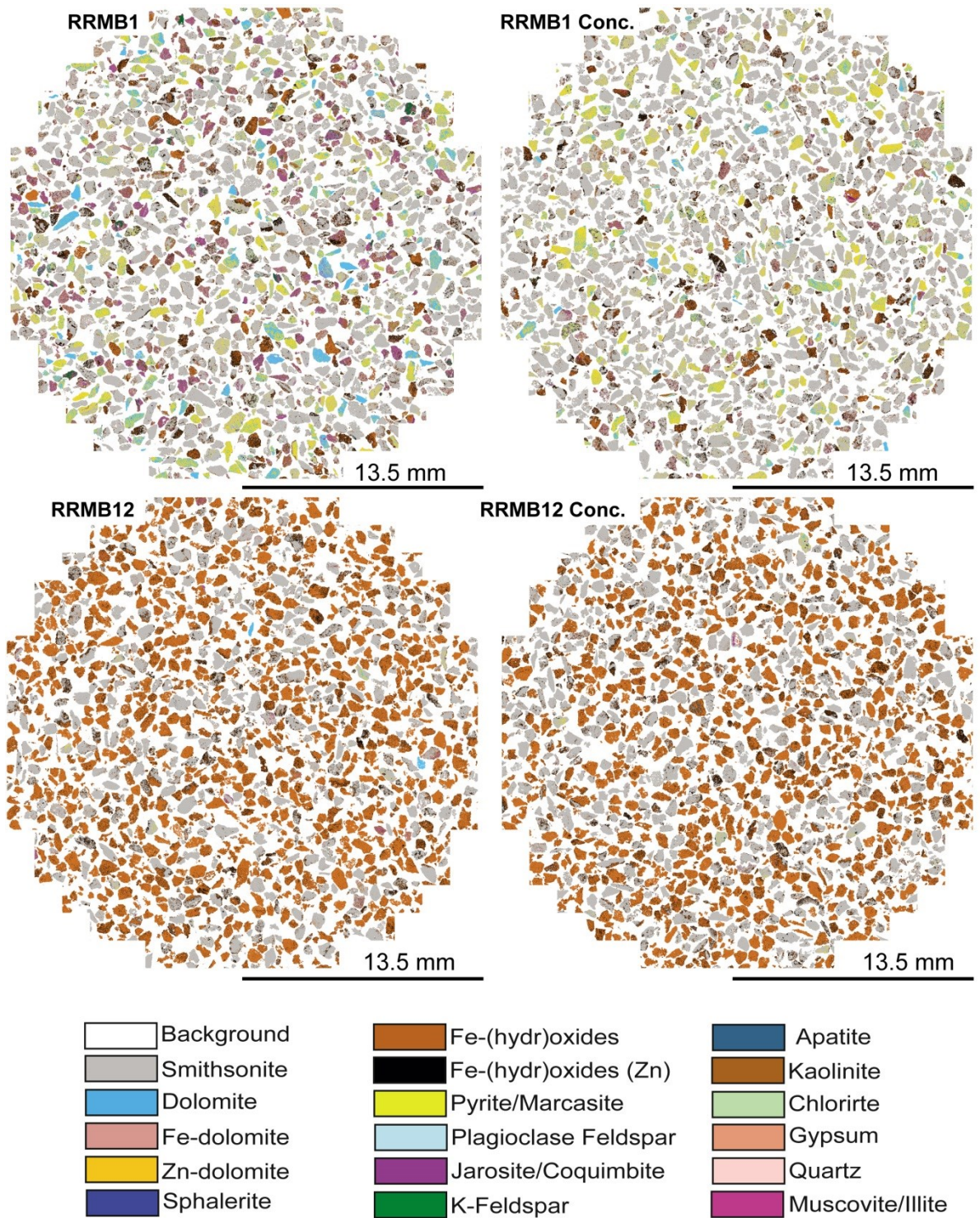
Figure 5.16: False-color fieldscan images of two selected samples and their concentrates analyzed by QEMSCAN®.

5. 13. Results: Calculation of elements from QPA (QEMSCAN®)

In table 10 is reported the attempt made to reconcile the elemental values of Zn, Ca, Mg and Fe calculated from the QPA data (QEMSCAN® method) with total Zn, Ca, Mg and Fe (all wt.%) obtained by chemical analyses. The calculation was done for only eight samples (the same analyzed by QEMSCAN®). Here follows an element-per-element description of the results obtained by this calculation, using minerals quantities obtained with both the Rietveld and QEMSCAN® technologies:

Zinc: the calculation was made using the contributions from smithsonite and sphalerite as "*pure*" minerals respecting stoichiometry (Webmineral, www.webmineral.com), Zn-dolomite (7 wt.% ZnO), and Zn-rich Fe-(hydr)oxides (5 wt.% ZnO). The Zn calculated from QEMSCAN® generally fits well with that derived from chemical analyses, except for the sample RRMB4 where an under-estimation of ~5% has been detected (Table 10).

Iron: it was calculated considering the standard values of goethite, pyrite and jarosite reported by Webmineral (www.webmineral.com), but also the contribution of Fe-(hydr)oxides enriched in Zn (56 wt.% FeO). The comparison between Calculated and Measured Fe shows that the discrepancy between the two is generally variable and difficult to explain, as there is not a general trend. The reasons, fully explained in the discussion, could be the fine grain size of Fe-(hydr)oxides that could create a misidentification of Fe-phases, or the impossibility to distinguish between the different types of Fe-(hydr)oxides and hence the different Fe wt.% values to be considered.

Calcium: The Ca % has been calculated considering the contribution of dolomite, gypsum and apatite respecting the stochiometry (Webmineral, www.webmineral.com), and also the contribution of Fe-dolomite (28 wt.% CaO) and Zn-dolomite (30 wt.% CaO). The results show an overall good fit between the Ca calculated by QEMSCAN®analyses and that measured by chemical analyses.

Magnesium: the calculation of Mg was done considering pure dolomite (21.86 wt.% MgO according to the standard composition), but also Fe-dolomite (20 wt.% MgO) and Zn-dolomite (14 wt.% MgO). The results are listed in table 10, and show that the data fit quite well with those of the chemical analyses.

Table 10: Zinc, calcium, magnesium, and iron amount (Zn%, Ca%, Mg%, Fe%) calculated from whole rock chemical assays (CA), compared with the metal percentages derived from the Zn-bearing minerals measured by QEMSCAN quantitative method (QPA-QEMSCAN®).

Sample n	Zn%			Fe %			Ca%			Mg%		
	Σ_{QPA}[1]	CA[2]	Σ_{QPA}-CA[3]	Σ_{QPA}[1]	CA[2]	Σ_{QPA}-CA[3]	Σ_{QPA}[1]	CA[2]	Σ_{QPA}-CA[3]	Σ_{QPA}[1]	CA[2]	Σ_{QPA}-CA[3]
RRMB1	32.72	34.00	-1.28	9.42	6.71	2.71	2.86	3.54	-0.68	1.43	2.05	-0.62
RRMB2	22.42	22.79	-0.37	6.70	5.38	1.32	8.92	9.57	-0.65	5.01	5.23	-0.22
RRMB3	30.44	29.00	1.44	2.72	1.93	0.79	7.95	9.01	-1.06	4.17	4.82	-0.65
RRMB4	10.65	15.63	-4.98	43.01	33.20	9.81	1.83	2.06	-0.23	1.01	1.18	-0.17
RRMB6	5.63	6.62	-0.99	10.33	7.40	2.93	12.61	14.69	-2.08	7.07	7.02	0.05
RRMB10	11.54	9.90	1.64	3.86	2.43	1.43	15.40	17.31	-1.91	8.89	8.50	0.39
RRMB11	31.68	32.87	-1.19	0.24	0.62	-0.38	10.74	11.74	-1.00	6.23	5.79	0.44
RRMB12	18.37	19.94	-1.57	39.72	22.61	17.11	0.06	0.27	-0.21	0.03	0.24	-0.21

[1] Σ_{QPA}:is the sum of element (Zn, Pb, Ca, Mg, Fe) coming from Quantitative values of minerals detected in Rietveld analysis; [2]CA: is the element value from Chemical analyses; [3]ΣQPA-CA: is the difference l

5. 14. Results: Mineral association

In Figure 5.17 are shown the pie charts of the mineral association; a few enlargements of the crushed particles synoptically show what the mineral association corresponds to.

The diagrams have been drawn considering the percentage of contacts between smithsonite (which is the most important economic phase) and all the other minerals detected by QEMSCAN®.

From Figure 5.17 it is clear that smithsonite is mostly associated with Zn-dolomite (from a minimum of ~2% (sample RRMB12) to a maximum of ~56% (sample RRMB3), with Fe-(hydr)oxides from ~2% (sample RRMB11) up to a maximum of ~33% (sample RRMB12), and with Zn-enriched Fe-(hydr)oxides, from ~1% (sample RRMB11) to ~29% (sample RRMB13).

Dolomite from the host rock is associated with smithsonite up to a maximum of ~20% (sample RRMB11), and the value of this association depends on the quantity of dolomite occurring in the samples. Although Fe-dolomite is low at Reef Ridge, it can be associated with smithsonite from a minimum of ~1% to a maximum of ~10%.

Smithsonite can also be locally associated with minor kaolinite (up to ~5% in sample RRMB2) and muscovite (up to ~6% in sample RRMB1), depending on the relative quantity of every mineral species in each sample.
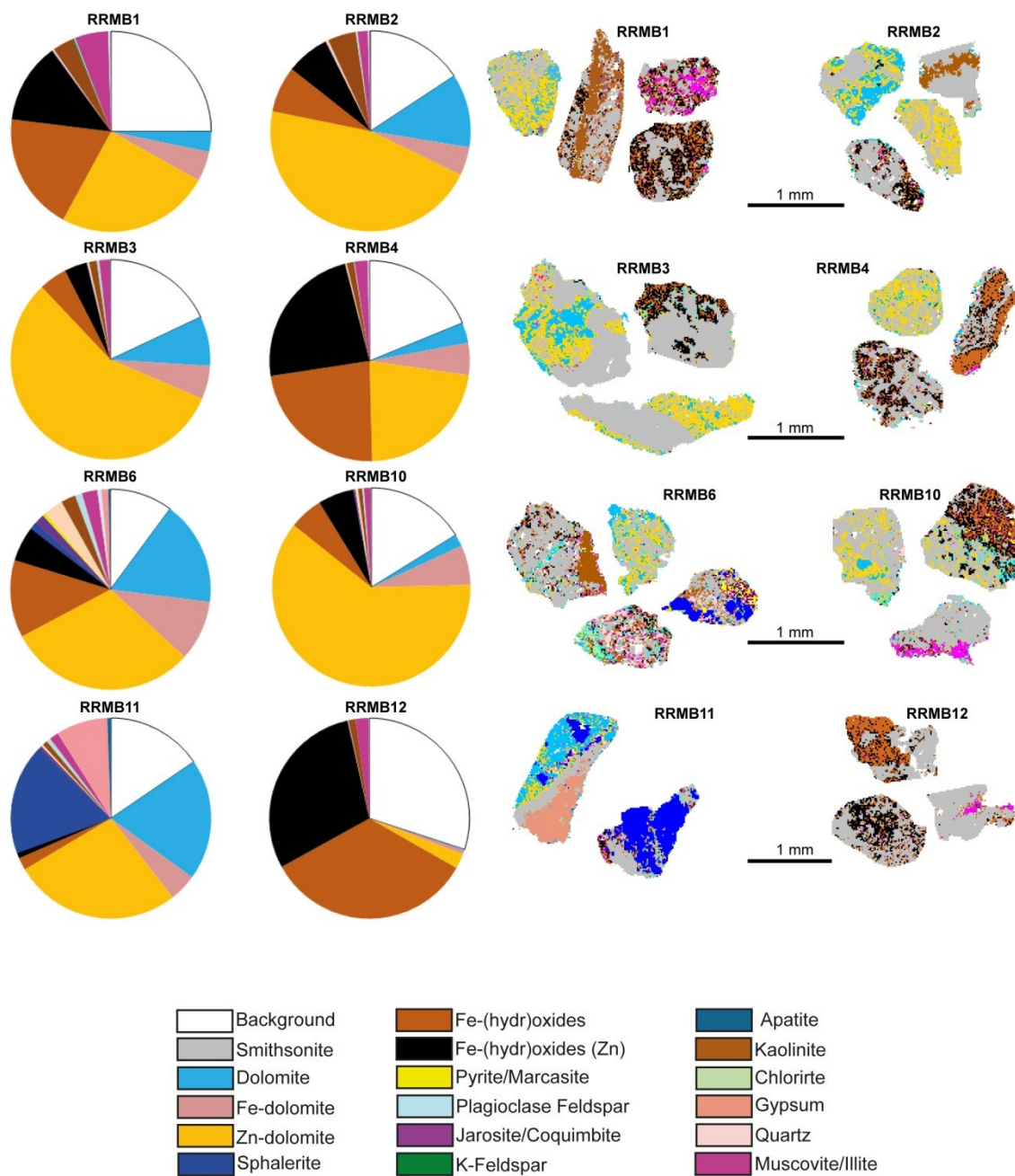
Figure 5.17: Pie diagrams of the mineral association for all the samples and enlargements of selected particles. The diagrams show the association between smithsonite and the other minerals in percentages. The color keys indicate the occurring mineral phases. Smithsonite is inserted in the color key as it occurs in the enlarged particles.

5. 15. Discussion

A detailed characterization of the supergene nonsulfide ore deposit of Reef Ridge has been carried out in term of mineralogy, petrography, and geochemistry. This characterization is also comprehensive of quantitative phase analyses pursued by XRD- and QEMSCAN®-QPA, in order to obtain an accurate and reliable image of the Reef Ridge mineral association.

The Reef Ridge prospect is one of several typical "*calamine-like*" nonsulfide zinc mineralizations (Large, 2001; Hitzman et al., 2003), derived from the weathering of a small primary sulfide deposit (sphalerite>pyrite>>galena), hosted in brecciated and dolomitized carbonates of the Nixon Fork sub-terrane (Alaska).

The high Zn percentages at Reef Ridge (up to 34 wt.%, locally) occur in the Western Zone, which is the more economically interesting. Smithsonite is the main ore mineral, while remaining sphalerite is very low. The high Fe values (up to 54 wt.%), detected both in the Western and Eastern Zone, are contained in the abundant Fe-(hydr)oxides.

The abundance of sphalerite, pyrite and marcasite as remnant of the primary mineralization, and the occurrence of epigenetic dolomite in the host rock, suggest a Mississippi Valley-type genesis for the original sulfides. The low concentrations of other metallic elements (Cu, Ni, Mo, Co), argue against a polymetallic igneous-related source for the primary Reef Ridge mineralization. Similar to other nonsulfide Zn deposits worldwide (SW Sardinia, Italy, Boni et al., 2003; Silesia-Cracow, Poland, Coppola et al., 2009; Jabali, Yemen, Mondillo et al., 2014), at Reef Ridge smithsonite (1) tends to replace almost totally both primary sphalerite and the dolomite host rock. For this reason, the prospect can be classified to belong both to "*direct replacement*" and "*wall-rock replacement*" deposit types (Hitzman et al., 2003).

A late smithsonite generation (2) precipitated as cement in vugs, cavities, and fractures and is commonly zoned, with alternating bands containing different amounts of MgO. Ca^{2+} and Mg^{2+} ions in solution were derived from dolomite alteration. Calcium re-precipitated as calcite and gypsum and Mg was trapped into smithsonite (Mg^{2+} and Zn^{2+} have a very similar ionic radius). Concretionary smithsonite clusters show habits and shapes similar to smithsonite type-IV described in Sardinia by Boni et al. (2003), and in the Irish nonsulfides by Balassone et al. (2008).

The two different generations of smithsonite (replacive and concretionary) can be distinguished also on the basis of their different luminescence under CL: the first is strongly blue, the second one shows alternating rims with red and blue luminescence. Compared to luminescence of other carbonates (Götze, 2012), the different luminescence patterns in replacement and concretionary smithsonite are related to different crystalline states: blue colors indicate the presence of lattice defects, and red colors are associated with more crystalline mineral structures (but also with higher Mn contents). Smithsonite generally precipitates at deeper levels in the host rock during the "oxidation stage" (Reichert and Borg, 2008), due to a progressing neutralization and increasing pH values of the downward migrating aqueous solution. Since the oxidation stage is associated with

a highly elevated $P_{CO2(g)}$, the formation of this high $P_{CO2(g)}$ zinc carbonate predominates over the precipitation of the low-$P_{CO2(g)}$ zinc hydroxy-carbonate hydrozincite.

Sphalerite at Reef Ridge occurs in the unweathered core samples, and as remnants in the oxidized core sections. Remnants of pyrite/marcasite have been locally detected in association with Zn-sulfide. Fe-(hydr)oxides such as goethite, lepidocrocite and hematite are fairly abundant; they may contain up to 13 wt.% of Zn, some Pb (maximum 7 wt.%), as well as silica. Anomalous GeO values have been detected in the Fe-(hydr)oxides from the Eastern Zone.

The inclusion of Zn and other metals onto Fe-hydroxides (goethite, ferrihydrite) is controlled by the pH of the aqueous solutions (Dzombak and Morel, 1990). Ferric hydroxides have particularly high reactive surface areas (up to 600 m^{2}g$-$ 1493; Lee and Saunders, 2003). The high-surface area, associated with the affinity of Fe-hydroxides to Me(II)-ions, results in an effective absorption controlled by pH and metal concentrations (Reichert and Borg, 2008). Lead and zinc show different degrees of absorption onto ferrihydrite, with quantitative zinc adsorption starting at pH oscillating from 5.5 to 7.5 (Dzombak and Morel, 1990), which is a pH range compatible with smithsonite precipitation (Takahashi, 1960).

In Figure 5.18 it is displayed a scheme summarizing the interpreted paragenesis of the main mineral phases occurring at Reef Ridge.
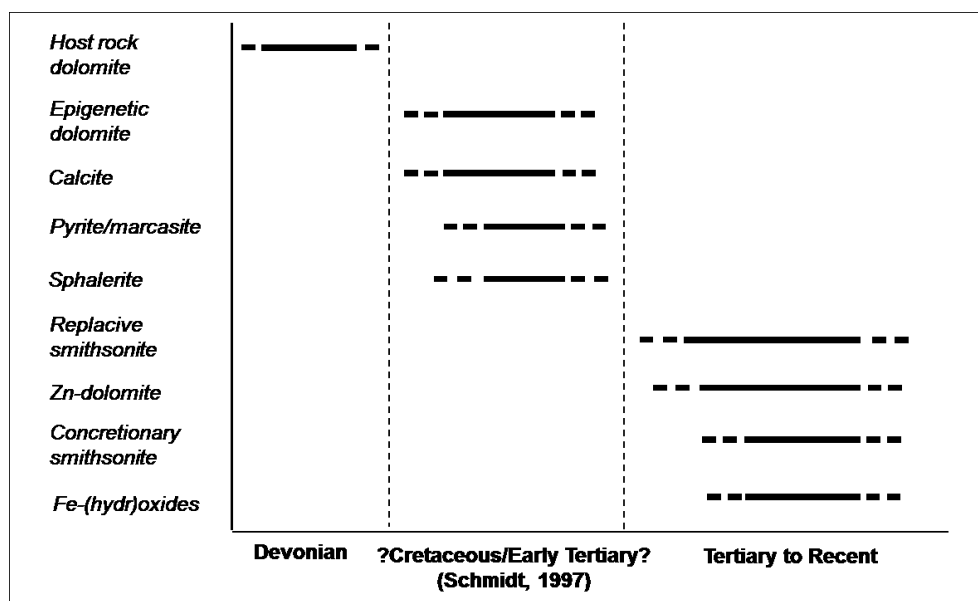
Figure 5.18: Interpreted mineralogical paragenesis for the Reef Ridge mineralization (Santoro et al., in press).

Analysis of carbon and oxygen isotope ratios carried out on the Reef Ridge carbonates indicates the genetic conditions for both the dolostone host rock, and the supergene nonsulfide ores (Santoro et al., in press). The $\delta^{18}O$ values (Figure 5.14) are within the range of 26 to 28‰ VSMOW (-5‰ to -2‰ VPDB): these are values typical for Middle Devonian marine carbonates (Yang et al., 1995 and references therein). The $\delta^{13}C$ values (0 to 2‰ VPDB) (Figure 5.17) also correspond to carbon isotope ratios of Middle

Devonian marine carbonate rocks (Keith and Weber, 1964; Lindth et al., 1981; Hurley and Lohmann, 1989; Yang et al., 1995; Joachimski et al., 2004; Prokoph et al., 2008). This suggests that the dolomite of the host rock inherited the carbon isotope signature from the precursor limestone during both diagenesis and hydrothermal alteration (Santoro et al., in press).

The carbon and oxygen isotope values of smithsonite at Reef Ridge are quite different from those of other supergene smithsonites worldwide (Gilg et al., 2008) (Figure 5.14). The $\delta^{18}O$ values range from 19.1 to 21.9‰ VSMOW and the $\delta^{13}C$ values from -0.7 to 2.1‰ VPDB. In contrast, the values of supergene smithsonite reported in the literature show a much wider range, being significantly depleted in ^{13}C (from 0 to -12‰ VPDB). This large range in $\delta^{13}C$ suggests different carbon sources, with high $\delta^{13}C$ values indicating a contribution of inorganic carbon from host rock carbonates and the low $\delta^{13}C$ values indicating an imprint of isotopically light soil-gas CO_2 (Gilg et al., 2008 and references therein; Coppola et al., 2009; Mondillo et al., 2014). At Reef Ridge, negative $\delta^{13}C$ values occur in only two samples, and the majority of the $\delta^{13}C$ values are similar to those of the host rock. This suggests that the predominant carbon source for smithsonite was the host carbonates, with a limited contribution from organic carbon (Santoro et al., in press). The study area was in the Arctic/sub-Arctic region since the Mesozoic, and has been (and still is) subjected to freezing-ice melting cycles during summer. The Reef Ridge deposit, located on exposed mountain peaks is rocky and dry, almost barren of vegetation–with only rare shrubs. The soil consists of a thin detrital layer, derived from physical weathering of underlying carbonate rocks. Therefore, there is a limited contribution from organic carbon to the supergene minerals (Santoro et al., in press).

The narrow range in $\delta^{18}O$ is typical for supergene nonsulfides, as the oxygen source in supergene deposits is generally meteoric water, and hence the nonsulfide carbonates (such as smithsonite) show only a minor variation in $\delta^{18}O$. However, the oxygen isotope ratios of Reef Ridge smithsonite are more depleted in ^{18}O compared to supergene nonsulfides from other parts of the World (see Gilg et al., 2008 and reference therein). To explain this difference, it is necessary to consider the oxygen isotope fractionation equation for water and smithsonite (given by Gilg et al., 2008):

$$\ln \alpha_{\text{smithsonite-water}} = 3.10\ (106/T^2) - 3.50,$$

which relates the $\delta^{18}O$ value of the mineralizing solution, the formation temperature of smithsonite and its final $\delta^{18}O$ composition (Figure 5.19). In the case of a weathering-related nonsulfide deposit (as Reef Ridge), the mineralizing solution consists of rainwater, infiltrating the lower vadose zone where smithsonite generally precipitates (Boni et al., 2003). In high latitudes (see Alaska), rainwater is strongly depleted in ^{18}O as water vapor contains less ^{18}O as a result of preferential rainout of the heavy isotope during the transfer of air masses from low to high latitudes (Rozanski et al., 1993). Rainwater currently measured in Yukon shows an annual $\delta^{18}O$ average value of ~ −20‰ VSMOW, with values ranging from ~ −14‰ VSMOW on average in summer to ~ −24‰ VSMOW on average in winter (Anderson et al., 2005 and references therein). It has not

been demonstrated how long the isotopic depletion persisted in the sub-arctic regions in the time frame between Early Tertiary up to now. Considering an annual average $\delta^{18}O$ value of $-20‰$ VSMOW for precipitation in the Yukon, calculated smithsonite formation temperatures would be around 0°C. However, this estimate is too low (Takahashi, 1960). Taking into account the strong climatic variations in the Reef Ridge area, and using the average $\delta^{18}O$ values of meteoric waters during the summer season (~ $-14‰$ VSMOW), the calculated temperatures would be in the range of 5 to 10° C (Figure 5.19).
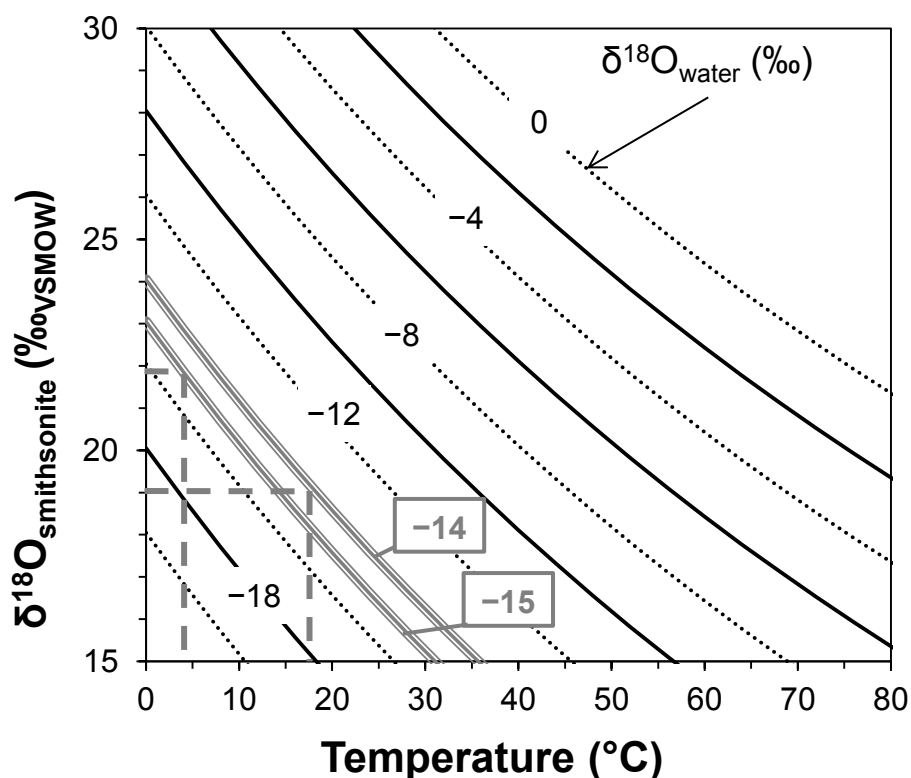
Figure 5.19: Graphical representation of oxygen isotope equilibrium curves between smithsonite and water according to Gilg et al. (2008), calculated for different $\delta^{18}O$ water values as a function of temperature. Calculated temperatures for smithsonite formation are based on the $\delta^{18}O$ value of -14 and -15 ‰ for the local meteoric water. Note: dashed grey line maximum and minimum $\delta^{18}O$ values.

These temperatures are substantially lower compared to precipitation temperatures for other supergene Zn-carbonates worldwide. With these temperature estimates, and assuming that supergene nonsulfide concentrations at Reef Ridge formed in a climate similar to today, it seems probable that the precipitation of smithsonite was restricted to the summer periods (Santoro et al., in press). No permafrost was encountered in the drilling at Reef Ridge: thus, it is possible that nonsulfide precipitation occurred beyond the short summer months as well. The current average daily maximum temperature in summer is around 20±2°C (Alaska Climate Research Center, http://akclimate.org/Climate/Fairbanks), whereas the average daily minimum

temperature in winter is about -40°C and occasionally even lower in case of low sunshine radiation (The Alaska Climate Research Centre).

During Pliocene and Holocene (after the Last Glacial Maximum - LGM), the climate in Alaska, characterized by minor seasonal variations in temperature, resembled the modern summer season (Sloan et al., 1996; Palmer et al., 2002; Ballantyne et al., 2006, 2010 and references therein; Haywood et al., 2009; Csank et al., 2011a,b). This considered, the supergene nonsulfides at Reef Ridge may have been formed either during the modern summer periods, or even in Pliocene or Holocene (after LGM).

At any case, without further evidence through independent dating, the weathering age associated with the supergene alteration of the Reef Ridge sulfides is difficult to define. The only time constraint is given by the relation of the formation of the nonsulfide deposit with the development of the Sleetmute Upland Surface (Fernald, 1960), which started in the late Tertiary and continues to the present. In addition, a formation of this supergene deposit under completely different climatic conditions can be excluded, because most supergene deposits worldwide, formed under warm-humid, temperate or semi-arid climates (Reichert and Borg, 2008), have $\delta^{18}O$ signatures of smithsonites less depleted in ^{18}O than the Reef Ridge smithsonite (Gilg et al., 2008).

Several ore deposits in Alaska (Cu-porphyry, skarn, sulfide veins, etc.) and northern Canada have gossan zones of variable thickness, and some of them are strongly oxidized into considerable depths.. It is important to quote the British Columbia nonsulfide deposits (Paradis et al., 2011), even if their age is so far unknown. Another possible example of nonsulfide precipitation in colder climates is the small supergene Howard Pass prospect (Selwyn Mountains, Yukon), located around the better-known massive sulfide deposit (Jonasson et al., 1983): here smithsonite and minor hemimorphite replace a Holocene moss cover and precipitate as cement within talus.

Quantitative phases analyses (QEMSCAN®)

The use of the QEMSCAN® technology, applied to the characterization of the ores from the Reef Ridge Project brought several advantages. One of them was the possibility of building mineral maps for each sample that can be used to identify quantitatively the various mineral phases. These maps were also useful to identify synoptically the mineral associations, and could be eventually used also to determine the processing options. QEMSCAN® analyses, in fact, allowed the calculation of an accurate modal mineralogy for the economic and gangue minerals, and the definition of their spatial distribution. In addition, detailed information on Zn deportment could also been collected. QEMSCAN® analyses confirmed the occurrence of the mineral phases already detected by traditional analytical methods, but added also new data about mineral compounds not previously identified (chlorite, jarosite/coquimbite, K-feldspar, plagioclase), and allowed to distinguish between *"pure"* and *"impure"* mineral phases. It was possible to detect and quantify Fe-dolomite (Fe≤5 wt.%), and Zn-dolomite (Zn≤10 wt.%), which could be well distinguished from *"pure dolomite"*. A rough comparison with QPA-Rietveld (Table 10) shows that the mineral abundances obtained by QEMSCAN® are poorly comparable with the latter. This is due to the difference in the analytical methodology. As already explained, the mineral compounds discriminated by QEMSCAN® are classified on the

basis of chemical analysis, whereas X-ray-QPA carried out by Rietveld classifies the minerals on the basis of their structure, hence many "*impure*" phases cannot be identified by Rietveld with a consequent change in the percentages of each detected mineral.

Therefore, there are some limitations in using QEMSCAN® on the Reef Ridge prospect, as it is the case for many other nonsulfides and similar deposits worldwide (Rollinson et al., 2011; Santoro et al., in press).

In Figure 5.20 are displayed the correlation diagrams of the calculated element amounts (Zn, Fe, Ca, Mg) plotted vs. the measured (QEMSCAN®-QPA) element concentrations. All the points in the diagrams represent the relationship between the amount of the element calculated from QPA analyses and the element directly measured in each sample. In a hypothetical case of perfect stoichiometry for all the minerals occurring in the deposit, all the points should follow along the theoretical dotted line (considering the possible measurement errors), having a unitary coefficient. The samples falling below the lines, hence, contain a amount of the element lower than the corresponding calculated values, and vice versa for the samples above the line.

Even if the data do not match perfectly (this is the case for Zn and especially Fe) the diagrams show an overall good correlation if compared to similar diagrams drawn for Hakkari and Jabali. The best correlation is for Ca and Mg. The reason of a better result in the correlation between QEMSCAN®-QPA and Chemical analyses could be ascribed to the simpler mineralogy of Reef Ridge, compared with the more complex mineralogical associations of Jabali and Hakkari.

The still existing discrepancies could be due to several reasons fully explained in the conclusion chapter.

The comparison between the non-concentrated and the concentrated samples at Reef Ridge showed only a weak increase of the economic mineral phases (smithsonite) in the latter. This could be due either to the presence of heavy metallic elements within the structure of the uneconomic minerals (e.g. Zn, Fe in dolomite), or to liberation issues (e.g. light dolomite grains still attached to heavier smithsonite grains).
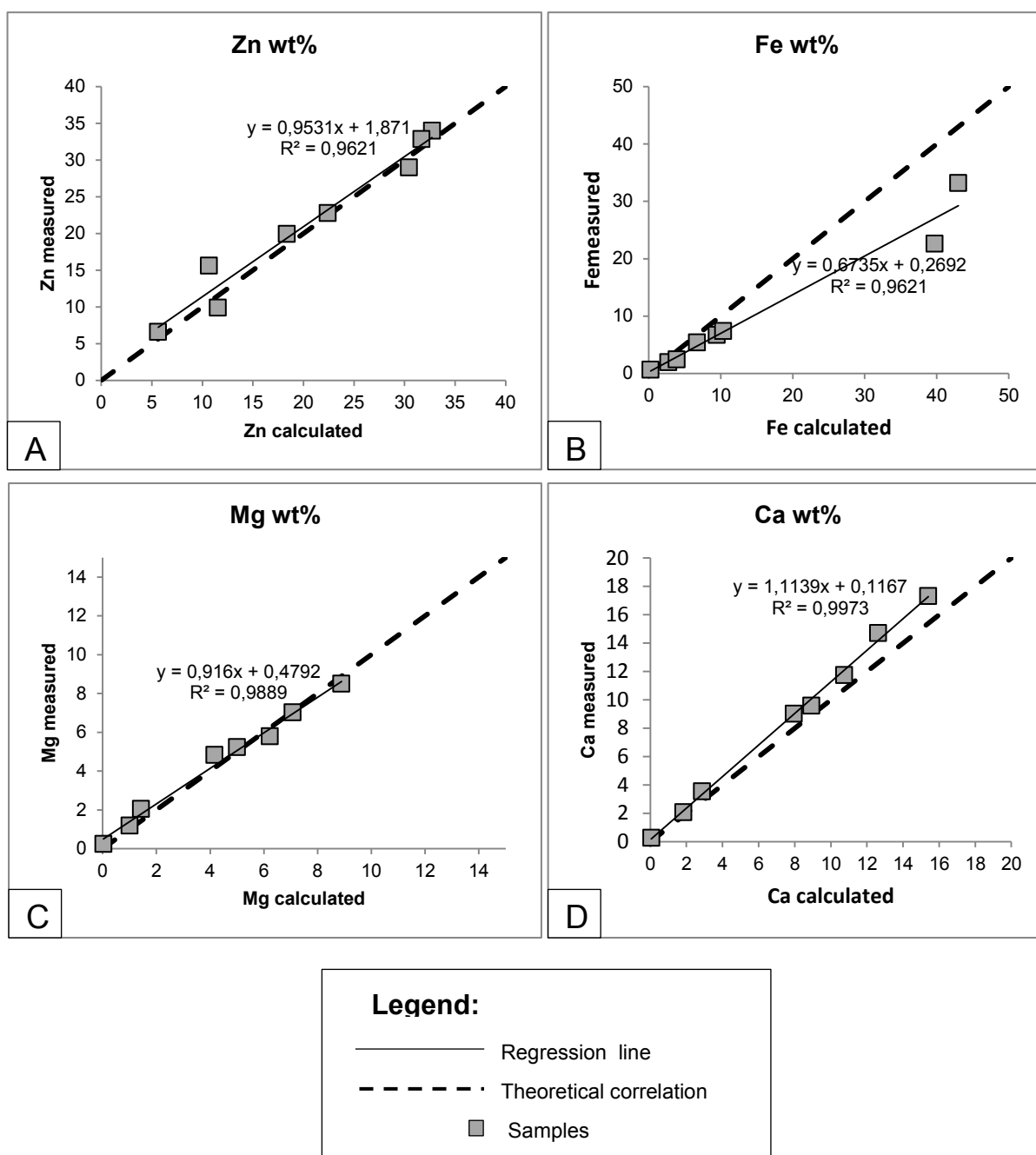
Figure 5.20. Diagrams of calculated element amounts from QEMSCAN® analyses plotted vs. measured element concentrations. (A) Zn wt.% calculated from mineral QEMSCAN® analyses vs. Zn wt.% from chemical analyses; (B) Fe wt.% calculated from mineral QEMSCAN® analyses vs. Fe wt.% from chemical analyses; (C) Mg wt.% calculated from mineral QEMSCAN® analyses vs. Mg wt.% from chemical analyses (D) Ca wt% calculated from the minerals on QEMSCAN® analyses vs. Ca wt.% calculated by chemical analyses.

The data of the mineral association indicate that smithsonite in the Reef Ridge samples is mostly associated with Zn-dolomite (generally occurring in low quantity in the deposit), and with Fe-(hydr)oxides, Zn-rich Fe-(hydr)oxides, and in minor % with dolomite and Fe-dolomite.

Conclusions

This study indicates that:

1. The Reef Ridge deposit is a typical carbonate-hosted supergene nonsulfide zinc mineralization (Large, 2001; Hitzman et al., 2003), formed by the weathering of Zn sulfide ores belonging to a no better-specified MVT primary deposit. The host rock is a microcristalline dolostone, locally cut and replaced by macrocristalline *saddle* dolomite. Remnants of sphalerite occur only locally. The nonsulfide concentrations can be described as belonging to both "*direct replacement*" and "*wall-rock replacement*" supergene types (Hitzman et al., 2003), in which the main Zn-minerals are smithsonite [$ZnCO_3$] and hemimorphite [$Zn_4Si_2O_7(OH)_2 \cdot H_2O$]. In the Reef Ridge case the only economic Zn-mineral is smithsonite.

2. Mineralogical and petrographic analyses revealed the occurrence of 2 generations of smithsonite (one replacing sulfides and host rock, and the other in concretions). Fe-(hydr)oxides (Zn- and silica-rich goethite) are quite abundant. Smithsonite is generally stochiometric, with very low amounts of AsO and CdO. Concretionary smithsonite is commonly zoned, due to alternating MgO content.

3. Chemical analyses revealed that the most common elements at Reef Ridge are Zn and Fe, followed by Ca and Mg. Sulfur can occur in samples with high amounts of remnant sulfides. Between the minor elements, Sr (correlated to the dolomite host rock) is quite abundant, as well as Pb, As and Cd. C-O stable isotopes analyses showed that the Reef Ridge supergene mineralization formed in one or several weathering phases, under a cold/humid climate (5-14°C). The age of the secondary deposit is probably spanning from late Tertiary to Recent.

4. Quantitative analyses (both Rietveld and QEMSCAN®) confirmed that the mineralogy at Reef Ridge is quite simple: smithsonite and Fe-(hydr)oxides are the most abundant mineral phases. Dolomite can be quite abundant in unaltered samples. The comparison between the non-concentrated and concentrated samples showed only a weak increase of the economic mineral phases in the latter.

5. The comparison between the directly measured elements (Zn, Ca, Mg and Fe) and the same elements calculated using QEMSCAN®-QPA, revealed a good fitting of the data. This indicates that, in the case of Reef Ridge, the use of QEMSCAN® for the mineral and quantitative characterization of the deposit worked quite well, and hence that the analyses can be considered reliable. Only Fe shows a small discrepancy that could be ascribed to analytical issues.

Discussion and Conclusions

This thesis is primarily a study on the steps required, and more precisely on the best route to follow during the feasibility studies, in order to obtain an accurate characterization of supergene nonsulfide Zn-Pb(Ag) deposits, with the aim of gathering more precise information on this kind of ores prior to the processing stages. As declared in the Introduction, this thesis is regarded as an attempt to integrate the traditional analytical technologies with the *"Automated Mineralogy"* analysis system, to be applied to the evaluation of nonsulfide Zn(Pb) deposits. In the previous chapters, it has been given an exhaustive geological description of three nonsulfide Zn-(Pb) deposits: Hakkari, Jabali and Reef Ridge, followed by a petrographic, geochemical and mineralogical quantitative ore characterization, obtained by the use of several analytical techniques. Although the considered deposits represent three typical examples of supergene nonsulfide Zn-(Pb) ore concentrations, their study has revealed several important mineralogical and petrographic differences. At the end of each chapter, there is a specific discussion in which the main findings are reported.

This chapter is mainly focused on the comparison between the results obtained by different analytical methods: the strenghts and weaknesses of each technique for the characterization of the supergene nonsulfide Zn-Pb ores will be highlighted. Considering the fact that in this thesis have been reported and discussed the earliest attempts to characterize nonsulfide Zn-(Pb) deposits by the use of QEMSCAN®, a particular attention will be given to the advantages and disadvantages of using this technology for the characterization of this kind of ore deposits.

Jabali is the most mineralogically complex of the three, with smithsonite (Zn-carbonate) hosted in dolomite host rock and associated with variable amounts of Fe-(hydr)oxides, cerussite (Pb-carbonate), anglesite (Pb-sulfate), remnants of sphalerite and galena and several other minor phases (Ag-minerals, sauconite, kaolinite, gypsum, calcite). The mineralogy of the Hakkari deposit is also not quite straightforward, with Zn mainly occurring as smithsonite and hemimorphite (Zn-hydrosilicate), minor cerussite and anglesite, associated with Fe- and Mn-(hydr)oxides, barite, detrital quartz and remnants of sphalerite. The mineralogy of the Alaskan deposit, instead, is quite simple, because it consists mainly of smithsonite hosted in dolomite, with some Fe-(hydr)oxides and rare sphalerite.

Optical Microscopy (OM) and cathodoluminescence (CL) observations can give useful petrographic information on the mineral occurence, texture, and the presence of different mineral generations. However, OM and CL have some limitations:

a) sample preparation issues (the sample must be prepared as well as possible for more accurate interpretation);
b) poor statistical information and scarce accuracy (the quality of the interpretation is strictly dependent on the expertise of the operator).

More advanced analytical techniques are needed for a better identification of supergene Zn-Pb nonsulfide deposits. Traditionally, the first step in the characterization of this kind of ores after OM observation makes use of Chemical Analyses (CA) of major and minor elements, followed by X-Ray Powder Diffraction (XRPD). The first method is useful to detect the elemental concentration in each sample, defining the presence and the abundance of the economic metals. Chemical analyses are also crucial to detect the occurrence of problematic elements (i.e. As, Hg, Cd, Tl), but they do not give any information on the mineralogy. XRPD, hence, results to be the first essential technology to gain information on the mineral phases as it allows identifying (and eventually quantifying) the minerals occurring in the ore samples (over the 2% detection limit). More accurate analytical techniques are needed to obtain the quantitative evaluation of the ore and gangue minerals occurring in a deposit. In this thesis, the Quantitative Phase Analysis (QPA) for all three deposits has been carried out by the use of two different methods: XRPD-Rietveld and QEMSCAN®.

A further step in Zn-Pb nonsulfide ore characterization is through SEM-EDS and/or WDS analyses. These two analytical techniques are very useful for "image analysis", as they can be used to catch high resolution *"real time"* images of the analyzed area, in order to obtain the morphology of the minerals (3D image on rock chips) or the textural parameters and spatial relationships between minerals (2D image on the thin sections) by the registration of SE signals produced by the interaction between the electron beam and the solid surface of the samples. Nevertheless, because of their capability in obtaining high resolution images of the samples, SEM-EDS and WDS analyses are primarily used for the definition of the chemistry of minerals. It is also important to highlight that SEM-EDS (and WDS) are punctual analyses. This means that they can define the precise chemical composition of a specific analyzed point. For each point it is possible to obtain a spectrum of the elements occurring in it: from the interpretation of the spectra it is possible to precisely detect the composition of the analyzed mineral phase. For each point of analysis, it is also possible to get the abundance of elements in wt.%, and this information is useful for a precise identification of the mineral phase on the basis of its stoichiometry. Moreover, these two methods can also detect and quantify the concentration of *"exotic elements"* eventually occurring as impurities in the crystal lattice of a mineral. This means that a comparison between chemical and SEM-EDS/WDS analyses can help to understand the distribution of economic and uneconomic elements on the basis of the occurring mineral phases. SEM-EDS and WDS analyses are very similar in term of results obtained. The main difference is the detection limit, which is 1-3 % rel. for SEM-EDS and 0.01% for WDS; this means that SEM-EDS is generally used for faster mineral identification and semi-quantitative chemical analyses of the minerals,

whereas WDS is generally used for more accurate quantitative chemical analyses. SEM-EDS and WDS technologies are extremely useful for the characterization of Zn-nonsulfides, as they allow to:

a) obtain the textural parameters of the analyzed areas,

b) identify with precision the occurring mineral species,

c) infer the element deportment in minerals. The latter information is really important for the characterization of supergene Zn-nonsulfide deposits. In fact, during weathering the metallic elements, leached out from primary minerals are mobilized throughout the system and can precipitate in secondary phases when suitable conditions occur, or be trapped as traces in the crystal lattices of other minerals (i.e. Zn trapped in Fe-(hydr)oxides and in dolomite). In this thesis I have used the term *"impure"* minerals to indicate the minerals formed through the latter process. As reported in the previous chapters, several *"impure"* phases have been recognized and analyzed by the use of SEM-EDS and WDS technologies. For example, in the Jabali samples (*chapter 4*) part of the Zn mobilized by weathering of primary sphalerite was trapped into dolomite (that can contain up to 20% Zn in the lattice), instead of precipitating as smithsonite (Mondillo et al., 2011, 2014). Similarly, some minor Zn amounts were also trapped in the Hakkari (Santoro et al., 2014), and Reef Ridge dolomite host rock. SEM-EDS analyses also detected variable amounts of metallic elements (Zn, Pb, As) trapped in the Fe-Mn-(hydr)oxides of the three deposits.

The Quantitative Phase Analysis (QPA), carried out with XRPD-Rietveld and QEMSCAN® (field scan mode, 10µm grid size) on selected samples from the three deposits showed different results. The comparison between these two different analytical technologies indicates that the results obtained were poorly comparable for all three deposits. This is due to the differences between the two methods used, already mentioned in Boni et al. (2013) and Rollinson et al. (2011) and here briefly reported (Table 1) and discussed. The discrepancy between the Rietveld and QEMSCAN® data is due primarily to a difference in the analytical approach: the Rietveld method classifies the minerals on the basis of their structure, while QEMSCAN® discriminates the mineral compounds on the basis of their chemical composition. It derives that, even if both methods can be used for the quantification of the mineral phases in an orebody, the Rietveld-QPA is not the best method to quantify the eventually occurring *"impure"* phases. For example, even if the presence of Zn-dolomite in the Jabali deposit was detected by SEM-EDS analyses, the Rietveld-QPA calculation carried out by Mondillo et al. (2011, 2014), was not capable to quantify the abundance of this *"impure"* mineral. The same is also for other *"impure"* phases occurring in Hakkari and Reef Ridge (i.e. Zn-enriched Fe-(hydr)oxides, Zn-Mn dolomite, Fe-dolomite, Mg-smithsonite, etc.). Moreover, being the weight fraction of each crystalline component, calculated from the corresponding refined scale parameter from the X-Ray spectrum, it derives that the quantification of the phases is strictly dependent on the detection limit of the instrument used to obtain X-Ray spectra.

Table 1: Analytical differences between QEMSCAN®- QPA and XRD-QPA analyses.

	QEMSCAN®	XRD-QPA
Determining bulk mineralogy	Yes	Yes
Determining trace mineralogy	Yes	No (limited by detection sensitivity)
Identification of amorphous and semi-amorphous phases	Yes; not affected as chemical analyses	Amorphous phases can be quantified (internal standard needed)
Identification of Polymorphs	No, because it is a chemical analysis	Yes, because it is a crystallographic analysis
Sample volume analyzed	Small, a representative sample or more samples are needed	Large, bulk powder is examined, so representativety is increased
Identification of clay	Yes, but limited by excitation volume and thus quality of database used	Yes, but difficult with mixed clays
Detail of mineral classification	Database can be customized to any detail required	Limited to existing database entries; not customizable by users

Clay minerals can be quantified by the Rietveld-QPA, but big issues come out when mixed clays occur in the sample. One of the advantages of the Rietveld is the possibility to quantify polymorphs and amorphous phases (by the use of internal standards). In the case of the Hakkari deposit, for example, the use of internal standard resulted in the quantification of several amounts of not specifically identified amorphous phases (Santoro et al., 2013). Only by the use of QEMSCAN® it was possible to define the amorphous as a mixture of phases bearing the chemical signature of jarosite/pyrite/Fe-hydroxides. Compared to the Rietveld method, QEMSCAN® is able to detect and quantify the "*impure*" minerals, the trace minerals (because of the high detection limit) and, as mentioned above, to identify the amorphous phases on the basis of their chemistry. However, QEMSCAN® it is not capable to identify in a sample the polymorphs of the same mineral, and detect the amorphous phases as such.

To state the accuracy of each method, a comparison was carried out between the results of QPAs (made by Rietveld and QEMSCAN® technologies) and those of the chemical analyses of each sample. The results of the comparison are listed and partially discussed at the end of *chapters 3, 4* and *5.* The comparison was done considering the amount of the most important elements (Zn, Pb, Ca, Mg and Fe) measured by chemical analyses *vs* the amount of the same elements calculated by Rietveld- and QEMSCAN® - QPA analyses.

The main finding of this comparison show that: *as a rule, there is a better matching between QEMSCAN®-QPA results and Chemical analyses; this is an index of a mayor accuracy of QEMSCAN®-QPA compared to Rietveld-QPA.* The reasons are in the capabilities of QEMSCAN®, that allows:

a) to define and quantify accurately all the minerals occurring in the samples (also those occurring in very low amounts),

b) to quantify the "*impure*" phases,

c) to obtain the average abundance of the element deportment in the minerals.

Hence, QEMSCAN® could be a really valuable method to obtain an accurate characterization of Zn-nonsulfide ores.

However, with the exception of the Reef Ridge prospect, in which the mineralogy is simple, some important discrepancies between the elemental values measured and calculated have been observed in the Hakkari and Jabali deposits. More specifically, Pb and Fe seem to be generally incorrectly evaluated, relative to the measured element concentrations: Pb is always over-evaluated relative to the measured element concentration, and Fe is always poorly constrained (it can be randomly over-evaluated or under-evaluated relative to the measured element concentration). Better correlations (even if with still some discrepancies) were observed for Zn, Ca and Mg. These discrepancies are due to several reasons here briefly listed:

1) *Complex mineralogy*: this is the principal reason for a discrepancy between the calculated element amount and measured chemistry. QEMSCAN® uses the average chemistry for each mineral but, if the mineralogy is complex (as in the case of Hakkari and Jabali), the estimated average chemistry for each mineral could be incorrect. For this reason, calculating "*accurate*" chemical values of Fe, Pb, Zn from minerals, based on average theoretical values is difficult. This problem may be corrected checking the minerals chemistry by manual SEM, and adjusting the values placed into the SIP file for calculation;

2) *Sample preparation:* it may affect especially the Pb evaluation, as Pb-phases are heavier than others. Hence, when mixed into the resin they could preferentially accumulate at the base of the mould (which is the surface that will be analyzed by QEMSCAN®): according to gravity and Stokes law, heavier minerals will settle quicker. This issue may be solved by examining multiple blocks for each sample;

3) *Homogenization issues*: the coarser the particles, the less representative they are. The samples prepared for QEMSCAN® have particles around 450 μm in size (which is a good size range to be analyzed), whereas the samples for chemical assays were ground to <50 μm (good homogenization). This may cause strong discrepancies between the directly measured Zn amounts and the calculated values. This problem could be resolved by measuring more blocks, or, by grinding the samples to a finer size, in order to gain more representative data. Both solutions are highly time and money consuming in case of complex mineralogy;

4) *Representativity issues*: the quantity of the material analyzed by QEMSCAN® (1gr) is lower than that used for chemical analyses (~10gr). The solution, once again, is to analyze more blocks of one sample, enhancing in this way the representativity;

5) *Assaying technique*: different methods are generally used to dissolve the minerals for chemical analysis. This means that the less effective method is used on a certain type of mineralogy, the less precise the chemical assays will be. In the case of Hakkari, the use of *aqua regia* digestion for ICP-MS, may

not have been adequate to dissolve all the minerals, especially the Zn silicates (hemimorphite). This may have resulted in an under-estimation of the Zn measured compared to that evaluated;

6) *Analytical issues:* they influenced the calculation of Fe especially. Iron, in fact, was poorly constrained (in Hakkari, Jabali and in minor part also in Reef Ridge), as it is contained mainly in (hydr)oxides, which are poorly distinguished by QEMSCAN®, because of the similarity of their spectra at low values of X-ray counts (Anderson et al., 2014). Moreover, the presence of very tiny Fe-(hydr)oxide particles (<10 μm is used for routine analyses) dispersed in other minerals (i.e. in the dolomite host rock at Jabali), can cause a misidentification of the mineral compounds, resulting in a wrong element re-calculation. The last problem can be solved, if necessary, by enhancing the resolution of QEMSCAN analyses (at 5 μm or very rarely less).

The QEMSCAN®-QPA analyses carried out on some concentrate block samples (heavy liquids method) show a low effectiveness of the concentration step for the processing of nonsulfide zinc minerals. In fact, roughly comparing the *"normal feed"* samples with the *"concentrates"*, it was possible to notice only a small increase of the economic minerals in the latter. This is probabably due to two main issues:
a) the occurrence of heavy metallic element in the *"gangue"*, such as Zn in dolomite or Zn-Pb in (hydr)oxides or clays. Zinc and lead tend to render the gangue phases heavier, thus generating a selective concentration of the latter in the concentrate blocks. This would be a positive aspect, if the enriched gangue phases (i.e. Zn-dolomite) could be amenable to be processed by the chosen processing method, a negative one otherwise;
 b) the economic phases were not liberated completely at the chosen grain size. To enhance the concentration by using the heavy liquid method, it is necessary to grind the sample fine enough, but this would probably not be economic as ultrafine grinding is very expensive. These two issues must be carefully considered when planning a processing method, as they could decrease the effectiveness of the metal recovery or might increase the processing costs.

QEMSCAN® can also be used a valuable method of image analysis. Compared to other methods (OM, SEM-EDS, WDS), one of the biggest advantages of QEMSCAN® is the possibility to build, contemporarily to the QPA analyses, several maps of the sample, in which each color corresponds to a mineral or to a mineral compound. In this way it would be easy to observe synoptically the occurrence and position of the minerals in the samples. By carrying out several analyses of whole thin sections, for example, it is possible to easily understand the ore texture without using other methods.

Another useful information that can be gained by QEMSCAN® is the mineral association, which is a very useful information to predict Zn(Pb) recovery, as it shows with which minerals, and how frequently the economic phases are related to the not-economic ones. By this information, hence, it is possible also to determine the processing

options for the preliminary concentration of zinc/lead-bearing minerals, thus identifying potential processing problems. For example, in the Jabali ore, the QEMSCAN® analyses revealed that Zn-dolomite is strongly associated with smithsonite, hence the impossibility to recover the zinc trapped in the dolomite lattice unless a more effective technology would be used. The mineral association may be a source of important information when choosing the processing method, as it reveals to which other mineral phases the potentially economic minerals are associated to.

The results of this thesis are largely positive, because they have revealed that the use of QEMSCAN® can be crucial to solve some of the uncertainties on the characterization of Zn-Pb supergene nonsulfide ores, still left by the traditional methods. However, it is important to keep in mind that several limitations came out from the use of QEMSCAN® technology. Some of these limitations can be figured out only by the compared/joint use of traditional methods and QEMSCAN®, in order to reach a high level of accuracy. Here below a list of the main limitations:

1) QEMSCAN® is not able to discriminate between minerals with similar spectra (i.e. smithsonite/hydrozincite/zincite, hemimorphite/willemite). This is because the 1000 counts per spectra (used in QEMSCAN® routine analyses) are inadequate to distinguish between minerals, which differ only by their light element content (Rollinson et al., 2011). Moreover, the X-ray detection signals for C and O occurring in their crystal structure is limited, which is an issue regarding the only way to discriminate between the above quoted minerals by their different concentrations of hydroxide (OH) and carbonate (CO_2). To solve this issue, it is necessary to carry out quick SEM-EDS validation analyses, in order to detect the possible occurence of smithsonite+hydrozincite or hemimorphite+willemite associations. It can be also worthy to carry out XRPD analyses, in order to detect the presence of these minerals.

2) Another limitation of using QEMSCAN® on lead- bearing nonsulfide deposits is the problem of discriminating between cerussite ($PbCO_3$) and anglesite ($PbSO_4$), because of the X-ray interference of S-Kα and Pb Mα using EDS, which causes an overlap of the Pb and S peaks. Moreover, the detection of C is not reliable due to the carbon coating of the samples, and the typical weak response of C at 1000 counts. Hence, again, the only way to solve the C issue is to run SEM-EDS or XRPD analyses to resolve this uncertainty. In the case of Hakkari and Reef Ridge deposits, anglesite was not detected by traditional methods (Santoro et al., 2013). In the Jabali case, instead, anglesite was locally detected by Mondillo et al. (2011, 2014). Anyway, this mineral being very rare, the overall accuracy of the QEMSCAN®-QPA results was not affected. However, it is clear that the QEMSCAN® method cannot be used to obtain an accurate characterization of a deposit containing high amounts of cerussite and anglesite.

3) Another possible negative issue could be the misidentification of minerals: the mineral phases characterized by large chemical variability and/or smaller than the beam size excitation volume (i.e. clays), or also smaller than the used resolution

(which in the routine analyses is 10μm), may produce mixed X-ray spectra (Chapman, 1986). In fact, their detection and quantification remains a challenge. In the case of Hakkari a low amount of sauconite, which had been detected by SEM-EDS (Santoro et al., 2013) was identified in a few samples. Though not excluding a possible occurrence of this Zn-smectite, it is also likely that the Hakkari "sauconite" may correspond instead to a mixed blend of kaolinite with tiny grains of smithsonite and/or hemimorphite. Again, for the Hakkari deposit, a high amount of jarosite was detected by QEMSCAN®. Since no jarosite was detected previously, new SEM-EDS validation analyses were carried out and revealed the occurrence of minerals having mixed composition between pyrite/jarosite and Fe-hydr(oxides). Moreover, the first QEMSCAN® analyses showed the occurrence of ankerite and Zn-ankerite, that was in reality dolomite mixed with Fe-dolomite and Zn-dolomite. Similar problems were also encountered in the Jabali deposit: kaolinite at Jabali is finely intergrown with sauconite (Zn-smectite), and as such it was impossible to distinguish between the two. Also the identification of sauconite, instead of a rough smithsonite-kaolinite mixture, was challenging, because of the fine size of these clay mineral particles. Other examples of this type of problem in the Jabali ore was the QEMSCAN® detection of Cd-sphalerite (which was found to be greenockite at the border and within sphalerite specks), Pb-acanthite (under SEM-EDS galena specks were revealed in acanthite), and Ag-smithsonite (small patches of acanthite occurring in smithsonite revealed by SEM-EDS analyses). At Reef Ridge QEMSCAN® detected some ankerite and Zn-ankerite: the SEM-EDS analyses revealed that no Zn-ankerite was present, because "ankerite" was in reality Fe-dolomite and the "Zn-ankerite" was dolomite mixed with Fe-dolomite and Zn-dolomite. All these doubtful cases may be technically resolved by increasing the X-ray resolution from 10 to 5 μm or less. However, the very low amount of the above mentioned phases and hence their negligible importance in a feasibility study, means that the higher cost of more accurate analyses is likely prohibitive, as higher resolution is generally considered uneconomic for most industry projects. In my case the best option was to corroborate these data, solely for a scientific purpose, with a scanning electron microscope.

The main conclusion of this study is that the characterization of nonsulfide Zn-deposit, and especially their quantitative evaluation (QPA) may be quite tricky because of the difficult mineralogy. The worst case is when abundant clay minerals are part of the ore paragenesis. However, a good characterization of this type of ores is important as most metallurgical problems can be mitigated by a better identification of the mineralogical association of metallic and nonmetallic minerals. Therefore, for a good feasibility study it is necessary to take into account both the mineralogical and chemical properties of the ores and their gangue minerals. QEMSCAN® is an useful tool for ore characterization of not particularly complex nonsulfides, because it allows to get improved details of the textural characterization, adding significant information on the major and trace mineral

distribution and a good quantitative evaluation of the isomorphic phases that typically characterize many minerals occurring in this type of deposit. Even though all these positive aspects, it is important to remark that QEMSCAN® data cannot be always used alone, because of some ambiguity in minerals identification. Careful sample preparation and the combined use of complementary mineralogical techniques are therefore necessary to obtain accurate results.

ACKNOWLEDGEMENTS

First of a long list is Richard Herrington, Chief of the Earth Science Department at the Natural History Museum (NHM) in London, who has been always there when I needed help, and above all for his "English kindness" and his "Italian warmth". A big thank goes also to John Spratt, William Brownscombe and to the whole staff of the Earth Science Department at NHM, that have been of great help both in scientific matters and not (including my thumb accident!!). Thanks, I always went back to Italy "full of wonder" as we say here.

Many thanks are due also to the staff of the Camborne School of Mines (CSM), where I worked scientifically for six months. In particular, I would like to thank Frances Wall and Charlie Moon for having allowed me to the classes of the Master course in Economic Geology and to several field activities in beautiful Cornwall.

I also would like to thank Doyon Ltd. in the person of John Woodman and his wife Priscilla, for having hosted me in "the middle of nowhere" when I went to Alaska. Big part of this work was only possible because of their support. Thanks are also due to Alan Clegg, who during his time at Red Crescent Resources provided financial support for the study on the Hakkari deposit.

I cannot forget the SEG (Society of Economic Geology) organization, particularly Christine Horrigan: her support to all students was invaluable. Whithout her help, it would have been impossible for me to have access to many people in the field of Economic Geology.

Last but not least, I thank Thilo Bechstädt, and Susanne Paradis for having shared their geological knowledge with me. Their company has made unforgettable the 7-8 hours/day in the car during the Namibia fieldtrip.

A special thank goes to all people who have been at my side during these years. The family: my mother and father, who supported me in all these years (maybe too many), emotionally and financially, my sister and the two diamonds of the family who are giving a lot of happiness to my life: Chiara and the new entry, Ginevra. A big thank to all my friends and collegues for the light-heartedness of the days and evenings spent together (unfortunately always too few!!).

Finally, I wish to remember a special person, the one who has been most at my side, giving me courage in the discouragement periods and helping me in those of indecision and doubt. Thank you Domi, for having always been at my side everyday even when I was very far from you. Thanks for having supported me, for having always believed in my possibilities and for having been always proud of me, been happy for me and with me for my small "successes". Simply thank you from my heart.

RINGRAZIAMENTI

Desidero ricordare tutti coloro che mi hanno sostenuto ed aiutato durante questi tre anni di dottorato e durante la stesura della tesi con suggerimenti, critiche ed interessanti osservazioni.

In primis, desidero ringraziare il mio supervisor di dottorato, la Prof.ssa Maria Boni, per avermi dato la possibilità di entrare a far parte di un magnifico e produttivo team di ricerca. La ringrazio per avermi supportato e "sopportato" in questi cinque anni di collaborazione che hanno portato al compimento di due tesi (Master e Dottorato) e alla pubblicazione di numerosi articoli scientifici su riviste internazionali. Il suo sostegno, la sua pazienza e perizia sono stati indispensabili durante l'intera fase di stesura, correzione e conclusione della tesi. La ringrazio inoltre di avermi introdotto nel mondo dei Giacimenti Minerari, consentendomi così di fare esperienze che la maggior parte delle persone definirebbe "fuori del comune". Il suo supporto è stato essenziale da un punto di vista scientifico, lavorativo e ancor più importante, umano.

Un ringraziamento speciale va inoltre a due guide, due "guru" per me in questi tre anni, ai quali ho sempre guardato con rispetto e ammirazione, e da cui ho cercato di apprendere gli strumenti necessari per andare avanti cercando di "arrubbà o' mestiere". Ringrazio quindi Giuseppina Balassone e Nicola Mondillo per la loro collaborazione ed il valido aiuto in questioni di natura scientifico-tecnica fornitomi in questi anni. Vanno qui menzionati inoltre i membri dello staff della sezione di Mineralogia dell'Università di Napoli: Roberto de'Gennaro per l'aiuto con le analisi SEM-EDS, Piergiulio Cappelletti, Vincenzo Morra, e Luigi Franciosi, per avermi autorizzato a lavorare all'interno del loro laboratorio per la preparazione dei campioni.

Proseguo ringraziando i reviewers di questa tesi: Gavyn Rollinson (Camborne School of Mines, Università di Exeter) e Michael Joachimski (GeoZentrum Nordbayern, University of Erlangen-Nuremberg). Le loro correzioni e suggerimenti hanno contribuito a migliorare la valenza scientifica del lavoro e la qualità dell'intero manoscritto.

Vorrei, inoltre ringraziare tutte le persone che ho incontrato e con cui ho interagito (direttamente ed indirettamente) in questi tre anni. Il loro supporto o anche la loro sola presenza hanno contribuito ad arricchire significativamenteil mio bagaglio culturale.

Il primo di una lunga lista è Richard Herrington, direttore della Sezione di Scienze della Terra del Natural History Museum (NHM) a Londra, per la sua disponibilità nell'accogliermi nei laboratori del NHM ogni qualvolta ne avevo bisogno e soprattutto per la sua "cortesia anglosassone" e il suo "calore italiano". Ringrazio John Spratt, William Brownscombe, e tutto lo staff del Dipartimento di Scienze della Terra del NHM, che mi è stato di aiuto in questioni scientifiche e non (incidenti a pollici compresi!!). Grazie: non ricordo una volta in cui non sia ritornata in Italia "carica di meraviglia". Ringrazio inoltre lo staff della Camborne School of Mines (CSM), che mi ha ospitato per sei mesi. In particolar modo ringrazio Frances Wall (mia referente alla CSM), e Charlie Moon per avermi permesso di partecipare ai corsi di Master in Economic Geology e alle numerose escursioni previste durante in corso.

Ringrazio infinitamente la Doyon Ltd., nella persona di John Woodman e la sua consorte Priscilla, per la loro disponibilità nell'accogliermi nel "middle of nowhere" dell'Alaska. Gran parte di questo lavoro di tesi è stato possibile grazie a loro. Ringrazio anche Alan Clegg che durante la sua direzione alla Red Crescent Resources ha contribuito finanziariamente allo studio di Hakkari.

I miei ringraziamenti vanno anche all'intera organizzazione della SEG (Society of Economic Geology), ed in particolar modo a Christine Horrigan, per la sua disponibilità e per il supporto che fornisce a tutti gli studenti. Senza il suo contributo non sarebbe stato possibile capire che cosa realmente s'intenda con il termine "ECONOMIC GEOLOGY" e che cosa questa scienza comprenda.

Ringrazio inoltre Thilo Bechstädt e Susanne Paradis per avere condiviso con me le loro conoscenze sulla base dei loro anni di esperienza geologica, rendendo indimenticabili le 7-8 ore di macchina al giorno durante il viaggio in Namibia.

Infine desidero ringraziare tutte quelle persone che mi sono state vicino, anche se al di fuori dell'ambiente accademico. La famiglia, innanzitutto: mia madre "Cara Matra" e mio padre, che mi hanno sostenuto in questi anni, emotivamente e finanziariamente; mia sorella, e i due diamanti della famiglia: le piccole Chiara e Ginevra. Il solo guardarvi mi dona pace e serenità. Un grazie enorme anche ai miei amici universitari, e colleghi di dottorato per la spensieratezza donatami nelle giornate e serate passate insieme (purtroppo sempre troppo poche!!). In particolar modo voglio ricordare la "salsera" Marianna, "Benjamin Button" Alessandro e l'ormai "crucco" Pierluigi. Grazie anche a chi ha speso tutti i suoi risparmi per accompagnarmi in Sud-Africa (Melman e Alex), il vostro remake di "Robin Hood e Little John" ormai è un evergreen nelle mie visualizzazioni video.

Infine vorrei ringraziare particolarmente una persona, colui che più di tutti mi è stato vicino in questi anni, infondendomi coraggio nei momenti di sconforto e rimproverandomi in quelli di incertezza, perplessità e dubbi. Grazie Domi, per essermi sempre stato accanto tutti i giorni, nonostante i (e soprattutto nei) lunghi periodi di lontananza, per avermi sostenuto, per aver sempre creduto nelle mie possibilità e per essere sempre stato orgoglioso di me, gioendo per me e con me per i miei piccoli "successi". Semplicemente grazie di cuore.

References

Abdel-Aal, E.A., 2000. Kinetics of sulfuric acid leaching of low-grade zinc silicate ore. Hydrometallurgy, 55(3), 247-254.

Ahlbrandt, T.S., 2002. Madbi Amran/Qishn Total Petroleum System of the Ma'Rib-Al Jawf-Shabwah, and Masila-Jeza Basins, Yemen. USGS Bulletin, 2202-G, 1–28.

Alaska Climate Research Centre: <http://akclimate.org/Climate/Fairbanks> (accessed October 2014).

Al Ganad, I., 1991. Etude géologique du gisement Zn-Pb-Ag de Jabali (Bordure sud du bassin du Wadi al Jawf). Unpublished Doctoral thesis, Université Orleans, France, 180 p.

Al Ganad, I., 1992. Possibility of important Zn-Pb mineralization in sedimentary formations in Yemen: in Minerals Exploration Board, 1992, documental file on Open House Presentations May 3 to 7, 1992, Mineral exploration board report, Sana'a, Republic of Yemen, 63 p.

Al Ganad, I., Lagny, Ph., Lescuyer, J.L., Rambo, C., and Touray, J.C., 1994. Jabali, a Zn-Pb-(Ag) carbonate-hosted deposit associated with Late Jurassic rifting in Yemen. Mineralium Deposita, 29, 44–56.

Alexander Mining Plc: <http://www.alexandermining.com> (accessed 10/1/2015).

Allen, C.R., 2000. Jabali ZnOx Deposit, Yemen. Unpublished report, Cominco American.

Allen, M.B., and Armstrong, H.A., 2008. Arabia–Eurasia collision and the forcing of mid- Cenozoic global cooling. Palaeogeography, Palaeoclimatology Palaeoecology, 265, 52–58.

Altiner, D., 1989. An example for the tectonic evolution of the Arabian Platform margin (SE Anatolia) during the Mesozoic and some criticisms of the prviously suggested models, *in:* Sengör, A. M. C., Tectonic evolution of Tethyan regions. Dordrecht, Netherlands, Kluwer Academic Publishing, 117-129.

Amato, J., Toro, J., Miller, E., Gehrels, G.E., Farmer, G.L., Gottlieb, E.S., and Till, A.B., 2009. Late Proterozoic-Paleozoic evolution of the Arctic Alaska-Chukotka terrane based on U-Pb igneous and detrital zircon ages: implications for Neoproterozoic paleogeographic reconstructions. Geological Society of America Bulletin, 121, 1219-1235.

Anderson, L., Abbott, M.B., Finney, B.P., and Burns, S.J., 2005. Regional atmospheric circulation change in the North Pacific during the Holocene inferred from lacustrine carbonate oxygen isotopes, Yukon Territory, Canada. Quaternary Research, 64, 21–35.

Anderson, K.F.E., Wall, F., Rollinson, G.K., and Moon, C.J., 2014. Quantitative mineralogical and chemical assessment of the Nkout iron ore deposit, Southern Cameroon. Ore Geology Reviews, 62, 25-39.

Andersen, J.C.Ø., Rollinson, G.K., Snook, B., Herrington, R., and Fairhurst, R., 2009. Use of QEMSCAN® for the characterization of Ni-rich and Ni-poor goethite in laterite ores. Minerals Engineering, 22, 1119–1129.

Andrews, T., and Rishel, J., 1982, Annual Report for 1981, Reef Ridge I-to-XIII Project Areas, Kuskokwim Block, Alaska: Anchorage, Alaska, WGM Inc., Project Report 4, 45 p., 2 sheets, scales 1:63,360 and 1:20,000. (Report held by Doyon, Limited, Fairbanks, Alaska).

As-Saruri, M.L., 1999. Lithostratigraphie der Tertiär-Sedimente der Republik Jemen. Schriftenreihe für Geologische Wissenschaften. 10, p. 131.

As-Saruri, M.A., Sorkhabi, R., and Baraba, R., 2010. Sedimentary basins of Yemen: their tectonic development and lithostratigraphic cover. Arabian Journal of Geosciences, 3, 515–527.

Ayling, B., Rose, P., Petty, S., Zemach, E., and Drakos, P., 2012. QEMSCAN® (Quantitative Evaluation of Minerals by Scanning Electron Microscopy): capability and application to fracture characterization in geothermal systems. Thirty-Seventh Workshop on Geothermal Reservoir Engineering Stanford University, Stanford, California, January 30.

Ayuso, R.A., Kelley, K.D., Leach, D.L., Young, L.E., Slack, J.F., Wandless, G., Lyon, A.M., and Dillingham, J.L., 2004. Origin of the Red Dog Zn-Pb-Ag deposits, Brooks Range, Alaska: Evidence from regional Pb and Sr isotope sources. ECONOMIC GEOLOGY, 99, 1533–1554.

Balassone, G., Rossi, M., Boni, M., Stanley, G., and McDermott, P., 2008. Mineralogical and geochemical characterization of nonsulfide Zn-Pb mineralization at Silvermines and Galmoy (Irish Midlands). Ore Geology Reviews, 33, 168-186.

Ballester, A., Blazquez, M.L., and Gonzalez, F., 1989. Microstructural aspects of PbS/Cu_2S matte bioleaching. Canadian Metallurgical Quarterly, 28(4), 361-365.

Barbieri, R., Benjamini, C., Monechi, S., and Reale, V., 2003. Stratigraphy and benthic foraminiferal events across the Middle–Late Eocene transition in the Western Negev, Israel, *in*: Prothero, D.R., Ivany, L.C., Nesbitt, E.A. (Eds.), From Greenhouse to

Icehouse: The Marine Eocene–Oligocene Transition. Columbia University Press, New York, 453–471.

Battaglia-Brunet, F., d´Hugues, P., Cabral, T., Cezac, P., García, J.L., and Morin, D. 1998. The mutual effect of mixed Thiobacilli and Leptospirilli populations on pyrite bioleaching. Mineral Engineering, 11, 195-205.

Bazard, D.R., Butler, R.F., Gehrels, G.E., and Soja, C.M., 1995. Early Devonian paleomagnetic data from the Lower Devonian Karheen Formation suggest Laurentia-Baltica connection for the Alexander terrane. Geology, 23, 707-710.

Bektas, O., Sen, C., Atici, Y., and Köprübasi, N., 1999. Migration of the Upper Cretaceous subduction-related volcanism toward the back-arc basin of the Eastern Pontide magmatic arc (NE Turkey). Geological Journal, 34, 95-106.

Beranek, L.P., van Staal, C., Gordee, S.M., McClelland, W.C., Israel, S., and Mihalynuk, M., 2013a. Baltican crustal provenance for Cambrian-Ordovician sandstones of the Alexander terrane, North American Cordillera: evidence from detrital zircon U-Pb geochronology and Hf isotope geochemistry. Journal of the Geological Society of London, 170, 7-18.

Beranek, L.P., van Staal, C., Gordee, S.M., McClelland, W.C., Israel, S., and Mihalynuk, M., 2013b. Detrital zircon Hf isotopic compositions indicate a northern Caledonian connection for the Alexander terrane. Litosphere, 5, 163-168.

Beydoun, Z.R., 1997. Introduction to the revised Mesozoic stratigraphy and nomenclature for Yemen. Marine and Petroleum Geology, 14, 617–629.

Beydoun, Z.R., As-Saruri, M.L., El-Nakhal, H., Al-Ganad, I.N., Baraba, R.S., Nani, A.S.O., and Al-Aawah, M.H., 1998. International lexicon of stratigraphy, Volume III, Republic of Yemen, Second Edition: International Union of Geological Sciences and Ministry of Oil and Mineral Resources, Republic of Yemen Publication n. 34, p. 245.

Bish, D.L., and Howard, S.A., 1988. Quantitative phase analysis using the Rietveld method. Journal of Applied Crystallography, 21, 86-91.

Bish D.L., and Post J.E., 1993. Quantitative mineralogical analysis using the Rietveld fullpattern fitting method. American Mineralogist, 78, 932-940.

Bladh, K.W., 1982. The formation of goethite, jarosite, and alunite during the weathering of sulfide-bearing felsic rocks. ECONOMIC GEOLOGY, 77, 176–184.

Blodgett, R.B., Rohr, D.M., and Boucot, A.J., 2002. Paleozoic links among some Alaskan accreted terranes and Siberia based on megafossils. Geological Society of America, Special Paper 360, 273-290.

Bodas, M.G., 1996. Hydrometallurgical treatment of zinc silicate ore from Thailand. Hydrometallurgy, 40 (1-2), 37-49.

Bol, A.J., Coe, R.S., Grommè, C.S., and Hillhouse, J.W., 1992. Paleomagnetism of the Resurrection Peninsula, Alaska: implications for the tectonics of southern Alaska and the Kula Farallon ridge. Journal of Geophysical Research, 97, 17213-17232.

Boland, M.B., Clifford, J.A., Meldrum, A.H., and Poustie, A., 1992. Residual base metal and barite mineralization at Silvermines, County Tipperary, Ireland, *in:* Bowden, A.A., Earls, G., O'Connor, P.G., and Pyne, J.F., eds., The Irish minerals industry 1980–1990: Dublin, Ireland. Irish Association for Economic Geology, 247–260.

Boni, M., Balassone, G., and Iannace, A., 1996. Base metal ores in the lower Paleozoic of southwestern Sardinia, *in:* Sangster, D.F., ed., Carbonate-hosted lead-zinc deposits. Society of Economic Geologists Special Publication 4, 18–28.

Boni, M., Gilg, H.A., Aversa, G., and Balassone, G., 2003. The "Calamine" of SW Sardinia (Italy): geology, mineralogy and stable isotope geochemistry of a supergene Zn-mineralization. ECONOMIC GEOLOGY, 98, 731–748.

Boni, M., and Large, D., 2003. Non-sulfide Zinc mineralization in Europe: an overview. ECONOMIC GEOLOGY, 98, 715–729.

Boni, M., 2005. The geology and mineralogy of nonsulfide zinc ore deposits. LEAD and ZINC '05, Kyoto, Japan, 17–19 October 2005, Proceedings, 1299–1314.

Boni, M., Gilg, H.A., Balassone, G., Schneider, J., Allen, C.R., and Moore, F., 2007. Hypogene Zn carbonate ores in the Angouran deposit, NW Iran. Mineralium Deposita 42, 799–820.

Boni, M., Balassone, G., Arseneau, V., and Schmidt, P., 2009. The Nonsulfide Zinc Deposit at Accha (Southern Peru): Geological and Mineralogical Characterization: ECONOMIC GEOLOGY, 104, 267-289.

Boni, M., Mondillo, N., and Balassone, G., 2011. Zincian dolomite: a peculiar dedolomitization case? Geology, 39, 183–186.

Boni, M., Rollinson, G., Mondillo, G., Balassone, G., and Santoro L., 2013. Quantitative mineralogical characterization of karst bauxite deposits in the Southern Apennines, Italy. ECONOMIC GEOLOGY, 108, 813–833.

Boni M., and Mondillo N., 2015. The "Calamines" and the "Others": the great family of supergene nonsulfide zinc ores. Review paper. Ore Geology Reviews, 67, 208-233.

Boon, M., and Heijnen, J.J. 1998. Chemical oxidation kinetics of pyrite in bioleaching processes. Hydrometallurgy, 48, 27-41.

Borchardt, G., 1989. Smectites *in:* Dixon, J.B., and Weed, S.B., eds., Minerals in Soil Environments: Soil Science Society of America Journal Special Publication, 1, 675–727.

Borg, G., Kärner, K., Buxton, M., Armstrong, R., and van der Merwe, S.W., 2003. Geology of the Skorpion supergene Zn deposit, southern Namibia. ECONOMIC GEOLOGY, 98, 749–771.

Botha, P.W.S.K., Butcher, A.R, Horsch, H.E., Rickman, D., Wentworth, S.J., Schrader, C.M., Stoeser, D., Benedictus, A., Gottlieb, P., and McKay, D., 2008. Ultrafast Phase Mapping of Thin-Sections from An Apollo 16 Drive Tube – a New Visualization of Lunar Regolith. GSA 2008 Joint Annual Meeting, 5-9 October 2008, Houston, Texas, Abstract 345-3.

Bowring, S.A., and Podosek, F.A., 1989. Nd isotopic evidence for 2.0-2.4 Ga crust in western North America. Earth Planet Science Letter, 94, 217-230.

Box, S., 1985. Early Cretaceous orogenic belt in northwestern Alaska: Internal organization, lateral extent, and tectonic interpretation. Circum-Pacific Council for Energy and mineral Resources, Earth Sciences Series, 1, 137-145.

Box, S.E., Moll-Stalcup, E.J., Wooden, J.L., and Bradshaw, J.Y., 1990. Kilbuck Terrane: Oldest rocks in Alaska. Geology, 18, 1219-1222.

Box, S.E., 1985. Terrane analysis of the northern Bristol Bay region, southwestern Alaska, *in:* Bartsch-Winkler, S., (Ed.), The U.S. Geological Survey in Alaska—Accomplishments during 1984: U.S. Geological Survey Circular 967, 32-37.

Box, S.E., Moll-Stalcup, E.J., Wooden, J.L., and Bradshaw, J.Y., 1990. Kilbuck Terrane: Oldest rocks in Alaska. Geology, v.18, 1219-1222.

Boyle, D.R., 1994. Oxidation of massive sulfide deposits in the Bathurst mining camp, New Brunswick: Natural analogues for acid drainage in temperate climates: *in:* Alpers, C.N., and Blowes, D.W., eds., Environmental geochemistry of sulfide oxidation. American Chemical Society Symposium Series 550, 535–550.

Boztuğ, D., Kuşçu, İ., Erçin, A.İ., and Avcı, N., 2003. Mineral deposits associated with the pre-, syn- and post-collisional granitoids of the Neo-Tethyan convergence system between the Eurasian and Anatolian plates in NE and Central Turkey, *in:* Eliopoulos, D., et al. (Eds.), Mineral Exploration and Sustainable Development. Millpress, Rotterdam, 1141–1144.

Bradley, D.C., Dumoulin, J., Layer, P., Sunderlin, D., Roeske, S., McClelland, W., Harris, A.G., Abbott, G., Bundtzen, T., and Kusky, T., 2003. Late Paleozoic orogeny in Alaska's Farewell terrane. Tectonophysics, 372, 23-40.

Bradley, D.C., Miller, M.L., McClelland, W.C., Dumoulin. J.A., Friedman, R., and O'Sullivan, P., 2007. Links between Alaska's Kilbuck, Farewell and Arctic Alaska terranes and the Siberian and Laurentian cratons. Norsk Geologisk Forening, International Conference on Arctic Margins (ICAMV), TromsØ, Norway, p. 230.

Brannan, J., Gerdes, K.D., and Newth, I.R., 1997. Tectono-stratigraphic development of the Qamar basin, Eastern Yemen. Marine and Petroleum Geology, 14, 701–730.

Brugger, J., McPhail, D.C., Wallace, M., Waters, J., 2003. Formation of willemite in hydrothermal environments. ECONOMIC GEOLOGY 98, 819–835.

Bruch, A.A., and Zhilin, S.G., 2006. Early Miocene climate of Central Eurasia - evidence from Aquitanian floras of Kazakhstan. Palaeogeography, Palaeoclimatology, Palaeoecology, 248, 32–48.

Bundtzen, T.K., Kline, J.T., Smith, T.E., and Albanese, M.D., 1988. Geology of the McGrath A-2 quadrangle, Alaska: Alaska Division of Geological and Geophysical Surveys Professional Report, 91, p. 20.

Bundtzen, T.K., Swainbank, R.C., Clough, A.H., Henning, M.W., and Hansen, E.W., 1994. Alaska's mineral industry 1993: Alaska Division of Geological and Geophysical Surveys Special Report 48, p. 84.

Bundtzen, T.K., and Miller, M.L., 1997. Precious metals associated with Late Cretaceous - Early Tertiary igneous rocks of southwestern Alaska. ECONOMIC GEOLOGY Monograph 9, 242-286.

Bush, A.B.G., 1997. Numerical simulation of the Cretaceous Tethys circumglobal current. Science, 275, 807–810.

Butcher, A.R., and Botha, P.W.S.K., 2010. Automated mineralogy derives key characteristics directly from reservoir rock. The American Oil & Gas Reporter, January 2010, p. 4.

Cady, W.M., Wallace, R.E., Hoare, J.M., and Webber, E.J., 1955. The Central Kuskokwim Region, Alaska. USGS Professional Paper 268, p. 129.

Çamur, M. Z., Guven, I. H., and Er, M., 1996. Geochemical characteristics of the eastern Pontides volcanics, Turkey: an example of multiple volcanic cycles in the arc evolution. Turkish Journal of Earth Sciences, 5, 123-144.

Capaldi, G., Chiesa, S., Manetti, P., and Piccardo, G.B., 1983. Preliminary investigations on volcanism of the Sadah region (Yemen Arab Republic). Bulletin of Volcanology, 46, 413–427.

Cawood, P.A., Kroner, A., Collins, W.J., Kusky, T.M., Mooney, W.D., and Windley, B.F., 2009. Accretionary orogens through Earth history. Geological Society of London, Special Pubblication 318, 1-36.

Chapman, S.K., 1986. Working with a scanning electron microscope. Lodgemark Press Ltd., Orpington (Kent), p. 113.

Charland, A., Kormos, L., Whittaker, P., Arrue-Canales, C., Fragomeni, D., Lotter, N., Mackey, P., and Anes, J., 2006. A Case Study for integrated use of automated mineralogy in plant optimization: the Falconbridge Montcalm Concentrator, Automated Mineralogy Conference, Brisbane, 17-18 July.

Chávez, W.X., 2000. Supergene oxidation of copper deposits: Zoning and distribution of copper oxide minerals. Society of Economic Geologists Newsletter 41(1), 10–21.

Christmann, P., Lagny, P., Lescuyer, J.L., and Sharaf Ad Din, A., 1989. Discovery of the Jabali deposit (Zn-Pb-Ag) in the Jurassic cover of the Yemen Arab Republic. Chronique de la Recherche Miniere, special issue, 43–52.

Ceyhan, N., 2003. Lead isotope geochemistry of Pb-Zn deposits from Eastern Taurides, Turkey. Unpub. MSc Dissertation. Graduate School of Natural and Applied Sciences of the Middle East Technical University, Ankara (Turkey), p. 105.

Clautice, K.H., Bowman, N.D., Clough, J.G., Gilbert, W.G., Kline, J.T., Smith, T.E., and Blodgett, R.B., 1993. Land selection Unit 8 (Kantishna River, Ruby, and Medfra quadrangles); References, lead isotope, geochemical and major oxide data: Alaska Division of Geological and Geophysical Surveys, 42 p., 1 sheet, scale 1:250,000.

Clay, J.E., and Schoonraad, G.P., 1976. Treatment of zinc silicates by Waelz Process. Journal of the South African Institute of Mining and Metallurgy, 77(1), 11-14.

Clegg, A., Grodner, M., and Johnstone, G., 2014. Economic exploitation of non-sulphide zinc deposits in Turkey, *in:* International Mineralogical Association Meeting 2014, Johannesburg, Abstract, p. 1.

Clifford, J.A., Ryan, P., and Kucha, H., 1986. A review of the geological setting of the Tynagh orebody, Co. Galway, *in*: Andrew, C.J., Crowe, R.W.A., Finlay, S., Pennell, W.M., and Pyne, J.F., eds., Geology and genesis of mineral deposits in Ireland: Dublin, Irish Association for Economic Geology, 419–439.

Cole, P.M., and Sole, K.C., 2002. Solvent extraction in the primary and secondary processing of zinc. Journal of the South African Institute of Mining and Metallurgy 102, 451-456.

Colpron, M., Nelson, J.L., and Murphy, D.C., 2006. A tectonostratigraphic framework for the pericratonic terranes of the northern Canadian Cordillera. Geological Association of Canada, Special Paper 45, 1-23.

Colpron, M., Nelson, J.L., and Murphy, D.C., 2007a. Northern Cordilleran terranes and their interactions through time. GSA Today, 17 (4/5), 4-10.

Colpron, M., Nelson, J.L., and Israel, S., 2007b. A transect through the accreted terranes

of the northern Canadian Cordillera from Cassiar, British Columbia to Kluane Lake, Yukon: Yukon Geological Survey, Open File 2007-3, p. 84.

Colpron, M., and Nelson, J.L., 2009. A Paleozoic Northwest Passage: incursion of Caledonian, Baltican, and Siberian terranes into eastern Panthalassa, and the early evolution of the North American Cordillera. Geological Society of London, Special Publication 318, 273-307.

Colpron, M., and Nelson, J.L., 2011. A digital atlas of terranes for the northern Cordillera: Yukon Geological Survey, www.geology.gov.yk.ca/bedrock_terrane.html, accessed December 2012; also BC Geological Survey, BC GeoFile 2011-11 (accessed 10/01/2015),
<http://www.empr.gov.bc.ca/Mining/Geoscience/PublicationsCatalogue/GeoFiles/Pages/2011-11.asp>

Coney, P.J., Jones, D.L., and Monger, J.W.H., 1980. Cordilleran suspect terranes. Nature, 288, 329-333.

Coppola, V., Boni, M., Gilg, H.A., and Strzelska-Smakowska, B., 2009. Nonsulfide zinc deposits in the Silesia-Cracow district, southern Poland. Mineralium Deposita, 44, 559-580.

Corrans, R.D., Gewald, H., Whyte, R.M., and Land, B.N., 1993. The Skorpion SZ secondary zinc deposit, southwestern Namibia [abs.]: Mining Investment in Namibia Conference, Windhoek, Namibia Department of Mining and Energy, 46–52.

Csato, I., Habib, A., Kiss, K., Kocz, I., Kovacs, Z., Lorincz, K., and Milota, K., 2001. Play concepts of oil exploration in Yemen. Oil and Gas Journal, 99, 68–74.

Decker, J., Bergman, S.C., Blodgett, R.B., Box, S.E., Bundtzen, T.K., Clough, J.G., Conrad, W.I., Gilbert, W.G., Miller, M.I., Murphy, J.M., Robinson, M.S., and Wallace, W.K., 1994. Geology of southwestern Alaska, *in:* Plafker, G. (Ed.), The geology of Alaska: Boulder, Colorado, Geological Society of America, Geology of North America, G-1, 285-310.

de Wet, J.R., and Singleton, J.D., 2008. Development of a viable process for the recovery of zinc from oxide ores. The Journal of the Southern African Institute of Mining and Metallurgy, 108, 253-259.

Díaz, J., Cisterna, C., Riquelme, R., and Boric, R., 2009. Validation by means of QEMSCAN® technique of mineralogical mapping used as a base for the bioleaching model in the Radomiro Tomic (RT) copper sulfide mine, CODELCO Chile División Norte, Chile, p. 10.

Diehl, S.F., Hofstra, A.H., Koenig, A.E., Emsbo, P., Christiansen, W., and Johnson, C., 2010. Hydrothermal zebra dolomite in the Great Basin, Nevada - attributes and relation to Paleozoic stratigraphy, tectonics, and ore deposits. Geosphere, 6, 663–690.

Diekmann, B., Kuhn, G., Gersonde, R., and Mackensen, A., 2004. Middle Eocene to early Miocene environmental changes in the sub-Antarctic Southern Ocean: evidence from biogenic and terrigenous depositional patterns at ODP Site 1090. Global and Planetary Change, 40, 295–313.

Dobson, D-C., 1979. Report on the Mo and Udall claims: Anchorage, Alaska, Anaconda Co., Unpublished report, p. 18.

Dove, P.M., and Rimstidt, J.D., 1994. Silica–water interactions. *in*: Heaney, P.J., Prewitt, C.T., Gibbs, G.V. eds., Silica, Physical Behavior, Geochemistry and Materials Applications. Reviews in Mineralogy, 29, 259 308.

Dufresne, R.E., 1976. Quick leach of siliceous zinc ores. Journal of Metals, 28, 8-12.

Dumoulin, J.A., Harris, A.G., Gagiev, M., Bradley, D.C., and Repetski, J.E., 2002. Lithostratigraphic, conodont, and other faunal links between Lower Paleozoic strata in northern and central Alaska and northeastern Russia, *in:* Miller, E.L., et al., (Eds.), Tectonic Evolution of the Bering Shelf–Chuckchi Sea–Arctic Margin and Adjacent Landmasses. Geological Society of America Special Paper 360, 291–312.

Duttweiler, K.A., 1987. Use of factor analysis in locating base metal mineralization in the Killik River quarangle, Alaska: U.S. Geological Survey Circular 998, p. 27-30.

Dusel-Bacon, C., Hopkins, M.J., Mortensen, J.K., Williams, I., Heslop, K., Dashevsky, S.S., Bressler, J.R., and Day, W.C., 2006. Paleozoic tectonic and metallogenetic evolution of the Yukon-Tanana terrane, east-central Alaska. Geological Association of Canada, Special Paper 45, 25-74.

Dutro, J.T. Jr., and Patton, W.W. Jr., 1982. New Paleozoic formations in the northern Kuskokwim Mountains, west-central Alaska: U.S. Geological Survey Bulletin 1529-H, H13-H22.

Dzombak, D.A., and Morel, F.M.M., 1990. Surface Complexation Modeling: Hydrous Ferric Oxide, 1st Edition, John Wiley & Sons Ed., 393 pp.

Edwards, G.V., and Butcher, A.R., 1999. A new application for QEMSCAN® quantifying the mineralogy of drill cuttings from oil and gas exploration and production wells. CSIRO Report, DMR-1140, p. 97.

Einaudi, M.T., and Hitzman, M.W., 1986. Mineral deposits in northern Alaska: introduction. ECONOMIC GEOLOGY, 81, 1583-1591.

Ellersieck, I.F., Jansons, U., Mayfield, C.F., and Tailleur, I.L., 1982. The Story Creek and Whoopee Creek lead-zinc-silver occurrences, western Brooks Range, Alaska (west of the 141st meridian). U.S. Geological Survey Open-File Report 92-20B, p. 55.

Ellis, A.C., Kerr, H.M., Cornwell, C.P., and Williams, D.O., 1996. A tectono-stratigraphic framework for Yemen and its implications for hydrocarbon potential. Petroleum Geoscience, 2, 29–42.

Fair, E.E., and Bright, T.D., 1989. Reef Ridge Project: Pasminco exploration report, Report 89-23, p. 32 (Report held by Doyon, Ltd., Fairbanks, Alaska.).

Fandrich, R., Gu, Y., Burrows, D., and Moeller, K., 2007. Modern SEM-based mineral liberation analysis. International Journal of Mineral Processing, 84(1-4), 310-320.

Faure, G., 1998. Principles and applications of geochemistry, 2nd edition. Prentice-Hall, New Jersey, 600 pp.

Faust, G.T., 1951. Thermal analysis and X-ray studies of sauconite and of some zinc minerals of the same paragenetic association. The American Mineralogist, 36, 795-822.

Fennel, M., Guevara, J., Canchaya, S., Velarde, G., Baum, W., and Gottlieb, P., 2013. QEMSCAN® mineral analysis for ore characterization and plant support at Cerro Verde. XXVII Convención Minera Arequipa (Perú), p. 11.

Fernald, A.T., 1960. Geomorphology of the Upper Kuskokwim Region, Alaska. U.S. Geological Survey Bulletin 1071G, 191-279.

Flower, B.P., and Kennett, J., 1993. Middle Miocene Ocean-Climate Transition: High-Resolution Oxygen and Carbon Isotopic Records from Deep Sea Drilling Project Site 558A, Southwest Pacific. Paleoceanography 8, 811–843.

Fontaine, J.M., Monod, O., Braud, J., and Perinçek, D., 1989. The Hezan Units: a fragment of the south Neo-Tethyan passive continental margin in SE Turkey. American Journal of Petroleum Geologists, 12 (1), 29-50.

Forrest, K., 1983. Geologic and isotopic studies of the Lik deposit and the surrounding mineral district, Delong Mountains, western Brooks Range, Alaska: Unpublished Ph.D dissertation, Minneapolis, Minnesota, University of Minnesota, 161 pp.

Foster, H.L., Weber, F.R., Forbes, R.B., and Brabb, E.E., 1973. Regional geology of the Yukon-Tanana Upland, Alaska, *in:* Pitcher, M.G., ed., Arctic Geology: American Association of Petroleum geologists, Memoir 19, 388-395.

Fourcade, E., Dercourt, J., Günay, Y., Azéma, J., Kozlu, H., Belier, J. P., Cordey, F., Cros, P., De Wever, P., Enay, R., Hernandez, J., Lauer, J.P., and Vrielynck, B., 1991. Stratigraphie et paleogeographie de la marge septentrionale de la plate-forme arabe au Mésozoique (Turquie du Sud- Est). Bulletin de la Société Géologique de France, 162/1, 27-41.

Frenay, J., 1985. Leaching of oxidized zinc ores in various media. Hydrometallurgy, 15(2), 243-253.

Gabrielse, H., Monger, J.W.H., Wheeler, J.O., and Yorath, C.J., 1991. Part. A. Morphological belts, tectonic assemblages and terranes, *in:* Gabrielse, H., and Yorath, C.J., eds., Chapter 2 of Geology of the Cordillera Orogen in Canada: Geological Survey of Canada, Geology of Canada, v. 4, p. 15-28.

Gallen, S.F., 2008. An investigation into the magnetic fabrics and paleomagnetism of the Ghost Rocks Formation, Kodiak Islands, Alaska: Unpublished M.Sc thesis, Bellingham, Washington, Western Washington University, 119 pp.

Gamble, B.M., and Till, A.B., 1993. Maps showing metallic mineral resources of the Bendeleben and Solomon quadrangles, western Alaska: U.S. Geological Survey Miscellaneous Field Studies Map MF-1838-D, p. 22.

Garavelli, C.G., Vurro, F., and Fioravanti, G.C., 1982. Minrecordite, a new mineral from Tsumeb. Mineralogical Record, 13, 131–136.

Gardner, M.C., Bergman, S.C., MacKevett, E.M.Jr., Plafker, G., Campbell, R.C., Cushing, G.W., Dodds, C.J., and McClelland, W.D., 1988. Middle Pennsylvanian pluton stitching of Wrangellia and Alexander terrane, Wrangell Mountains, Alaska. Geology, 16, 967-971.

Gehrels, G.E., and Saleeby, J.B.,1987. Geology of Southern Prince of Wales Island, southeastern Alaska. Geological Society of America Bulletin, 98, 123-137.

Gehrels, G.E., and Berg, H.C., 1994. Geology of southeastern Alaska, *in:* Plafker, G., and Berg, H.C., eds, The geology of Alaska: Boulder, Colorado, Geological Society of America, Geology of North America, G-1, 451-467.

Gehrels,G.E.,Butler,R.F., and Bazard,D.R.,1996. Detrital zircon geochronology of the Alexander terrane, southeastern Alaska. Geological Society of America Bulletin, 108, 722-734.

Gilg, H.A., Boni, M., Hochleitner, R., and Struck, U., 2008. Stable isotope geochemistry of carbonate minerals in supergene oxidation zones of Zn-Pb deposits. Ore Geology Reviews, 33, 117–133.

Goldfarb, R.J., 1997. Metallogenic evolution of Alaska. ECONOMIC GEOLOGY Monograph 9, 4–34.

Goodall, W.R, Scales, P.J, and Butcher, A.R., 2005. The use of QEMSCAN® and diagnostic leaching in the characterization of visible gold in complex ores. Minerals Engineering, 18(8), 877–886.

Goodall,W.R., and Scales, P.J., 2007. An overview of the advantages and disadvantages of the determination of gold mineralogy by automated mineralogy. Minerals Engineering, 20, 506–517.

Gottlieb, P., Wilkie, G., Sutherland, D., Ho-Tun, E., Suthers, S., Pereira, K., Jenkins, B., Spencer, S., Butcher, A., and Rayner, J., 2000. Using quantitative electron microscopy for process mineralogy applications. Journal of the Minerals, Metals and Materials Society, 52(4), 24-25.

Götze, J., 2012. Application of cathodoluminescence microscopy and spectroscopy in geosciences. Microscopy and Microanalysis, 18, 1270–1284.

Grammatikopoulos, T., Mercer, W., and Gunning, C., 2013. Mineralogical characterisation using QEMSCAN® of the Nechalacho heavy rare earth metal deposit, Northwest Territories, Canada. Canadian Metallurgical Quarterly, 52(3), 265-277.

Grauch, R.I., Eberl, D.D., Butcher, A.R., and Botha, P.W.S.K., 2008. Quantitative mineralogy of fine-grained sedimentary rocks: a preliminary look at QEMSCAN®. Microscopy and Microanalysis, 14(2), 532-533.

Griffith, S.V., 1956. The mineral resources of Burma. Mining Magazine, 95, 9–18.

Grist, B., 2006, Development of Yemen's first large scale base metal mine: 9th Arab Conference for Mineral Resources, Jeddah, Saudi Arabia, extended abstract volume, p. 7.

Grodner, M., 2010. The Hakkari zinc oxide project, Turkey. *in*: IAEG–ZINC 2010 Conference, 17–19 September 2010, Cork (Ireland), 23–26.

Groves, I., and Carman, C.E., 2003. Geology of the Beltana willemite deposit, Flinders Ranges, South Australia. ECONOMIC GEOLOGY, 98, 797–818.

Günay, Y., Şenel, M., 2002. 1:500,000 Turkey Geological Map, Sheet Cizre.

Gunning, M.H., Hodder, R.W.H., and Nelson, J.L., 2006. Contrasting volcanic styles within the Paleozoic Stikine assemblage, western Stikine terrane, northwestern British Columbia. Geological Association of Canada, Special Paper 45, 201-227.

Habashi, F., 2002, A Textbook of Pyrometallurgy. Quebec City, Laval University, 592 pp.

Haberlah, D., Williams, M.A.J., Halverson, G., McTainsh, G.H., Hill, S.M., Hrstka, T., Jaime, P., Butcher, A.R., and Glasby, P., 2010. Loess and floods: High-resolution multi-proxy data of Last Glacial Maximum (LGM) slackwater deposition in the Flinders Ranges, semi-arid South Australia. Quaternary Science Reviews, 29, 2673–2693.

Haberlah, D., Owen, M., Botha, P.W.S.K., and Gottlieb, P., 2011. SEM-EDS based protocol for subsurface drilling mineral identification and petrological classification, *in:* Broekmans, M.A.T.M. ed., Proceedings of the 10th International Congress for Applied Mineralogy (ICAM), 01-05 August 2011, Trondheim, Norway, 265–273.

Hallam, A., 1969. Faunal realms and facies in the Jurassic. Palaeontology, 12, 1–18.
Hardardóttir, V., Hannington, M., Hedenquist, J., Kjarsgaard,I., and Hoal, K., 2010. Cu-Rich scales in the Reykjanes Geothermal System, Iceland. ECONOMIC GEOLOGY, 105, 1143–1155.

Herbert, R.B., 1999. Sulfide oxidation in mine waste deposits, a review with emphasis on dysoxic weathering. Mitigation of the environmental impact from mining waste (MiMi). MiMi Print, Lulea, Sweden, 1, 45 pp.

Heyl, A.V., and Bozion, C.N., 1962. Oxidized zinc deposits of the United States, Part 1. General Geology: US Geological Survey Bulletin 1135-A, 52 pp.

Hill, R.J., 1991. Expanded use of the Rietveld method in studies of phase abundance in multiphase mixtures. Powder Diffraction, 6, 74-77.

Hitzman, M.W., Proffett, J.M., Schmidt, J.M., and Smith, .E., 1986. Geology and mineralization of the Ambler District, northwestern Alaska. ECONOMIC GEOLOGY, 81, 1592-1618.

Hitzman, M.W., Reynolds, N.A., Sangster, D.F., Allen, C.R., and Carman, C.E., 2003. Classification, genesis, and exploration guides for nonsulfide zinc deposits. ECONOMIC GEOLOGY, 98, 685–714.

Housen, B.A., Roeske, S.M., and Gallen, S., 2008. Paleomagnetism of the Paleocene Ghost Rocks, Kodiak Islands, Alaska: implications for Paleocene Pacific Basin/North American plate configurations [abs]: EOS Transactions, American Geophysical Union, 89(53), Fall Meeting Supplementary, Abstract GP44A-02.

Huber, B.T., and Sloan, L.C., 2001. Heat transport, deep waters, and thermal gradients: coupled simulation of an Eocene greenhouse climate. Geophysical Research Letters, 28, 3481–3484.

Huchon, P., Jestin, F., Cantagrel, J.M., Gaulier, J.M., Al Khirbash, S., and Gafaneh, A., 1991. Extensional deformations in Yemen since Oligocene and the Afar triple junction:.Annales Tectonicae, 5, 141–163.

Huchon, P., and Khanbari, Kh., 2003. Rotation of the syn-rift stress field of the northern Gulf of Aden margin, Yemen. Tectonophysics, 364, 147–166.

Hurley, N.F., and Lohmann, K.C., 1989. Diagenesis of Devonian reefal carbonates in the Oscar Range, Canning Basin, Western Australia. Journal of Sedimentary Petrology, 59, 127-146.

Hye In Ahn, B.S., 2010. Mineralogy and geochemistry of the nonsulfide Zn deposits in the Sierra Mojada district, Coahuila, Mexico: Unpublished Ph.D dissertation. University of Texas at Austin, USA 193 pp.

Jacobs, E., Weissert, H., and Shields, G., 1996. The Monterey event in the Mediterranean: a record from shelf sediments of Malta. Paleoceanography, 11, 717–728.

Jassim, S.Z., and Goff, J.C., 2006. Phanerozoic development of the northern Arabian Plate, *in:* Jassim, S.Z., Goff, J.C. (Eds.), Geology of Iraq. Dolin, Prague, 32–44.

Jenkyns, H.C., Jones, C.E., Gröcke, D.R., Hesselbo, S.P., and Parkinson, D.N., 2002. Chemostratigraphy of the Jurassic System: application, limitations and implications for palaeocenography. Journal of Geological Society London, 159, 351–378.

Joachimski, M.M., van Geldern, R., Breisig, S., Buggisch, W., and Day, J., 2004. Oxygen isotope evolution of biogenic calcite and apatite during the Middle and Late Devonian. International Journal of Earth Science, 93, 542–553.

Johnson, C.A., 2001. Geochemical constraints on the origin of the Sterling Hill and Franklin zinc deposits, and the Furnace magnetite bed, northwestern New Jersey. Society of Economic Geologists Guidebook Series, 35, 89–97.

Jonasson, I.R., Jackson, L.E., and Sangster, D.F., 1983. A Holocene zinc orebody formed by supergene replacement of mosses. Journal of Geochemical Exploration, 18, 189–194.

Jones, D.L., Howell, D.G., Coney, P.J., and Monger, J.W.H., 1983. Recognition, character, and analysis of tectonostratigraphic terranes in western North America, *in:* Hashimoto, M., and Uyeda, S., eds., Accretion tectonics in the Circum-Pacific Regions. Tokyo, Terra Scientific Publishing Company, 21-35.

Jurjovec, J., Ptacek, C.J., and Blowes, D.W., 2002. Acid neutralization mechanisms and metal release in mine tailings: a laboratory column experiment. Geochimica et Cosmochimica Acta, 66, 1511–1523.

Karig, D.E., and Kozlu, H., 1990. Late Paleogene evolution of the triple junction region near Maras, south-central Turkey. Journal of Geological Society of London 147, 1023–1034.

Keith, M. L., and Weber, J. N., 1964. Carbon and oxygen isotopic composition of selected limestones and fossils. Geochimica et Cosmochimica Acta, 28, 1787-1816.

Kelley, K.D., Leach, D.L., and Johnson, C.A., 2000. Sulfur-, oxygen-, and carbon-isotope studies of Ag-Pb-Zn vein breccia occurrences, sulfide bearing concretions, and barite deposits in the north-central Brooks Range, with comparisons to shale-hosted massive sulfide deposits, *in:* Kelley, K.D., and Gough, L.P., (Eds.), Geologic studies in Alaska by the U.S. Geological Survey, 1998. U.S. Geological Survey Professional Paper 1615, 189–201.

Kelley, K.D., and Kelley, D.L., 2003. Metal dispersion and mobility in soils from the Lik Zn-Pb-Ag sulfide deposit, NW Alaska: environmental and exploration implications. Geochemistry, Exploration, Environment, Analysis, 3, 179–195.

Kelley, K.D., Leach, D.L., and Johnson, C.A., Clark, J.L., Fayek, M., Slack, J.F., Anderson, V.M., Ayuso, R.A., and Ridley, W.I., 2004. Textural, compositional, and sulfur isotope variations of sulfide minerals in the Red Dog Zn-Pb-Ag deposits, Brooks Range, Alaska: implications for ore formation. ECONOMIC GEOLOGY, 99, 1509–1532.

Kelley, K.D., and Jennings, S., 2004. A special issue devoted to barite and Zn-Pb-Ag deposits in the Red Dog district, western Brooks Range, Alaska. ECONOMIC GEOLOGY, 99, 1267–1280.

Kesler, S.E., and Ascarrunz-K, R., 1973. Lead-zinc mineralization in carbonate rocks, central Guatemala. ECONOMIC GEOLOGY, v. 68, 1263–1274.

Ketin, I., 1966. Tectonic units of Anatolia (Asia Minor). Mineral Resource and Exploration Institute of Turkey (MTA) Bulletin, 66, 22–34.

Kim, S.T., Mucci, A., and Taylor, B.E., 2007. Phosphoric acid fractionation factors for calcite and aragonite between 25 and 75° C, revisited. Chemical Geology, 246, 135–146.

Koptagel, O., Ulusoy, U., and Efe, A., 2005. A study of sulfur isotopes in determining the genesis of GšynŸk and CelaldaÛÝ Desandre Pb–Zn deposits, Eastern YahyalÝ, Kayseri, Central Turkey. Journal of Asian Earth Science, 25, 279–289.

Lange, I.M., Nokleberg, W.J., Newkirk, S.R., Aleinikoff, J.N., Church, S.E., and Krouse, H.R., 1993. Devonian volcanogenic massive sulfide deposits and occurrences, southern Yukon-Tanana terrane, eastern Alaska Range, Alaska. ECONOMIC GEOLOGY, 88, 344-376.

Large, D., 2001. The geology of non-sulphide zinc deposits - an overview. Erzmetall, 54, 264–276.

Larson A.C., and Von Dreele R.B., 2000. GSAS General Crystal Structure Analysis System. Report No. LAUR-86-748, Los Alamos National Laboratory, NM, USA.

Leach, D.L., Marsh, E., Emsbo, P., Rombach, C., Kelley, K.D., Reynolds, J., and Anthony, M., 2004. Nature of the hydrothermal fluids at the shale-hosted Red Dog zinc-lead-silver deposits, Brooks Range, Alaska. ECONOMIC GEOLOGY, 99, 1449–1480.

Leach, D.L., Sangster, D.F., Kelley, K.D., Large, R.R., Garven, G., Allen, C.R., Gutzmer, J., and Walters, S., 2005. Sediment-hosted lead-zinc deposits: a global perspective, *in:* Hedenquist, J.W., Thompson, J.F.H., Goldfarb, R.J., and Richards, J.P., (Eds.), ECONOMIC GEOLOGY 100th Anniversary Volume, 1905-2005: Littleton, Colorado, Society of Economic Geologists, Inc., 561-608.

Lindth, T. B., Saltzman, E. S., Sloan, J.L., Mattes, B.W., and Holser, W.T., 1981. A revised 13C-age curve. Geological Society of America, Abstracts with Programs, 13(498), 561–607.

Lips, A.L.W., 2007. Geodynamic causes of copper and gold concentrations in the Tethys Belt, *in:* Andrew, C.J., et al. eds., Proceedings of the Ninth Biennial Meeting of the Society for Geology Applied to Mineral Deposits (SGA), Dublin, Ireland, August 20–23, 2007, 93–96.

Liu, Y., Gupta, R., Sharma, A., Wall, T., Butcher, A., Miller, G., Gottlieb, P., and French, D., 2005. Mineral matter-organic matter association characterisation by QEMSCAN® and applications in coal utilization. Fuel, 84(10), 1259-1267.

Loan, M., Newman, O.M.G., Cooper, R.M.G., Farrow, J.B., and Parkinson, G.M., 2006. Defining the paragoethite process for iron removal in zinc hydrometallurgy. Hydrometallurgy, 81(2), 104-129.

Lotter, N.O., Kowal, D.L., Tuzun, M.A., Whittaker, P.J., and Kormos, L., 2003. Sampling and flotation testing of Sudbury Basin drill core for process mineralogy modelling. Minerals Engineering, 16(9), 857-864.

Lotter, N.O., 2011. Modern process mineralogy: an integrated multi-disciplined approach to flowsheeting. Minerals Engineering, Special issue. Process Mineralogy, 24(12), 1229-1237.

Mair, J.L., Hart, C.J.R., and Stephens, J.R., 2006. Deformation history of the northwestern Selwyn Basin, Yukon, Canada: implications for orogen evolution and mid-Cretaceous magmatism. GSA Bulletin, 118, 304-323.

Mattash, M.A., Vaselli, O., Minissale, A., Ad-Dukhain, A., and Hazza, M., 2005. The First Geothermal Resources Map of Yemen, at a 1: 125 000 scale, Ministry of Oil and Mineral Resources, ed., Sana'a (Republic of Yemen).

Mattash, M.A., and Balog, K., 1994. K-Ar radiometric age data on Cenozoic volcanics and their associated Tertiary intrusions from Yemen. Acta Mineralogica-Petrographica, Sgezed-Hungary, 83-92.

Matthew, I.G., and Elsner, D., 1977. The processing of zinc silicate ores- a review. Metallurgical and Materials Transactions B, 8, 85-91.

Mayfield, C.F., Curtis, S.M., Ellersieck, I.F., and Tailleur, I.L. et al., 1979. Reconaissance geology of the Ginny Creek Zn-Pb-Ag and Nimiuktuk barite deposits, northwestern Brooks Range, Alaska. U.S. Geological Survey Open File Report 79-1092, p. 19.

McClelland, W.C., Kusky, T., Bradley, D.C., Dumoulin, J., and Harris, A.G., 1999. The nature of Nixon Fork ''basement'', west-central Alaska. Geological Society of America, Abstracts with Programs 31(6), A-78.

McPhail, D.C., Summerhayes, E., Welch, S., and Brugger, J., 2003. The geochemistry and mobility of zinc in the regolith, *in:* Roach, I.C., (Ed.), Advances in Regolith 2003, 287–291.

Megaw, P.K.M., Ruiz, J., and Titley, S.R., 1988. High temperature, carbonate-hosted Ag-Pb-Zn(Cu) deposits of northern Mexico. ECONOMIC GEOLOGY, 83, 1856–1885.

Menzies, M., Al-Kadasi, M.A., Al-Khirbash, S., Al-Subbary, A.K., Baker, J., Blakey, K.R., Nichols, G., and Yelland, A., 1994. Geology of Yemen, *in:* Geological Survey and Mineral Exploration Board, Ministry of Oil and Mineral Resources, Republic of Yemen, (Ed.), Geology and Mineral Resources of Yemen, 21–48.

Menzies, M., Gallagher, K., Yelland, A., and Hurford, A.J., 1997. Volcanic and non-volcanic rifted margins of the Red Sea and Gulf of Aden: crustal cooling and margin evolution in Yemen. Geochimica Cosmochimica Acta, 61, 2511–2527.

Metaleach: <http://www.metaleach.com> (accessed 10/01/2015).

Miller, P.R., Reid, A.F., and Zuiderwyk, M.A., 1982. QEM*SEM image analysis in the determination of modal assays, minerals associations and mineral liberation. Proceedings of the 14th International Mineral Processing Congress, October 17-23, Toronto, Canada.

Miller, E.L., Gehrels, G. Pease, V., and Sokolov, S., 2010. Stratigraphy and U-Pb detrital zircon geochronology of Wrangel Island, Russia: Implications for Arctic paleogeography. American Association of Petroleum Geologists Bulletin, 94, 665-692.

Miller, E.L., Kuznetsov, N., Soboleva, A., Udoratina, O., Grove, M.J., and Gehrels, G., 2011. Baltica in the Cordillera? Geology, 39, 791-794.

Miller, M.L., and Bundtzen, T.K., 1992. Geological history of the post-accretionary rock, Idiatrod quadrangle, west-central Alaska. Geological Society of America, Abstracts with Program, Cordilleran Section, 24, p.71.

Moll, E.J., Silberman, M.L., and Patton, W.W. Jr., 1981. Chemistry, mineralogy, and K-Ar ages of igneous and metamorphic rocks of the Medfra quadrangle, Alaska: U.S. Geological Survey Open-File Report 80-811-C, 15 p., 2 sheets, scale 1:250,000.

Mondillo, N., 2013. Supergene Nonsulfide Zinc-Lead Deposits: the examples of Jabali (Yemen) and Yanque (Peru), PhD dissertation, Università degli Studi di Napoli, Federico II, 185 pp.

Mondillo, N., Boni, M., Balassone, G., and Grist, B., 2011. In search of the lost zinc: a lesson from the Jabali (Yemen) nonsulfide zinc deposit. Journal of Geochemical Exploration, 108, 209–219.

Mondillo, N., Boni, M., Balassone, G., Joachimski, M., and Mormone, A., 2014. The Jabali Nonsulfide Zn-Pb-Ag Deposit, Western Yemen. Ore Geology Reviews, 61, 248-267.

Monger, J.W.H., Price, R.A., and Templeman-Kluit, D.J., 1982. Tectonic accretion and the origin of the major metamorphic and tectonic welts in the Canadian Cordillera. Geology, 10, 70-75.

Monteiro, L.V.S., Bettencourt, J.S., Juliani, C., and De Olivera, T.F., 2006. Geology, petrography, and mineral chemistry of the Vazante non-sulfide and Ambrosia and Fagundes sulfide-rich carbonate-hosted Zn–(Pb) deposits, Minas Gerais, Brazil. Ore Geological Reviews, 28, 201–234.

Moore, T.E., Wallace, W.K., Bird, K.J., Karl, S.M., Mull, C.G., and Dillon, J.T., 1994. Geology of northern Alaska, *in*: Palfker, G., and Berg, H.C., (Eds.), The Geology of Alaska. Geological Society of America, The Geology of North America, G-1, 49-140.

Moore, J.M., 1972. Supergene mineral deposits and physiographic development in southwest Sardinia, Italy. Transactions of the Institution of Mining and Metallurgy, Section B, 71, B59–B66.

Moscariello, A., Burns, S., Walker, D., Power, M.R., Kitson, W.S., and Sliwinski, J., 2010. Sequence Stratigraphy and Reservoir Characterization of Barren Fluvial Sequences Using Rock-Typing Analyses of Core and Cuttings, AAPG Geo 2010, Middle East Geoscience Conference and Exhibition, Innovative Geoscience Solutions – Meeting Hydrocarbon Demand in Changing Times. March 7-10 2010 – Manama, Bahrain.

Mosher, G., 1990. Reef Ridge Project: Pasminco Exploration Ltd., Doyon, Limited Report 92-72, 19 p. (Report held by Doyon, Limited, Fairbanks, Alaska).

MSA Group Ltd. Technical Report on the Hakkari Zinc Project, NI 43–101, August 3 2011, <http://www.sedar.com> (accessed 20/1/2015).

MSA Group Ltd., Technical Report on the Hakkari Zinc Project, Turkey, NI 43–101, July 26, 2013. <http://www.sedar.com< (accessed 20/1/2015).

Mutlu, H., Güleç, N., Hilton, D.R., Aydin, H., and Halldórsson, S.A., 2012. Spatial variation in gas and stable isotope compositions of thermal fluids around Lake Van: Implications for crust-mantle dynamics Turkey. Chemical Geology, 300-301, 165–176.

Nelson, J.L., Paradis¸ S., Christensen, J., and Gabite, J., 2002. Canadian Cordillera Mississipi Valley-type deposits: a case for Devonian-Mississipian back-arc hydrothermal origin. ECONOMIC GEOLOGY, 97, 1013-1036.

Nelson,J.L., Colpron, M., Piercey, S.J., Dusel-Bacon, C., Murphy, D.C., and Roots, C.F., 2006. Paleozoic tectonics and metallogenetic evolution of pericratonic terranes in Yukon, northern British Columbia and eastern Alaska. Geological Association of Canada, Special Paper 45, 323-360.

Nelson, J.L., and Colpron, M., 2007. Tectonics and metallogeny of the Canadian and Alaskan Cordillera, 1.8 Ga to present: Mineral Deposit Division, Geological Association of Canada, Special Pubblication 5, 755-791.

Nelson, J.L., Diakow, L.J., van Staal C., and Chipley, D., 2013. Ordovician volcanogenic sulfide occurrences in the southern Alexander terrane, coastal NW British Columbia: geology, Pb isotopic signature and a case for correlation with Appalachian and Scandinavian deposits; BC Geological Survey Fieldwork 2012, Paper 2013-1, 13-34.

Newberry, R.J., Crafford, T.C., Newkirk, S.R., Young, L.E., Nelson, S.W., and Duke, N.A., 1997. Volcanogenic massive sulfide deposits of Alaska. ECONOMIC GEOLOGY Monograph 9,120-150.

Nokleberg, W.J., and Winkler, G.R., 1982. Stratiform zinc-lead deposits in the Drenchwater Creek area, Howard pass quadrangle, northwestern Brooks Range, Alaska. U.S. Geological Survey Professional Paper 1209, 22 pp.

Nokleberg, W.J., Brew, D.A., Grybeck, D., Yeend, W., Bundtzen, T.K., Robinson, M.S., and Smith, T.E., 1994. Metallogeny and major mineral deposits of Alaska, in Plafker, G., and Berg, H.C., eds, The Geology of Alaska: Boulder, Colorado, Geological Society of America, The Geology of North America, G-1, 855-903.

Okay, A.I., and Şahintürük Ö., 1997. Geology of the Eastern Pontides, *in:* A. Robinson ed., Regional and Petroleum Geology of the Black Sea and Surrounding Regions. American Association of Petroleum Geologists, Memoir 68, 291-311.

Okay, A.I., and Tüysüz, O., 1999. Tethyan sutures of northern Turkey, *in:* Durand, B., Jolivet, L., Horvath, D., Serranne, M. eds.,The Mediterranean basins: Tertiary extension

within the Alpine Orogen. Geological Society of London, Special Publication, 156, 475–515.

Okay, A. I., Tansel, I., and Tüysüz, O., 2001. Obduction, subduction and collision as reflected in Upper Cretaceous-Lower Eocene sedimentary record of western Turkey. Geological Magazine, 138, 117-142.

Önal, M., Tuzcu, N., and Helvacı, C., 1990. Geological setting, mineralogy and origin of the Cafana (Malatya) Zn–Pb sulfide and carbonate deposit, E Anatolia, Turkey, *in:* Savascın, M.Y., Eronat, A.H. (Eds.), International Earth Sciences Congress on Aegean Regions, Proceedings, 1, 52–58.

Paradis, S., Keevil, H., Simandl, G.J., and Raudsepp, M., 2011. Geology and mineralogy of carbonate-hosted nonsulfide Zn-Pb mineralization in southern (NTS 082F/03) and central (NTS 093A/14E, 15W) British Columbia. Geoscience BC Summary of Activities 2010, Geoscience BC, Report 2011-1, 143–168.

Pascoe, R.D., Power, M.R., and Simpson, B., 2007. QEMSCAN® analysis as a tool for improved understanding of gravity separator performance. Minerals Engineering, 20, 487– 495.

Patton, W.W. Jr., Moll, E.J., Dutro, J.T., Jr., Silberman, M.L., and Chapman, R.M., 1980. Preliminary geologic map of the Medfra quadrangle, Alaska: U.S. Geological Survey Open-File Report 80-811, one sheet at 1:250,000 scale.

Patton, W.W., Box, S.E., Moll-Stalcup, E.J., and Miller, T.P., 1994. Geology of west-central Alaska. *in:* Plafker, G., Berg, H.C. (Eds.), The Geology of Alaska. Geological Society of America, Boulder, CO, DNAG Series, G-1, 241–269.

Perinçek, D., 1979. The geology of Hazro-Korudag-Çüngüs-Maden-Ergani-Hazer-Elazig-Malatya area. Ankara, Turkey, Türkiye Jeoloji Kurumu Yaini, 34 pp.

Perinçek, D., 1990. Hakkari ili ve dolayının stratigrafisi, Güneydoğu Anadolu, Türkiye. TPJD Bulletin, 2(1), 21-68 (in Turkish with English abstract).

Piercey, S.J., Nelson, J.L., Colpron, M., Dusel-Bacon, C., Simard, R.L., and Roots, C.F., 2006. Paleozoic magmatism and crustal recycling along the ancient Pacific margin of North America, northern Cordillera. Geological Association of Canada, Special Paper 45, 281-322.

Pirrie, D., Butcher, A.R., Power, M.R., Gottlieb, P., and Miller, G.L., 2004. Rapid quantitative mineral and phase analysis using automated scanning electron microscopy (QEMSCAN®); potential applications in forensic geoscience, *in:* Pye, K., Croft, D.J. (Eds.), Forensic Geoscience, Principles, Techniques and Applications, v. 232. Geological Society Special Publication, London, 23–136.

Pirrie, D., Rollinson, G.K., 2011. Unlocking the applications of automated mineral analysis. Blackwell Publishing Ltd, The Geologists' Association & The Geological Society of London, Geology Today, Vol. 27, No. 6, November–December 2011.

Plafker, G., and Berg, C., 1994. Overview of the geology and tectonic evolution of Alaska, *in:* Plafker, G., and Berg, H.C. (Eds.), The Geology of Alaska. Geological Society of America, The Geology of North America, G-1, 989-1022.

Prokoph, A., Shields, G.A., and Veizer, J., 2008. Compilation and time-series analysis of a marine carbonate $\delta^{18}O$, $\delta^{13}C$, $^{87}Sr/^{86}Sr$ and $\delta^{34}S$ database through Earth history. Earth-Science Reviews, 87, 113–133.

Raymo, M.E., and Ruddiman, W.F., 1992. Tectonic forcing of late Cenozoic climate. Nature, 359, 117–122.

Reichert, J., and Borg, G., 2008. Numerical simulation and a geochemical model of supergene carbonate-hosted non-sulphide zinc deposits. Ore Geology Reviews, 33, 134–151.

Reid, A.F., Gottlieb, P., MacDonald, K.J. and Miller, P.J. 1984. QEM*SEM image analysis of ore minerals: volume fraction, liberation and observational variances. Proceedings of the 2nd International Congress on Applied Mineralogy in the Minerals Industry, February 22-25, Los Angeles, California.

Reynolds, N., and Large, D., 2010. Tethyan zinc–lead metallogeny in Europe, North Africa, and Asia. ECONOMIC GEOLOGY Special Publication, 15, 339–365.

Ricou, L.E., 1994. Tethys reconstructed: plates, continental fragments and their boundaries since 260 Ma from central America to south-eastern Asia. Geodinamica Acta 7, 169–218.

Rigo de Righi, M., and Cortesini, A., 1964. Gravity tectonics in foothills structure belt of southeast Turkey. American Association of Petroleum Geology Bullettin, 48, 1911–1937.

Rietveld, H.M., 1969. A profile refinement method for nuclear and magnetic structures. Journal of Applied Crystallography, 2, 67-71.

Robertson Research Minerals Limited, 1993. Prospecting for lead-zinc in the region between Ataq and Al Mithaf, Republic of Yemen: Republic of Yemen Geological and Mineral Exploration Board, Mineral Planning, Coordination and Human Power, Development Programme. Report number 1, p. 14.

Robertson, A.H.F., Grasso, M., 1995. Overview of the Late Tertiary tectonic and paleoenviromental development of the Mediterranean region. Terra Nova, 7, 114–127.

Rockingham, C., 1993. Johnson River: Alaska's Jurassic Park (abs.): Alaska Mineral Association Annual Convention, Anchorage, Alaska, November 1-5, 1993, Abstracts and Papers, p.2.

Roeske, S.M., McClelland, W.C., and Bradley, D.C., 2006. Ruby terrane, north-central Alaska [abs.[: Composite of continental affinity rocks. Geological Society of America, Abstracts with Program, Cordilleran Section Meeting, 38(5), p.12.

Rollinson, G., Andersen, J.C.Ø., Stickland, R.J., Boni, M., and Fairhurst, R., 2011. Characterization of non-sulphide zinc deposits using QEMSCAN®. Minerals Engineering, 24, 778–787.

Rose, A.W., Hawkes, H.E., and Webb, J.S., 1979. Geochemistry in mineral exploration. London, Academic Press, 657 pp.

Rosenbaum, J., and Sheppard, S.M., 1986. An isotopic study of siderites, dolomites and ankerites at high temperatures. Geochimica et Cosmochimica Acta, 50, 1147–1150.

Ross, C.S., 1946. Sauconite – a clay mineral of the montmorillonite group. American Mineralogist, 31, 411–424.

Rowe, P.J., Mason, J.E., Andrews, J.E., Marca, A.D., Thomas, L., Van Calsteren, P., Jex, C.N., Vonhof, H.B., and Al-Omari, S., 2012. Speleothem isotopic evidence of winter rainfall variability in northeast Turkey between 77 and 6 ka. Quaternary Science Review, 45, 60–72.

Rubin, C.M., Miller, M.M., and Smith, G.M., 1990. Tectonic development of mid-Paleozoic volcanic-plutonic complexes: evidence for convergent margin tectonism. Geological Society of America, Special Paper 255, 1-16.

Sağıroğlu, A., 1988. Cafana (Görgü), Malatya carbonated Zn–Pb deposits. Bulletin of the Faculty of Eng., Cum. Uni., s. A-Earth Sciences, 5 (1) (in Turkish with English abstract).

Sangameshwar, S.R., and Barnes, H.L., 1983. Supergene processes in zinc-lead-silver sulfide ores in carbonate rocks. ECONOMIC GEOLOGY, 78, 1379–1397.

Santoro, L., Boni, M., Herrington, R., and Clegg, A., 2013. The Hakkari nonsulfide Zn–Pb deposit in the context of other nonsulfide Zn–Pb deposits in the Tethyan Metallogenic Belt of Turkey. Ore Geology Reviews, 53, 244–260.

Santoro, L., Boni, M., Rollinson, G.K., Mondillo, M., Balassone, G., and Clegg, A., 2014. Mineralogical characterization of the Hakkari nonsulfide Zn(Pb) deposit (Turkey): the benefits of QEMSCAN®. Minerals Engineering, 69, 29-39.

Santoro, L., Rollinson, G.K., Boni, M., and Mondillo, N., in press. Automated Scanning Electron Microscopy (QEMSCAN®) based mineral identification and quantification of the Jabali Zn-Pb-Ag nonsulfide deposit (Yemen). ECONOMIC GEOLOGY.

Santoro, L., Boni, M., Mondillo, N., Joachimski, M., and Woodman, J.A., in press. Cold Supergene Zinc Deposit in Alaska: the Reef Ridge case. Geological Society of America Bulletin.

Sass-Gustkiewicz, M., Dzulynski, S., and Ridge, J.D., 1982. The emplacement of zinc-lead sulfide ores in the Upper Silesian district—A contribution to the understanding of Mississippi Valley-type deposits. ECONOMIC GEOLOGY, 77, 392–412.

Schippers, A., 2003. Long-term anaerobic microbial processes in remediated mine tailings. Mitigation of the environmental impact from mining waste (MiMi). MiMi Print, Luleå, Sweden.

Schmidt, J.M., 1997a. Shale-hosted Zn-Pb-Ag and barite deposits of Alaska, *in*: Goldfarb, R.J., and Miller, L.D., (Eds.), Mineral deposits of Alaska, 1997. ECONOMIC GEOLOGY Monograph 9, 35-65.

Schmidt, J.M., 1997b, Strata-bound carbonate-hosted Zn-Pb and Cu deposits of Alaska, *in*: Goldfarb, R.J., and Miller, L.D., (Eds.), Mineral deposits of Alaska, 1997. ECONOMIC GEOLOGY Monograph 9, 90- 119.

Schmidt, J.M., and Zierenberg, R.A., 1987. The Red Dog Pb-Zn-Ag deposit, Alaska: an example of non-exhalative processes in the formation of syngenetic massive sulfides (abs.). U.S. Geological Survey Circular 995, p.61.

Schmidt, J.M., and Werdon, M.B., 1993. Clastic-hosted stratiform, vein/breccia and disseminated Zn-Pb-Ag deposits of the northwestern Brooks Range, Alaska: are they different expressions of dewatering of the same source basin? (abs.). Geological Society of America Abstracts with Programs, 25, p.143.

Şengör, A.M.C., 1987. Tectonics of the Tethysides: Orogenic collage development in a collisional setting. Annual Review of Earth and Planetary Sciences 15, 213-244.

Şengör, A.M.C., and Yilmaz, Y., 1981. Tethyan evolution of Turkey, a plate tectonic approach. Tectonophysics, 75, 181-241.

Silver, M., and Torma, A.E., 1974. Oxidation of metal sulfides by Thiobacillus ferrooxidans grown on different substrates. Canadian Journal of Microbiology, 20, 141-147.

Simard, R-L., Dostal, J., and Roots, C.F., 2003. Development of Late Paleozoic volcanic arcs in the Canadian Cordillera: an example from the Klinkit Group, northern British Columbia and southern Yukon. Canadian Journal of Earth Sciences, 40, 907-924.

Singer, P.C., and Stumm, W., 1970. Acidic mine drainage; rate-determining step. Science, 167, 1121-1123.

Skarpelis, N., and Argyraki, A., 2009. The geology and origin of supergene ores in Lavrion (Attica, Greece). Resource Geology, 59, 1-14.

Skerl, A.C., 1934. Vanadium at the Rhodesia Broken Hill. Mineralogical Magazine, 50, 280–283.

Slezak, P.R., Olivo, G.R., Diniz Oliveira, G., Marcel, A., and Dardenne, M.A., 2014. Geology, mineralogy, and geochemistry of the Vazante Northern Extension zinc silicate deposit, Minas Gerais, Brazil. Ore Geology Reviews, 56, 234–257.

Smythe, D.M., Lombard, A., and Coetzee, L.L., 2013. Rare Earth Element deportment studies utilising QEMSCAN® technology. Minerals Engineering, 52(3), 265-277.

Souza, A.D., Pina, P.S., Leão, V.A., Silva, C.A., and Siqueira, P.F., 2007. The leaching kinetics of a zinc sulphide concentrate in acid ferric sulphate. Hydrometallurgy, 89(1-2), 72-81.

SRK Consulting, 2005. Jabali Feasibility Study, Geology and Resources: Unpublished report, ZincOx Resources plc., p. 45.

Stampfli, G. M., 1996. The Intra-Alpine terrain: a Paleotethyan remnant in Alpine Variscides. Eclogae Geologicae Helvetiae, 89, 13-42.

Stumm, W., and Morgan, J.J., 1996. Acquatic Chemistry – Chemical Equilibria and Rates in Natural Waters, 3rd edition. John Wiley and Sons, New York. 1040 pp.

Sungurulu, O., 1974. VI, Bölge Kuzey sahalarinin jelojisi (Geology of the northern part of Petroleum district-VI), *in*: Okay, H., and Dileköz, E., (Eds.), 2nd Petroleoum Congress of Turkey, Proceedings: Ankara, Turkey, Association of Petroleoum Geologists, 87-107.

Szumigala, D.J., 1986. Geology and geochemistry of the Tin Creek skarn prospects, Farewell mining district, SW Alaska: Unpublished M.S. thesis, Fairbanks, Alaska, University of Alaska, 144 pp.

Takahashi, T., 1960. Supergene alteration of zinc and lead deposits in limestone. ECONOMIC GEOLOGY, 55, 1084-1115.

Thornber, M.R., and Taylor, G.F., 1992. The mechanisms of sulphide oxidation and gossan formation, *in:* Butt, C.R.M., and Zeegers, H., eds., Regolith exploration geochemistry in tropical and subtropical terrains, *in* Govett, G.J.S., ed., Handbook of exploration geochemistry, Amsterdam, Elsevier, 4, 119–138.

Toby B.H., 2001. EXPGUI, a graphical user interface for GSAS. Journal of Applied Crystallography 34, 210–213.

Tolun, N., and Pamir, H.N., 1975. Explanatory Booklet for the Hatay Sheet of the Geological Map of Turkey, 1:500,000 Scale. General Directorate of Mineral Research and Exploration, Ankara.

Tomizuka, N., and Yagisawa, M., 1978. Optimum conditions for leaching of uranium and oxidation of lead sulfide with thiobacillus ferrooxidans and recovery of metals from bacterial leaching solution with sulfate-reducing bacteria, *in:* Murr, L.E., Torma, A.E., Brierley, J.A. (Eds.), Metallurgical Applications of Bacterial Leaching and Related Microbiological Phenomena. Academic Press, New York, 321–344.

Tüysüz, O., Dellaloglu, A.A., and Terziglou, N., 1995. A magmatic belt within the Neotethyan suture zone and its role in the tectonic evolution of northern Turkey. Tectonophysics, 243, 173-191.

Tüysüz, O., 1999. Geology of the Cretaceous sedimentary basins of the Western Pontides. Geological Journal, 34, 75-93.

USGS mineral resources on-line spatial http://mrdata.usgs.gov/ardf/show-ardf.php?ardf_num=MG068 (accessed 24/01/2015).

USGS mineral resources on-line spatial http://mrdata.usgs.gov/ardf/show-ardf.php?ardf_num=MG059 accessed 24/01/2015).

USGS mineral resources on-line spatial http://mrdata.usgs.gov/ardf/show-ardf.php?ardf_num=MG089 accessed 24/01/2015).

USGS mineral resources on-line spatial http://mrdata.usgs.gov/ardf/show-ardf.php?ardf_num=MM166 accessed 24/01/2015).

Vache, R., 1964. Antitoroslardaki Bakırdağ Kurşun Çinko Yatakları (Kayseri). MTA dergisi, 62, 87–98 (in Turkish).

Van Staal, C., 2007. Pre-Carboniferous metallogeny of the Canadian Appalachians, *in:* Goodfellow, W.D. (Ed.), Mineral Deposits of Canada: A Synthesis of Major Deposit Types, District Metallogeny, the Evolution of Geological Provinces, and Exploration Methods. Mineral Deposit Division, Geological Association of Canada, Special Publication 5, 793-818.

Venter, M., and Robertson, M., 2009. Desktop, remote sensing and field validation. Internal Report for Red Crescent Resources A.Ş.

Veslov, V., 1990. Explanatory note to prediction minerogenic map of the southern part of Republic of Yemen on scale 1:500000: v. 1-2, v. 1, 291p., v. 2, 59 p., register of metallic and non-metallic mineral deposits and occurences, USSR Ministry of Geology, Moscow.

Walsh, J.N., Gill, R., and Thirlwall, M.F., 1997. Dissolution procedures for geological and environmental samples, *in*: Gill, R. (Ed.), Modern analyical geochemsitry, an introduction to quantitive chemical analysis for earth, environmental and materials scientists. Longman, 29-40.

Webmineral: http://www.webmineral.com (accessed 11/01/2015).

Weiss, C., O'Neill, D., Koch, R., and Gerlach, I., 2009. Petrological characterization of 'alabaster' from the Marib province in Yemen and its use as an ornamental stone in Sabaean culture. Arabian archaeology and epigraphy, 20, 54–63.

Werdon, M.B., 1996. Drenchwater, Alaska: Zn-Pb-Ag mineralization in a mixed black shale-volcanic environment, *in:* Coyner, A.R., and Fabey, P.L., (Eds.), Geology and ore deposits of the American Cordillera-geological Society of Nevada Symposium Proceedings, Reno/Sparks, Nev., April 1995, 1341-1354.

Whitehouse, M.J., Windley, B., Ba-Bttat, M.A.O., Fanning, C.M., and Rex, D.C., 1998. Crustal evolution and terrane correlation in the eastern Arabian Shield, Yemen: geochronological constraints. Journal of Geological Society (London), 155, 281–296.

Williams, P.A., 1990. Oxide zone geochemistry. Ellis Horwood Ltd., Chichester, UK, 286 pp.

Wilson, F.H., Dover, J.H., Bradley, D.C., Weber, F.R., Bundtzen, T.K., and Haeussler, P.J., 1998. Geologic map of central (interior) Alaska: U.S. Geological Survey Open-File Report 98–133, p. 64, scale 1:500,000 (also released as a CD-ROM).

Woollett, A., 2005. The processing of non-sulphide zinc deposits, *in:* Boni, M., Gilg, H.A. eds., European Science Foundation (ESF) Workshop on Nonsulfide Zn–Pb Deposits, Iglesias, 21–23 April 2005. Abstract p. 1.

Woollett, A.C., Masson, N.J.G., and Stone, K.M., 2002. Jabali/Yambu – A new source of zinc in the Middle East: Society for Mining, Metallurgy, and Exploration Annual Meeting, Phoenix, Arizona, 25–27 February 2002, Preprint 02-123, p. 9.

Woodruff, F., and Savin, S.M., 1989. Miocene deepwater oceanography. Paleoceanography 4, 87–140.

Woodruff, F., and Savin, S.M., 1991. Mid-Miocene isotope stratigraphy in the deep sea: high resolution correlations, paleoclimatic cycles, and sediment preservation. Paleoceanography 6, 755–806.

Yalçin, N., 1976. Geology of the Narince-Gerger area (Adıyaman province) and its petroleum possibilities. Revue de la Faculté des Sciences de l'Université d'Istanbul, serie B, 41, 57-82.

Yang, W., Spencer, R., and Krouse, R.H., 1995. Stable isotope and major element compositions of fluid inclusions in Devonian and Cambrian dolomite cements, Western Canada. Geochimica et Cosmochimica Acta, 59, 3159-3172.

Yemen Geological Survey and Mineral Resources Board, 1994. Metallic Mineral Resources, *in:* Geological Survey and Mineral Exploration Board, Ministry of Oil and Mineral Resources, Republic of Yemen, (Ed.), Geology and Mineral Resources of Yemen, 61–87.

Yemen Geological Survey and Mineral Resources Board, 2009, Zn-Pb: *in* Geological Survey and Mineral Exploration Board, Ministry of Oil and Mineral Resources, Republic of Yemen, (Ed.), Mineral Resources of Yemen, 1, 8 pp..

Yigit, O., 2009. Mineral deposits of Turkey in relation to Tethyan metallogeny: implications for future mineral exploration. ECONOMIC GEOLOGY, 104, 19–51.

Ylmaz, Y., 1990. Comparisons of the young volcanic associations of the west and east Anatolia under the compressional regime: A review. Journal of Volcanology and Geothermal Research, 44, 69-87.

Yilmaz, Y., 1993. New evidence and model on the evolution of the Southeast Anatolian orogeny. Geological Society of America, Bulletin, 105, 251–271.

Yilmaz, A., Ünlü, T., and Sayili, I.S., 1992. An approach to the origin of Keban Lead-Zinc Mineralizations, Elaziğ, Turkey: a preliminary study. Mineral Resource Exploration Bulletin 114, 27–50.

Ylmaz, Y., Tüysüz, O., Ygtbas, E., Genç, S. C., and Sengör, A. M. C., 1997. Geology and tectonic evolution of the Pontides, *in*: Robinson, A. (Ed.), regional and Petroleoum geology of the Black Sea and surrounding region. American Association of Petroleum Geologist Memoir, 68, 183-226.

Yilmaz, Y., Genç, S.C., Gürer, Ö.F., Bozcu, M., Yilmaz, K., Karacik, Z., Altunkaynak, Ş., and Elmas, A., 2000. When did the western Anatolian grabens begin to develop? *in*: Bozkurt, E., Winchester, J.A., Piper, J.D.A. (Eds.), Tectonics and Magmatism in Turkey and the Surrounding Area. Geological Society of London, Special Publication, 173, 353–384.

Young, L.E., 1989. Geology and genesis of the Red Dog deposit, western Brooks Range, Alaska. Canadian Mining and Metallurgy Bulletin, 82(929), 57-67.

Youssef, E.S.A.A., 1998. Sequence stratigraphy of the Upper Jurassic evaporite-carbonate: sequence at the western area of Wadi Al-Jawj-Marib basin, Yemen. Carbonates and Evaporites, 13, 168–173.

Zeman, J., 1985. Supergene alteration of sulfides, II. A laboratory electrochemical study. Scripta Facultatis Scientiarum Naturalium Universitatis Purkynianae Brunensis. Geologia 15, 115–136.

ZincOx Resources plc. 2007. Annual Company Report. To be accessed at: <http://www.zincox.com/userfiles/file/pdf/080619_ZincOxAR07.pdf>.